
**Max-Planck-Institut für Metallforschung**
Stuttgart

# Segregation of Interstitial Impurities at Grain Boundaries in Transition Metals - Electronic Structure Calculations -

Rebecca Janisch

Dissertation
an der
**Universität Stuttgart**

Bericht Nr. 139
Juli 2003

# Segregation of Interstitial Impurities at Grain Boundaries in Transition Metals - Electronic Structure Calculations -

Von der Fakultät Mathematik und Physik der Universität Stuttgart zur Erlangung der Würde eines Doktors der Naturwissenschaften (Dr. rer. nat.) genehmigte Abhandlung

vorgelegt von

Rebecca Janisch

geboren in Bergneustadt

| | | |
|---|---|---|
| Hauptberichter | : | Prof. Dr. C. Elsässer |
| Mitberichter | : | Prof. Dr. U. Weiss |
| Tag der mündlichen Prüfung | : | 25.07.2003 |

Max-Planck-Institut für Metallforschung
Stuttgart
2003

Parts of this work are already published:

- R. Janisch and C. Elsässer
  *Segregated Light Elements at Grain Boundaries in Niobium and Molybdenum*
  Phys. Rev. B **67**, 224101 (2003).

# Zusammenfassung

In der vorliegenden Arbeit werden Ergebnisse von Elektronenstrukturrechnungen zum Thema Segregation an Korngrenzen in Übergangsmetallen vorgestellt. Die Rechnungen wurden mit einer ab-initio Methode der Dichtefunktionaltheorie in lokaler Näherung durchgeführt. Das hierzu benutzte "mixed-basis Pseudopotentialprogramm" [81] verwendet Pseudopotentiale zur Beschreibung der Wechselwirkung von Valenz- und Rumpfelektronen, sowie eine gemischte Basis aus ebenen Wellen und lokalisierten Funktionen zur Darstellung der Einelektron-Wellenfunktionen.

Die Arbeit lässt sich thematisch in drei Teile gliedern. Neben der Segregation von leichten interstitiellen Elementen (B, C, N, und O) an der $\Sigma 5$ (310)[001] symmetrischen Kippkorngrenze (eng.: symmetrical tilt grain boundary, STGB) in Mo und Nb (Kapitel 5) beschäftigt sie sich mit der Ausscheidung von nicht-stöchiometrischem Molybdänkarbid an der $\Sigma 5$STGB in Mo (Kapitel 6) und den Eigenschaften von einkristallinen Molybdänkarbiden bzw. -semikarbiden (Kapitel 7). Dabei werden die ab-initio Ergebnisse unter verschiedenen Blickwinkeln diskutiert:

- Was lernen wir über die Materialeigenschaften, und lassen sich diese Erkenntnisse anhand bekannter Modelle erklären, oder können sie zur Modellbildung beitragen?

- Inwiefern legen die Erfahrungen bei der Durchführung der Rechnungen, oder die Ergebnisse selbst die Anwendung eines weniger zeitaufwändigen, semi-empirischen Verfahrens nahe, und wenn ja, welches semi-empirische Modell scheint geeignet?

- Welche Informationen sind relevant für die Anpassung der freien Parameter eines solchen Modells und was wäre eine sinnvolle Fit-Strategie?

Die Resultate sollen im Folgenden zusammengefasst werden.

# Interstitielle Verunreinigungen an der Σ5 STGB in Mo und Nb

In Kapitel 5 wird eine detaillierte Analyse des Einflusses leichter interstitieller Fremdatome (B, C, N und O) an der Σ5 STGB in Nb und Mo auf die atomare Struktur und die Kohäsion der Grenzfläche durchgeführt. Teilweise motiviert wurde diese Untersuchung durch kontrovers diskutierte Ergebnisse experimenteller sowie theoretischer Untersuchungen des mikroskopischen Translationszustands der *reinen* Σ5 (310)[001] STGB in verschiedenen kubisch raumzentrierten (eng.: body-centred cubic, bcc) Übergangsmetallen.
Campbell et al. untersuchten diese Korngrenze mit Hilfe der hochauflösenden Transmissions-Elektronenmikroskopie (eng. High Resolution Transmission Electron Microscopy, HRTEM) und fanden einen spiegelsymmetrischen Translationszustand in Nb [14, 15] und eine Struktur, in der diese Spiegelsymmetrie durch eine relative Verschiebung der Körner entlang der [001]-Richtung gebrochen ist, in Mo [12] und Ta [13]. Kürzlich durchgeführte Untersuchungen von Sigle [108] weisen jedoch auf einen spiegelsymmetrischen Translationszustand in Mo hin. Aus theoretischer Sicht war die Situation lange Zeit ebenfalls nicht eindeutig. Semi-empirische Rechnungen ([78](Mo), [14, 93](Nb)) führten zu unterschiedlichen Ergebnissen in Abhängigkeit davon, ob das verwendete Wechselwirkungspotential winkelabhängige Beiträge enthielt, oder nicht. Dieser Punkt wurde von Ochs et al. aufgeklärt, die ab initio Gesamtenergierechnungen zur Σ5 STGB in den bcc Übergangsmetallen Nb, Mo, Ta und W durchführten. Die Ergebnisse zeigten einen interessanten, eindeutigen Trend: der Translationszustand der Korngrenze wird vom Füllungsgrad der Energiebänder mit *d*-Orbital Charakter bestimmt. Dies weist u.a. darauf hin, dass in der Tat nur Modelle, die winkelabhängige Vielteilchen-Wechselwirkungen enthalten, den korrekten Translationszustand in den bcc Übergangsmetallen vorhersagen können.
In dieser Arbeit verlassen wir nun die Annahme einer perfekten, reinen Korngrenze, um die teilweise widersprüchlichen experimentellen Ergebnisse und die zum Teil nicht vorhandene Übereinstimmung von Theorie und Experiment zu erklären. In der Tat lassen sich in einem realen System strukturelle Defekte wie z.B. Versetzungen oder Verunreinigungen kaum vermeiden. Der Einfluss von Verunreinigungen auf den Translationszustand stellt für ab-initio Rechnungen ein reizvolles Gebiet dar, da er relativ einfach zu untersuchen ist und einen Weg darstellt, die Zahl der Valenzelektronen im System systematisch zu variieren. Vorausgehende Untersuchungen der Segregation von C in Mo [65, 66] wiesen auch bereits darauf hin, dass interstitielle Verunreinigungen an der Σ5 STGB den Translationszustand

verändern können.
Es wurden nacheinander B, C, N und O als interstitielles Fremdatom an der $\Sigma 5$ STGB in Nb und Mo, sowohl in der spiegelsymmetrischen als auch in der nicht-spiegelsymmetrischen Konfiguration untersucht. Dabei ergab sich auch in der vorliegenden Arbeit ein eindeutiger Trend: Während mit B an der Korngrenze in Mo eindeutig die spiegelsymmetrische Konfiguration bevorzugt wird, nimmt dieser energetische Vorteil im Fall von C an der Grenzfläche ab, ist für N als Verunreinigung praktisch Null und wechselt dann das Vorzeichen, d.h. mit O an der Grenzfläche in Mo ist die nicht-spiegelsymmetrische Korngrenze energetisch günstiger. Dass dieser Trend mit der Valenzkonfiguration der betreffenden Elemente zusammenhängt, sieht man an der Tatsache, dass der beschriebene Vorzeichenwechsel für Nb als Wirtsmetall, das ein $d$-Elektron weniger als Mo hat, "ein Element später" auftritt, also erst mit O an der Korngrenze.
Parallel zu diesem strukturellen Trend kann man einen Wandel der elektronischen Struktur an der Korngrenze beobachten, welcher wiederum die verschiedenen Translationszustände plausibel macht. Die platzprojizierten Zustandsdichten für das jeweilige Metallatom an der Korngrenze zeigen, dass zwischen den $s$- und $p$-Zuständen des Bors mit den $d$-Zuständen des Übergangsmetalls eine starke Hybridisierung auftritt, die Bindungen mit stark kovalentem Charakter erwarten lässt. Diese Hybridisierung wird von B über C und N zu O an der Korngrenze hin kontinuierlich schwächer. Bei O hat sich eine ausgeprägte Pseudolücke zwischen den $p$- und $d$-artigen Bändern entwickelt, ein Indiz für eine stark polare Bindung. Diese Ergebnisse lassen sich mit Hilfe von Abbildungen der Bindungselektronendichte veranschaulichen. Letztere weisen auch darauf hin, dass die kovalent bindenden Elemente Bindungen über die Korngrenze hinweg verstärken und so die Kohäsion der Grenzfläche erhöhen, ein Punkt auf den wir gleich noch zu sprechen kommen werden. Der genaue Mechanismus der Ausbildung von Bindungen an der Korngrenze lässt sich aus den Ergebnissen der integrierten Zustandsdichte sowie aus Überlapp-Populationen lokalisierter, Atomorbital-ähnlicher Wellenfunktionen ableiten. Dies wurde exemplarisch für die Korngrenze in Mo durchgeführt. Die Ergebnisse zeigen, dass ein Ladungsübertrag von den Metallatomen, die die nächsten Nachbarn des Fremdatoms an der Korngrenze darstellen, zum Fremdatom hin stattfindet. Dadurch wird die Metall-Metall Bindung über die Grenzfläche hinweg geschwächt. Je nach Stärke der Hybridisierung wird die übertragene Ladung zur Ausbildung kovalenter Bindungen benutzt, oder aber bleibt um das Fremdatom herum lokalisiert, was zu einer stark polaren Ladungsverteilung führt. Dieser Vorgang ist derselbe an beiden Konfigurationen der Korngrenze, da er durch die relative Lage der elektronischen

Zustände der beteiligten Elemente bestimmt wird, und nicht durch die genaue Geometrie der Korngrenze.
Der Einfluss der Fremdatome auf die Kohäsion der Korngrenze wurde einem Ansatz von Geng et al. [39] folgend getestet, der auf der thermodynamischen Theorie der Korngrenzenbrüchigkeit von Rice und Wang [104] beruht. Demnach ist die Differenz der Bindungsenergien des Fremdatoms an der Korngrenze und des Fremdatoms an der entsprechenden freien Oberfläche ein Maß für die versprödende, bzw. die Kohäsion erhöhende Wirkung des jeweiligen Elements auf die Korngrenze. Diese Rechnungen, wiederum exemplarisch für Mo durchgeführt, ergaben, dass B und C die Kohäsion der Korngrenze in Mo erhöhen, während N und O sie schwächen.
Insgesamt ergibt sich also folgendes Bild: Die eher kovalent bindenden Elemente B und C bevorzugen den spiegelsymmetrischen Zustand der $\Sigma 5$ STGB. Hier finden sie eine eher offene Struktur mit optimaler Anzahl an Bindungspartnern in nahezu gleichem Abstand vor, zu denen sie kovalente Bindungen ausbilden. Diese Bindungen überkompensieren die geschwächten Metall-Metall Bindungen, so dass die Korngrenze insgesamt stabilisiert wird. Die polar bindenden Elemente N und O bevorzugen die eher dichtgepackte Struktur der Korngrenze, bei der die Spiegelsymmetrie gebrochen ist. Die polare Ladungsverteilung trägt nicht zu einer Bindung über die Grenzfläche hinweg bei, so dass die Korngrenze insgesamt geschwächt wird.
Unsere Ergebnisse belegen in eindrucksvoller Weise die Gültigkeit eines "universellen Modells" von Cottrell [19]. Cottrell entwickelte ausgehend von einfachen Elektronenstruktur-Modellen eine Theorie, die den Einfluss von Fremdatomen auf die Korngrenzenkohäsion in Metallen vorhersagen soll. Zusammengefasst besagt sie, dass, abhängig von der relativen Lage der Energieniveaus der beteiligten Elemente, Fremdatome an Korngrenzen in Metallen entweder kovalente oder polare Bindungen ausbilden, und dass erstere die Kohäsion der Korngrenze erhöhen, während letztere sie reduzieren. Das Modell beruht auf einer Reihe teilweise recht drastischer Näherungen, so dass seine Rechtfertigung bislang noch ausstand. Mit unseren ab-initio Ergebnissen konnten wir für die Fremdatome in Nb und Mo die Gültigkeit von Cottrell's Modell bestätigen. Das Modell ist unabhängig von der Geometrie der Korngrenze. Auch das kann bis zu einem gewissen Grad bestätigt werden, da auch die hier präsentierten Ergebnisse zeigen und erklären, dass der Charakter der Bindung zwischen Fremdatom und Metall nicht vom Translationszustand der Korngrenze abhängt. Es ist vielmehr so, das der Bindungscharakter, festgelegt durch die relative Lage der Energieniveaus der beteiligten Elemente, den Translationszustand bestimmt! Man

muss jedoch bei der Verallgemeinerung dieser Ergebnisse auf Korngrenzen mit völlig anderer Geometrie vorsichtig sein. Eine Aufspaltung der Bindungsenergie-Differenz nach Geng et al. [39] in chemische und elastische Anteile hat gezeigt, dass der elastische Anteil der Bindung, hervorgerufen durch Relaxation der atomaren Positionen beim Einbau des Fremdatoms an der Korngrenze, einen zum Teil erheblichen Beitrag zu dieser Differenz leistet. Dieser ist aber u.a. abhängig von der Geometrie der Korngrenze.
Die Tatsache, dass die Anwesenheit leichter Fremdatome den Translationszustand einer Korngrenze in den bcc Übergangsmetallen auf verschiedene Weise ändern kann, ist im Hinblick auf experimentelle Untersuchungen der Korngrenzenstruktur in diesen Materialien von großer Bedeutung. In den oben beschriebenen Studien wurde immer davon ausgegangen, dass es sich um Korngrenzen in absolut reinen Materialproben handelt. Man muss jedoch davon ausgehen, dass auch sehr kleine Konzentrationen von Fremdatomen zumindest lokal den Translationszustand der Korngrenze verändern. Da man leichte Elemente, zumindest in Form unregelmäßig an der Korngrenze verteilter Verunreinigungen, im HRTEM Bild nicht sieht und, wie wir gezeigt haben, verschiedene Elemente gegensätzliche Effekte hervorrufen können, die sich u.U. gegenseitig aufheben, ist die experimentelle Bestimmung des *intrinsischen* Translationszustands einer Korngrenze eine sehr anspruchsvolle Aufgabe. Wir hoffen daher, dass die vorliegende Arbeit experimentelle Untersuchungen von gezielt mit bestimmten Elementen dotierten Korngrenzen stimuliert, um den Einfluss einzelner Elemente zu isolieren und zu bestimmen.

## Ausscheidung von $MoC_x$ an der $\Sigma 5$ (310)[001] STGB in Mo

Kapitel 6 beschäftigt sich mit der Ausscheidung von $MoC_x$ an der $\Sigma 5$ (310)[001] STGB in Mo. Dieser Teil der Rechnungen wurde motiviert durch die Arbeit von Pénisson et al. [94], die HRTEM Untersuchungen an der $\Sigma 5$ (310)[001] STGB in Mo, vor und nach dem Anreichern mit C, durchführten. Pénisson et al. beobachteten die intergranulare Ausscheidung von tetragonal dichtgepacktem (eng.: body-centred tetragonal, bct) $MoC_x$ mit $x \approx 0.4$ an der Korngrenze, die wir mit einfachen Modellen nachvollziehen wollten. Die Rechnungen zeigen, dass eine tetragonale Ausscheidung in einer Orientierung wächst, in der ihre c-Achse unter einem Winkel von ca. 108° auf die Korngrenze trifft. Im Vergleich zu anderen, aufgrund der Geometrie denkbaren, Orientierungen führt dies zwar zu einer

stärkeren Aufweitung der Struktur senkrecht zur Grenzfläche, ist jedoch günstiger, da auf diese Weise die Periodizität der Korngrenze erhalten bleibt.
Das so geartete Wachstum der Ausscheidung führt zu zwei neuen Mo-$MoC_x$ (mit $x \approx 0.4$) Grenzflächen, die ebenfalls von Pénisson et al. [94] beobachtet wurden. Um diese mit einer möglichst kleinen Superzelle zu modellieren, wurde eins der zwei bcc Mo-Körner in der Zelle durch ein Korn aus stöchiometrischem, tetragonalen MoC ersetzt. Um die Gitterfehlpassung zwischen den einkristallinen bcc Mo und bct MoC Phasen auszugleichen, wurde das Volumen des MoC Gitters um 13% komprimiert. Bei der Berechnung der Separationsenergie der neuen Grenzflächen musste der Einfluss dieser Kompression, sowie der der erhöhten Kohlenstoffkonzentration im Vergleich zum experimentellen Befund, berücksichtigt werden. Dies wurde näherungsweise erreicht, indem die Kompressionseigenschaften der Ausscheidung mit denen einer einkristallinen tetragonalen $Mo_2C$ Phase verglichen wurden. Die so erhaltenen Separationsenergien liegen nur wenig unter denen für die reine $\Sigma 5$ STGB in Mo, die Adhäsionseigenschaften dieser sonst sehr verschiedenen Grenzflächen sind also energetisch ähnlich. Die Ausscheidung erhöht damit nicht wesentlich die Korngrenzensprödigkeit in Mo.
Durch die Gitterfehlpassung wirkt die Mo-MoC Grenzfläche als Senke für Versetzungen, wie dies in der Tat auch von Pénisson et al. beobachtet wurde [94]. In Bezug auf die makroskopischen Eigenschaften bedeutet das, dass eine solche tetragonale MoC Ausscheidung an der $\Sigma 5$ STGB in Mo das Metall zu einem gewissen Grad versteift. Experimentelle Beobachtungen zeigen jedoch auch, dass die tetragonale $MoC_x$ Ausscheidung nicht stabil ist. Strukturelle Phasenumwandlungen von einem tetragonalen zu einem hexagonalen Molybdän Untergitter wurden sowohl von Pénisson et al. [94] als auch schon früher von Lepski et al. [73, 74] beobachtet.
Die HRTEM Aufnahmen in der Arbeit von Pénisson et al. [94] zeigen einen intergranularen, tetragonalen MoC Film, dessen Grenzflächen zu den reinen bcc Mo Körnern nicht atomar scharf erscheinen. Die Erklärung für diese Beobachtung kann nach der Analyse der ab-initio Ergebnisse geliefert werden. An "Grenzfläche I", die im ursprünglichen Modell atomar scharf aussieht, findet eine Verlagerung von Kohlenstoff aus dem MoC Korn über die Grenzfläche hinweg statt, was lokal zu einer Verzerrung des Mo Gitters führt. An "Grenzfläche II" wird das Mo Untergitter unter einer nur kleinen Verkippung von 6° fortgesetzt, und das Ausmaß der tetragonalen Verzerrung steigt nicht sprunghaft, sondern kontinuierlich an, wenn man sich von der Grenzfläche in das MoC Korn bewegt. Grenzfläche II wirkt daher auf den HRTEM-Bildern, auf denen man nur Mo, aber nicht C sieht,

ebenfalls atomar unscharf.

Bei der Untersuchung des Ausscheidungsprozesses anhand ausgewählter Modellsituationen mussten einige Abstriche gemacht werden, um die Superzelle für die Rechnungen auf eine mit ab-initio Methoden handhabbare Größe zu beschränken. Dies führt den Bedarf eines guten semi-empirischen Modells für die Mo-C Wechselwirkung vor Augen, mit dem Rechnungen mit großen Superzellen und dynamische Simulationen möglich sind.

# Molybdänkarbide

## Eigenschaften der Bulk-Phasen

Es wurden die Bildungsenergien von Molybdänkarbiden und -semikarbiden in verschiedenen Kristallstrukturen berechnet. Die Ergebnisse werden in Kapitel 7 vorgestellt. Für die Monokarbide stellte sich die hexagonal primitive (eng.: hexagonal primitive, hpr) "Wolframkarbid-Struktur" (WC) als die stabile heraus, für die Semikarbide ist es die hexagonal dichtgepackte (eng.: hexagonal close-packed, hcp). Diese Resultate decken sich mit experimentellen Ergebnissen [77, 112, 119].
Die Kompressionsmodule der verschiedenen Strukturen zeigen, dass sowohl für die Monokarbide als auch für die Semikarbide diejenigen Strukturen die günstigsten sind, die am wenigsten kompressibel sind.
Die Bindungsmechanismen zwischen Molybdän und Kohlenstoff wurden z.T. schon während der Untersuchung der Segregation von C an der $\Sigma 5$ STGB in Mo klar, sie konnten an dieser Stelle noch einmal bestätigt und präzisiert werden. Im Vergleich zu einem reinen Mo Kristall werden beim Einbau von C in den Kristall Elektronen aus den Mo-Mo Bindungen abgezogen und diese somit geschwächt, bzw. teilweise durch Mo-C Bindungen ersetzt. Die entstehenden Mo-C Bindungen sind jedoch so stark, dass sie diese Schwächung überkompensieren. Anhand der platzprojizierten Zustandsdichten lässt sich erkennen, dass die starke Hybridisierung zwischen den Kohlenstoff $s$- und $p$-Zuständen und den Molybdän $d$-Zuständen und damit der kovalente Charakter der Bindung, nicht von der C Konzentration abhängt. Je höher jedoch die C Konzentration ist, desto vollständiger ist die Hybridisierung und desto weniger Mo-$d$-Zustände bleiben für die reinen Metall-Metall Bindungen. Energieaufgelöste Orbital-Überlapp-Populationen zeigen, dass die verbleibenden Mo-Mo Bindungen zusätzlich dadurch geschwächt werden, dass nun, im MoC-Kristall, auch antibindende Zustände besetzt werden, was im reinen Metall nicht der Fall ist. Dafür

weisen jedoch die Mo-C Bindungen maximale Stärke auf, da bei ihnen die Energieniveaus genau bis zum Umschlagspunkt von bindenden zu antibindenden Zuständen gefüllt sind. Der Vergleich verschiedener Kristallstrukturen führt zu dem Ergebnis, dass die Struktur die günstigste ist, in der am meisten Mo-$d$-Zustände für reine Metall-Metall Bindungen verbleiben, und bei der diese zudem im Vergleich mit anderen Strukturen energetisch am tiefsten liegen.
Die Frage, was nun eine bestimmte Kristallstruktur gegenüber einer anderen stabiler macht, kann auch anschaulich mit Hilfe relativ simpler physikalischer Konzepte beantwortet werden. Die Drehimpulse der im MoC Kristall vorhandenen Orbitale lassen prinzipiell $d^2sp^3$ oder $d^4sp$ Hybridisierung an einem an einer Mo-C Bindung beteiligten Atom zu. Dies führt entweder zu oktaedrischer oder trigonal-prismatischer Koordinierung des Atoms, wenn wir für diese Betrachtung den Grenzfall rein kovalenter Bindungen annehmen. Die Analyse der Orbital-Populationen in MoC spricht für eine $d^4sp$ Hybridisierung, also trigonal-prismatische Koordinierung, was die Stabilität der WC Struktur erklärt. Dies passt auch in die Vorstellung, dass in einer Verbindung Bindungen verschiedener Art (in diesem Fall Mo-Mo- und Mo-C-Bindungen), die vom selben Atom ausgehen, sich so gut wie möglich ausweichen sollten [25]. In Molybdän-Semikarbiden, in denen die reinen Metall-Metall Bindungen eine dominierende Rolle spielen, konnten wir ableiten, dass die $d^2sp^3$ Hybridisierung mehr Elektronen für die reinen Mo-Mo-Bindungen übriglässt, was die Stabilität der hexagonal dichtgepackten Struktur plausibel macht.

## Semi-Empirische Modelle - Ausblick

An vielen Stellen der vorliegenden Arbeit wird klar, dass es eine Reihe materialwissenschaftlicher Fragen gibt, auf die die Anwendung eines semi-empirischen Verfahrens sinnvoller als eine ab-initio Rechnung ist. Die Methode, die in dieser Arbeit ausgewählt wurde, um in Zukunft z.B. kinetische Aspekte der Karbidausscheidung in Mo zu untersuchen, beruht auf einem orthogonalen, zwei-Zentren tight-binding Modell mit umgebungsabhängiger Parametrisierung [47, 48, 116]. Für dieses Modell gibt es bereits zwei Sätze von Parametern, die angepasst und getestet wurden, um die reine Mo-Mo [47, 48] und C-C [116] Wechselwirkung zu beschreiben. Um auch Mo-C Wechselwirkungen zu beschreiben, musste das Modell an einigen Stellen erweitert werden. Das erweiterte Modell wurde in einen Code für ab-initio und semi-empirische Elektronenstruktur-Rechnungen von Methfessel et al. implementiert (Einzelheiten der Implementierung sind im Anhang dieser Arbeit beschrieben). Die in dieser Arbeit vorgestellten Daten zur elektronischen Struktur

von Molybdänkarbiden stellen eine umfassende Grundlage für die Anpassung der freien Parameter des Modells dar.
Zunächst kann aus den ab-initio Daten "allgemeine", für die Anpassung nützliche Information extrahiert werden. Aus Überlapp-Populationen und kovalenten Bindungsenergien für die einzelnen Beiträge zu einer Mo-C Bindung lassen sich die relativen Amplituden der im tight-binding Modell auftretenden interatomaren Matrixelemente abschätzen. Untersuchungen der Abstandsabhängigkeit derselben Größen erlauben die Abschätzung von cut-off Radien und der Vergleich von nächsten und übernächsten Nachbarn demonstriert den Einfluss der Umgebungsabhängigkeit.
Anstatt nun - unter den Randbedingungen, die durch oben beschriebene Erkenntnisse entwickelt werden - die freien Parameter mehr oder weniger "willkürlich" zu variieren, bis das so angepasste Modell die wesentlichen Größen der Molybdänkarbide reproduziert (z.B. Bandstrukturen, Energie-Volumen Relationen), wird ein alternativer Ansatz vorgeschlagen. Obwohl die lokalen Matrixelemente, die im "mixed-basis" Programm berechnet werden, in einer nicht-orthogonalen Basis dargestellt werden - im Gegensatz zur tight-binding Implementierung, in der eine orthogonale Basis angenommen wird - scheint es ein vielversprechender Ansatz zu sein, die freien Parameter der tight-binding "hopping"- Terme direkt an die entsprechenden ab-initio Daten anzufitten. In zwei-Zentren tight-binding Modellen werden im Allgemeinen die Hamilton Matrixelemente nach einem Ansatz von Slater und Koster [109] als Linearkombinationen der sogenannten "fundamentalen hopping Integrale" dargestellt. Damit bezeichnet man interatomare Matrixelemente, die in einer Basis aus Orbitalen dargestellt werden, für die die Quantenzahl $m$ der Projektion des Drehimpulses $l$ auf die Bindungsachse eines Atompaares ganzzahlige Werte annimmt. Mit diesen fundamentalen Integralen kann man die Anzahl der unabhängigen interatomaren Matrixelemente deutlich reduzieren, z.B. in einem *spd* tight - binding Modell wie es in dieser Arbeit vorgestellt wird, auf zehn. Diese "hopping"-Terme kann man nun umgekehrt auch als Linearkombination der Hamilton Matrixelemente darstellen, in dem man das lineare Gleichungssystem nach Slater und Koster - das eigentlich dazu dient, die Hamilton Matrixelemente in Form der fundamentalen "hopping"-Terme auszudrücken - invertiert. Formal kann man dasselbe Verfahren auch auf die (ab-initio) Überlapp-Matrixelemente anwenden. Erste Tests dieses Verfahrens wurden durchgeführt. Dabei wurde die Beziehung zwischen Nicht-Orthogonalitätseffekten, wie dem Auftreten einer nichtdiagonalen Überlappmatrix in der ab-initio Rechung, und der Umgebungsabhängigkeit der Hamilton Matrixelemente untersucht. Hier deutet sich die Möglichkeit an, den rein abstandsabhängigen Anteil und die

Abschirmfunktion in der umgebungsabhängigen tight-binding Parametrisierung getrennt aus den ab-initio Daten abzuleiten. Dieser Ansatz verspricht eine hohe Übertragbarkeit der angepassten Parameter auf unterschiedliche Kristallstrukturen und relative Konzentrationen.

# Contents

# Chapter 1

# Introduction

"*Though in 1974 only 4% of molybdenum world production were used in various branches of technics, these applications are particularly important. This indispensability, and new possibilities of applications which cannot be foreseen today, make the pure metal and its alloys promising construction materials in the future*"[2]. Today's uses of molybdenum, the element which is the central topic of this study, indeed cover a wide range of high-temperature applications. The earliest one is the use in incandescent lamps and electron tubes, but Mo is a favoured element also in furnace construction used for different metallurgical processes. A very promising field is the use in turbine blades. However, up to today this is limited by the tendency of Mo to oxidise at high temperatures, and by the intrinsic grain boundary embrittlement which is characteristic for the body-centred cubic (bcc) transition metals.

In general the macroscopic properties of polycrystalline materials and hence their potential technological applications are vitally influenced by the behaviour of their microstructural interfaces. The cohesion at these grain boundaries affects the hardness, deformability and toughness of the material and it can be enhanced or decreased by segregated impurities. In this context, it is essential to understand interfacial cohesion and impurity segregation in detail, and it is vital to investigate the relationship between these microscopic features and the macroscopic properties in order to find general rules describing the latter. Knowing these rules will enable us not only to understand but also to some extent manipulate the material properties.

What are the quantities that we have to know for finding these rules? With or without impurities, intergranular strength is closely related to the atomic structure of a grain boundary and to the detailed atomistic nature [17], thus experimental and computational

investigations on a nanometre scale are essential. Furthermore we want to know the qualitative and quantitative cohesive characteristics of the interface.
Experimentally, the atomic structure of a grain boundary can be determined, for instance, by high resolution transmission electron microscopy (HRTEM) [11]. In order to investigate the cohesive properties it is important to find an adhesion process having model-character. Such a model would provide an appropriate starting point for calculations as well as an ideal limit for experimental adhesion. This would enable comparison of experimental findings with theoretical predictions. Contact experiments with metal tips of atomic force microscopes on metal or ceramic surfaces, as described e.g. in [53, 91], can be used for adhesive strength measurements. The surface energy of adhesion and its increase or decrease $\Delta$E due to the presence of impurities can also be used then to characterise grain boundaries [10].
Among existing computational approaches electronic structure calculations are a valuable tool for the investigation of material properties. Ab-initio methods, e.g. based on the density functional theory [59, 68], are parameter-free methods including only very few approximations. They allow accurate and quantitative predictions on the properties of a wide range of materials. In addition to the atomic structure ab-initio methods provide detailed information on the electronic structure, supporting the understanding of the microscopic behaviour being responsible for the macroscopic properties. Ab-initio calculations suffer, however, from their high computational cost, limiting the system size to the order of 100 atoms. Thus, for many problems semi-empirical methods are advantageous. Linear combination of atomic orbitals (LCAO) methods, e.g. tight-binding methods [52], are still based on quantum mechanical concepts, but include simplifications (explained in detail in chapter 4.1) making them two or even three orders of magnitude faster than the ab-initio methods. They represent a compromise between the highly accurate, but computationally very expensive ab-initio methods and the fast but limited fully empirical methods, such as molecular dynamics simulations with Lennard-Jones [72] or Tersoff [117] potentials, used in order to investigate dynamical properties of complex materials.

After having collected the characteristic data concerning an interface, we need on the one hand a theory which relates the microscopic features to the macroscopic properties - in this work the interfacial embrittlement and how it is changed by the presence of impurities - and on the other hand some simple physical models that can explain these findings in a descriptive way.
Smith and Cianciolo [110] as well as Rice and Wang [104] assume the difference in interfa-

cial adhesive energies with and without impurities to be the dominant factor in controlling the interfacial embrittlement and develop thermodynamical models to calculate it. The authors show that the grain boundary adhesion is decreased if segregation of the impurities to the surface is exothermic, and it it has a larger free energy gain than for grain boundary segregation. Smith and Cianciolo describe the energy of adhesion by a universal binding energy relation [34] which goes back to the universal binding curve [111]. It is interesting to note that this universal binding curve also seems to hold for the adhesion of metal-ceramic interfaces [61], indicating strong similarities to the underlying mechanisms.
Geng et al. [39] developed a phenomenological model based on the work of Rice and Wang [104] and on an extensive ab-initio data set [40, 41, 120, 121, 124]. They define the energy of adhesion as the difference in binding energies of an impurity at the grain boundary and at the corresponding free surface. Besides providing a way of quantifying the effect of impurities on interfacial cohesion the authors suggest a way of splitting the difference in binding energy in mechanical and chemical contributions. This is a useful approach, since experiments investigating the embrittlement of iron [53], or metal-sapphire contacts [95], as well as ab-initio calculations concerning impurities at an Mo-$MoSi_2$ interface [60], showed that the influence of impurities can not always be explained by chemical interactions alone, even if the bonding character plays a significant role.
There are numerous publications on the bonding character between host metals and impurity elements explaining the experimental observations of different impurities having different influence on the grain boundary cohesion ([56, 122, 54, 79, 8]). In general they agree in their conclusion that covalently bonding elements increase the interfacial cohesion in the transition metals, while polarly bonding elements decrease it. In 1990 Cottrell proposed a "unified theory" in order to explain the effects of segregated interstitial impurities on the grain boundary cohesion [19]. Starting from the assumptions of the electron theory of chemisorption and looking at the example of light interstitial impurities, such as H, B, C, N and O, in Fe, Cottrell demonstrated that it can be determined from the relative position of the electronic states whether elements form covalent-like bonds with the host metal or not. He also concluded that covalently bonding impurities always increase interfacial cohesion in a metal, while all others decrease it. This was assumed to be generally true for light elements in transition metals and independent of the grain boundary geometry.

In this work the focus is on special grain boundaries in bcc transition metals. They have been the object of interest of many investigations during recent years, both experimentally and theoretically. The grain boundary which was chosen for our case study of the

influence of impurities on the interface properties is the Σ5 (310) [001] symmetrical tilt grain boundary (STGB)[1]. The intrinsic translation state of the pure grain boundary has been the subject of various investigations. Campbell et al. performed HRTEM studies on the Σ5 (310) [001] STGB and found a mirror-symmetric translation state in Nb [14, 15], and a shifted structure in which the mirror symmetry is broken by a shift along the [001] axis in Mo [12] and Ta [13]. Recent investigations by Sigle, however, indicate a mirror symmetric structure of the Mo grain boundary [108]. From the theoretical point of view the situation also was ambiguous for some time. Semi-empirical investigations ([78](Mo), [14, 93](Nb)) showed different results depending on whether the interaction potential used included angle-dependent contributions or not. This point was clarified by ab-initio total-energy calculations of the Σ5 STGB in the bcc transition metals Nb, Mo, Ta and W [5, 31, 89, 90]. The results showed a clear trend: the translation state depends on the degree of filling of energy bands with *d*-orbital character. This also tells us that only models including angle-dependent many-body interactions can predict the correct translation state in the bcc transition metals.

In this work, in order to explain the contradictive experimental findings we leave the concept of a perfect grain boundary. So far the grain boundary was considered to be absolutely pure. In a real system, however, one can never completely avoid structural imperfections (e.g. point defects, dislocations) or impurities. The latter seem to be a challenging and promising field for ab-initio investigations, because they are simpler to treat as additional structural defects, and especially because they provide a way of varying the number of valence electrons systematically in order to test the effect on the translation state. Preceeding investigations concerning the segregation of C in Mo already indicated that interstitial impurities at the Σ5 STGB can change the translation state [65, 66].

As mentioned above, impurities alter grain boundary properties, such as interfacial cohesion. For instance, among the light elements O is known to have an embrittling influence on transition metal grain boundaries, whereas B often enhances cohesion. In this work it is partly proceeded in the line of Geng et al. in order to validate Cottrell's theory, and furthermore it is extended to the issue of interfacial structure. In this context, the influence of light elements (B, C, N, O) on the geometric translation state and on the cohesion of symmetrical tilt grain boundaries in the body-centred cubic (bcc) transition metals niobium and molybdenum is investigated. Through insertion of the light elements at the interface the number of valence electrons is varied systematically. Their effect on the

[1]For details about the geometry and nomenclature of special grain boundaries see appendix A

translation state and on the stability of the grain boundary against brittle fracture is examined by calculating total and bonding energies. An explanation is derived by analysing electronic structures in terms of local densities of states, bonding electron densities, and orbital overlap populations.

After varying the atomic species the next step to evaluate the influence of impurities on grain boundary properties is to vary the concentration of the impurity element. By means of HRTEM Pénisson et al. [94] investigated the $\Sigma 5$ STGB in Mo before and after carburisation heat treatment, and they observed segregation of C to the Mo grain boundary, followed by intra- and intergranular precipitation of different $MoC_x$ phases. In this work it was tried to model some of these processes to see how they might change the macroscopic properties of the material. In this context the possibilities of ab-initio calculations are limited, because they are restricted to systems with rather high periodicity to keep the computational effort reasonable. So "snapshots" of the dynamical processes of segregation and precipitation were picked out, idealised situations where the symmetry is adequate. In a previous study the segregation of a single C atom to and at the $\Sigma 5$ STGB in Mo [65, 66] has been investigated. In this study the concentration is increased atom by atom in order to monitor the very beginning of the precipitation of $MoC_x$ at the boundary. Thereafter a big jump of thought to the final stage is made, a precipitate of tetragonal MoC at the interface, a carbide phase which Pénisson et al. [94] also observed. This case is modelled by constructing a Mo-MoC heterophase interface, and the orientation relationship and the translation state possessing the lowest energy are determined. At this point we are getting close to the limits of the ab-initio electronic structure method. A significant difference between the grain boundaries in metals and the metal-carbide interface is that in the case of the latter a lattice misfit occurs, leading to residual elastic stresses. In order to solve the problem with a sufficiently small supercell one has to make approximations. In this case the misfit is compensated by expanding the carbide lattice. It is then tried to find out more about the properties of the new phase by comparing the results to those obtained from calculations of the properties of $MoC_x$ bulk phases. Energies of formation and electronic structures of different $MoC_x$ crystal phases are analysed. The relative stabilities of the different phases are explained by looking for distinctive characteristics in their electronic structures. Besides completing our picture of the MoC precipitates in Mo and getting an estimation of the consequences of the approximations which were made, this investigation of the molybdenum carbides provides further insight in the bonding mechanisms of Mo and C.

On the one hand we extend our understanding of the molybdenum carbides, which have many attractive properties of their own, for example high hardness, high melting point and high catalytic activity, making them an object of strong interest in materials science. Therefore there are numerous examples of ab-initio investigations of molybdenum and other transition metal carbides present in the literature (see e.g. [44, 45, 50, 77] and references therein), where efforts are made to derive a complete phase diagram on the basis of ab-initio data.

On the other hand such a series of crystal structures for a binary compound generates a broad data set for semi-empirical modelling of interatomic interactions, specifically by tight-binding models for Mo-C interactions. On the basis of this data base the possibilities of fitting the parameters of an environment-dependent tight-binding model will be discussed, with the aim of applying the model then to simulate a larger range of complex processes such as segregation and precipitation.

# Part I

# Electron Theory of Solids

# Chapter 2

# The Schrödinger Equation

To calculate the total energy of a solid, taking into account the detailed electronic structure, we have to solve the Schrödinger equation for a many-particle system, consisting of $\mathrm{N}_N$ atomic nuclei and $\mathrm{N}_e$ electrons:

$$\widehat{H}|\Psi\rangle = E|\Psi\rangle, \tag{2.1}$$

where

$$|\Psi\rangle = |\{\mathbf{r}_i\}, \{\mathbf{R}_\alpha\}\rangle,$$

is the many-particle wave function[1]. The Hamiltonian $\widehat{H}$ consists of the following terms:

$$\widehat{H} = \widehat{T}_N + \widehat{T}_e + \widehat{V}_{N-N} + \widehat{V}_{N-e} + \widehat{V}_{e-e}. \tag{2.2}$$

$\widehat{T}_N$ and $\widehat{T}_e$ are the operators of the kinetic energy of atomic nuclei and electrons,

$$\widehat{T}_N = \sum_{\alpha=1}^{N_N} \frac{\widehat{p}_\alpha^2}{2M_\alpha} \qquad \text{and} \qquad \widehat{T}_e = \sum_{i=1}^{N_e} \frac{\widehat{p}_e^2}{2m_e} \quad .$$

[1]For clarity, all equations are written for a non-relativistic, spinless system, as this is a valid approximation for the systems considered here.

$\widehat{V}_{N-N}$, $\widehat{V}_{e-e}$ and $\widehat{V}_{N-e}$ are the interaction energies,

$$\widehat{V}_{e-e} = \frac{1}{2} \sum_{i \neq j; i,j=1}^{N_e} \frac{e^2}{|\mathbf{r}_i - \mathbf{r}_j|} \quad , \tag{2.3}$$

$$\widehat{V}_{N-N} = \frac{1}{2} \sum_{\alpha \neq \beta; \alpha,\beta=1}^{N_N} \frac{Z_\alpha Z_\beta e^2}{|\mathbf{R}_\alpha - \mathbf{R}_\beta|} \quad , \tag{2.4}$$

$$\text{and} \qquad \widehat{V}_{N-e} = -\sum_{\alpha=1}^{N_N} \sum_{i=1}^{N_e} \frac{Z_\alpha e^2}{|\mathbf{R}_\alpha - \mathbf{r}_i|} \quad . \tag{2.5}$$

$\mathbf{r_i}, \mathbf{R}_\alpha$ are the positions of electrons and atomic nuclei, $e$ is the electronic charge, $m_e$ the mass of an electron, $M_\alpha$ is the nuclear mass of atom $\alpha$, $Z_\alpha$ the nuclear charge of atom $\alpha$, and $\widehat{p_i}$ and $\widehat{p_\alpha}$ are the operators of the electron's respective nuclei's momentum.
An exact solution of equation (2.1) in this form is not possible. However, there are several useful approaches to solve this problem on different levels of accuracy and transferability. The common first step is to treat the electrons and nuclei of a solid as decoupled, using the Born-Oppenheimer approximation (BOA) [7]. It states that the movement of the electrons is so much faster than the one of the atomic nuclei that the former are able to follow changes in the arrangement of the latter instantaneously and thus are always found in their ground state. This is called *adiabatic approximation* or *Born-Oppenheimer approximation*. Thus we can set up a Schrödinger equation for the electrons in which the coordinates $\{\mathbf{R}_\alpha\}$ of the atoms only enter as a parameter:

$$\{\widehat{T}_e + \widehat{V}_{e-e} + \widehat{V}_{N-e}\}|\psi_i\rangle \quad = \quad E^{el}(\{\mathbf{R}_\alpha\})|\psi_i\rangle \quad . \tag{2.6}$$

$|\psi_i\rangle$ is the wave function of the electrons. The atomic nuclei move in the adiabatic potential of the electrons,

$$\{\widehat{T}_N + \widehat{V}_{N-N} + E_0^{el}(\{\mathbf{R}_\alpha\})\}|\Phi_\alpha\rangle \quad = \quad E^{tot}|\Phi_\alpha\rangle \quad , \tag{2.7}$$

where $E_0^{el}$ is the ground state energy of the electron system and $|\Phi_\alpha\rangle$ is the wave function of the atomic nuclei. With the ansatz

$$|\Psi\rangle = |\Phi_\alpha\rangle|\psi_i\rangle \tag{2.8}$$

for the total wave function we can solve equations (2.6) and (2.7). As the movement of the atomic nuclei takes place so much slower than the one of the electrons, many problems can be dealt with by assuming fixed atomic positions $\{\mathbf{R}_\alpha\}$ and setting $\widehat{T}_N = 0$ in (2.7). Then the ground state of the complete system can be obtained by minimising the total energy, the solution of (2.7), with respect to the parameter $\{\mathbf{R}_\alpha\}$.
The next step thus is to solve the electronic Schrödinger equation, (2.6). The trouble is that it is a many-body problem. The potential in which the particles are moving depends on the positions of the particles themselves. Thus we have to project the many-body problem onto an effective one-particle problem and then solve (2.6), respectively the corresponding one-particle equation, self-consistently.
There are different physical models that build the descriptive background of todays computational methods. A way to solve our problem "ab initio" (see chapter 3) is given by the density functional theory (DFT), presented in section 3.1. Ab-initio methods are "parameter-free" methods, where only very few approximations are made and nothing has to be fitted to experimental data for specific materials. Thus they allow for quantitative predictions of many properties. In the density functional theory the electronic ground state energy is expressed as a functional of the electron density. This approach is based on the nearly free electron (NFE) picture, in which the electrons can move freely inside the crystal, the only influence of the atomic lattice on the electrons are scattering effects. Thus the electron density is spatially rather homogeneous and the wave function of an electron in a crystal can be described as a plane wave, with a superposed modulation by a function that has the periodicity of the crystal. Such a modulated wavefunction is known as a Bloch function.
The other extreme case, known as the "tight binding" model, is composed of electrons being tightly bound to the atoms that build up the crystal lattice. Thus the Bloch function of an electron in the crystal is a periodic repetition of atomic-like orbitals, i.e. a linear combination of atomic orbitals (LCAO). This picture is the basis of the semi-empirical tight-binding methods, described in more detail in section 4. They are still based on quantum mechanical concepts, but self-consistency is neglected and the Hamiltonian matrix elements are parametrised. The free parameters are fitted to experimental or ab-initio data. The loss of reliability and transferability is compensated by the drastically reduced computation time.

# Chapter 3

# Ab-initio Methods

## 3.1 Density Functional Theory

A way to trace back the many electron problem to an effective one-electron problem - the Schrödinger equation of which can be solved - is to express the energy of the electron system as a functional of the electron density:

$$E = E[n(r)]$$

Minimising the energy by means of a variational principle then leads to the solution of equation 2.6. This procedure, which had already been used earlier by Thomas [118], Fermi [33], and Dirac [28], has been justified by two theorems, established and proven by Hohenberg and Kohn in 1964.

### 3.1.1 The Theorems of Hohenberg and Kohn and the Equations of Kohn and Sham

The theorems of Hohenberg and Kohn state [59]

1. The ground state properties of an electron system in an external potential $v_{ext}$ are unique functionals of the ground state electron density $n_0(\mathbf{r})$. E.g. the ground state total energy

$$E_0^{el}(\{\mathbf{R}_\alpha\}) = E^{el}[n_0]. \tag{3.1}$$

2. For a given $v_{ext}$ $E_{el}[n]$ takes on a minimum if and only if $n = n_0(\mathbf{r})$. Then $E_{el}[n] = E_0^{el}$.

Hohenberg and Kohn decomposed $E[n]$ in the following way:

$$E[n] = F[n] + \int v_{ext}(\mathbf{r})\, n(\mathbf{r})\, d^3r, \tag{3.2}$$
$$\text{where} \qquad F[n] = T[n] + E_H[n] + E_x[n] + E_c[n]$$

is a universal functional, i.e. it is the same functional for all systems, independent of $v_{ext}$. $E_H[n]$ is the Hartree energy. $E_x[n]$ is the exchange energy, accommodating the fact that electrons with a parallel orientation of their spins avoid each other and thus lower the Coulomb energy. $E_c[n]$ is the correlation energy, which occurs between electrons with antiparallel orientation of their spins. Even though the Coulomb interaction leads to a mutual repulsion of these electrons a correlated movement by pairing of spins leads to a lower energy. $T[n]$ is the kinetic energy which comprises classical terms (i.e. spin-independent terms) as well as correlation effects. To be able to summarise all correlation effects in one term, Kohn and Sham expressed $T$ as

$$T = \tilde{T} + \Delta T \tag{3.3}$$

[68]. $\tilde{T}$ corresponds to the kinetic energy of a system of non-interacting electrons with the same (inhomogeneous) density $n$ as the real system. $\Delta T$ is the difference between the kinetic energy of a system of interacting electrons and that of non-interacting electrons. Then the exchange-correlation energy $E_{xc}$ is defined as the collectivity of exchange and correlation contributions

$$E_{xc} = E_x + E_c + \Delta T. \tag{3.4}$$

The universal functional becomes

$$F[n] = \tilde{T}[n] + E_H[n] + E_{xc}[n]. \tag{3.5}$$

$n$ is now the density of a system of non-interacting electrons with the same density as the real system. Thus it can simply be expressed by one-electron wave functions:

$$n(\mathbf{r}) = \sum_{i=1}^{N} |\phi_i(\mathbf{r})|^2 \tag{3.6}$$

In this way the many-electron problem is projected onto a one-electron problem with the Schrödinger equation

$$\left\{ -\frac{\hbar^2 \Delta}{2m} + v_{\mathit{eff}}\left(\mathbf{r}\right) \right\} \phi_i\left(\mathbf{r}\right) = \epsilon_i \phi_i\left(\mathbf{r}\right), \tag{3.7}$$

$$\text{with} \qquad v_{\mathit{eff}}\left(\mathbf{r}\right) = v_H\left(\mathbf{r}\right) + v_{xc}\left(\mathbf{r}\right) + v_{ext}(\mathbf{r}). \tag{3.8}$$

It describes the movement of an electron in the effective potential $v_{\mathit{eff}}$ of all electrons and the atomic nuclei. The Hartree potential $v_H\left(\mathbf{r}\right)$ and the exchange-correlation potential $v_{xc}\left(\mathbf{r}\right)$ depend on the density $n$:

$$v_H(\mathbf{r}) = \int \frac{e^2 n(\mathbf{r}')}{|\mathbf{r} - \mathbf{r}'|} d\mathbf{r}' \tag{3.9}$$

$$v_{xc}(\mathbf{r}) = \frac{\delta E_{xc}[n(\mathbf{r})]}{\delta n(\mathbf{r})} \tag{3.10}$$

Equations (3.6) to (3.10) are called the Kohn-Sham equations. In practice they are solved self-consistently, by assuming a starting electron density, calculating the effective potential, solving the one-electron Schrödinger equation, and calculating the new electron density and the new input-potential. This cycle is repeated until the calculation is converged, i.e. until the resulting electron density does not differ from the preceeding density within a given accuracy[1]. Then the electronic ground state energy, equation 3.2, can be calculated, using

$$\begin{aligned} \tilde{T} &= \sum_{i=1}^{N_e} \langle \phi_i | -\frac{\hbar^2}{2m} \Delta | \phi_i \rangle \\ &= \sum_{i=1}^{N_e} \epsilon_i - \int n(\mathbf{r}) v_{\mathit{eff}}(\mathbf{r}) d^3\mathbf{r} \end{aligned} \tag{3.11}$$

[1] In practice the output-potential is mixed with the output-potentials of earlier iteration steps before using it as input-potential. This means a damping of the iteration process. Experience has shown that in most cases this is the only way to achieve convergence.

for the kinetic energy of non-interacting electrons, as

$$E_0^{el}[n_0] = \sum_{i=1}^{N_e} \epsilon_i - E_H[n_0] - \int n_0(\mathbf{r}) v_{xc}[n_0(\mathbf{r})] d^3\mathbf{r} + E_{xc}[n_0]. \tag{3.12}$$

What is still missing for that are expressions for $v_{xc}$ and $E_{xc}$ within the density functional theory, a representation of $v_{ext}$ and a basis set for the one electron wave functions $|\phi_i\rangle$. These points shall be discussed in the following sections. There is of course more than one possibility to represent these quantities. Here we will describe those that are used in the ab-initio code used for this work, the "mixed-basis pseudopotential code" [32, 57, 80, 81] (in the course of the following sections, this name will also become clear).

### 3.1.2 The Local Density Approximation

So far we do not have an analytic expression for $v_{xc}(\mathbf{r})$ and $E_{xc}[n]$. Kohn and Sham suggested to approximate the exchange-correlation energy by

$$E_{xc}[n(\mathbf{r})] = \int n(\mathbf{r}) \epsilon_{xc}(n(\mathbf{r})) d^3\mathbf{r}. \tag{3.13}$$

$\epsilon_{xc}(n)$ is the exchange-correlation energy per electron in an interacting electron gas of uniform density $n(\mathbf{r})$. $E_{xc}(\mathbf{r})$ at position $\mathbf{r}$ depends only on the local charge density $n(\mathbf{r})$ at the same point. This is known as the local density approximation (LDA)
For our calculations $\epsilon_{xc}(n)$ has been given by interpolation formulae of Perdew and Zunger [96], which are based on the Quantum Monte Carlo calculations of Ceperley and Alder [16]. With Quantum Monte Carlo methods the total energy of a homogeneous interacting electron system can be calculated with arbitrarily high accuracy. By subtracting $\tilde{T}[n]$ and $E_H[n]$, $\epsilon_{xc}$ is received, containing exchange and correlation effects as well as $\Delta T$. With the LDA we get

$$v_{xc}(\mathbf{r}) = \frac{d}{dn}\{n\epsilon_{xc}(n)d^3r\}\Big|_{n(\mathbf{r})}. \tag{3.14}$$

The LDA works surprisingly well for most (non-magnetic) systems. Only in materials like the $4f$ rare earths and the transition metal oxides where correlation effects of highly localised orbitals become important the assumption of a locally homogeneous electron density breaks down.

## 3.2 The Pseudopotential Method

In a simple picture the external potential $v_{ext}$ of the crystal can be imagined as a lattice of atomic potentials. If free atoms are brought together to form such a crystal, their valence orbitals overlap and the valence electrons redistribute to form chemical bonds between the atoms. The electrons in inner shells remain almost unaffected by this redistribution as they are localised in the core region and their wavefunctions hardly overlap with those of electrons at neighbouring atoms. Even in the case of the valence electrons it is only the part of the wavefunction remote from the core in the interatomic region which is important for the bond. Thus it is suggestive to introduce simplifications which reduce the calculational complexity. The two measures that shall be taken here then lead to so-called ionic pseudopotentials.

### 3.2.1 Ionic Pseudopotentials

In a first step the effect of the core electrons on the valence electrons is combined with that of the nucleus Coulomb potential to an *ionic core potential*. This is called the *frozen core approximation* which states that the core electrons are not involved in the bonding, as mentioned above. Of course they are not strictly unaffected by changes in the valence one-electron wavefunctions, as those always have to be orthogonal to the ones of the core electrons, and vice versa. But the error in the ground state electron density only leads to a very small error in the ground state energy and thus can mostly be neglected. The big advantage of this approximation is that the number of electrons in the system is drastically decreased. This does not only save computation time but also results in a much smaller total energy. Thus very small energy differences can be resolved automatically, without additional demands on the accuracy of the calculation of core states, as in an "all-electron" method.

Because of the mutual orthogonality of valence and core electron wavefunctions, the valence electron wavefunction has nodes in the ionic core region. To represent such functions e.g. in a basis of plane waves a very large basis set is needed. But fortunately these oscillations are spatially restricted and in the interatomic region the wavefunction is running smoothly and nodeless. As only this is the region of interest for the bonding the shape of the wavefunction in the core region is not important. Therefore we can replace the ionic core potential by an ionic pseudopotential which is constructed such that the corresponding

pseudowavefunctions are identical with the real valence one-electron wavefunctions outside a sphere of radius $r_c$, but do not have nodes and oscillations inside the sphere. Such nodeless pseudowavefunctions can be represented with a sufficiently low number of basis functions. In order to construct these pseudowavefunctions $\phi_l^{ps}$ associated to the pseudopotential $v_l^{ps}$ the following conditions have to be fulfilled:

- $\phi_l^{ps}$ shall be smooth and without nodes,
- $\phi_l^{ps} = \phi_l$ for $r \geq r_{c,l}$,
- $\epsilon_l^{ps} = \epsilon_l$,
- $\int_0^{r_{c,l}} |\phi_l^{ps}(\mathbf{r})|^2 d^3r = \int_0^{r_{c,l}} |\phi_l(\mathbf{r})|^2 d^3r$ (normalisation condition).

The first requirement makes sure that the wave function can be described by a rather small set of energy independent plane waves (or other basis functions). The second and third demand ensure that the pseudopotential is identical with the real ionic potential in the region $r \geq r_c$ and also displays the same scattering properties for the energy $\epsilon_l$. The normalisation condition guarantees the transferability of the scattering properties of the pseudopotential, which is constructed for a fixed $\epsilon_l$, to an energy interval $[\epsilon_l \pm \delta\epsilon]$. The conditions given above still leave degrees of freedom concerning the explicit analytical form of the pseudopotential. Thus there are several construction schemes, the most popular of which are described e.g. in the appendix of [80].

**"Unscreening"**

The so constructed pseudopotentials for each valence state of quantum number $l$ are still screened by the Hartree- and the exchange-correlation potentials $v_H[n_c]$ and $v_{xc}[n_c]$ originating from the core states and the Hartree and exchange-correlation contributions $v_H[n_v]$ and $v_{xc}[n_v]$ from the valence density. To get an ionic pseudopotential which is independent of the valence states the latter contributions have to be subtracted, i.e. the potential has to be "unscreened". This is simple for the Hartree potential, which is a linear function of the density:

$$v_H[n_c + n_v^{PS}] = v_H[n_c] + v_H[n_v^{PS}]. \tag{3.15}$$

$v_{xc}$ is not linear in $n$, therefore we substract $v_{xc}[n_c + n_v^{PS}]$ completely from $v_{ion}^{PS}$ and add $n_c$ to $n_v^{PS}$ later in the self-consistent calculation when $v_{xc}$ is calculated. With this procedure

the core-electron density remains the same in different environments, as it is assumed by the frozen-core approximation.

### Partial Cores

However, the problem with this way of calculating $v_{xc}$ is that due to the non-linear behaviour of $v_{xc}$ small errors in $n_v$ can become big in $E_0$ by adding the big core density $n_c$. Furthermore the strongly oscillating $n_c$ can not be represented in Fourier space. Both problems can be overcome by replacing the core density by a *partial core density* $n_{pc}$ [75]. For this purpose the density in the core region is split into two parts. In an outer part, where the electron density has the same order of magnitude as $n_v$, and an inner part, where $n_c$ is high, but the true form is not important for our calculations. In the outer region of the core $n_{pc}$ shall be equal to the true $n_c$, but in the inner region we can replace it by a smooth function which can be represented easily in Fourier space. In the inner region $n_v \ll n_c$, thus errors in the linearisation can be neglected.
So finally we end up with the ionic pseudopotential belonging to the valence state with quantum number $l$

$$v_{ion,l}^{PS}(r) = v_{eff,l}^{PS}(r) - v_H[n_v^{PS}] - v_{xc}[n_{pc} + n_v^{PS}] \tag{3.16}$$

and the total ionic pseudopotential

$$\hat{v}_{ion}^{PS} = \sum_l v_{ion,l}^{PS} \widehat{P}_l, \tag{3.17}$$

where $\widehat{P}_l$ is a projection operator that selects the contribution of the quantum state $l$ out of the wavefunction.

## 3.2.2 Crystal Pseudopotentials

Before now superposing the ionic pseudopotentials to a crystal potential it is useful to split them in local and nonlocal contributions,

$$\hat{v}_{ion}^{PS} = v_{ion}^{PS,loc}(r) + \left( \sum_l v_{ion,l}^{PS}(r) - v_{ion}^{PS,loc} \right) \widehat{P}_l. \tag{3.18}$$

$v_{ion}^{PS,loc}(r)$ can be chosen freely, e.g. to be the $l = 0$ component:

$$\hat{v}_{ion}^{PS} = v_{ion}^{PS,loc}(r) + \sum_{l=1}^{l_{max}} v_{ion,l}^{PS}(r)\widehat{P}_l. \tag{3.19}$$

As the contributions from the different $l$ fall off like a Coulomb-Potential outside the inner core region and as we assume this to be true also for the local part of the ionic pseudopotential, we conclude that the nonlocal part only occurs inside the ionic core. Finally the crystal pseudopotential can be written as

$$\hat{v}^{PS} = v^{PS,loc}(\mathbf{r}) + \hat{v}^{PS,nl} \tag{3.20}$$

$$\text{with} \quad v^{PS,loc}(\mathbf{r}) = \sum_{\mathbf{T},\alpha} v_{ion,\alpha}^{PS,loc}(|\mathbf{r} - \mathbf{T} - \mathbf{R}_\alpha|) \tag{3.21}$$

$$\text{and} \quad \hat{v}^{PS,nl} = \sum_{\mathbf{T},\alpha} \sum_{l=1}^{l_{max}} v_{ion,\alpha l}^{PS,nl}(|\mathbf{r} - \mathbf{T} - \mathbf{R}_\alpha|)\widehat{P}_l \tag{3.22}$$

Still, this is not the end of the story. Our (artificial) division of the charge density - $v_H$ is caused only by negative charges, the ionic pseudopotential only by positive ones - leads to the problem that the individual sums over these potentials in an infinite crystal must diverge. In a real crystal the diverging terms are compensating each other. We can imitate this by introducing homogeneous positive and negative background charge densities, screening $v_H$ and $v_{ion,\alpha}^{PS}$ respectively, so that their sums are converging. To express the local part of the ionic pseudopotential we can use a simple representation in Fourier space,

$$v^{PS,loc}(\mathbf{r}) = \sum_{\mathbf{G}} v^{PS,loc}(\mathbf{G})e^{i\mathbf{G}\mathbf{r}}. \tag{3.23}$$

Due to the background charge density the $\mathbf{G}$=0 component has a finite value. However, it is not determined and can be chosen. It can be interpreted in real space as a shift of the zero level of the energy eigenvalues. In our calculations we set $v^{PS,loc}(\mathbf{G} = 0) = 0$.

All terms in the expression for the total energy are discussed in detail for instance in [80].

## 3.3 A Mixed Basis

Finally, to solve the Kohn-Sham equations, the one electron wave functions $|\phi_i\rangle$ are expanded in a basis of vectors $|n\rangle$,

$$|\phi_i\rangle = \sum_n a_n^i |n\rangle. \tag{3.24}$$

Inserting this representation into the Schrödinger equation (3.7) leads to the eigenvalue problem

$$\sum_n H_{mn} a_n^i = \epsilon_i \sum_n S_{mn} a_n^i \quad , \tag{3.25}$$

with the elements of the Hamiltonian and the overlap matrix

$$H_{mn} = \langle m|H|n\rangle$$
$$S_{mn} = \langle m|n\rangle.$$

The basis functions $|n\rangle$ can be plane waves, Gaussian or Slater functions or other localised or non-localised functions. Plane waves have the advantage that they are orthogonal and the overlap matrix is a diagonal matrix. Furthermore it is simple to add additional functions to systematically increase the accuracy with which the one electron wavefunctions are described and thus test the criteria of convergence. The disadvantage is that many plane waves are needed to describe strongly localised functions. Even with the use of pseudopotentials there are valence functions, like the $3d$-orbitals of transition metals and the $2p$-orbitals of main group elements treated in this study, which are nodeless pseudovalencefunctions localised in the core region. Such pseudowavefunctions can be described very well in a localised basis with not too many functions. The disadvantages in this case are that the influence of the basis on the criteria of convergence can be less easily tested and that multi-centre integrals appear in the Hamiltonian matrix elements that can be solved only at high computational cost. However it is possible to combine both types of functions, plane waves and a few localised functions to a "mixed basis" such that the benefits of both remain but their disadvantages do not occur, as done by Louie et al. [76], Fu

and Ho [38] and Elsässer et al. [32]. Then the wave functions of the crystal look like this:

$$|\psi_{\mathbf{k}j}\rangle = \sum_{\mathbf{G}} \psi_{\mathbf{G}}^{\mathbf{k}j} |\mathbf{k}+\mathbf{G}\rangle + \sum_{\alpha lm} \beta_{\alpha lm}^{\mathbf{k}j} |\phi_{\alpha lm}^{\mathbf{k}}\rangle, \tag{3.26}$$

with the plane waves

$$\langle \mathbf{r}|\mathbf{k}+\mathbf{G}\rangle = \frac{\mathbf{1}}{\sqrt{\Omega}} \mathbf{e}^{\mathbf{i}(\mathbf{k}+\mathbf{G})\mathbf{r}} \tag{3.27}$$

and the Bloch-transformed localised functions

$$\langle \mathbf{r}|\varphi_{\alpha lm}^{\mathbf{k}}\rangle = \sum_{\mathbf{T}} e^{i\mathbf{k}(\mathbf{T}+\mathbf{R}_\alpha)} \varphi_{\alpha lm}(\mathbf{r}-\mathbf{T}-\mathbf{R}_\alpha). \tag{3.28}$$

$\alpha$ is the index of the atoms in the unit cell and $l$ and $m$ are the quantum number of the angular momentum and the magnetic quantum number, respectively. The functions $\phi_{\alpha lm}$ are localised at the atomic sites and have the form

$$\varphi_{\alpha lm}(\mathbf{r}') = f_{\alpha l}(r') i^l K_{lm}(\hat{\mathbf{r}}'), \qquad \mathbf{r}' = \mathbf{r}-\mathbf{T}-\mathbf{R}_\alpha. \tag{3.29}$$

$f_{\alpha l}$ is a radial atomic-like pseudowavefunction and $K_{lm}$ a cubic harmonic. $f_{\alpha l}$ is chosen such that functions localised at neighbouring atoms do not overlap. Thus multi-centre integrals between the localised functions in the Hamiltonian matrix elements are avoided and at the same time strongly localised orbitals can be described with a small number of basis functions. The bonding in the interatomic region is still well described by the plane waves, which are present everywhere in the unit cell.

## 3.4 The Total Energy and Atomic Forces

Within the LDA we can write the total energy of the system of $N_e$ electrons and $N_N$ nuclei as

$$\begin{aligned} E_{tot} &= E_0^{el}[n_0] + E_{N-N} \\ &= \sum_{i=1}^{N_e} \epsilon_i - E_H[n_0] - \int n_0(\mathbf{r}) v_{xc}[n_0(\mathbf{r})] d^3\mathbf{r} + E_{xc} + E_{N-N}. \end{aligned} \tag{3.30}$$

$E_{N-N}$ is the electrostatic interaction energy of the ionic cores. As explained in section 2 where we introduced the Born-Oppenheimer approximation, the kinetic energy of the nuclei can omitted, as most problems can be treated by assuming fixed atomic positions. They can be relaxed statically after calculating the forces

$$\mathbf{F}_\alpha = -\nabla_{\mathbf{R}_\alpha} E_0^{tot}(\{\mathbf{R}_\alpha\}). \tag{3.31}$$

We use the Hellmann-Feynman theorem[35], which states that

$$\mathbf{F}_\alpha = -\left.\frac{\partial E^{tot}}{\partial \mathbf{R}_\alpha}\right|_{n_0}. \tag{3.32}$$

(3.32) brings about the big advantage that we do not have to determine the energy hyperface $E_0^{ges}(\{\mathbf{R}_\alpha\})$ by shifting the atoms. Instead, the forces can directly be obtained as derivatives of the energy functional with respect to the atomic positions. Problems may occur if we use a set of basis functions that depend explicitly on the positions of the nuclei, e.g. localised atomic-like functions. The reason for this is that relation (3.32) is true only for the real ground state density $n_0$. Strictly speaking, as we will be working with a limited set of basis functions, we will never be able to describe it exactly. This leads to the necessity of a correction term, the so-called "incomplete basis set correction"[2][80].

## 3.5 Analysing the Results

Once we have obtained the equilibrium structure of a certain material we also want to understand *why* the structure looks like it does, i.e. what makes it so stable in contrast to other possible geometries or internal coordinates. We will be looking for answers to these kinds of questions in the electronic structure of our systems. Therefore we now introduce some quantities that are useful for such an analysis and whose calculation means are available within the "mixed-basis" code.

Valence electron density distributions give a picture of the arrangement of the bonding charge in real space and provide at least qualitative insight into the nature of the bonds. They will be briefly described in section 3.5.1. Densities of states (DOS) represent the energetic eigenvalue spectra of valence states. They are, e.g., useful to look for energy gaps or to analyse the contributions of single angular momenta to the valence bands. How this

[2]It is interesting to see that the correction term is vanishing not only for the limit of a complete basis, but also for a basis consisting only of plane waves (see e.g. [80])

is done is explained in section 3.5.2. Finally, a projection of the crystal wave function onto an atomic-like basis set enables us to analyse specific bonds between selected atoms, as described in section 3.5.3. The contributions of these bonds to the bonding energy can be evaluated with the help of covalent bond energies, presented in section 3.5.4.

### 3.5.1 Electron Density Distributions

To get an impression of the spatial distribution of the self-consistent valence electron density one has to define cuts through the crystal. Then the amplitude of the electron density (or also of ionic, Hartree or exchange-correlation potentials) is represented in these planes by two-dimensional plots of, e.g., contour lines.

### 3.5.2 Densities of States

If $N(\epsilon)$ is the number of valence states per unit cell with energies up to $\epsilon$, then the density of states $D(\epsilon)$ is defined as the number $dN$ of states per unit cell within the energy interval $(\epsilon, \epsilon + d\epsilon)$:

$$dN(\epsilon) = D(\epsilon)d\epsilon \quad . \tag{3.33}$$

After integrating over the first Brillouin-zone we know the number of states up to $\epsilon$ and their occupation weights $f_{\mathbf{k}j}$[3] at each k-point (j is the band index) and can calculate $D(\epsilon)$:

$$D(\epsilon) = \frac{2}{n_{kpt}} \sum_{\mathbf{k}j} \frac{\partial}{\partial \epsilon} f_{\mathbf{k}j}(\epsilon) \quad . \tag{3.34}$$

To get information about the DOS at individual atomic sites and different angular momenta, we display the crystal wavefunction in terms of eigenfunctions $K_{lm}(\hat{\mathbf{r}}')$ of the angular momentum with respect to the site $\mathbf{R}_\alpha$:

$$\psi_{\mathbf{k}j}(\mathbf{r}) = \sum_{lm} R^{\mathbf{k}j}_{\alpha lm}(r') K_{lm}(\hat{\mathbf{r}}'), \qquad \mathbf{r}' = \mathbf{r} - \mathbf{R}_\alpha \quad . \tag{3.35}$$

[3]The states are filled up to the Fermi level according to the Fermi-Dirac statistics and such that $\sum_{\mathbf{k}j} f_{\mathbf{k}j} = N_e$, with $N_e$ being the total number of electrons in the unit cell.

Then the probability that an electron is found at the atomic site $\mathbf{R}_\alpha$ in a state of angular momentum $l$ and with magnetic quantum number $m$ is given by

$$p_{\alpha lm}^{\mathbf{k}j} = \int_0^{r_{dos,\alpha}} |R_{\alpha lm}^{\mathbf{k}j}(r')|^2 r'^2 dr' d^3\mathbf{r} \quad . \tag{3.36}$$

$r_{dos,\alpha}$ is the radius of a sphere around the atom with index $\alpha$. Its choice is more or less a matter of taste. One common way is to choose the radius of touching but non-overlapping spheres in an equilibrium reference structure. The $p_{\alpha lm}^{\mathbf{k}j}$ can be summed up to the probability of finding an electron within a sphere of radius $r_{dos,\alpha}$ around the atom $\alpha$,

$$p_\alpha^{\mathbf{k}j} = \sum_{lm} p_{\alpha lm}^{\mathbf{k}j} \quad . \tag{3.37}$$

With these probability factors the site- and angular-momentum projected DOS $D_{\alpha lm}$ as well as the "total" site-projected DOS $D_\alpha$ can be calculated,

$$D_{\alpha lm}(\epsilon) = \frac{2}{n_{kpt}} \sum_{\mathbf{k}j} \frac{\partial}{\partial \epsilon} f_{\mathbf{k}j}(\epsilon) p_{\alpha lm}^{\mathbf{k}j} \tag{3.38}$$

$$\text{and} \qquad D_\alpha(\epsilon) = \frac{2}{n_{kpt}} \sum_{\mathbf{k}j} \frac{\partial}{\partial \epsilon} f_{\mathbf{k}j}(\epsilon) p_\alpha^{\mathbf{k}j} \quad . \tag{3.39}$$

For details see e.g [80].

### 3.5.3 Orbital Overlap Populations

To analyse the chemical bond between two atoms it is useful to present the crystal wave-function as a linear combination of atomic (atomic-like) orbitals (LCAO). So we choose a LCAO basis $\{|\varphi_{\alpha lm}\rangle\}$ consisting of localised functions centred at the atomic site $\alpha$, with variable ranges of overlaps for different atomic sites.

$$\varphi_{\alpha lm}(\mathbf{r}') = f_{\alpha l}(r') i^l K_{lm}(\hat{\mathbf{r}}'), \qquad \mathbf{r}' = \mathbf{r} - \mathbf{T} - \mathbf{R}_\alpha \quad , \tag{3.40}$$

with $l$ and $m$ being again the angular momentum and the magnetic quantum number. The $K_{lm}(\hat{\mathbf{r}}')$ are eigenfunctions of the angular momentum (cubic harmonics) and $f_{\alpha l}(r') i^l$ is a

radial function[4]. With these localised functions the Bloch functions

$$\langle \mathbf{r}|\varphi^{\mathbf{k}}_{\alpha lm}\rangle = \sum_{\mathbf{T}} e^{i\mathbf{k}(\mathbf{T}+\mathbf{R}_\alpha)}\varphi_{\alpha lm}(\mathbf{r}-\mathbf{T}-\mathbf{R}_\alpha) \tag{3.41}$$

are built. For this basis we get the overlap and Hamiltonian matrix

$$S_{\mu\nu} = \langle \varphi^{\mathbf{k}}_\mu|\varphi^{\mathbf{k}}_\nu\rangle \quad , \tag{3.42}$$

$$H_{\mu\nu} = \langle \varphi^{\mathbf{k}}_\mu|\widehat{H}|\varphi^{\mathbf{k}}_\nu\rangle \quad , \tag{3.43}$$

where the indices $\mu$ and $\nu$ comprise the former $\alpha, l$ and $m$, and where $\widehat{H}$ is the self consistent effective one-electron Hamiltonian of the Schrödinger equation 3.7 in the LDA, and for instance represented by the mixed basis.
As our localised basis functions are normalised but non-orthogonal, we have to define the dual basis $\left\{|\varphi^{\mathbf{k}+}_\mu\rangle\right\}$ by demanding

$$\langle \varphi^{\mathbf{k}+}_\mu|\varphi^{\mathbf{k}}_\nu\rangle = \delta_{\mu\nu} \quad , \tag{3.44}$$

with

$$|\varphi^{\mathbf{k}+}_\mu\rangle = \sum_\nu |\varphi^{\mathbf{k}}_\nu\rangle S^{-1}_{\mu\nu}(\mathbf{k}) \quad . \tag{3.45}$$

Then we can construct the projection operator

$$\widehat{P}(\mathbf{k}) = \sum_\mu |\varphi^{\mathbf{k}}_\mu\rangle\langle\varphi^{\mathbf{k}+}_\mu| \tag{3.46}$$

to project the crystal wave functions on the local basis. The projected wave function $|\chi_{\mathbf{k}j}\rangle$ is

$$|\chi_{\mathbf{k}j}\rangle = \widehat{P}(\mathbf{k})|\psi_{\mathbf{k}j}\rangle = \sum_\mu c^{\mathbf{k}j}_\mu|\varphi^{\mathbf{k}}_\mu\rangle, \tag{3.47}$$

with the coefficients

$$c^{\mathbf{k}j}_\mu = \langle\varphi^{\mathbf{k}+}_\mu|\psi_{\mathbf{k}j}\rangle. \tag{3.48}$$

[4]In this work atomic pseudowavefunctions have been used for $f_{\alpha l}(r')i^l$, contracted with a factor $\lambda_{\alpha l}$ and limited to a certain range by a cut-off function.

$|\chi_{\mathbf{k}j}\rangle$ will never equal $|\psi_{\mathbf{k}j}\rangle$ perfectly. To test and to optimise the quality of our basis we can use the spillage [105, 106]

$$S = \frac{1}{N_e}\frac{2}{n_{kpt}}\sum_{\mathbf{k}j} f_{\mathbf{k}j}\langle\psi_{\mathbf{k}j}|(1-\widehat{P}(\mathbf{k}))|\psi_{\mathbf{k}j}\rangle. \tag{3.49}$$

It varies between 0 and 1 and tells which charge fraction per valence electron in the unit cell is lost by projecting the crystal wavefunction onto the local basis set. As we said the projected crystal wavefunctions $|\chi_{\mathbf{k}j}\rangle$ are close to but not identical with the self-consistent $|\psi_{\mathbf{k}j}\rangle$, the same holds for their overlap matrix $R$,

$$R_{ij}(\mathbf{k}) = \langle\chi_{\mathbf{k}i}|\chi_{\mathbf{k}j}\rangle = \sum_{\mu\nu} c_\nu^{\mathbf{k}j*} S_{\mu\nu}(\mathbf{k}) c_\mu^{\mathbf{k}j}. \tag{3.50}$$

The $R_{jj}$ will be $\leq 1$ and we can write

$$S = \frac{1}{N_e}\frac{2}{n_{kpt}}\sum_{\mathbf{k}j} f_{\mathbf{k}j}\left(1 - R_{jj}(\mathbf{k})\right). \tag{3.51}$$

With this local basis set we can now calculate bonding charges, occupation numbers and bonding energies for the crystal.
The charge accumulated in a bond through overlap of two orbitals characterised by $\mu$ and $\nu$ is given by

$$q_{\mu\nu} = 2\frac{2}{n_{kpt}}\sum_{\mathbf{k}j} f_{\mathbf{k}j} Re\left(c_\nu^{\mathbf{k}j+} S_{\mu\nu}(\mathbf{k}) c_\mu^{\mathbf{k}j}\right) \quad \text{, with} \quad \mu \neq \nu \quad , \tag{3.52}$$

$$\text{where} \quad c_\nu^{\mathbf{k}j+} = \sum_i R_{ij}^{-1}(\mathbf{k}) c_\nu^{\mathbf{k}j*} \quad . \tag{3.53}$$

The occupation number of orbital $\mu$ is then given after Mulliken [86] just by dividing the overlap population $q_{\mu\nu}$ by two after summing over all orbitals $\nu$ with whom $\mu$ overlaps:

$$q_\mu = \frac{2}{n_{kpt}}\sum_{\mu}\sum_{bfkj} f_{\mathbf{k}j} Re\left(c_\nu^{\mathbf{k}j+} S_{\mu\nu}(\mathbf{k}) c_\mu^{\mathbf{k}j}\right) \quad . \tag{3.54}$$

With the energy dependent occupation weights $f_{\mathbf{k}j}$ we can also receive the energy resolved

bonding charge or overlap population

$$COOP_{\mu\nu}(\epsilon) = 2\frac{2}{n_{kpt}} \sum_{\mathbf{k}j} \frac{\partial}{\partial \epsilon} f_{\mathbf{k}j}(\epsilon) Re\left(c_{\nu}^{\mathbf{k}j+} S_{\nu\mu} c_{\mu}^{\mathbf{k}j}\right) \quad . \tag{3.55}$$

This expression was first defined by Hoffmann [58] as "crystal orbital overlap population" (COOP) to analyse bonding in crystals. The corresponding energy resolved bonding energy, the "crystal orbital Hamilton population" was introduced by Dronskowski [29]:

$$COHP_{\mu\nu}(\epsilon) = 2\frac{2}{n_{kpt}} \sum_{\mathbf{k}j} \frac{\partial}{\partial \epsilon} f_{\mathbf{k}j}(\epsilon) Re\left(c_{\nu}^{\mathbf{k}j+} H_{\nu\mu} c_{\mu}^{\mathbf{k}j}\right) \quad . \tag{3.56}$$

The bonding energy is given by

$$E_{\mu\nu} = 2\frac{2}{n_{kpt}} \sum_{\mathbf{k}j} f_{\mathbf{k}j} Re\left(c_{\nu}^{\mathbf{k}j+} H_{\nu\mu}(\mathbf{k}) c_{\mu}^{\mathbf{k}j}\right) \quad . \tag{3.57}$$

The disadvantage of expressions (3.56) and (3.57) is their variability with respect to a shift in the effective potential. As we have seen in section 3.2.2 the zero level of the effective potential is a parameter that can be chosen freely in our ab-initio calculations. Therefore a new energy partitioning scheme of the total energy has been introduced by Bester et al. [6] which leads to the definition of a "covalent bond energy" which is independent of any shift in the effective potential. Furthermore the partitioning allows a very descriptive interpretation of the individual contributions to the band energy. It shall be described in section 3.5.4.

Yet, first we want to place another remark. So far we have looked at the overlap of Bloch states which we constructed by performing a Bloch sum over atomic-like orbitals, as given by (3.41). However, if we want to analyse the chemical bond between two atoms locally, i.e. to receive information about the local overlap of two atomic-like orbitals and not of the extended Bloch states, we have to invert the Bloch transformation:

$$S_{\mu\nu}(\mathbf{T}) = \frac{1}{n_{kpt}^2} \sum_{\mathbf{k}} e^{-i\mathbf{k}(\mathbf{T}-\mathbf{R}_{\mu}+\mathbf{R}_{\nu})} S_{\mu\nu}(\mathbf{k}) \tag{3.58}$$

$$H_{\mu\nu}(\mathbf{T}) = \frac{1}{n_{kpt}^2} \sum_{\mathbf{k}} e^{-i\mathbf{k}(\mathbf{T}-\mathbf{R}_{\mu}+\mathbf{R}_{\nu})} H_{\mu\nu}(\mathbf{k}) \tag{3.59}$$

$S_{\mu\nu}(\mathbf{T})$ and $H_{\mu\nu}(\mathbf{T})$ are the real space matrix elements between to orbitals localised at

atoms being separated by a lattice vector $\mathbf{T}$[5] .
Then the bonding charge created by the overlap of orbitals $\mu$ and $\nu$ is

$$q_{\mu\nu}(\mathbf{T}) = 2\frac{2}{n_{kpt}} \sum_{\mathbf{k}j} f_{\mathbf{k}j} Re\left(e^{i\mathbf{k}(\mathbf{T}+\mathbf{R}_\mu-\mathbf{R}_\nu)} c_\nu^{\mathbf{k}j+} S_{\nu\mu}(\mathbf{T}) c_\mu^{\mathbf{k}j}\right) . \tag{3.60}$$

The energy resolved crystal orbital overlap population in the real space formulation is

$$COOP_{\mu\nu}^{\mathbf{T}}(\epsilon) = 2\frac{2}{n_{kpt}} \sum_{\mathbf{k}j} \frac{\partial}{\partial\epsilon} f_{\mathbf{k}j}(\epsilon) Re\left(e^{i\mathbf{k}(\mathbf{T}+\mathbf{R}_\mu-\mathbf{R}_\nu)} c_\nu^{\mathbf{k}j+} S_{\nu\mu}(\mathbf{T}) c_\mu^{\mathbf{k}j}\right) \quad . \tag{3.61}$$

Analogous equations can be derived for the occupation numbers (3.54) and the bonding energies (3.57) and as well for the covalent bond energies that will be introduced in the next section.

### 3.5.4 The Covalent Bond Energy

From equation (3.30) we can derive the following expression for the total energy:

$$\begin{aligned} E_{tot} &= E_{band} + E_{N-N} + D & (3.62)\\ &= \sum_{\mathbf{k}j} f_{\mathbf{k}j} \langle\psi_{\mathbf{k}j}|\widehat{H}|\psi_{\mathbf{k}j}\rangle + E_{N-N} \\ &\quad \underbrace{-\int n_0(\mathbf{r}) v_{eff}(\mathbf{r}) d^3\mathbf{r} + E_H + E_{xc} + \int n_0(\mathbf{r}) v_{ext}(\mathbf{r}) d^3 r}_{+D} \quad . & (3.63) \end{aligned}$$

D is the so-called double-counting term. We see that the total energy is invariant with respect to a shift in the effective potential, as such a shift is cancelled out by a shift of the same amount but opposite sign in the band energy (compare e.g. (3.11)) and the remaining terms are unambiguous (see e.g. [80]).
From the total energy we can derive the cohesive energy $E_{coh}$ by subtracting the energy of

[5]Another possibility would be to use a considerably larger supercell for the calculations, sufficiently big that the Bloch states centred at atom $\alpha$ well inside the cell do not overlap with that of its image in the adjacent cell. An alternative which is of course much more time-consuming and requires various test calculations to ensure that the supercell is large enough.
However, also in the case of a "real-space formulation" test calculations are necessary to ensure the convergence of the matrix elements with respect to the number of **k**-points. We have done this when calculating the overlap populations in different molybdenum carbides, as described in section 7.6

the free atoms, $E^{free\ atom}$:

$$E_{coh} = E_{tot} - E^{free\ atom} \tag{3.64}$$

The cohesive energy shall now be repartitioned into terms with an apparent physical meaning. For this we express the crystal wave function in a basis of atomic-like functions, as in section 3.5.3 and add and substract the terms

$$Re\left(\sum_{\mathbf{k}j}\sum_{\mu\nu}\left[f_{\mathbf{k}j}c_\mu^{\mathbf{k}j}\left(c_\nu^{\mathbf{k}j}\right)^* S_{\nu\mu} - N_\mu^{free\ atom}\delta_{\nu\mu}\right]H_{\mu\mu}\right) \tag{3.65}$$

and

$$Re\left(\sum_{\mathbf{k}j}\sum_{\mu\nu} f_{\mathbf{k}j}c_\mu^{\mathbf{k}j}\left(c_\nu^{\mathbf{k}j}\right)^* S_{\nu\mu}H_{\mu\mu}\right) \tag{3.66}$$

in the expression for the band structure energy. For the remaining terms in (3.63) we approximate $n(\mathbf{r})$ by

$$n(\mathbf{r}) = \sum_\alpha n_\alpha^{free\ atom}(\mathbf{r} - \mathbf{R}_\alpha). \tag{3.67}$$

Then D can be expressed as a sum of atomic contributions, $\sum_\alpha D[n_\alpha^{free\ atom}(\mathbf{r})]$, a pair-potential contribution $E_{pair}$ and a small term $E_{mb}$ taking into account many-body interactions. With this we get the energy of the free atoms

$$E^{free\ atom} = \sum_\mu N_\mu^{free\ atom}H_{\mu\mu}^{free\ atom} + \sum_\alpha D[n_\alpha^{free\ atom}(\mathbf{r})] \tag{3.68}$$

and can finally rearrange the terms in equation 3.64 such that we get [6]

$$E_{coh} = E_{prom} + E_{cf} + E_{polar} + E_{cov} + E_{pair} + E_{mb} \quad . \tag{3.69}$$

To explain the physical meaning of the different contributions to the cohesive energy it is useful to imagine the process of the bonding of atoms to a crystal step by step. First, the valence electrons of the free atom are redistributed within its orbitals. The new orbital population is given by (3.54). The energy needed for that is the promotion energy $E_{prom}$,

$$E_{prom} = \sum_\mu \left(q_\mu - N_\mu^{free\ atom}\right)H_{\mu\mu}^{free\ atom} \quad . \tag{3.70}$$

As the atoms approach each other the electrons begin to feel the crystal potential which leads, first, to a shift in the on-site energies, expressed by the crystal field energy $E_{cf}$:

$$E_{cf} = \sum_{\mu} q_{\mu} \left( H_{\mu\mu} - H_{\mu\mu}^{free\ atom} \right) \quad . \tag{3.71}$$

Afterwards the orbitals *at one atomic site* $\alpha$ hybridise, leading to the polar energy $E_{polar}$,

$$E_{polar} = Re \left( \sum_{\mathbf{k}j\alpha\, l\, l'} f_{\mathbf{k}j} c_{\alpha l}^{\mathbf{k}j} \left( c_{\alpha l'}^{\mathbf{k}j} \right)^{*} \left[ H_{\alpha l\, \alpha l} \right] \right) \quad . \tag{3.72}$$

And finally the orbitals localised *at different atoms* hybridise, gaining the covalent bond energy $E_{cov}$ for the whole bond:

$$E_{cov} = \sum_{\substack{\alpha l\, \alpha' l' \\ \alpha \neq \alpha'}} E_{cov,\, \alpha l\, \alpha' l'} \quad , \tag{3.73}$$

with

$$E_{cov,\, \alpha l\, \alpha' l'} = Re \left( \sum_{\mathbf{k}j} f_{\mathbf{k}j} c_{\alpha l}^{\mathbf{k}j} \left( c_{\alpha' l'}^{\mathbf{k}j} \right)^{*} \left[ H_{\alpha' l' \alpha l} - S_{\alpha' l'\, \alpha l}\, \overline{\epsilon_{\alpha' l'\, \alpha l}} \right] \right) \tag{3.74}$$

$$\overline{\epsilon_{\alpha' l'\, \alpha l}} = \frac{1}{2} \left( H_{\alpha l\, \alpha l} + H_{\alpha' l'\, \alpha' l'} \right) \quad . \tag{3.75}$$

$E_{cov,\, \alpha l\, \alpha' l'}$ is the orbital resolved covalent bond energy. It can be shown that not only the cohesive energy (3.64) but also all respective contributions, among them the covalent bond energies (3.74, 3.73) are invariant with respect to any shift in the effective potential [6].

# Chapter 4

# Semi Empirical Methods

With a semi-empirical method, in our case the tight-binding (TB) method, we make a compromise between the highly accurate, but computationally very expensive ab-initio methods introduced in the last chapter, and the fast but limited fully empirical methods, like molecular dynamics simulations with Lennard-Jones or Tersoff potentials, used to investigate dynamical properties of complex materials. Tight-binding calculations are typically two or even three orders of magnitudes faster than ab-initio calculations, depending on the degree of approximations made for the Hamiltonian and overlap matrix elements and on the complexity of the parametrisation. This gain in computational speed is mainly due to the neglect of self-consistency and the use of a minimal basis set, as will be explained below. On the other hand tight-binding methods suffer from a reduction in transferability, due to the approximations made. Summarising, one can say that TB models are useful in those situations (not too far away from the ones the model was fitted to) in which quantum mechanical effects are significant, but the system size makes ab-initio calculations impractical.

There are many different approaches within TB theory. A recent overview over the existing branches and methods is given e.g. in [42]. A summary of the basic concepts and their application to transition metals and their alloys can be found e.g. in [100].

## 4.1 Tight Binding Theory

In a TB-band model the total energy of the system is divided in a repulsive part $U_{rep}$ and a bonding part coming from the band structure, $U_{band}$:

$$U_{tot} = U_{rep} + U_{band}. \tag{4.1}$$

The repulsive part is represented as a sum over pairwise functions,

$$U_{rep} = \sum_{\substack{i,j \\ i \neq j}} \phi(r_{ij}), \tag{4.2}$$

where the sum is running over all pairs of atoms within a given range of interaction. The band energy is the sum over all occupied one-particle eigenstates of the electron system,

$$U_{band} = \sum_i f_i \epsilon_i, \tag{4.3}$$
$$\text{with} \qquad \sum_i f_i = N_e.$$

$f_i$ are the occupation numbers, $N_e$ the number of electrons. Equations (4.1) to (4.3) originally have been established intuitively, but can be justified by deriving them via the Harris-Foulkes functional, as shown in sections 4.1.1 and 4.1.2. They build the basis of the semi-empirical tight binding band methods [1]

### 4.1.1 The Harris-Foulkes Functional

One of the reasons why a DFT calculation is computationally time consuming is the fact that it is not a one-step calculation, but a self consistence cycle. So as a first step towards a faster, even though approximate method one can ask, how accurate is the electronic energy after just the first iteration step? Equation (3.12) gives for the total energy of the

[1] By subtracting the energy of free atoms in equation 4.1 and rearranging the terms $U_{tot}$ becomes $U_{bond}$, the bonding energy. This kind of equation is the basis of the *TB bond models.*

electronic system after one iteration step

$$E^{el}[n] = \sum_{i=1}^{N_e} \epsilon_i^{out} - e^2 \iint \frac{n^{out}(\mathbf{r}) n^{in}(\mathbf{r}')}{|\mathbf{r}-\mathbf{r}'|} d\mathbf{r} d\mathbf{r}' + \frac{e^2}{2} \iint \frac{n^{out}(\mathbf{r}) n^{out}(\mathbf{r}')}{|\mathbf{r}-\mathbf{r}'|} d\mathbf{r} d\mathbf{r}' - \int v_{xc}[n^{in}] n^{out}(\mathbf{r}) d\mathbf{r} + E_{xc}[n^{out}], \quad (4.4)$$

where $n^{in}$ and $n^{out}$ are the input and output electron densities, respectively. The error of this functional in second order is

$$E[n^{out}] - E[^{sc}] = O([n^{out} - n^{in}][n^{out} - n^{sc}]) \quad . \quad (4.5)$$

Experience shows however, that $n^{out}$ tends to overcompensate the error in $n^{in}$, thus $E[n^{out}]$ might be a worse approximation than the initial guess, $E[n^{in}]$. Consequently, Harris and Foulkes introduced a new energy functional [37, 51]

$$E[n] = \sum_{i=1}^{N_e} \epsilon_i^{out} - \frac{e^2}{2} \iint \frac{n^{in}(\mathbf{r}) n^{in}(\mathbf{r}')}{|\mathbf{r}-\mathbf{r}'|} d\mathbf{r} d\mathbf{r}' - \int v_{xc}[n^{in}] n^{in}(\mathbf{r}) d\mathbf{r} + E_{xc}[n^{in}] \quad . \quad (4.6)$$

For the self-consistent electron density $n^{sc}$ (4.6) equals (4.4), otherwise it is chosen arbitrarily. It can not be varied anymore, but therefore has the advantage that it is not necessary to calculate $n^{out}$. The results for non-self-consistent calculations are often better than with functional (4.4). The error which is now linear in $n^{out}$ can be approximated as

$$E[n^{out}] - E[n^{sc}] = O([n^{out} - n^{in}][n^{in} - n^{sc}]) \quad . \quad (4.7)$$

To reduce the computational effort even more, the integrals in equation (4.6) can be simplified by making a special ansatz for $n^{in}$. This leads then to an expression for the total energy which can be used as the basis of any tight-binding band model.

### 4.1.2 The Total Energy

In the local density functional theory we approximated the electron system by an electron gas in which the electrons are more or less homogeneously distributed and move rather freely between the ionic cores. In contrast to this approach in the tight binding theory the electrons are imagined to be tightly bound to the atoms and a crystal is imagined to consist of a lattice of rather isolated atoms which interact only weakly. Within this picture

it is natural then to expand the one-electron wavefunctions in a basis set of atomic-like orbitals. This will be done in section 4.1.3. For the charge density we assume for now a superposition of atomic-like, spherically symmetric electron densities:

$$n^{in}(\mathbf{r}) = \sum_{\alpha} n_{\alpha}(|\mathbf{r} - \mathbf{R}_{\alpha}|) \quad . \tag{4.8}$$

With this ansatz and the Harris-Foulkes functional (4.6) the total energy becomes

$$\begin{aligned} E^0 \;=\; & \sum_i f_i \epsilon_i \\ & \underbrace{- \frac{e^2}{2} \sum_{\alpha\beta} \iint \frac{n_{\alpha}(|\mathbf{r} - \mathbf{R}_{\alpha}|) n_{\beta}(|\mathbf{r}' - \mathbf{R}_{\beta}|)}{|\mathbf{r} - \mathbf{r}'|} d\mathbf{r} d\mathbf{r}' + \frac{e^2}{2} \sum_{\alpha,\, \beta \neq \alpha} \frac{Z_{\alpha} Z_{\beta}}{|\mathbf{R}_{\alpha} - \mathbf{R}_{\beta}|}}_{E_1[n^{in}]} \\ & \underbrace{- \int v_{xc}\big[\sum_{\alpha} n_{\alpha}\big] \sum_{\beta} n_{\beta} d\mathbf{r} + E_{xc}\big[\sum_{\alpha} n_{\alpha}\big]}_{E_2[n^{in}]} \quad . \end{aligned} \tag{4.9}$$

$E_1[n^{in}]$ describes the Hartree energy of electrons and nuclei. The first term, the contribution of the electrons, can be split in the interatomic and intraatomic Hartree energies. The interatomic part is then summarised with the repulsive interaction of the nuclei to a common pair potential $\Phi_1$. So finally we can express $E_1[n^{in}]$ by

$$E_1[n^{in}] = \sum_{\alpha} E_H[n_{\alpha}] + \sum_{\alpha,\, \beta \neq \alpha} \Phi_1(|\mathbf{R}_{\beta} - \mathbf{R}_{\alpha}|) \quad . \tag{4.10}$$

As $v_{xc}$ and $E_{xc}$ do not depend linearly on $n$ it is not possible to represent $E_2[n^{in}]$ in a similarly exact way by pair potentials. However, we can expand $E_2[n^{in}]$ in terms of many-body interactions and truncate the expansion after the two-body term. Then we can eventually find an expression analogous to (4.10) for $E_2[n^{in}]$,

$$E_2[n^{in}] = \sum_{\alpha} E_2[n_{\alpha}] + \sum_{\alpha,\, \beta \neq \alpha} \Phi_2(|\mathbf{R}_{\beta} - \mathbf{R}_{\alpha}|) \quad , \tag{4.11}$$

with a structure independent intraatomic term and the sum over pair potentials. If we neglect now the structure-independent expressions in (4.10) and (4.11) and summarise $\Phi_1$ and $\Phi_2$ we end up with the expression for the total energy that is the basis of all TB-band

models,

$$\begin{aligned} E^0(\mathbf{R}_\alpha) &= \sum_i f_i \epsilon_i + \sum_{\alpha,\,\beta\neq\alpha} \Phi(|\mathbf{R}_\beta - \mathbf{R}_\alpha|) \\ &= U_{band} + U_{rep} \quad . \end{aligned} \tag{4.12}$$

The band energy is the sum over one-particle energies that are solutions of the effective one-particle Schroedinger equation. They are calculated in a non-self-consistent way that shall be described in the next sections.

### 4.1.3 The Band Energy

To calculate $U_{band}$ we have to solve the eigenvalue problem, (3.25). Therefore, the first step is to choose a convenient basis set.

#### The Tight-Binding Basis

As mentioned above, the main assumption of all tight binding models is that the electrons are tightly bound to the atoms and their wavefunctions keep their atomic-like character when the atoms are brought together to form a crystal. Thus it is natural to choose a basis of localised functions. This basis should be complete in the sense that all occupied eigenstates (in the ground state) can be described, but at the same time as small as possible to keep the computational complexity small, thus a so-called "minimal basis set" is used. The one-electron wavefunctions become

$$|\phi_i\rangle = \sum_{\alpha,l} c^i_{\alpha l} |\varphi_{\alpha l}\rangle, \tag{4.13}$$

where the $|\varphi_{\alpha l}\rangle$ are localised at the atomic site $\mathbf{R}_\alpha$ and are a product of a radial function $R_l$ that only depends on the distance of the electron from the atom, and an angle dependent function $Y_l$ (spherical or cubic harmonics):

$$|\varphi_{\alpha l}\rangle = R_\ell(|\mathbf{r} - \mathbf{R}_\alpha|) Y_l(\theta, \varphi). \tag{4.14}$$

The index l comprises the quantum number of angular momentum, $\ell$, and the magnetic quantum number $m$. With this set of basis functions the eigenvalue problem (eq. 3.25)

becomes

$$\sum_{\alpha,l} H_{\alpha' l',\alpha l} c^i_{\alpha l} = \epsilon_i \sum_{\alpha,l} S_{\alpha' l',\alpha l} c^i_{\alpha l}, \tag{4.15}$$

with the matrix elements

$$H_{\alpha' l',\alpha l} = \langle \varphi_{\alpha' l'} | \widehat{H} | \varphi_{\alpha l} \rangle \tag{4.16}$$

$$\text{and} \qquad S_{\alpha' l',\alpha l} = \langle \varphi_{\alpha' l'} | \varphi_{\alpha l} \rangle \tag{4.17}$$

We should keep in mind that to calculate the crystal wave function, we have to build Bloch functions from the local functions (compare e.g. (3.28))

$$\chi_{\mathbf{k}j} = \langle \mathbf{r} | \varphi^{\mathbf{k}}_{\alpha l m} \rangle \tag{4.18}$$

$$= \sum_{\mathbf{T}} e^{i\mathbf{k}(\mathbf{T}+\mathbf{R}_\alpha)} \varphi_{\alpha l m}(\mathbf{r} - \mathbf{T} - \mathbf{R}_\alpha) \quad , \tag{4.19}$$

Then the eigenvalue problem becomes

$$\sum_{\alpha,l} H^{\mathbf{k}}_{\alpha' l',\alpha l} c^{\mathbf{k}i}_{\alpha l} = \epsilon_{\mathbf{k}i} \sum_{\alpha,l} S^{\mathbf{k}}_{\alpha' l',\alpha l} c^{\mathbf{k}i}_{\alpha l} \quad , \tag{4.20}$$

with the matrix elements

$$H^{\mathbf{k}}_{\alpha' l',\alpha l} = \langle \chi^{\mathbf{k}}_{\alpha' l'} | \widehat{H} | \chi^{\mathbf{k}}_{\alpha l} \rangle \tag{4.21}$$

$$= \sum_{\mathbf{T}} e^{i\mathbf{k}(\mathbf{R}_\alpha - \mathbf{R}_{\alpha'} - \mathbf{T})} \langle \varphi_{\alpha' l'}(\mathbf{r} - \mathbf{R}_\alpha - \mathbf{T}) | \widehat{H} | \varphi_{\alpha l}(\mathbf{r} - \mathbf{R}_\alpha) \rangle \tag{4.22}$$

and

$$S^{\mathbf{k}}_{\alpha' l',\alpha l} = \langle \chi^{\mathbf{k}}_{\alpha' l'} | \chi^{\mathbf{k}}_{\alpha l} \rangle \tag{4.23}$$

$$= \sum_{\mathbf{T}} e^{i\mathbf{k}(\mathbf{R}_\alpha - \mathbf{R}_{\alpha'} - \mathbf{T})} \langle \varphi_{\alpha' l'}(\mathbf{r} - \mathbf{R}_\alpha - \mathbf{T}) | \varphi_{\alpha l}(\mathbf{r} - \mathbf{R}_\alpha) \rangle \quad . \tag{4.24}$$

Solving the eigenvalue problem provides the energy eigenvalues and thus the band energy

$$E_B = \sum_{\mathbf{k}j} f_{\mathbf{k}j} \epsilon_{\mathbf{k}j} \quad . \tag{4.25}$$

The sum over $\mathbf{k}$ runs over the first Brillouin zone and $j$ is the band index.
In principle we could still calculate the matrix elements $\langle \varphi_{\alpha' l'} | \widehat{H} | \varphi_{\alpha l} \rangle$ and $\langle \varphi_{\alpha' l'} | \varphi_{\alpha l} \rangle$ self-

consistently for any given arrangement of atoms. But instead we will approximate them (and the repulsive potential) by an analytical expression which contains free parameters to fit e.g. to ab-initio data. To keep the analytical form rather simple some assumptions and approximations will be introduced in the following. Being as simple as possible the approximate expressions still have to mirror the main dependencies of the matrix elements between two orbitals, which are

- the interatomic distance $|\mathbf{R}_\alpha - \mathbf{R}_{\alpha'}|$,
- the direction cosines of the connecting vector $\mathbf{R}_\alpha - \mathbf{R}_{\alpha'}$,
- the angular momenta l and l' of the orbitals involved
- the atomic species of $\alpha$ and $\alpha'$.
- the environment of the atoms $\alpha$ and $\alpha'$

In many tight binding models the last point is neglected, however. The first approximation we are going to make is the tight-binding approximation.

### 4.1.4 The Tight Binding Approximation

As mentioned repeatedly in this section the main assumption in the tight binding models is that the electrons are well localised around the atomic sites. Among other things this means the Hamilton and overlap integrals between them will decrease rapidly with increasing interatomic distance. So it is legitimate to neglect them after a certain cut-off radius $r_{cut}$:

$$\left.\begin{array}{c}\langle\varphi_{\alpha' l'}|\widehat{H}|\varphi_{\alpha l}\rangle \\ \langle\varphi_{\alpha' l'}|\varphi_{\alpha l}\rangle\end{array}\right\} = 0 \quad \text{for} \qquad |\mathbf{R}_{\alpha'} - \mathbf{R}_\alpha| > r_{cut} \quad . \tag{4.26}$$

The choice of $r_{cut}$ depends on the system. In many cases, especially covalent materials, simple models that include only nearest-neighbour interactions perform very well. The bcc transition metals treated in this work, however do condense in close packed structures where the nearest- and next-nearest-neighbour distances are very similar. So it is sensible to include at least also the second-nearest-neighbours to prevent discontinuities.

### 4.1.5 Orthogonality

We want to assume that the atomic-like basis functions $|\varphi_{\alpha l}\rangle$ are orthogonal. This is a momentous assumption leading to several simplifications. With an orthonormal basis set

the overlap matrix equals the unity matrix:

$$S_{\alpha' l' \, \alpha l} = \delta_{\alpha \alpha'} \delta_{l l'} \quad . \tag{4.27}$$

With this the number of free parameters is considerably reduced. But most important the eigenvalue problem simplifies to

$$\sum_{\alpha, l} H_{\alpha' l', \alpha l} c^i_{\alpha l} = \epsilon_i c^i_{\alpha' l'} \quad . \tag{4.28}$$

This orthogonal eigenvalue problem is computationally much less demanding and thus saves a lot of calculation time.
Now how to justify the assumption of orthogonal basis states? One can argue that it is always possible to perform a so-called Löwdin transformation which converts the non-orthogonal $|\varphi_{\alpha l}\rangle$ into orthogonal Löwdin orbitals $|\varphi'_{\alpha l}\rangle$,

$$\varphi' = \varphi \mathbf{S}^{-\frac{1}{2}} \quad . \tag{4.29}$$

From equation (4.29) we see the problem that arises from this transformation: the Löwdin orbitals have parts which are localised at neighbouring atoms. Thus the Hamilton matrix elements have a much more complicated environment dependency than in an non-orthogonal basis set. This environment dependency is hard to capture with an as simple as possible analytical expression and therefore will reduce the transferability of the free parameters once they are fitted to a limited set of structures. We will come back to this point when discussing the environment dependent parametrisation in chapter 4.2.

### 4.1.6 The Two Centre Approximation

When starting with the Harris-Foulkes functional, we expressed the input electron density by a superposition of spherically symmetric (atomic) charge densities and neglected all non-linearities in $v_{xc}$ to derive expression (4.12) for the TB total energy. With these assumptions our Hamiltonian now looks like this:

$$H_{\alpha' l', \alpha l} = \langle \varphi_{\alpha' l'} | - \frac{\hbar^2}{2m} \Delta + \sum_{\alpha''} v_{\mathit{eff}, \alpha''}(|\mathbf{r} - \mathbf{R}_\alpha|) | \varphi_{\alpha l} \rangle \quad . \tag{4.30}$$

Three different kinds of integrals occur:

- one-centre terms: $\alpha = \alpha' = \alpha''$ ,
- two-centre terms: $\alpha \neq \alpha' = \alpha''$ ,
- three-centre terms: $\alpha \neq \alpha' \neq \alpha'' \neq \alpha$.

The three-centre terms describe the overlap of two orbitals at different sites with a potential at a third site. This overlap is small in comparison to the one- and two-centre terms and shall be neglected. This is called the *two centre approximation*. It has extensive consequences as it eventually enables the decomposition of the Hamiltonian matrix elements into only a few fundamental integrals, as we will see below. Among the one- and two-centre integrals we distinguish between "on-site" and "hopping" terms (intra- and interatomic matrix elements), depending on whether the orbitals involved are localised at the same or at different atomic sites.

### Intraatomic Matrix Elements

The intraatomic matrix elements describe the "on-site" energies, energies of orbitals localised at the same atom $\alpha$, interacting with the potential at the same site (one-centre terms) or at different sites (two-centre terms). We neglect the interaction of orbitals with different angular momenta $l$. Then the intraatomic Hamiltonian elements are

$$H_{\alpha l,\alpha l} = \epsilon_{\alpha l} = \epsilon^0_{\alpha l} + \sum_{\alpha''} \langle \varphi_{\alpha l} | v_{\mathit{eff},\alpha''} | \varphi_{\alpha l} \rangle \quad , \tag{4.31}$$

with the one-centre term

$$\epsilon^0_{\alpha l} = \langle \varphi_{\alpha l} | -\frac{\hbar^2}{2m}\Delta + v_{\mathit{eff},\alpha} | \varphi_{\alpha l} \rangle \quad . \tag{4.32}$$

### Interatomic Matrix Elements

The interatomic matrix elements describe the "hopping" energies, energies of orbitals localised at neighbouring atoms, interacting via the potentials at the two sites:

$$H_{\alpha' l',\alpha l} = \langle \varphi_{\alpha' l'} | -\frac{\hbar^2}{2m}\Delta + v_{\mathit{eff},\alpha} + v_{\mathit{eff},\alpha'} | \varphi_{\alpha l} \rangle \quad . \tag{4.33}$$

If we ignore the implicit environment dependency that is hidden in $v_{\mathit{eff}}$[2] the interatomic matrix elements do not contain any environment dependency anymore. Thus they can be

[2] as actually it should be determined self-consistently

described by an analytic function containing information only about absolute value and direction of the connecting vector between the two sites and the angular character of the orbitals. For this we decompose the orbitals $|\varphi_{\alpha l}\rangle$ in functions $|\varphi_{\alpha lm}\rangle$, where the quantum number $m$ mirrors the projection of the angular momentum $l$ onto the connecting vector. Thus a $p$-orbital can be decomposed in $\sigma$ and $\pi$-contributions and a $d$-orbital in $\sigma$-, $\pi$- and $\delta$- terms. The Greek letters $\sigma$, $\pi$ and $\delta$ denote a state with quantum number $m = 0$,1 and 2, respectively. Of the Hamiltonian integrals

$$H_{\alpha' l' m', \alpha l m} = \langle \varphi_{\alpha' l' m'} | -\frac{\hbar^2}{2m}\Delta + v_{eff,\alpha} + v_{eff,\alpha'} | \varphi_{\alpha l m} \rangle \tag{4.34}$$

those with $m \neq m'$ vanish due to the orthogonality relations of the cubic harmonics $|\varphi_{\alpha lm}\rangle$. In the end, if using a basis containing $s$-, $p$- and $d$-orbitals, we end up with only ten independent interatomic matrix elements $V_{ll'm}$, schematically shown in figure 4.1. With them integrals between orbitals of any orientation can be calculated in form of linear combinations. The coefficients are composed of the direction cosines of the connecting vector. These linear combinations were constructed and tabulated first by Slater and Koster [109] for $s$-, $p$- and $d$-orbitals and extended to $f$- and $g$- orbitals by Sharma [107]. As an example see figure 4.2, where a matrix element between two p-orbitals (e.g. two $p_x$-orbitals) is decomposed in $\sigma$- an $\pi$- contributions.

## 4.2 The Environment-Dependent Parametrisation

### 4.2.1 The Environment-Dependent Model for Carbon

The environment-dependent tight binding model that we are going to introduce in this chapter has been developed by Tang et al. [116] to model a variety of carbon structures. It is based on a previous TB model of Xu et al. [123], a traditional orthogonal, two centre model. Tang et al. added two important features, environment dependency via a screening function and bond length scaling, which significantly improved the transferability of the model and the predicted properties of the carbon structures, e.g. phonon frequencies and elastic constants [116]. All pairwise functions are expressed as

$$h(r_{\alpha\,\alpha'}) = A_1 R_{\alpha\,\alpha'}^{-A_2} exp\left[-A_3 R_{\alpha\,\alpha'}^{A_4}\right](1 - S_{\alpha\,\alpha'}) \quad . \tag{4.35}$$

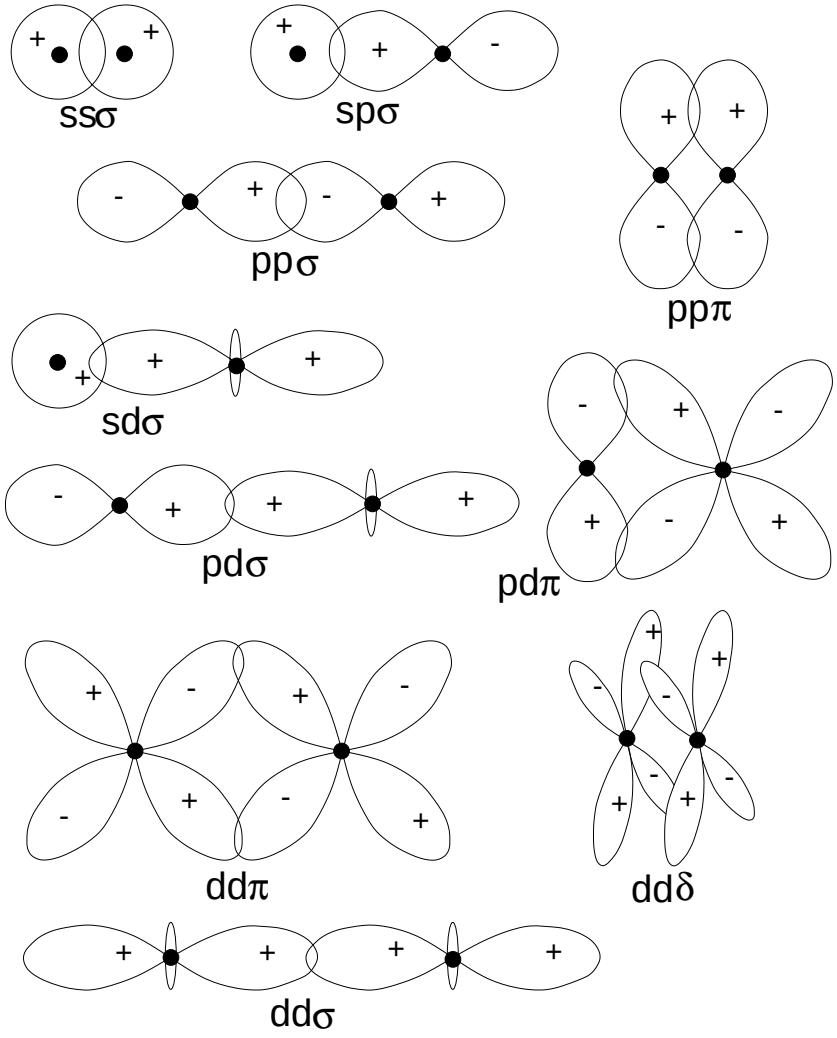


Figure 4.1: Independent interatomic matrix elements for an s- p- d- basis, constructed after Slater and Koster.

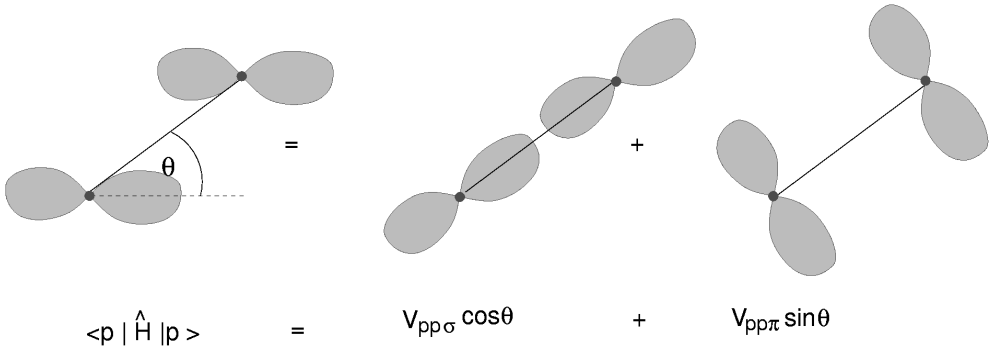


Figure 4.2: Slater-Koster decomposition of an $\langle p|\widehat{H}|p\rangle$ matrix element.

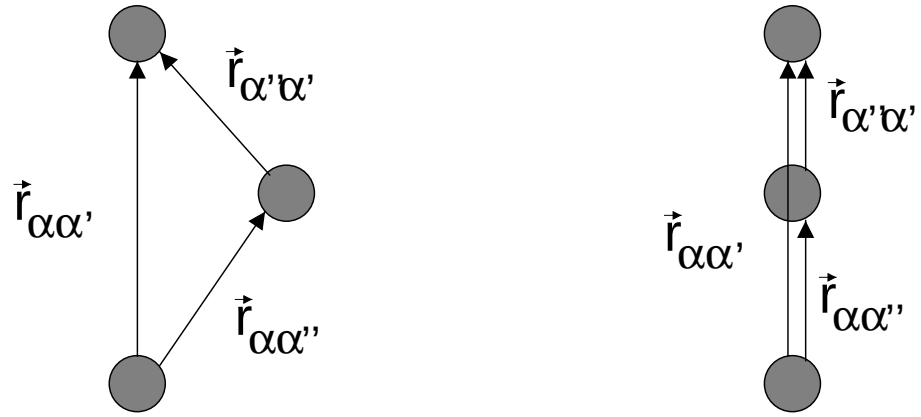


Figure 4.3: For illustration of the screening effect of a third atom $\alpha''$ in the vicinity of a pair of interacting atoms, $\alpha$ and $\alpha'$.

$h(r_{\alpha\,\alpha'})$ can be a hopping integral $V_{ll'm}$ or the repulsive potential $\Phi(r_{\alpha\,\alpha'})$ between the atoms $\alpha$ and $\alpha'$. $r_{\alpha\,\alpha'}$ is the real distance and $R_{\alpha\,\alpha'}$ the scaled distance between the two atoms (compare (4.38)). $S_{\alpha\,\alpha'}$ is a screening function, given by

$$S_{\alpha\,\alpha'} = \frac{e^{\xi_{\alpha\,\alpha'}} - e^{-\xi_{\alpha\,\alpha'}}}{e^{\xi_{\alpha\,\alpha'}} + e^{-\xi_{\alpha\,\alpha'}}} = tanh(\xi_{\alpha\,\alpha'}) \quad , \tag{4.36}$$

with

$$\xi_{\alpha\,\alpha'} = B_1 \sum_l exp\left[-B_2\left(\frac{r_{\alpha\,\alpha'} + r_{\alpha'\,\alpha''}}{r_{\alpha\,\alpha''}}\right)^{B_3}\right] \quad . \tag{4.37}$$

The parameters $A_i$ and $B_i$ are different for different hopping integrals and the repulsive potential. The screening function $S_{\alpha\,\alpha'}$ varies between 0 and 1 and describes the influence of a third atom $\alpha''$ on the bond between atoms $\alpha$ and $\alpha'$. The contribution of $\alpha''$ to $\xi_{\alpha\alpha'}$ is largest if $\alpha''$ is situated in the connecting line between $\alpha$ and $\alpha'$. Then the screening of the interaction takes on a maximum. For illustration see figure 4.3. The scaled bond length $R_{\alpha\,\alpha'}$ in equation (4.35) is given by

$$R_{\alpha\,\alpha'} = r_{\alpha\,\alpha'}\left\{1 + \frac{\delta}{2}\left[\left(\frac{g_\alpha - g_0}{g_0}\right) + \left(\frac{g_{\alpha'} - g_0}{g_0}\right)\right]\right\} \quad , \tag{4.38}$$

where $g_\alpha$ ($g_{\alpha'}$) is the effective coordination number of atom $\alpha$ ($\alpha'$) in a given atomic arrangement and $g_0$ is the reference coordination number of $\alpha$ in the equilibrium structure. The bondlength scaling can be understood as a reflection of the behaviour of over- and undersaturated bonds. If the atom $\alpha$ is coordinated by more bonding partners than in

the equilibrium structure, less electrons per bond will be available and the bonds will be slightly weaker. In the TB calculation this weaker interaction is received by a larger (scaled) bond length $R_{\alpha\,\alpha'}$. The analogous argumentation holds for a smaller coordination number than in the equilibrium structure. The coordination numbers are "effective" coordination numbers as the coordination partners of atom $\alpha$ are screened:

$$g_\alpha = \sum_{\alpha'} (1 - S_{\alpha\,\alpha'}) \quad . \tag{4.39}$$

In the intraatomic matrix elements (4.40) the two-centre terms $\Delta\epsilon_l(r_{\alpha\,\alpha'})$ are also modelled by expression (4.35), so the on-site energy for an orbital with angular momentum $l$ is

$$\epsilon_{l,\alpha} = \epsilon_{l,0} + \sum_{\alpha'} \Delta\epsilon_l(r_{\alpha\,\alpha'}) \quad , \tag{4.40}$$

with the one-centre terms $\epsilon_{l,0}$. The repulsive energy is expressed as a fourth-order polynomial the argument of which is the sum over all pairwise repulsive interactions $\Phi$:

$$E_{rep} = \sum_\alpha f\Big(\sum_{\alpha'} \Phi(r_{\alpha\,\alpha'})\Big) \tag{4.41}$$

with (4.42)

$$f(x) = \sum_{n=0}^{n=4} C_n x^n \quad . \tag{4.43}$$

With their parametrisation Tang et al. reintroduced to a certain extend the environment dependency of the Hamiltonian elements that has been neglected by choosing an orthogonal basis and the two-centre approximation. By this their model gained a very high transferability, from C as a linear chain (coordination number = 2), to C in the close-packed structures (coordination number = 12). The price one has to pay is of course a higher computational time, as additional loops over all pairs of atoms have to be performed to calculate the screening function. However, this is still far easier than taking into account explicitly three-centre matrix elements.

### 4.2.2 The Environment-Dependent Model for Molybdenum

In the case of Mo, extreme geometries like a linear chain do not play a role. This brings about some simplifications. Haas et al. used Tang's model for a TB-description of Molybdenum including *s*-, *p*- and *d*-orbitals in the basis [47, 48]. They started with a simplified

version, neglecting the bond-length scaling [48], but introduced it later to improve the transferability of the parameters to more crystal structures (e.g. A15) [47]. Still, the model is a little less complex as they set the parameters $A_2 = 0$ and $A_4 = 1$. Then the expression for all pairwise functions (4.35) becomes

$$h(r_{\alpha\,\alpha'}) = A_1 exp\left[-A_3 R_{\alpha\,\alpha'}\right](1 - S_{\alpha\,\alpha'}) \quad . \tag{4.44}$$

The intraatomic energies are given by

$$\epsilon_{\alpha,d} = \epsilon_d^0 + \sum_{\alpha'} \Delta\epsilon_d(R_{\alpha\,\alpha'}) \tag{4.45}$$

$$\epsilon_{\alpha,s} = \epsilon_{\alpha d} + \epsilon_{s-d}^0 + \sum_{\alpha'} \Delta\epsilon_d(R_{\alpha\,\alpha'}) \tag{4.46}$$

$$\epsilon_{\alpha,p} = \epsilon_{\alpha d} + \epsilon_{p-d}^0 + \sum_{\alpha'} \Delta\epsilon_d(R_{\alpha\,\alpha'}) \tag{4.47}$$

$$\tag{4.48}$$

where the $\Delta\epsilon_l$ are also parametrised according to (4.44). To reduce the number of free parameters, the canonical relationships [52] were used for the *d*-*d* and *p*-*d* matrix elements:

$$V_{dd\sigma} : V_{dd\pi} : V_{dd\delta} = -6 : 4 : -1 \tag{4.49}$$

$$V_{pd\sigma} : V_{pd\pi} = -\sqrt{3} : 1 \quad . \tag{4.50}$$

This means that in the fitting procedure the constants $A_1$ of the $V_{ddm}$ and $V_{pdm}$ were determined unter the restrictions of relations (4.49) and (4.50) and the $A_1$ and $B_1$ to $B_3$ of the $V_{ddm}$ and of the $V_{pdm}$ were set equal, respectively:

$$C(V_{dd\sigma}) = C(V_{dd\pi}) = C(V_{dd\delta}) \tag{4.51}$$

$$\text{and} \qquad C(V_{pd\sigma}) = C(V_{pd\pi}) \quad , \tag{4.52}$$

where C is any of the constants mentioned above. Furthermore $V_{pp\pi}$, as being comparatively small, has been neglected completely.
In contrast to the model of Tang et al. the repulsive energy is simply given by

$$E_{rep} = \sum_{\substack{\alpha\alpha' \\ \alpha \neq \alpha'}} \Phi(r_{\alpha\,\alpha'}), \tag{4.53}$$

what corresponds to choosing $C_1 = 1$ and setting all other $C_i = 0$ in expression (4.43). Altogether this parametrisation contains 55 free parameters which had been fitted to reproduce ab-initio data like bonding energies and energies of vacancy formation as well as experimental data like phonon frequencies and the elastic constant $C_{44}$ [46, 47, 48]. It should be noted that the parameters $B_1$ to $B_3$ for the screening function which is used for the bond length scaling are the same as those chosen by Tang et al. So the bond length scaling can be understood as a material-independent, purely geometric effect.

### 4.2.3 Mo-C Interactions

So far the environment dependent parametrisation of Tang et al. [116] and Haas et al. [47, 48] have been applied successfully to model the properties of pure Carbon and Molybdenum. In this work processes like segregation of C in Mo and the precipitation of $MoC_x$ at a Molybdenum grain boundary shall be described. Therefore we need a parametrisation of the Mo-C interaction. As the environment dependent descriptions of Mo and C are based on the same analytical expressions it is tempting to adopt the same form for the Mo-C matrix elements and the repulsive interaction. This means we will "simply" need an extra set of parameters $\{A_i, B_i$ and $C_i\}$. An extension which is necessary refers to the bond length scaling. The scaled bond length is now calculated by

$$R_{\alpha\,\alpha'} = r_{\alpha\,\alpha'} \left\{ 1 + \frac{\delta}{2} \left[ \left( \frac{g_\alpha - g_0}{g_0} \right) + \left( \frac{g_{\alpha'} - g_0'}{g_0'} \right) \right] \right\} \quad , \tag{4.54}$$

i.e. $\alpha$ and $\alpha'$ can have different reference coordination numbers if they belong to different atomic species. As said above the parameters of the screening function for the bond length scaling are the same for C and Mo and we consider the bond length scaling as a purely geometric effect. So it is plausible not to change them when calculating the rescaled bond length of a Mo-C pair. It is a point of discussion however, how the parameters of the screening function for the Hamiltonian matrix elements should dependend on the atomic species. The parameters of the screening of a $V_{ss\sigma}$ integral between a pair of C atoms by a C atom are different to those of the screening of a $V_{ss\sigma}$ between Mo atoms by a Mo atom. If we now have both atomic species in one system, how does the "screening-interaction" look like? Using the nomenclature of figure 4.3 we have to decide whether the choice of parameters shall depend on $\alpha$ and $\alpha'$ or on $\alpha''$, or on all of them. A semi-physical formulation of this question would be, does the disturbance of a bond between two atoms by a third atom depend on the properties of the bond (i.e. is it a Mo-Mo, C-C or Mo-C

bond screened by any atom X) or on the disturbing potential (i.e. do we look at any X-Y bond screened by a either a Mo or a C atom) or on both quantitites (Mo-Mo, C-C or Mo-C bond screened by either C or Mo). For the current implementation the first point of view was chosen. Then again the screening is a geometric effect, but the magnitude of the effect depends on the matrix element which is screened, so to say on the initial strength of the unscreened interaction. However, taking into account also the atomic species of the third atom, and thus increasing the number of parameters by a factor of two if needed is a straight forward task.

### 4.2.4 Atomic Forces

Like the total energy in a tight binding band model the force on atom $\beta$ can be split in two contributions, one part derived from the band energy and one from the repulsive interactions:

$$F_\beta = F_\beta^{rep} + F_\beta^{band} \quad . \tag{4.55}$$

We have an analytic expression for both types of interactions. The calculation of the forces originating from the repulsive interactions is straight forward:

$$F_\beta^{rep} = -\sum_{\alpha,\alpha' \neq \alpha} \frac{\partial}{\partial \mathbf{R}_\beta} \Phi(\mathbf{R}_\alpha, \mathbf{R}_{\alpha'}, \{\mathbf{R}_{\alpha''}\}) \quad . \tag{4.56}$$

It is important to keep in mind however, that due to the environment-dependent parametrisation $F$ is a many-body force. $\beta$ can be of type $\alpha$, $\alpha'$, $\alpha''$ or even $\alpha'''$[3]. This makes the calculation as well as the implementation rather complex.
For the contribution of the band energy to the forces we use the Hellmann-Feynman theorem again (compare section 3.4) and write

$$\begin{aligned} F_\beta^{band} &= -\frac{\partial}{\partial \mathbf{R}_\beta} \sum_{\mathbf{k}j} \langle \psi_{\mathbf{k}j} | \widehat{H} | \psi_{\mathbf{k}j} \rangle \\ &= \sum_{\mathbf{k}j} f_{\mathbf{k}j} \sum_{\alpha' l', \alpha l} c_{\alpha' l'}^{\mathbf{k}j} c_{\alpha l}^{\mathbf{k}j} \frac{\partial}{\partial \mathbf{R}_\beta} H_{\alpha' l', \alpha l}^{\mathbf{k}} (\mathbf{R}_\alpha, \mathbf{R}_{\alpha'}, \{\mathbf{R}_{\alpha''}\}) \quad . \end{aligned} \tag{4.57}$$

[3] $\alpha'''$ indicates an atom which is a nearest-neighbour of $\alpha'$ but not of $\alpha$. Atoms of these kind play a role in the derivatives of the scaled bondlength, where they occur in the derivatives of the effective coordination number of $\alpha'$.

This time we can forego any correction terms arising from the use of a basis set of localised functions, as the Hamiltonian elements in a tight-binding model do not depend explicitely on the basis functions.

### 4.2.5 Implementation of the Model and Fitting of the Parameters

The environment dependent model of Tang et al. was implemented in a code for ab-initio LMTO and semi-empirical TB-electronic structure calculations. The basic package of routines was created by van Schilfgaarde, Paxton, Klepeis and Methfessel. The new implementation includes the necessary extensions to Tang's model to treat not only elemental crystals but also compounds. A brief overview over the structure of the implementation and a discussion of the problems is given in appendix C.
For the fitting of the parameters the initial choice is very important. A set of parameters that leads to a good reproduction of the important crystal properties is never unique, so we have to make sure that it describes the distance dependency of matrix elements and repulsive interaction in a physically meaningful way. In chapter 7 we will therefore discuss (among other things) a possible fitting strategy. The accomplishment of the fit and the application of the model to our problems has become beyond the time frame of this work.

# Part II

# Application

# Chapter 5

# Segregation of Light Elements in Niobium and Molybdenum

## 5.1 Introduction

In this chapter the influence of segregated impurities on the atomic structure and the interfacial cohesion of the $\Sigma 5$ symmetrical tilt grain boundary in the bcc transition metals Nb and Mo is investigated. For this interface energies and geometric translation states are analysed and the observed trends are rationalised by studying the electronic structure at the grain boundary. Calculated bonding energy differences will be presented as a measure for the embrittling or cohesion enhancing influence the impurities on the grain boundary cohesion. The results will be compared to Cottrell's "unified theory" of the effects of segregated interstitials on grain boundary cohesion [19] to test the validity of this empirical approach.

The chapter starts with an overview over Cottrell's theory in section 5.2. In sections 5.3 and 5.4 the model for the calculations will be introduced. Then the results will be presented and compared to the predictions of this theory in section 5.5. The results of previous investigations, theoretical and experimental, concerning the pure grain boundary as well as theoretical predictions concerning C at the grain boundary in Mo that play a role for the actual work will be briefly summarised.

## 5.2 Cottrell's Unified Theory

With his "unified theory" [19] Cottrell is uniting different theoretical approaches that describe well different behaviours of interstitial elements at grain boundaries, i.e. the effective medium theory [27, 88] for polarly bonding impurities, and tight-binding or linear combination of atomic orbital schemes [52] for covalently bonding interstitials.
To predict the effects of interstitial elements on grain boundary cohesion in transition metals, Cottrell starts with the electron theory of chemisorption, describing the interactions of single adsorbate atoms with a free metal surface. Starting point is a free atom far away from the metal surface. The first ionisation level $I$ is a characteristic electronic energy level describing the highest filled electron state in a neutral free atom. In the metal the highest occupied level is given by the Fermi energy $\mathrm{E}_F$, which can be referred to the vacuum level by the work function $\Phi$ of the metal. The valence band in the transition metals is a $d$-band, that has a certain width $\mathrm{W}_d$ which can be approximated e.g. by the universal tight binding scheme of Harrison [52]. The relationship between these quantities is shown in figure 5.1.

The situations that can occur correspond to Pettifor's "common band" and "rigid band" model [99], except that the second binding partner is an impurity atom with discrete electronic levels instead of another metal. If, as in figure 5.1 the valence level of the impurity lies within the energy interval given by $\mathrm{W}_d^{occ.}$, the occupied part of the transition metal $d$-band, there is a dynamical equilibrium with an electron hopping from metal to atom and back as the atom now approaches the surface, and

$$I + U(n) \approx \Phi \tag{5.1}$$

where $U(n)$ is the electrostatic potential at the atom with the amount $n$ of excess electrons ($0 \leq n \leq 1$). The resulting electronic energy level of the atom

$$\epsilon_a = I + U(n) \tag{5.2}$$

is "floating" at the Fermi level and a strong hybridisation between the metal $d$-band and the atomic level takes place, leading to covalent bonds between metal and adsorbate atom. The other extreme cases are that the valence level of the impurity is lying far below the lower edge of the $d$-band or far above $\mathrm{E}_F$. In the first case, charge flows from the metal to the impurity until the energy level of the latter is filled and sinks down further, while the emptied metal bands rise in energy. In the second case charge is transferred from the

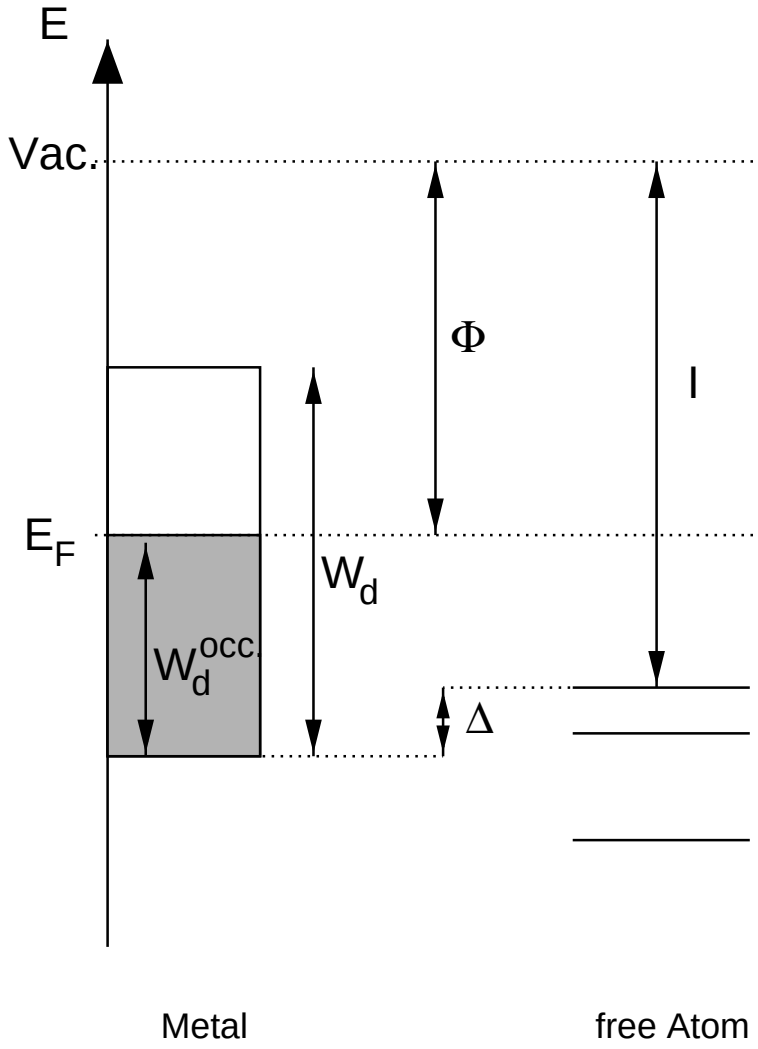


Figure 5.1: Schematic drawing of the transition metal $d$-band and the highest occupied valence state of a free atom. $E_F$ marks the Fermi level. $W_d$ is the width of the metal $d$-band and $W_d^{occ}$ the occupied part of it. $\Phi$ is the work function of the metal. $I$ is the first ionisation energy of the free atom. The energy difference $\Delta$ indicates the relative position of the electronic states, as explained in the text.

| | $EN$ [eV] | $\Phi$ [eV] | $W_d$ [eV] | $W_d^{occ}$ [eV] |
|---|---|---|---|---|
| Nb | 1.2 | 3.99[1] | 9.7 | 3.88 |
| Mo | 1.3 | 4.13[2] | 10.0 | 5.00 |

Table 5.1: Electronegativity $EN$ [4], work function $\Phi$,[1]: for polycrystalline Nb [1], [2]: for the (310) surface of Mo [3], width $W_d$ of the $4d$-bands [52] and the occupied part of it $W_d^{occ}$ for Nb and Mo.

| | $EN$ [eV] | $I$ [eV] | $\Delta^{Nb}$ | $\Delta^{Mo}$ |
|---|---|---|---|---|
| H | 2.2 | 13.598 | -5.73 | -4.47 |
| B | 2.0 | 8.298 | -0.43 | 0.83 |
| C | 2.5 | 11.260 | -3.39 | -2.13 |
| N | 3.1 | 14.534 | -6.66 | -5.40 |
| O | 3.5 | 13.618 | -5.75 | -4.49 |

Table 5.2: Electronegativity $EN$ [4] and first ionisation energy $I$ [4] for the impurity atoms, and the parameter $\Delta$ according to equation (5.3). The smaller the value of $\Delta$ the stronger is the hybridisation we expect.

adsorbate to the metal, the energy levels of the atom are emptied and raised further. In both cases the resulting charge distribution is ionic.

At this point we look at the elements that will play a role in our investigation later. Table 5.1 lists the work function $\Phi$ as well as the width of the $4d$-band for the transition metals Nb and Mo. Note that in the strict sense Cottrell's model is not completely independent of the grain boundary geometry, as the work function of the metal depends on the crystallographic surface orientation. However, compared to other assumptions made in the model, the energy differences between different $\Phi$ due to different surface orientations are small and do not change the general trend, which is all we want to derive here. For precise numbers the ab-initio method described in section 3 will be applied later on. Table 5.2 shows the first ionisation energies of the light interstitials H,B,C,N, and O that will be treateed and the energy difference

$$\Delta = \Phi + W_d^{occ} - I \tag{5.3}$$

which is an indication of the relative position of the valence level of the impurity and the transition metal $d$-band, as shown in figure 5.1.

In case that $\Delta$ is between zero and a positive value $\leq W_d^{occ}$ the highest occupied level of the free atom lies within the transition metal $d$-band, like in the "common band model",

and we expect covalent bonds. If $\Delta$ is negative with a big absolute value, the valence state of the free atom is lying well below the lower edge of the transition metal $d$-band, as in the "rigid band model", and we expect charge transfer from the metal host to the impurity atom, and resulting an ionic charge distribution. Hence, from table 5.2 we expect that B is very likely a candidate to form covalent bonds with Nb as well as Mo, where O and H surely are not, they should form ionic bonds. C and N are somewhere in between. Of course this is just a first estimate, since so far all effects of electronic interaction between metal and adsorbate atom were neglected.

For comparison the electronegativities of the different atomic species are also given in tables 5.1 and 5.2. They are defined as "the power of an atom in a molecule to attract electrons to itself"[92]. To simplify the argumentation even more one could also use their difference to estimate the ionicity of the bonds. This concept was developed by Pauling (see e.g. [92]) on a fully empirical basis to predict reasonably well the extent of ionicity of the chemical bonds in molecules. In our case, however, as the electronegativity of H is in between those of B and C this would predict a different trend - a wrong one, as will be seen later - in the bonding behaviour at the grain boundary than the calculated values for $\Delta$. This shows that for solids an approach based on the electronic states and bands is indeed necessary, even if it may be as elementary as the ansatz of Cottrell.

Now, what does the bonding behaviour at the surface mean for the situation at an internal interface? Cottrell argues that in the case of a covalently bonding impurity the largest part of the bonding energy $E_B$ is the hybridisation energy $E_{hyb}$, and thus $E_B \sim \sqrt{z}$, where $z$ is the coordination number of the impurity. This relationship is resulting when the bonding energy is described in terms of pair potentials based on the second-moment approximation of the band structure [26]. Thus a covalently bonding interstitial impurity always favours the surrounding of a grain boundary over that of a free surface, because of the twofold larger coordination number $z$. Such an impurity increases grain boundary cohesion. For a polarly bonding impurity on the other hand, the contribution of $E_{hyb}$ to $E_B$ is small, $E_B$ is dominated by a spatially homogeneous contribution $E_{hom}$ that can be derived from the effective medium theory [88]. At the same time a considerable amount of energy has to be invested for shifting levels, thus the impurity favours the free surface which provides a smaller coordination number $z$. Such an impurity promotes grain boundary brittleness.

Further in his paper [19] Cottrell is developing a comparatively simple but still extensive scheme of deriving an effective potential (including screening effects) for the adsorbate atom at the metal surface, as well as $E_{hyb}$ and $E_{hom}$. His approach shall not be followed

further here, but instead the energies and electronic structures of different grain boundaries with light interstitial impurities are calculated by means of the density functional theory. The results are compared to the predictions of the "unified theory".

## 5.3 Structures and Energies of the Pure Σ5 STGB in bcc Transition Metals - Theory and Experiment

### 5.3.1 The Model Supercell

For the study of the pure STGB in the bcc metals a supercell containing 20 atoms as shown in figure 5.2a) was used and validated in [31, 90, 89] as a model for the Σ5(310)[001] STGB. The base-centred orthorhombic supercell contains for instance the big grey atoms. The small grey atoms mark the translational repetition of the supercell to build up the bcc structure. Another, more schematic representation of the supercell is shown in figure 5.3 to visualise the influence of the periodic boundary conditions in combination with the special choice of supercell unit vectors. Here only the atoms at the grain boundary have been indicated. In addition to positions of the metal atoms, depicted as big and small grey circles, the positions of the impurity atoms which will be inserted into the supercell later on, are indicated as big and small black circles. The supercell consists of the (001) plane containing the big impurity atoms. The small circles are the periodic images of the respective atoms along the **a** and **b** directions. This model can be used without restrictions to calculate properties of the pure grain boundaries, because it allows full relaxation of the atomic positions. However, it should be noted already here that it is imposing some constraints on calculations with point defects (interstitial impurities): local relaxations parallel to the [001] direction are not possible with such a "one-layer" model. How far this affects the results will be discussed in due course.

### 5.3.2 Translation States of the Pure Σ5 STGB

An issue which has been widely investigated during the last years, both experimentally and theoretically, is that of the intrinsic geometric translation state of the Σ5 STGB in various bcc transition metals. Figure 5.4 shows a high-resolution TEM image of the Σ5 (310)[001] STGB in Mo recorded by W. Sigle [108]. The view is along the [001] direction. The mirror

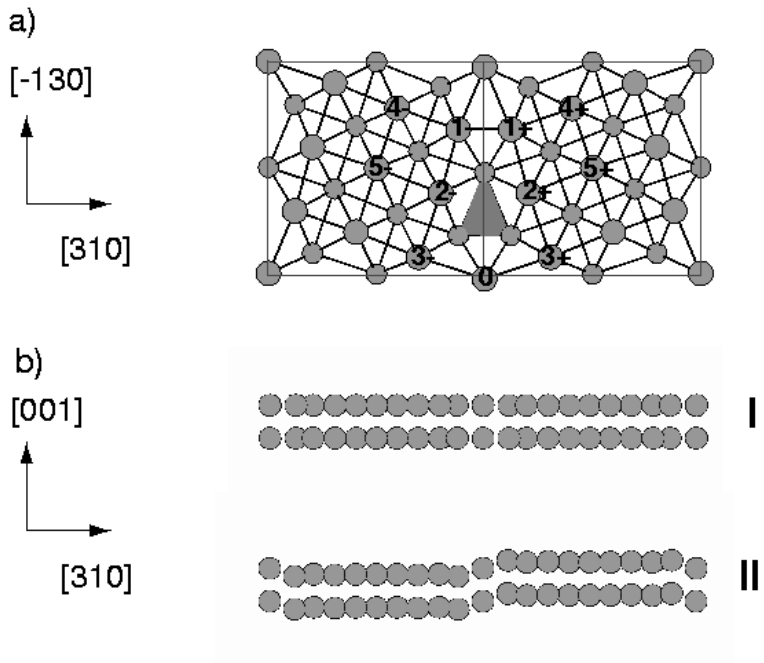


Figure 5.2: a) Supercell model for the Σ5 (310)[001] STGB. The base-centred orthorhombic supercell (cf. refs [31, 90, 89]) contains the large grey atoms. The small grey atoms mark the translational repetition of the supercell to build up the bcc structure. The grey triangle indicates the projection of the trigonal prism, the preferred segregation site for impurities (see section 5.4), into the (001) plane. b) Two lateral translation states: mirror-symmetric configuration I and non-mirror-symmetric configuration II.

symmetry of the structure with respect to the grain boundary plane is visible. Figure 5.5 shows the view along $[\bar{1}30]$. There is no relative shift of the grains along [001] and thus the grain boundary is hardly visible. In figure 5.6, which shows another view along $[\bar{1}30]$ at a different location of the TEM sample, we see regions where the translation state along [001] is a different one. There is a relative shift of grains parallel to the interface, breaking the mirror symmetry. However, due to the dislocations present in this area we can not conclude that this is the intrinsic translation state of the Σ5 grain boundary in Mo. In the contrary, the rather large undistorted area in figure 5.5 indicates a perfectly mirror symmetric structure.

These observations are contradictory to what Campbell et al. found earlier by performing HRTEM on the same grain boundary in Mo, i.e. a structure in which the mirror symmetry is broken by a shift along [001] [12]. Furthermore Campbell et al. investigated the Σ5 STGB in Nb and Ta and found a mirror symmetric structure in the former [15, 14] and a

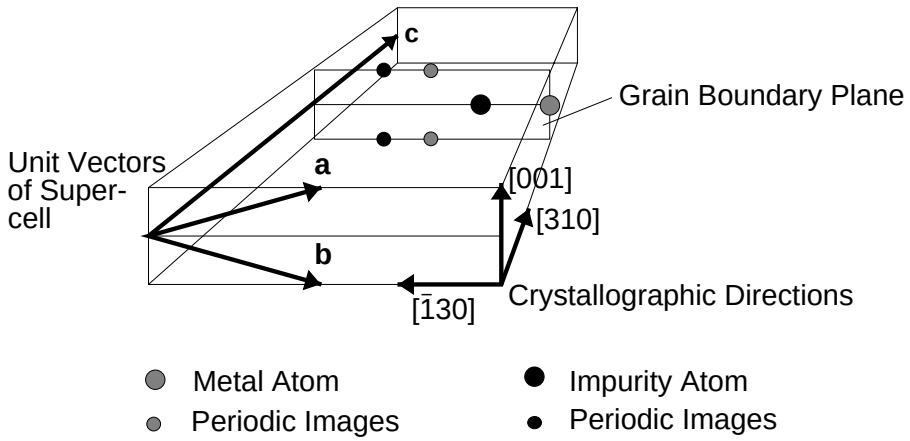


Figure 5.3: Schematic, three dimensional representation of the supercell. The metal atoms at the grain boundary are indicated as big and small grey circles. The positions of the impurity atoms are depicted as big and small black atoms. The supercell consists of the (001) plane containing the big circles. The small circles are periodic images of the respective atoms along the **a** and **b** directions.

symmetry-broken one in the latter [13].

In the diploma thesis of Beck and the doctoral thesis of Ochs the question of the translation state was investigated by means of ab-initio electronic structure calculations to determine the factors which lead to the preference of the one or the other translation state [5, 89]. The model supercell used is the one shown in figure 5.2. By purely geometric construction, e.g. by means of the coincidence-site lattice (CSL) model, this supercell of the $\Sigma 5(310)$ [001] STGB also shows mirror symmetry with respect to the grain boundary plane. By performing rigid grain shifts in all three spatial directions, as indicated in figure 5.7, followed by relaxation of the atomic positions for each shift, the stability of this configuration was probed ([5, 31, 90, 89]) for different bcc transition metals (Nb, Mo, Ta, W). As it was due, all grain boundaries show an expansion perpendicular to the grain boundary plane, parallel to the [310]-direction, arising from the unphysically small distance of the metal atoms at the grain boundary in the CSL supercell. This expansion does not affect the mirror symmetry and leads to what in the following is called configuration I. However, it was also demonstrated that by variation of the filling of the $d$-bands a different translation state can be stabilised which has this mirror symmetry broken (configuration II). The grains are shifted relative to each other along the [001] direction. This is shown schematically in figure 5.2b). The amount of the shift as well as the energy difference between configurations I

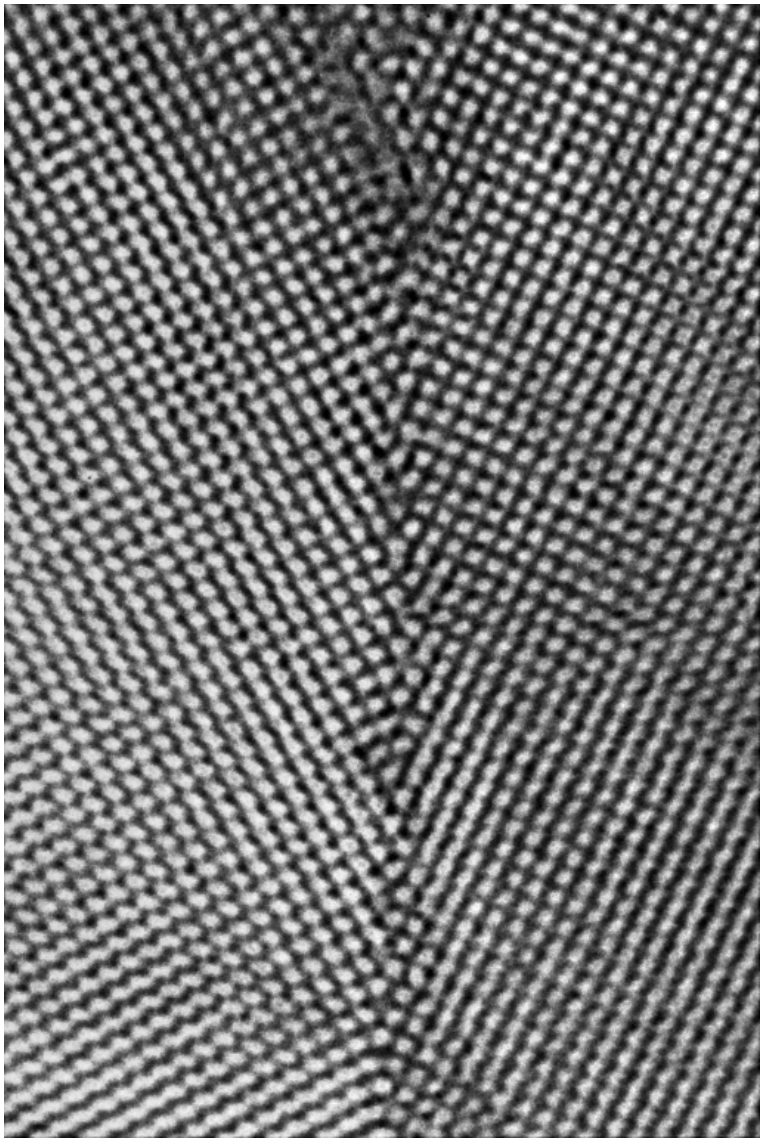

Figure 5.4: HRTEM image of the Σ5 (310)[001] STGB in Mo, view along the [001]-direction. *Courtesy of W. Sigle*

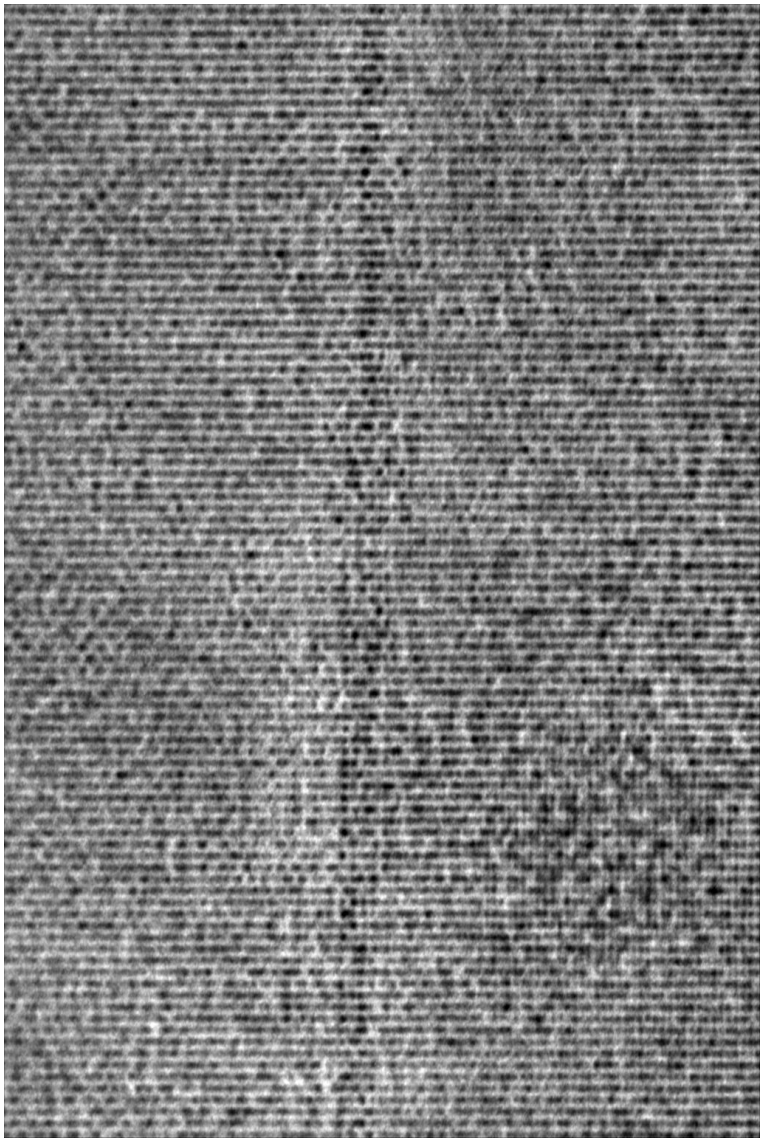

Figure 5.5: HRTEM image of the $\Sigma 5$ (310)[001] STGB in Mo, view along the $[\bar{1}30]$-direction. *Courtesy of W. Sigle*

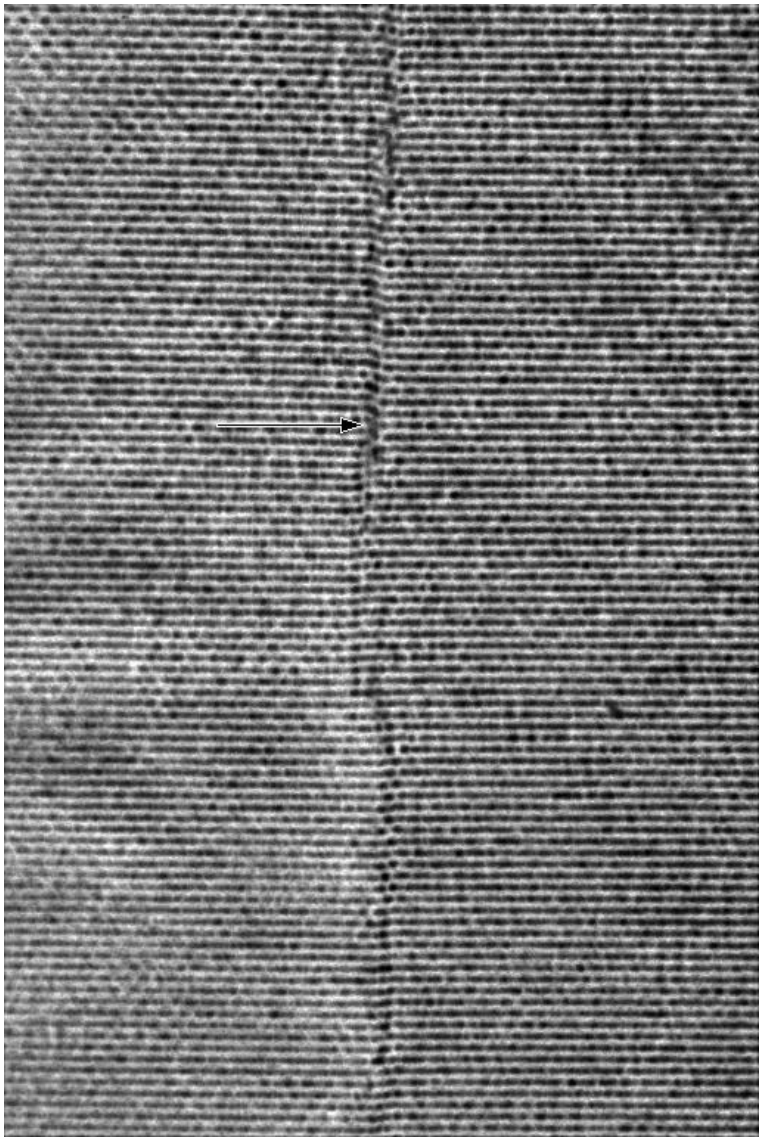

Figure 5.6: HRTEM image of the Σ5 (310)[001] STGB in Mo, view along the [$\bar{1}$30]-direction. *Courtesy of W. Sigle*

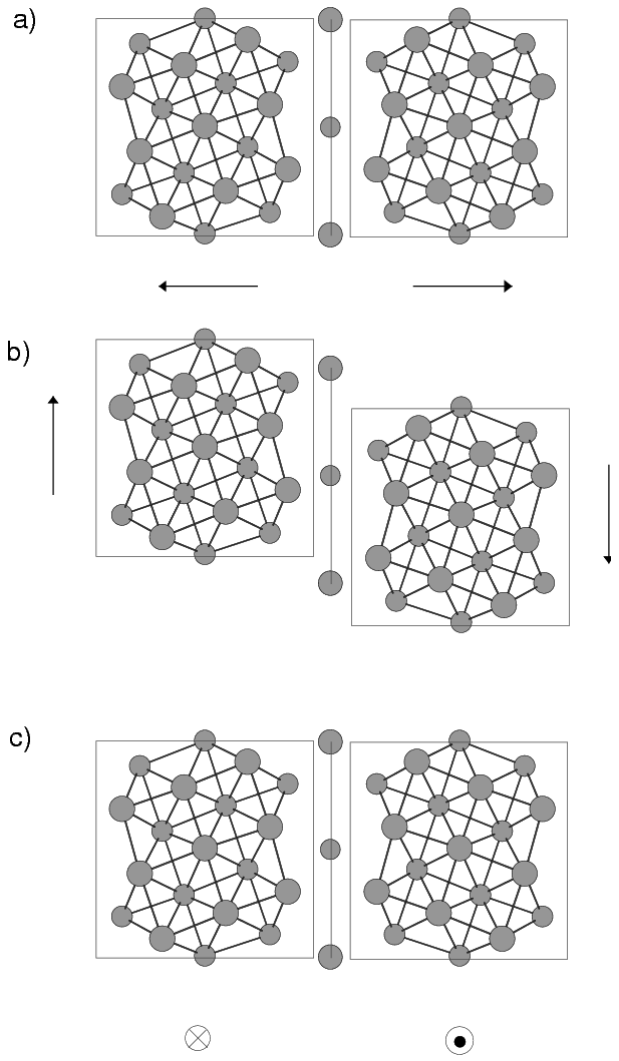


Figure 5.7: Rigid grain shifts of the Σ5 (310)[001] STGB performed in [31, 90] to find the stable translation state, a) conserving the mirror symmetry, b),c) breaking the mirror symmetry

| | atomic valence config. | expansion along[310] | $\Delta\sigma$ $[\frac{mJ}{m^2}]$ | $\Delta$t [%$a_0$] |
|---|---|---|---|---|
| Ta | $5d^3 6s^2$ | 5 | ($\star$) | 0 |
| Nb | $4d^4 5s^1$ | 5 | 8 | 8 |
| W | $5d^5 6s^1$ | 8 | 100 | 18 |
| Mo | $4d^5 5s^1$ | 6 | 108 | 20 |

Table 5.3: The translation states of the Σ5(310)[001] grain boundary in four bcc transition metals [5, 31, 90, 89]. Listed are the atomic valence configuration, the expansion at the grain boundary along [310] (configuration I) in percent of the cubic lattice parameter $a_0$, the energy difference between configurations I and II (cf. fig. 5.2b)) $\Delta\sigma = E_I - E_{II}$ in $\frac{mJ}{m^2}$, and the relative shift $\Delta$t of grains along the [001] direction in configuration II, again in percent of the cubic lattice parameter $a_0$. ($\star$) marks that only the mirror-symmetric case I was found stable.

and II increases with increasing number of d-electrons. No stable or metastable translation states along $[\bar{1}30]$ were found. The results of [5, 31, 90, 89] for energies and translations are summarised in table 5.3.

Paxton [93] proposed the explanation and the authors of [5, 31, 90, 89] supported it by quantitative calculations that the observed structural trend originates from a competition between the tendency of the bcc transition metals to form close packed structures and the angular-dependent bonds arising from the presence of partially filled *d*-states. These angular dependent bonds stabilise the mirror-symmetric, more open structure I of the Σ5(310) [001] STGB in Ta, Nb, W and Mo. However, in W and Mo the half-filled *d*-states show again spherical symmetry and the more close packed non-mirror-symmetric configuration II becomes more favourable. For Nb the situation is more subtle. The relative shift of grains is rather small (8% $a_0$) and there is only a slight energy difference between configurations I and II of 8 $\frac{mJ}{m^2}$, so that the two translation states can be called energetically degenerate.

In the following the number of valence electrons at the grain boundary is varied by putting light interstitial impurities, H, B, C, N and O, at the interface. As model system the Σ5(310) [001] STGB in Nb and Mo is chosen.

## 5.4 Segregation of Carbon in Molybdenum

The case of C in Mo has already been studied in detail in a previous work [65, 66]. Survey calculations have been performed to investigate the segregation of C at the Σ5 STGB in Mo. Starting from configurations I and II described above for the STGB in Mo, C was put at different octahedral sites of the bcc lattice, starting in the bulk and approaching the interface layer by layer. The respective positions of C have been relaxed, but the metal lattice has been kept fixed in the respective fully relaxed configuration of the pure grain boundary. Two main results are important for the present work:
First, the preferred segregation site is the centre of a trigonal prism built by the small grey Mo atoms in figure 5.2a) above and below the paper plane. Its projection is indicated by the grey triangle. The tip of this triangle corresponds to the periodic images of metal atoms 1+ and 1- therein, which are depicted in figure 5.3 as small grey circles. In the case of the non-mirror symmetric grain boundary this prism is sheared along its trigonal axis, i.e. along [001]. A schematic drawing of different projections of this prism are shown in figure 5.8. This segregation site is not surprising, as this position provides most space for the impurity and we expect this to be valid after a relaxation of the host lattice as well. In the following this is assumed to be the segregation site for all kinds of small interstitial atoms, H, B, C, N and O.
Second, with carbon at the grain boundary the mirror-symmetric configuration I is lower in energy than the non-mirror-symmetric configuration II, in contrast to the pure case. This means that indeed an interstitial impurity can alter the intrinsic translation state of the Σ5 (310)[001] STGB in Mo. We will investigate in how far we can generalise this result in the following sections.

## 5.5 H, B, C, N and O in Nb and Mo

### 5.5.1 Total Energies

Interstitial impurities were inserted at the grain boundary in configurations I and II described in section 5.3 for the pure metal. For the Brillouin zone integrations a k-point mesh with 64 k-points that was constructed following the scheme of Moreno and Soler [84] was applied. The cut-off energy for the plane waves in the basis set was $E_{pw}$=16 Rydberg. The local functions, five per atom with $d$ symmetry for Nb and Mo and three per impurity atom with $p$ symmetry, were confined to spheres centred at host-metal lattice sites ($r_{loc}^{Mo}$

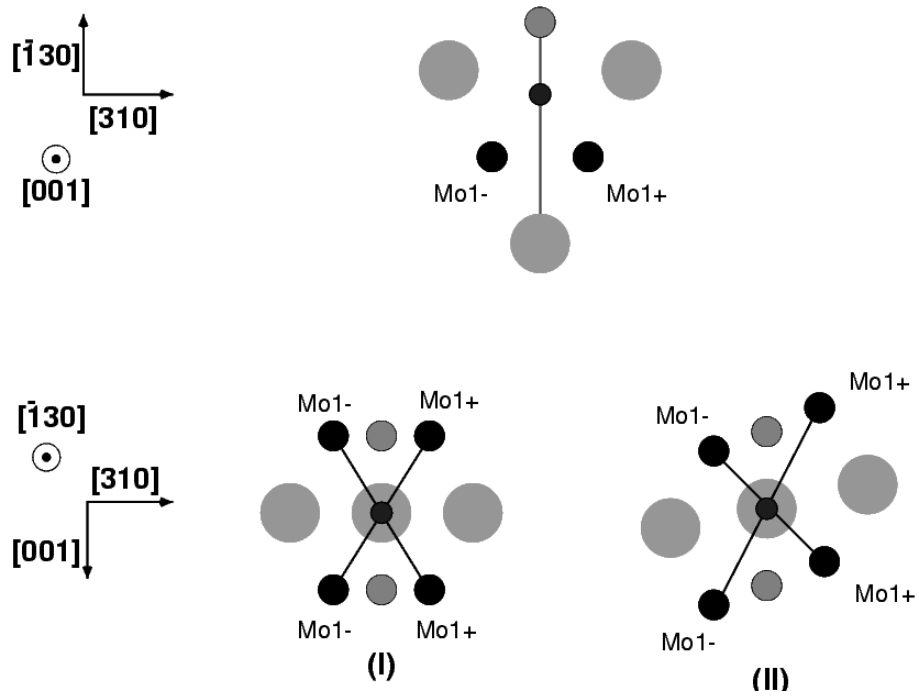


Figure 5.8: Different projections of the environment of the impurity at the grain boundary. The periodic images of Mo1± and Mo0 in figure 5.2 form the corners of a trigonal prism. They are indicated as small black and grey atoms. The impurity is located in the centre of the prism. In case of configuration II the prism is sheared along [001].

= 2.25 Bohr, $r_{loc}^{Nb}$ = 2.00 Bohr) and at impurity sites ($r_{loc}^{X}$ = 1.80 Bohr for all considered impurities X).

In a first step the position of the impurity was relaxed while keeping the metal lattice fixed in the relaxed state of the pure grain boundary, as done previously for C in Mo [65, 66]. As reported above, the preferred position of the impurity atom is in the centre of a trigonal prism of metal atoms at the grain boundary. For the example of the mirror symmetric grain boundary in Mo the distances between the respective impurity and its nearest-neighbour atoms are given in table 5.4. At the grain boundary in the mirror-symmetric configuration C is located perfectly in the middle of the trigonal prism, in the sense that all neighbours are at equal distance. The other impurities are slightly shifted off centre. For both configurations we observe a trend from B via C and N to O: the distance between the impurity and the Mo atom "0" decreases while the distance to Mo atoms "1+/1−" increases. Later in this work, after having examined the electronic structures at the grain boundary, this will become rationalised.

| | Configuration I | | | | Configuration II | | | |
|---|---|---|---|---|---|---|---|---|
| X | B | C | N | O | B | C | N | O |
| $d_{Mo1--X}$ | 4.389 | 4.417 | 4.483 | 4.724 | 4.040 | 4.094 | 4.151 | 4.245 |
| $d_{Mo1+-X}$ | 4.389 | 4.417 | 4.483 | 4.724 | 4.998 | 5.026 | 5.072 | 5.149 |
| $d_{Mo0-X}$ | 4.457 | 4.417 | 4.326 | 4.029 | 4.213 | 4.175 | 4.112 | 4.014 |

Table 5.4: Distance (in Bohr units) between the impurity atom X and its nearest-neighbour Mo atoms in the mirror-symmetric configuration I and the non-mirror-symmetric configuration II . The position of the impurity has been relaxed, the metal lattice has been kept fixed in the fully relaxed grain boundary configuration of the pure metal. For the labelling of the metal atoms see also fig. 5.2a). Due to the periodic boundary conditions "metal1±" and "metal0" also equal the small grey atoms forming the trigonal prism.

In the case of the non-mirror symmetric configuration II the prism is sheared along its c-axis, i.e. along [001] (cf. 5.8). The difference in energies of the two configurations I and II, $\Delta\sigma = E_I - E_{II}$, is shown in figure 5.9 for the different impurities, which are ordered according to their atomic number. Again, we observe a clear trend: starting from Boron, for which the mirror-symmetric configuration I is more favourable, this energetic advantage decreases with increasing number of valence electrons. Notice that this effect is indeed depending on the valence electrons by looking at the change of sign in $\Delta\sigma$ which occurs in Nb at the next heavier impurity element than in Mo. In Nb the described trend is the same as but less pronounced than in Mo, since already for pure Nb the difference between configurations I and II is very small. The difference in the local environment of the impurity with or without a relative shift of grains of $8\%a_0$ does have much less effect than the one of 20% $a_0$ in Mo.
In the following we analyse the electronic structure at the interface in order to work out correlations of its changes with the energetic trends.

### 5.5.2 Electronic Structure at the Grain Boundary

#### Densities of States

Figures 5.10 to 5.13 show the site projected densities of states (DOS) for the Mo or Nb atom at the grain boundary in configurations I and II, respectively. The respective top panel shows the pure case, and the lower panels the DOS of a metal atom at the impure grain boundaries. For comparison the density of states of the metal atom at the pure interface is displayed in these panels as well. Additionally to B, C, N and O we include the

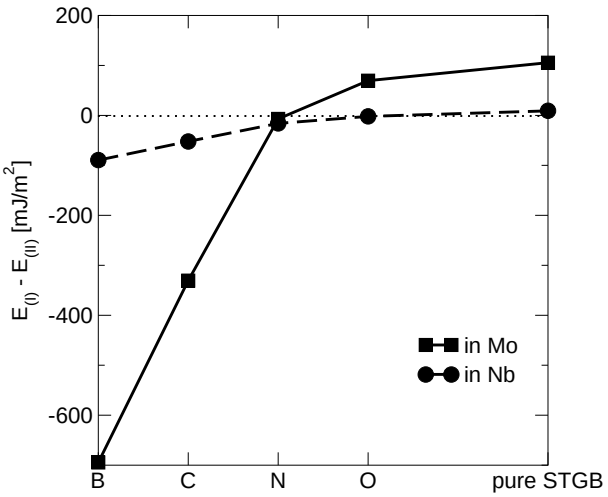


Figure 5.9: Difference of interface energies, E(I) - E(II), with impurities at the grain boundary. Energies below zero mean that the mirror-symmetric configuration I is favoured, while energies above zero indicate that the non-mirror-symmetric configuration II is preferred.

DOS for the case of H at the grain boundary, as an example of a strongly polarly bonding impurity [19, 40, 63, 64] that enhances grain boundary embrittlement of various transition metals [115, 67].

First, we want to discuss the mirror-symmetric configuration of the $\Sigma 5$ STGB in Mo, figure 5.10. Comparing the DOS at the pure interface with the DOS at the impure interfaces, "split-off bands" appear which arise from the hybridisation of the transition metal $d$-states with the impurity $s$- and $p$-states. With increasing valence of the impurity these bands move to lower energies, further away from the Fermi level, and the hybridisation becomes weaker. Here the "$p$-like" bands are of particular interest: in the case of B at the grain boundary these states are part of the valence band, but going via C to N they separate from the valence band and become more narrow. Finally, with O at the interface, there is a bandgap that shows the same width as the $p$-like band itself, a situation corresponding to that in the case of the "$s$-like" band for H at the grain boundary. This illustrates a transition from bonds with a dominantly covalent character (B) to bonds with a dominantly polar character (O). When we compare figure 5.10 with figure 5.11, which shows the DOS at the non-mirror-symmetric configuration II, we see that the translation state doesn't have any influence on the described features in the DOS, only very subtle differences in the respective plots can be noticed which do not change the general trend. So far the results presented here are in perfect agreement with the predictions of Cottrell and our first estimates. Not only the bonding character depends on the relative position of the

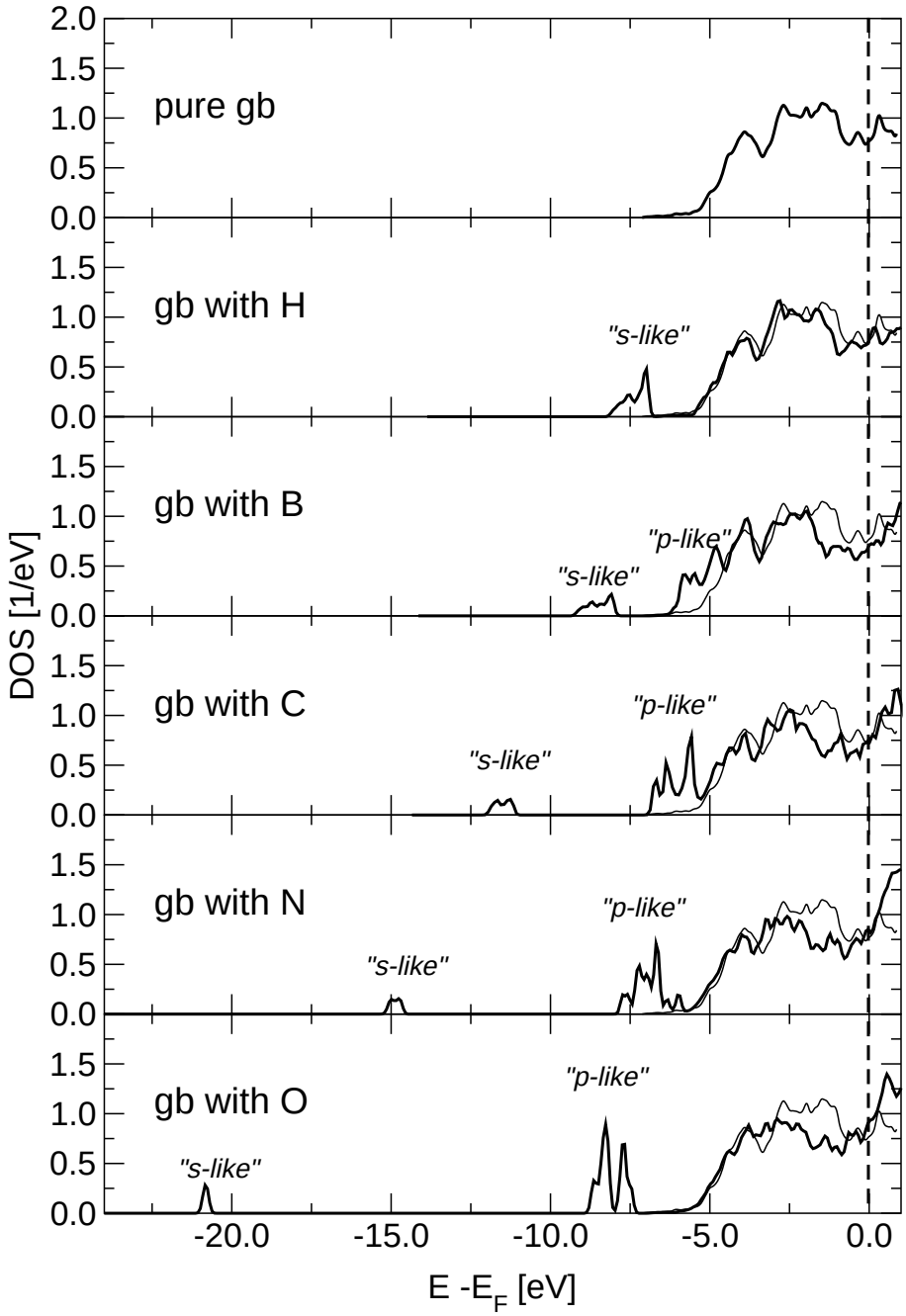


Figure 5.10: Site projected densities of states at the **Mo** grain boundary in the **mirror-symmetric configuration (I)**. In the top panel the DOS of a Mo atom at the pure STGB is displayed. In the lower five panels this plot is repeated (thin line) for better comparison with the DOS of the Mo atom next to the impurity atom (thick line) in the case of the impure grain boundary.

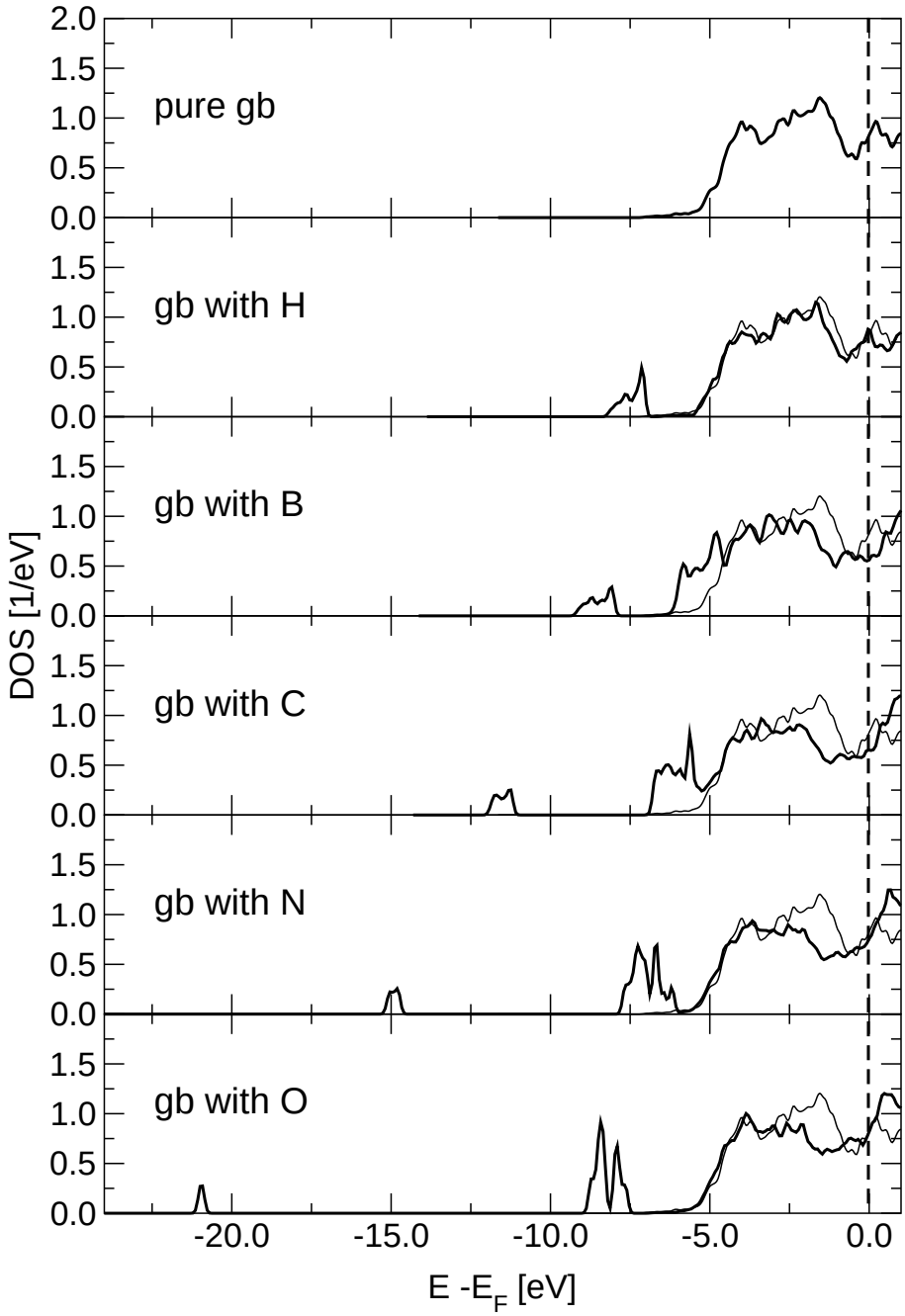


Figure 5.11: Site projected densities of states at the **Mo** grain boundary the **non-mirror-symmetric configuration (II)**. In the top panel the DOS of a Mo atom at the pure STGB is displayed. In the lower five panels this plot is repeated (thin line) for better comparison with the DOS of the Mo atom next to the impurity atom (thick line) in the case of the impure grain boundary.

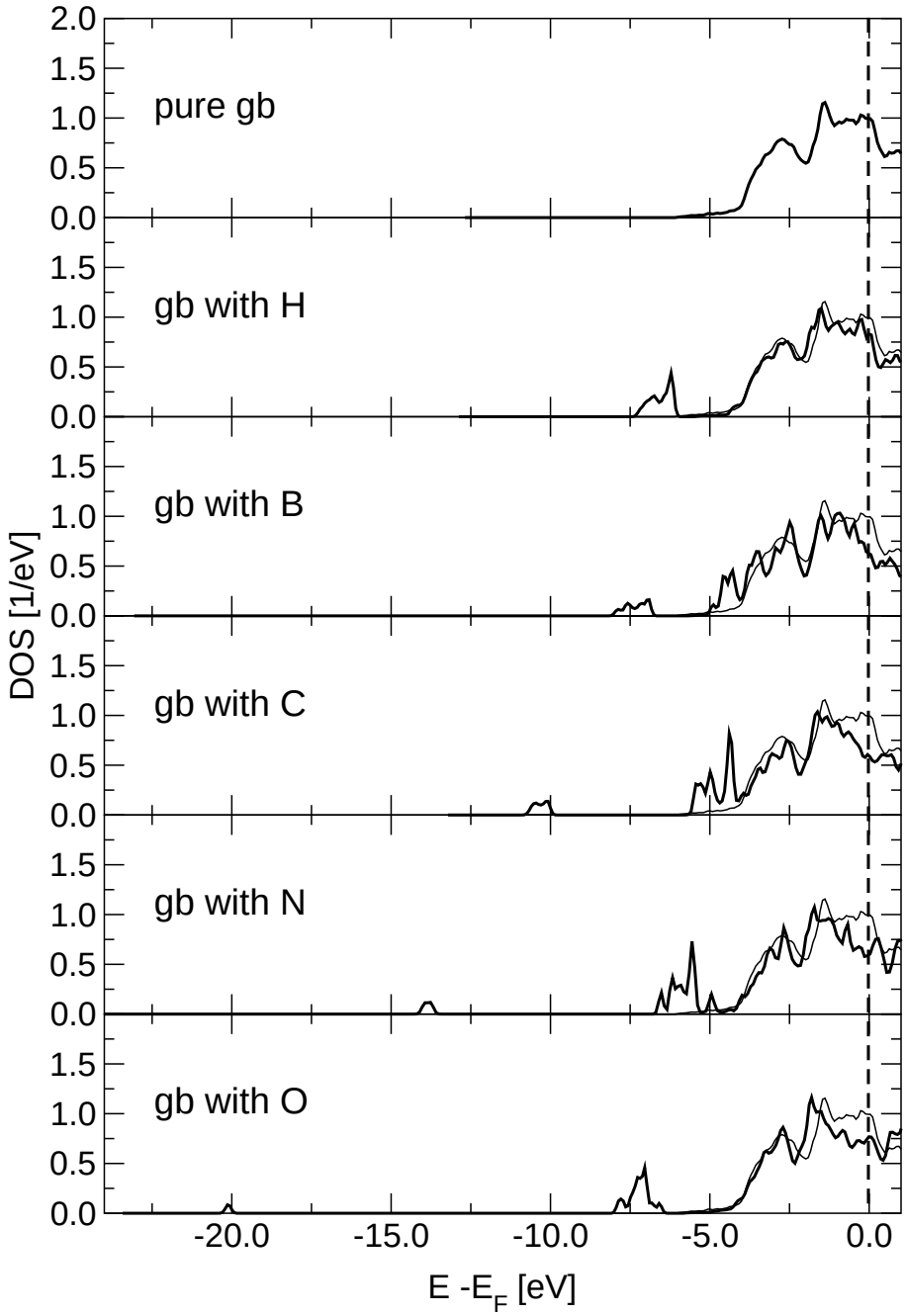


Figure 5.12: Site projected densities of states at the **Nb** grain boundary in the **mirror-symmetric configuration (I)**. In the top panel the DOS of a Nb atom at the pure STGB is displayed. In the lower five panels this plot is repeated (thin line) for better comparison with the DOS of the Nb atom next to the impurity atom (thick line) in the case of the impure grain boundary.

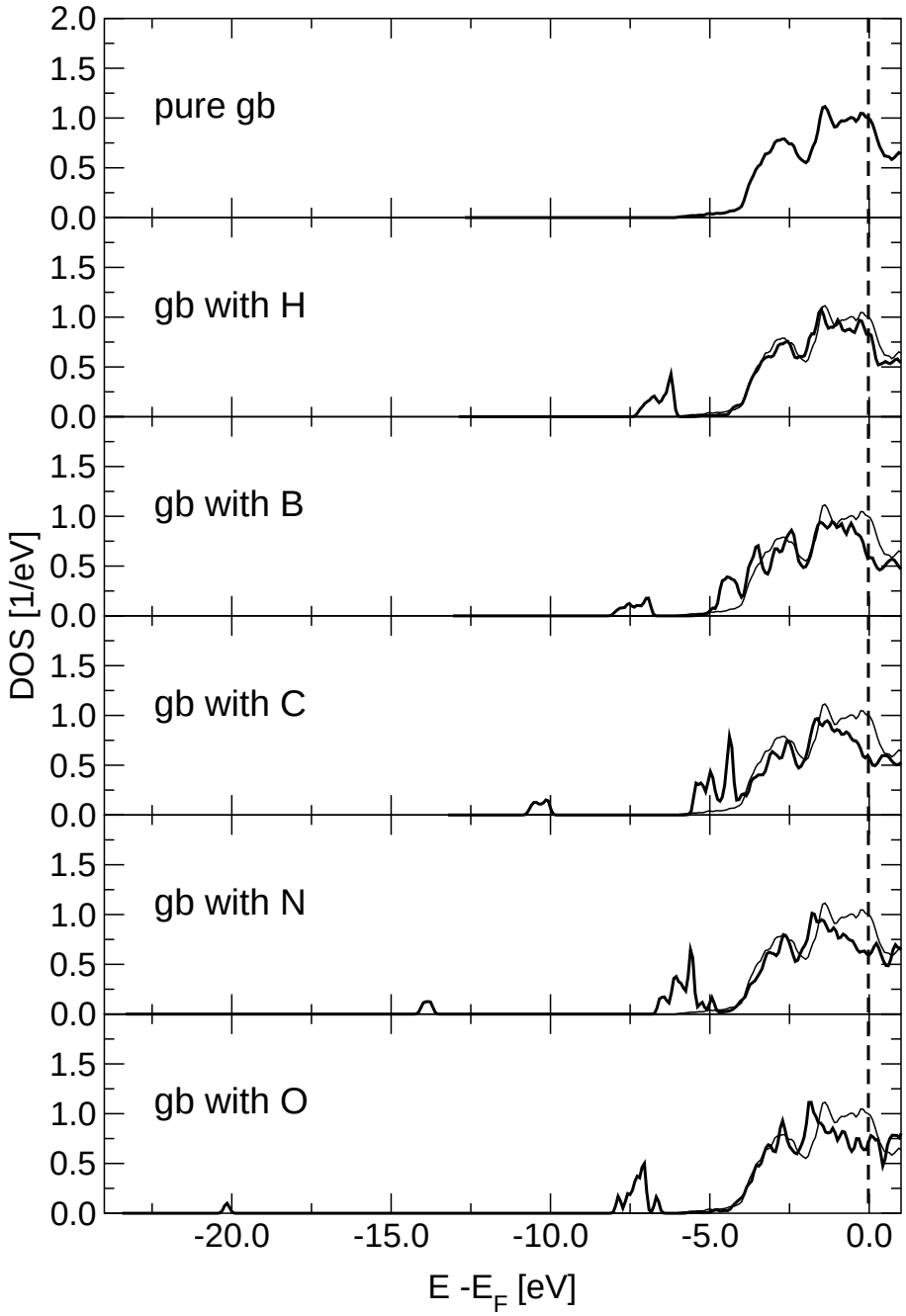


Figure 5.13: Site projected densities of states at the **Nb** grain boundary in the **non-mirror-symmetric configuration (Ⅱ)**. In the top panel the DOS of a Nb atom at the pure STGB is displayed. In the lower five panels this plot is repeated (thin line) for better comparison with the DOS of the Nb atom next to the impurity atom (thick line) in the case of the impure grain boundary.

electronic states involved, but also this is independent of the geometry, because, as can be seen by comparing figures 5.10 and 5.11, these results are equally true for the configurations I and II of the Mo grain boundary.
If we now look at the DOS at the Nb grain boundary, figure 5.12 and 5.13 we observe a very similar behaviour. When going from B via C and N to O at the interface, the hybridisation becomes weaker and the bonding character changes from covalent to polar. This is equally true for both translation states. As the relative shift of grains in the non-mirror symmetric configuration is only $8\%a_0$ hardly any differences can be spotted between the DOS for this translation state, figure 5.13 and the mirror-symmetric one, figure 5.12. However, we notice subtle differences when comparing the DOS-plots for the non-mirror symmetric configurations of the interface in Mo and Nb, figures 5.11 and 5.13. The site-projected states in Nb are slightly higher in energy than in Mo (compare table 5.1), so the strength of hybridisation between Nb states and impurity states are a little bit weaker. This can be seen e.g. from the gap in the DOS for the case of O at the interface. In Nb this gap between the O-$p$-states and the Mo-$d$-valence band is larger, as it was predicted by the larger value of $\Delta$ in table 5.1. This again confirms the predictions of Cottrell's model.

In the following the above drawn conclusions are quantified. First we integrate the site projected DOS up to the Fermi energy. Thus we get a value for the total number of valence electrons that we can attribute to a specific atom. By comparing it to the respective values in the pure supercell we can identify the changes introduced by the presence of the impurity. This allows conclusions concerning charge transfer between metal and impurity atoms and thus the polarity of the interatomic bonding. The strength of the bonds will be rendered more precisely in the next section by means of calculated local crystal orbital-resolved overlap populations.

The integrated site projected DOS is presented exemplarily for the Mo grain boundary. The DOS was integrated around the site of a Mo atom over a sphere of radius $r_{Mo} = 2.560$ Bohr, which is half the nearest-neighbour distance in bcc Mo, and around an impurity's site over a sphere of radius $r_X = 2.114$ Bohr, which is half the nearest-neighbour bond length in the diamond structure of C. In order to get a consistent spatial partitioning of electrons for the four impurity elements this radius of C was used for all of them. By using these radii at the grain boundary the projection spheres are spatially overlapping to some extent, as can be seen e.g. from the nearest-neighbour distances in table 5.4. The distance between the metal atoms facing each other at the grain boundary, Mo1− and Mo1+ is 4.665 Bohr in

| | pure GB | with B | with C | with N | with O |
|---|---|---|---|---|---|
| Mo5± | 4.626 | 4.606 | 4.625 | 4.603 | 4.625 |
| Mo4± | 4.606 | 4.606 | 4.607 | 4.603 | 4.609 |
| Mo3± | 4.634 | 4.640 | 4.642 | 4.641 | 4.638 |
| Mo2± | 4.590 | 4.696 | 4.679 | 4.665 | 4.674 |
| Mo1± | 4.651 | 4.783 | 4.736 | 4.687 | 4.692 |
| $\Delta^{1-5}$ | +0.025 | +0.177 | +0.111 | +0.084 | +0.067 |
| Mo0 | 4.450 | 4.553 | 4.529 | 4.521 | 4.586 |
| $\Delta^{0-5}$ | -0.176 | -0.053 | -0.096 | -0.082 | -0.039 |
| $X_{GB}$ | - | 2.940 | 4.143 | 5.387 | 6.549 |
| $X_{free}$ | - | 3.000 | 4.000 | 5.000 | 6.000 |
| $\Delta_X$ | - | -0.060 | +0.143 | +0.387 | +0.549 |

Table 5.5: Integrated density of states for different sites in the mirror-symmetric supercell (configuration I) for molybdenum (numbers are electrons per projection sphere volume). "Mo5±" is the Mo atom in the centre of the grain, "Mo0" the Mo atom at the grain boundary. With "Mo4±" to "Mo1±" we are approaching the interface layer by layer (compare fig. 5.2a)). "X" stands for the impurity atom.

the mirror-symmetric configuration and 4.699 in the non-mirror-symmetric configuration. Thus here as well we count some electrons twice. The results of the integration are given in tables 5.5 and 5.6 for the mirror-symmetric configuration I and the non-mirror-symmetric configuration II, respectively.

"Mo5±" stands for the big grey Mo atom in the centre of the grain (compare fig. 5.2a)). It can be considered as a Mo atom in the bulk interior. With "Mo4±" to "Mo3±" the grain boundary is approached layer by layer. The very small variations in the number of electrons in case of the mirror-symmetric configuration (cf. table 5.5) indicate that the influence of the interface is hardly "felt" by the charge distribution before atom number 2± is reached in the case of an impurity being present at the grain boundary, or even atom number 1± for the pure STGB. In the non-mirror-symmetric configuration (cf. table 5.6) the more close packed structure at the grain boundary makes the electronic structure at the interface even more bulk-like. In case of the pure grain boundary this leads to a rather homogeneous charge distribution throughout the whole supercell. An impurity at the grain boundary leads to a localised increase of charge at the interface. Hence, in all cases the interfacial metal-metal and the metal-impurity interaction are both well localised.

The Mo atoms 1± and 0 are most interesting for our study. Their periodic images are the corners of the trigonal prism and thus the nearest-neighbours of the impurity. Furthermore "Mo1−" and "Mo1+" are the nearest metal-metal neighbours across the boundary. In all

| | pure GB | with B | with C | with N | with O |
|---|---|---|---|---|---|
| Mo5± | 4.632 | 4.619 | 4.618 | 4.613 | 4.613 |
| M04± | 4.608 | 4.606 | 4.605 | 4.602 | 4.600 |
| Mo3± | 4.631 | 4.629 | 4.629 | 4.625 | 4.618 |
| Mo2± | 4.612 | 4.707 | 4.694 | 4.677 | 4.668 |
| Mo1± | 4.627 | 4.774 | 4.736 | 4.699 | 4.685 |
| $\Delta^{1-5}$ | -0.005 | +0.155 | +0.118 | +0.086 | +0.072 |
| Mo0 | 4.612 | 4.687 | 4.663 | 4.630 | 4.630 |
| $\Delta^{0-5}$ | -0.020 | +0.068 | +0.045 | +0.017 | +0.017 |
| $X_{GB}$ | - | 3.048 | 4.248 | 5.472 | 6.575 |
| $X_{free}$ | - | 3.000 | 4.000 | 5.000 | 6.000 |
| $\Delta_X$ | - | +0.048 | +0.248 | +0.427 | +0.575 |

Table 5.6: Integrated density of states for different sites in the non-mirror-symmetric supercell (configuration II) for molybdenum (numbers are electrons per projection sphere volume). "Mo5±" is the Mo atom in the centre of the grain, "Mo0" the Mo atom at the grain boundary. With "Mo4±" to "Mo1±" we are approaching the interface layer by layer (compare fig. 5.2a)). "X" stands for the impurity atom.

cases of "X" at the grain boundary we see that in the sphere around "Mo1±" more charge is accumulated than around atoms in the bulk interior ("Mo5±"), and also more than around "Mo1±" at the pure interface. As the metal lattice has been kept fixed this altered amount of charge around the molybdenum atom can not be due to a change in bonding distances but has to be an influence of the impurities. This additional amount of charge is larger with B and C at the interface than with N and O. However, in case of the non-mirror-symmetric configuration II (cf. table 5.6) these numbers represent an average value of e.g. the sphere around the Mo1+ atom being closer to the impurity and the Mo1+ atom being further away (cf. figure 5.8) and thus are of little significance.

With each "X" at the mirror-symmetric grain boundary (cf. table 5.5) less electrons are accumulated around Mo0 at than around a bulk Mo atom, but still more than around Mo0 at the pure interface. Here the variations between the different cases of "X" are too small to derive a significant trend. With each "X" at the non-mirror-symmetric grain boundary (cf. table 5.6) more electrons are accumulated around "Mo0" than around a bulk Mo atom and also more than around "Mo0" at the pure interface. This increase in the number of electrons becomes smaller when going from B via C and N to O at the grain boundary.

In the sphere around the impurity itself we find a small fraction of electrons less around B at the mirror-symmetric grain boundary (cf. table 5.5) than we would expect from the valence configuration of the free atom. In the case of the other impurities it is more,

with increasing tendency. At the non-mirror-symmetric grain boundary more charge is accumulated around the impurity than we would expect from the respective free atom, with increasing tendency when going from B via C and N to O. This fits well with the values of $\Delta$ given in table 5.2 that can be understood as a measure for the charge transfer between impurity and metal.
Cautiously we give a preliminary interpretation of these findings, taking into account that there are three interacting effects when going from B via C and N to O:

- The total amount of electrons at the grain boundary increases.
- The bond length between impurity and "Mo1±" increases, that between impurity and "Mo0" decreases.
- The polarity of the bond between metal and impurity increases.

Finally, it has to be remembered that we count some electrons twice due to the slight overlap of the projection spheres. So far we can identify three processes. Compared to the bulk configuration charge is transferred away from "Mo0", partly

- into the "Mo-X" bond, where "X" is the impurity.
- onto the impurities' site.
- into the metal-metal bond between "Mo1+" and "Mo1−" across the grain boundary. This can be confirmed at least for the mirror-symmetric case, configuration I.

The strength of the interfacial metal-metal bond and the degree of covalency of the "Mo-X" bond is decreasing when going from B via C and N to O at the interface. The charge transfer to the impurity and thus the polarity of the bond is increasing at the same time.

### Overlap Populations

By calculating local orbital-resolved overlap populations according to equation (3.60) the bond order at and across the grain boundary shall be analysed. For the radial parts of the local atomic-like basis functions (3.40) atomic pseudo wavefunctions were used, limited by a cut-off radius of 6.0 Bohr for Mo and 4.0 Bohr for the impurities. This basis set has been obtained by optimising the set of Mo pseudo wavefunctions separately for bcc Mo (resulting in a spillge of 0.0007) and then introducing C as an interstitital element and

| | Configuration I | | | | Configuration II | | | |
|---|---|---|---|---|---|---|---|---|
| | B | C | N | O | B | C | N | O |
| Mo1− – X | 0.1430 | 0.1426 | 0.1156 | 0.0425 | 0.2029 | 0.2109 | 0.1841 | 0.1099 |
| Mo1+ –X | 0.1430 | 0.1426 | 0.1156 | 0.0425 | 0.0630 | 0.0501 | 0.0293 | 0.0034 |
| Mo0 –X | 0.1441 | 0.1491 | 0.1420 | 0.1249 | 0.1796 | 0.1920 | 0.1799 | 0.1308 |
| Σ Mo–X | 0.4301 | 0.4343 | 0.3732 | 0.2099 | 0.4455 | 0.4530 | 0.3933 | 0.2441 |
| Mo1− – Mo1+ | 0.2462 | 0.2390 | 0.2344 | 0.2651 | 0.2383 | 0.2297 | 0.2255 | 0.2333 |

Table 5.7: Local orbital overlap populations at the Σ5 grain boundary in molybdenum between impurity atoms and their nearest-neighbour Mo atoms and between molybdenum atoms (1±) facing each other at the interface. At the pure interface the overlap population "Mo1− – Mo1+" building this metal-metal bond across the grain boundary is 0.2753 in configuration I and 0.2568 in configuration II.

optimising the complete set of functions for fcc MoC (resulting in a spillage of 0.0011)[1] . Again, in order to make the projection best consistent, the local basis for carbon was used for all other impurities as well. With the combination of the two basis sets the spillage (3.49) in the grain boundary calculations varied between $7 \cdot 10^{-4}$ and $1.3 \cdot 10^{-3}$

In the previous section the analysis of the integrated site projected DOS showed that the influence of the interface on the electronic structure is well localised. Thus it is mainly the bond between the metal atoms "Mo1−" and "Mo1+" which is responsible for the interfacial cohesion in the pure supercell. In the impure case also the bonds between the impurity at the grain boundary and its nearest-neighbours are of interest, and the influence of the impurity on the metal-metal bonds, as already indicated in the last section. Table 5.7 shows the overlap populations at the grain boundary in Mo for both, the mirror-symmetric configuration I and the non-mirror symmetric configuration II. Listed are the values for the overlap between the orbitals located at impurity X's site and the sites of its nearest-neighbours "Mo1−", "Mo1+" and "Mo0", and the overlap population of the metal-metal bond, between "Mo1−" and "Mo1+" for the case of different impurities being present at the grain boundary. In the pure supercell these are 0.2753 in configuration I and 0.2568 in configuration II. Looking first at the mirror-symmetric case we see that the bonds between boron and its nearest-neighbours are almost equivalent, but the bond with "Mo0" in the interface plane is slightly stronger than with "Mo1±" out of it. This is also true for carbon. Here the effect is even a little bit stronger, although C is perfectly

[1]Using the so obtained C atomic pseudo wavefunctions for pure C in the diamond structure results in a comparatively high spillage of 0.011. For an optimisation of this structure a larger cut-off radius should be chosen.

centred in the trigonal prism formed by the periodic images of "Mo0" and "Mo1±" (cf. table 5.4). Obviously the "in-plane" bonding at the interface is generally stronger than the "out-of-plane" bonding. This effect is very pronounced in the case of nitrogen and oxygen at the grain boundary. The total amount of overlap population between metal and impurity is clearly decreasing when going from B via C and N to O. The metal-metal bonds are weaker than at the pure grain boundary as they have partly been replaced by the Mo-X bonds. The strength of the metal-metal bonds is first decreasing when going from B via C to N as the charge transfer from metal to impurity is increasing, as could be seen from the integrated site projected DOS (and estimated from the relative positions of energy levels). However, from N to O the distance between impurity and "Mo1±" is drastically increasing compared to the distance to "Mo0", so the charge transfer from metal to impurity mainly takes place from "Mo0" to X in the case of X=O. Thus the bond strength between "Mo1+" and "Mo1−" is increasing again, but is still weaker than at the pure interface. The "Mo1±-X" bonds also have a component across the interface. To evaluate the contribution of this perpendicular component to the overall bonding across the grain boundary is difficult. But just by looking at the numbers we can already clearly say that in the case of B it will be so large that the total overlap population leading to bonds across the grain boundary is bigger than at the pure grain boundary, whereas in the case of O it is smaller. Hence, B will enhance the grain boundary cohesion, while O will decrease it. A quantification of this statement will be given in section 5.5.4, by the calculated bonding energy differences.

Before we continue we will briefly compare the situation at the mirror-symmetric and the non-mirror symmetric grain boundary. Due to the shearing of the prism along its trigonal axis ([001]) two of the four corners marked by the periodic images of "Mo1±" get closer to the impurity, two get further away, as shown schematically in figure 5.8. The distances are given in table 5.4. In table 5.7 "Mo1−" is the Mo atom closer to the impurity, "Mo1+" the one further away. It can be seen how the altered environment changes the overlap populations: the bonding charge in the now shorter bond increases with respect to the symmetric case for all types of impurities at the interface, while the charge in the now longer bond becomes less. In the shorter bond we find even more charge accumulated than in the "in-plane" bond for the cases of B, C and O. For the total amount of charge localised in the metal-X bonds we still observe the same trend, i.e. that it is decreasing when going from B via C and N to O at the grain boundary. The metal-metal bonds across the interface are again weaker than in the pure case.

After having examined the overlap populations we have to refine our interpretation of the integrated site-projected DOS: Charge is transferred from "Mo0" only to the impurity's site, not into the metal-metal bond across the grain boundary. Although the charge in the sphere around "Mo1±" is increasing with an impurity being present at the interface, the metal-metal bond between "Mo1−" and "Mo1+" is weaker than in the pure case. The additional charge is transferred into the Mo-X bonds which are partly replacing the metal-metal bonds and also have a component across the interface. Nevertheless, the general statement remains: bonding across the grain boundary is increased with boron at the interface and decreased by oxygen.
Obviously the process of bonding by redistribution of electrons is complex. Thus it is very helpful to have a descriptive quantity like the bonding electron densities presented in the following section.

### Bonding Electron Densities

The weaker hybridisation of electronic states that we observed in the DOS is matched by less overlap of orbitals in real space, as we have seen in the calculated local orbital overlap populations. Furthermore changes in the local bonding can be visually described by plots of bonding electron densities. They have the additional advantage of demonstrating very clearly also the change from covalent to polar bonding. This is shown exemplarily again for the Mo grain boundary. The bonding electron density is the full electron density of the grain boundary with impurity minus the electron densities of the respective individual metal and impurity sub-lattices. It is shown for the grain boundary plane in figures 5.14 and 5.15 for B, C, N, O and H (from top to bottom) at the mirror-symmetric and the non-mirror-symmetric grain boundary in Mo. One sees that both cases look very similar, the relative shift of grains doesn't affect very much the distribution of the bonding electron density in the grain boundary plane. If we look at B at the grain boundary, either in configuration I or II, we see bonding electron density stretching out from B to the metal atoms. Charge is located between the atoms, as in a covalent bond. Compared to that the bonding electron density retreats towards the impurity in the case of C at the interface, but there is still a considerable amount of it located between the atoms. N is already more isolated and the bonding electron density is becoming more spatially homogenous. Oxygen finally exhibits an "ion-like" charge distribution, comparable to that around H in the respective lowest panel.
Figures 5.16 and 5.17 show the bonding electron densities in a plane parallel to the (001)

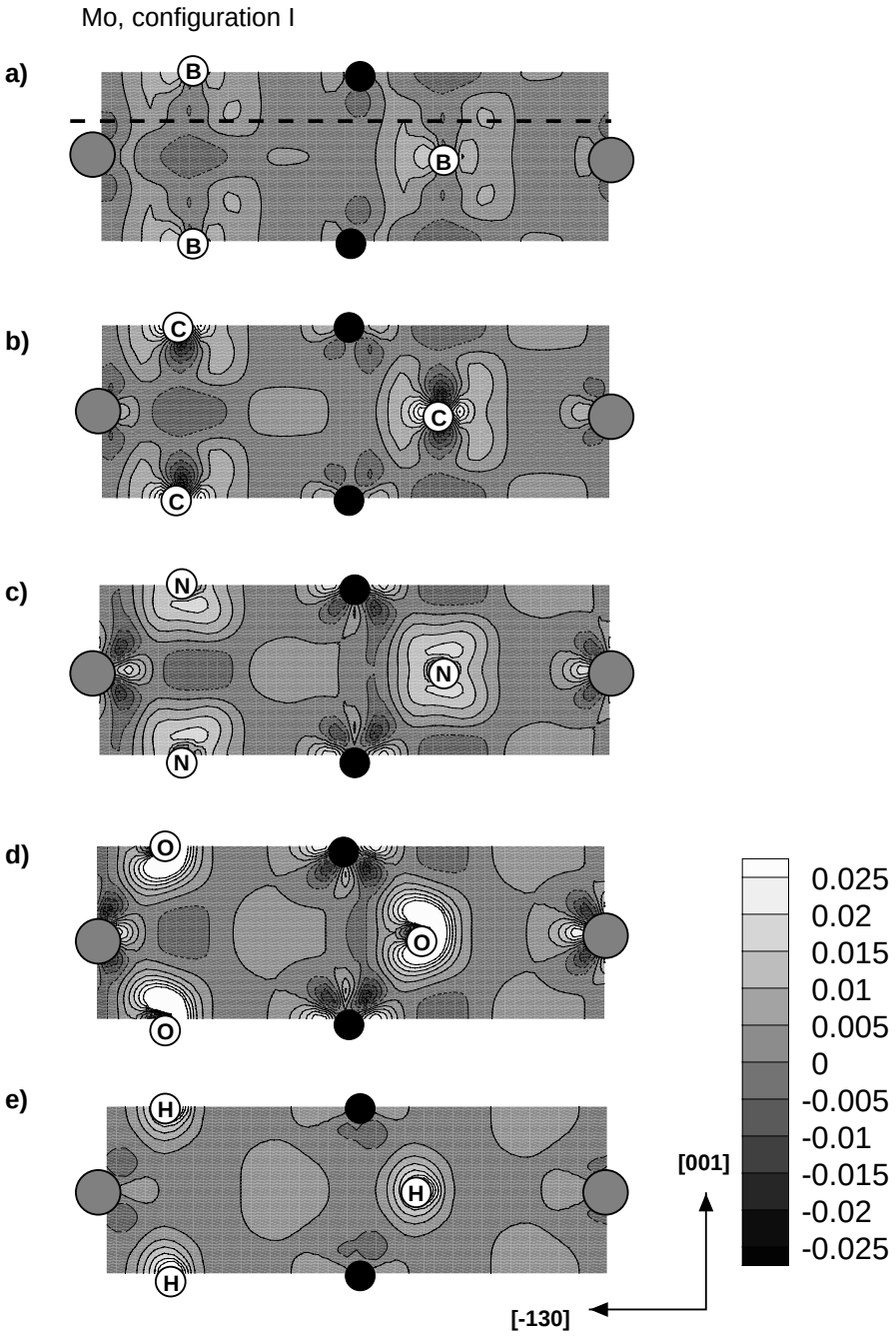


Figure 5.14: Bonding electron densities in [electron/Bohr$^3$] in the grain boundary plane for the mirror-symmetric configuration (I) with the impurities B, C, N, O, and H (from top to bottom). Grey and black circles represent Mo atoms (corresponding to the grey and black Mo atoms in fig 5.2), white circles represent the impurity atom.

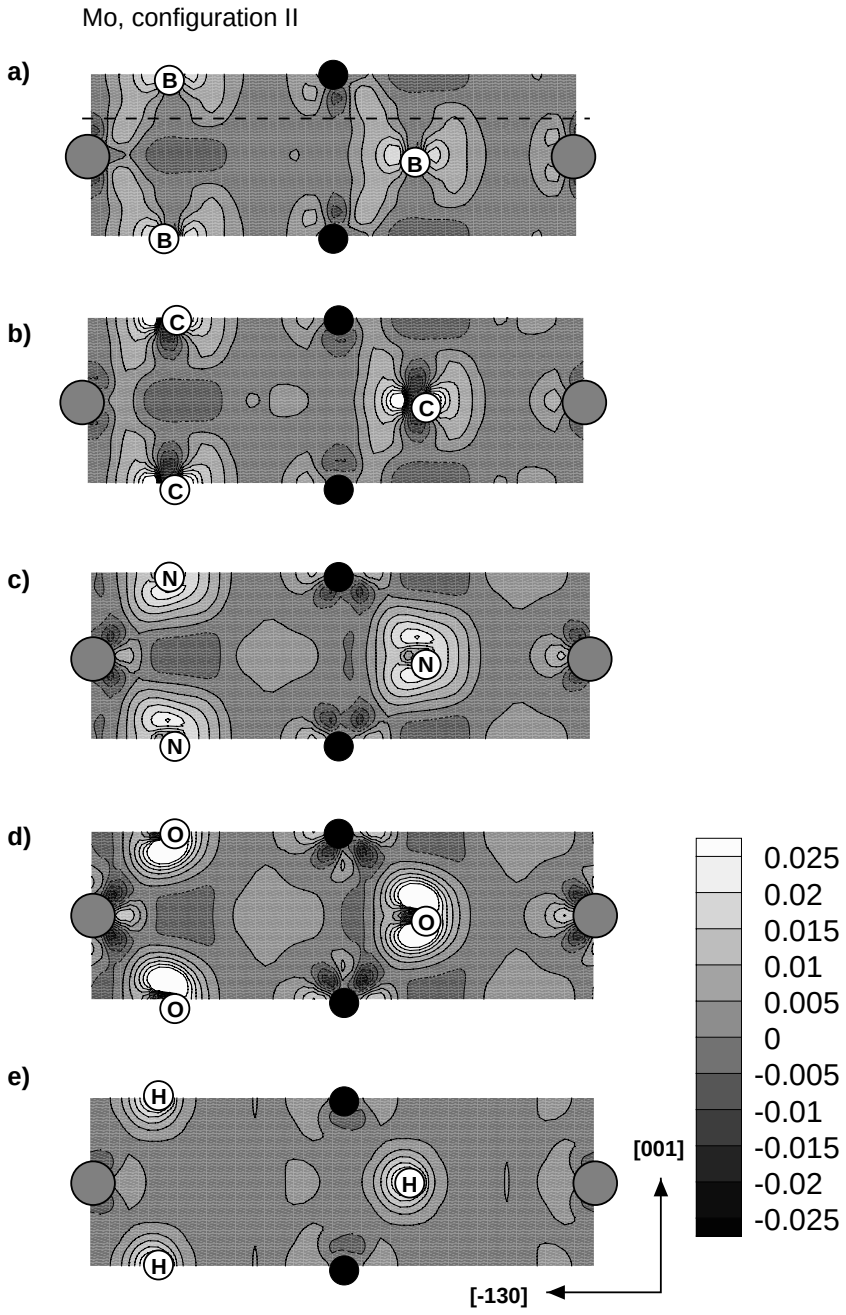


Figure 5.15: Bonding electron densities in [electron/Bohr$^3$] in the grain boundary plane for the non-mirror-symmetric configuration (II) with the impurities B, C, N, O, and H (from top to bottom). Grey and black circles represent Mo atoms (compare figure 5.2), white circles represent the impurity atom

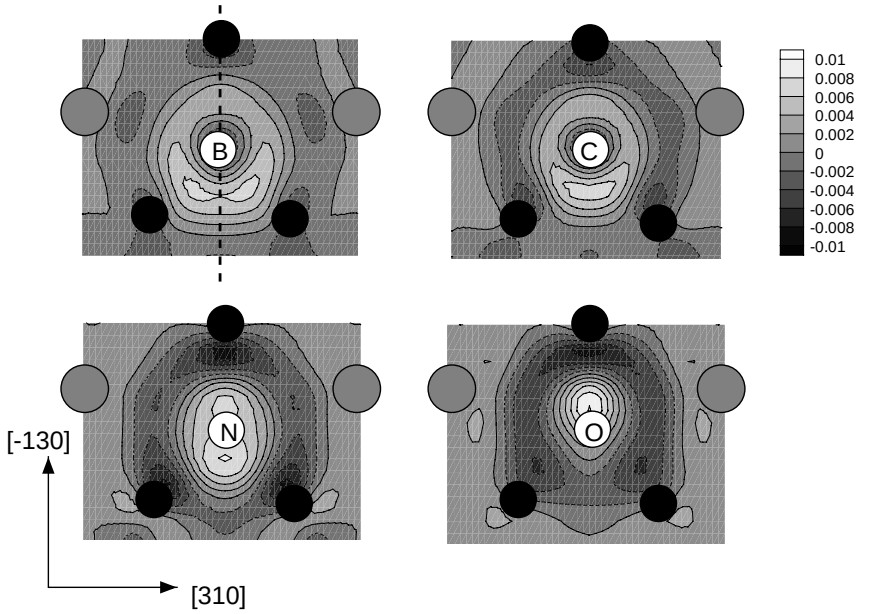


Figure 5.16: Bonding electron densities in [electron/Bohr$^3$] in a plane $\parallel$ (001) of the mirror-symmetric configuration (I) with the impurities B, C, N and O. The cut is taken half way in between the impurity and its nearest-neighbour atoms, as indicated by the dashed line in figure 5.14a). Grey and black circles represent Mo atoms (compare figure 5.2), white circles represent the impurity atom. The black dashed line in the first panel indicates the grain boundary (and the cut shown in figure 5.14).

plane, perpendicular to the grain boundary. There is no plane parallel to the (001) plane in which both, the impurity as well as its nearest host-metal neighbours (the corners of the trigonal prism) are situated. Therefore the cut was taken between the Molybdenum and the impurity atom as indicated by the black dashed line in figures 5.14a) and 5.15a). This plane shows all important features of the bond between metal and impurity. The small black atoms indicate the projection of the positions of the Mo atoms that build the upper side of the trigonal prism around the impurity. The large grey atoms are the next-nearest-neighbours of the impurity, corresponding to the grey atoms in figure 5.2. The white circles mark the projected position of the respective impurity.

In the case of the mirror-symmetric configuration I (figure 5.16) we observe the same behaviour as described above for the cut in the grain boundary plane: When going from B via C and N to O, the bonding electron density between the atoms decreases and is accumulated at the impurity's site. But in addition this cut also provides information about bonds across the interface: in the case of B at the grain boundary, the electron density between the two Mo atoms facing each other at the interface, "Mo1−" and "Mo1+" in-

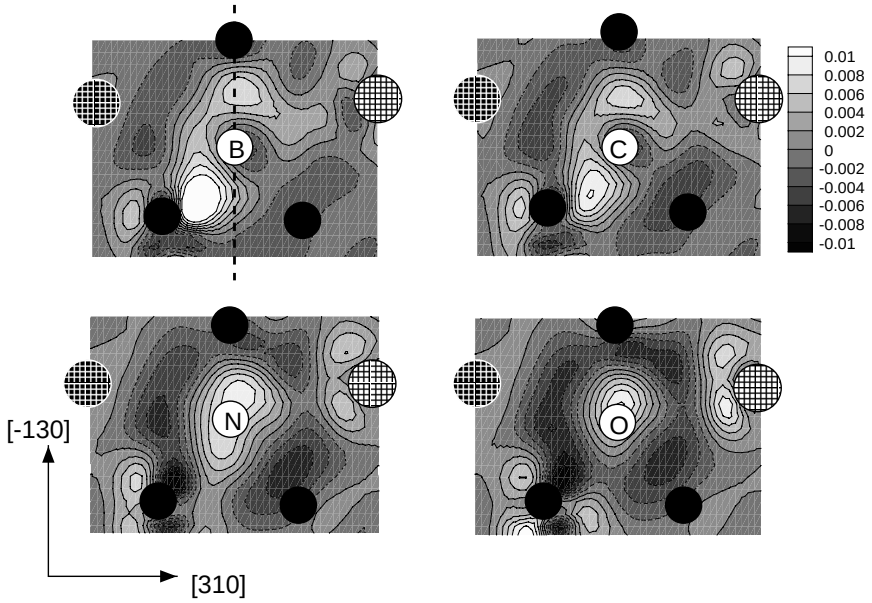


Figure 5.17: Bonding electron densities in [electron/Bohr$^3$] in a plane || (001) of the non-mirror-symmetric configuration (Ⅱ) with the impurities B, C, N and O. The cut is taken half way in between the impurity and its nearest-neighbour atom at the grain boundary, as indicated by the dashed line in figure 5.15a). Black and patterned circles represent Mo atoms, corresponding to the black and grey atoms in figure 5.2, white circles represent the impurity atom. Compared to figure 5.16 the atoms in the left grain are shifted down along [001], the ones in the right grain are shifted up. Thus the big patterned Mo atom on the right side of the grain boundary is getting closer to the impurity than the small black atom that marks one corner of the sheared trigonal prism. The black dashed line in the first panel indicates the grain boundary (and therefore the cut shown in figure 5.15).

creases. The same is true for C, but in the case of N and O a depletion occurs. From the results for the overlap populations we know that this density can not positively be assigned to the metal-metal bond, but it is a combination of the former and contributions of the out-of-plane metal-impurity bonds. The conclusion remains that the covalently bonding impurities also increase the overall bonding across the interface, while the polarly bonding impurities decrease it.

Figure 5.17 demonstrates very nicely again the influence of the different translation state in the non-mirror-symmetric configuration Ⅱ. Compared to figure 5.16 the atoms in the left grain are now shifted down, those in the right grain are shifted up. Thus the big grey atom on the right side is closer to the impurity than the small black one which has been shifted upwards. The bonding electron density adjusts itself to the new nearest-neighbour distances. The overall trend however, remains the same. The charge distribution changes

from covalent to ionic when going from B via C and N to O. At the same time a depletion of electron density between the metal atoms across the interface occurs.
These results together with the grain boundary energies in figure 5.9 lead to the conclusion that covalently bonding impurities like B and C prefer the mirror symmetric, more open structure of configuration I of the $\Sigma 5$ grain boundary, while for polarly bonding impurities like N and O the more densely packed configuration II is more suitable. This fits well into the picture that was gained in [31, 90] for the pure grain boundaries in the bcc transition metals, where the angular dependent bonds arising from the partially filled *d*-states stabilise the mirror-symmetric structure. Furthermore, we expect that covalently bonding impurities strengthen the grain boundary cohesion, as they increase the bonding electron density between Mo atoms across the interface, while polarly bonding interstitials promote embrittlement, as predicted by Cottrell.
In the next paragraph we will analyse the bonding energies to quantify the energetic effect of the interstitial impurities on the the cohesion at the grain boundary.

### 5.5.3 Relaxation of the Metal Lattice

When relaxing all atomic positions for B and C only the mirror symmetric configuration was found stable, while with N and O a shift of 26 and 19% $a_0$ respectively, is energetically favourable. For B and O at the grain boundary also the expansion perpendicular to the interface plane was calculated by performing rigid grain shifts followed by relaxation of the atomic positions after each step. For O this expansion amounts 12% $a_0$, for B 13% $a_0$. The expansion for C and N at the grain boundary then was estimated by interpolating to be 13% $a_0$ and 12% $a_0$, respectively. The translation states of the Mo grain boundary with different impurities are summarised in table 5.8.

### 5.5.4 Bonding Energies

A computational approach to determine the effects of segregated impurities, interstitial or substitutional ones, on grain boundary cohesion was promoted by Geng et al. who developed a phenomenological model [39] based on an extensive set of ab-initio data [120, 121, 124, 40, 41] and a thermodynamic theory of fracture by Rice and Wang[104]. According to this theory the potency of a segregated impurity to enhance or increase interfacial

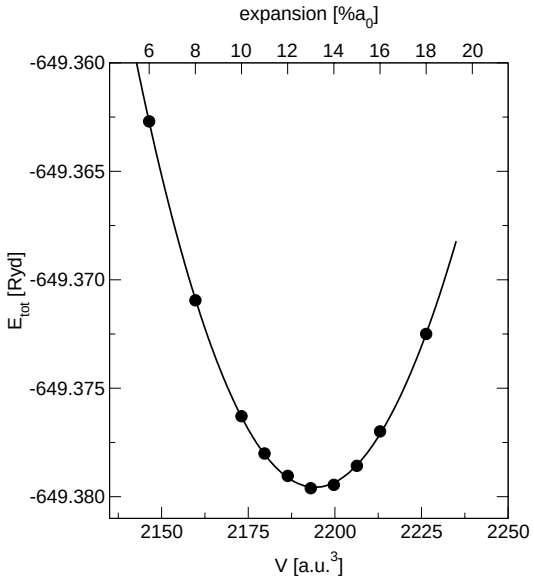


Figure 5.18: Total energy vs. expansion along [310] for the Mo grain boundary in the mirror-symmetric configuration I with B at the interface. At each point all atomic positions are relaxed. (Zero expansion corresponds to the ideal, unrelaxed CSL supercell volume of 2106 Bohr$^3$.)

cohesion is a linear function of the difference in binding energies for that impurity located either at the grain boundary or at the corresponding free surface. Geng et al. successfully applied this theory to explain the influence of the impurity elements H, B and P on grain boundary cohesion in fcc Ni [40]. We will now partly follow their approach to investigate the influence of B, C, N and O on the interfacial cohesion in Mo.

As said above, according to Rice and Wang [104], the difference $\Delta E_B$ of bonding energies of an impurity at a grain boundary and at the corresponding free surface is a measure for the enhancement of embrittlement or of cohesion that this impurity causes at the interface. The bonding energy is calculated by means of equation (5.4). "$S$" denotes either the free surface or the grain boundary. $\mathrm{E}_S$ is the total energy of a supercell with all atomic positions relaxed to zero forces, containing the pure free surface (grain boundary), $\mathrm{E}_{A@S}$ is that of a supercell containing the free surface (grain boundary) with an impurity atom A (A: B, C, N, O), and $\mathrm{E}_A$ is the energy of a free impurity atom.

$$E_B^S = E_S + E_A - E_{A@S} \tag{5.4}$$

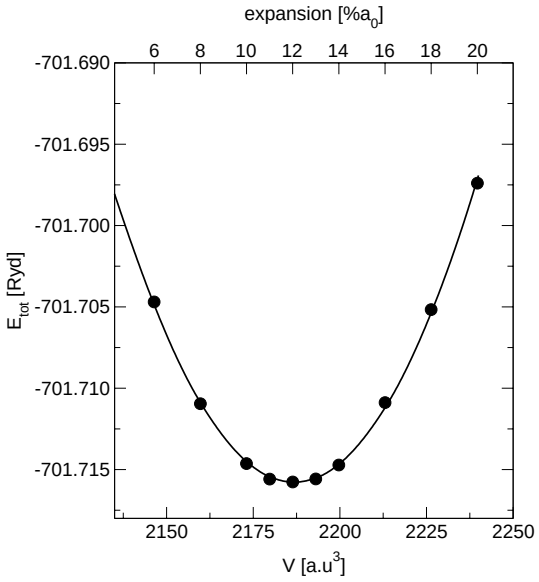


Figure 5.19: Total energy vs. expansion along [310] for the Mo grain boundary in the non-mirror-symmetric configuration II with O at the interface. At each point all atomic positions are relaxed. (Zero expansion corresponds to the ideal, unrelaxed CSL supercell volume of 2106 Bohr$^3$.)

For $E_{GB}$ we used the energy of the respective more favourable configuration. For N, after complete relaxation this was configuration II (cf fig.5.9, where only the positions of the impurity atom had been relaxed).

The bonding energies of B, C, N and O at the free (310) surface, at the $\Sigma 5$ grain boundary, and their differences $\Delta E_B = E_B^{KG} - E_B^{OF}$ are listed in table 5.9. N and O have negative $\Delta E_B$, which means that they enhance embrittlement, while B and C enhance cohesion according to their positive $\Delta E_B$. Recalling the findings of section 5.5.1 we conclude that polarly bonding impurities decrease and covalently bonding impurities increase the interfacial cohesion at the grain boundary in Mo. This is consistent with the fact that H decreases the grain boundary cohesion in Mo.

For further interpretation of the bonding energy it is useful to split it, according to ref. [40], in two parts, a chemical contribution $E_B^c$, which describes the interaction of the impurity with the host atom and is generally assumed to increase the bonding energy, and a mechanical contribution $E_B^m$, which is accommodating the relaxation of the metal lattice around the impurity and in general makes a negative contribution to the bonding energy. $E_B^c$ is the difference between the energy of the relaxed structure including the impurity and

| | expansion along [310][%$a_0$] | $\Delta$t [%$a_0$] |
|---|---|---|
| B | 13 | ($\star$) |
| C | 13 | ($\star$) |
| N | 12 | 26 |
| O | 12 | 19 |

Table 5.8: Translation and expansion of the $\Sigma 5$ grain boundary in Mo with different interstitial impurities at the interface. Listed are the relative shift $\Delta$t of grains along the [001] direction and the expansion along [310], perpendicular to the grain boundary plane in percent of the cubic lattice parameter $a_0$. ($\star$) only the mirror-symmetric case I was found stable.

that of the structure where the impurity has been removed without subsequently relaxing the host lattice again, plus the energy of the impurity itself:

$$E_B^{c,S} = E_{\Box@S} + E_A - E_{A@S} \tag{5.5}$$

Again, $S$ labels either the grain boundary or the free surface, and $\Box$ symbolises the vacant interstitial site that is created when the impurity is removed. The mechanical contribution then is

$$E_B^{m,S} = E_B^S - E_B^{c,S} \tag{5.6}$$

The results are also listed in table 5.9. The elastic contribution $E_B^m$ of the bonding energy is very small in all cases, with relative values between 2 and 7% of $E_B$. As the impurities are very small interstitial atoms this is expected. Geng et al. found similar results for H, B and P at a $\Sigma 5$ grain boundary in fcc Ni [40].

However, for the differences of bonding energies the elastic part becomes more important. Here chemical and mechanical contributions are in direct competition. Only in the case of the strongly covalently bonding B both terms contribute positively to $\Delta E_B$. For C the bonding at the grain boundary, although still partly covalent, is weaker than at the free surface and $\Delta E_B^c$ becomes negative. But the elastic contribution $E_B^m$ at the surface is so large that altogether the grain boundary remains the more favourable surrounding. Not so for N and O that do not develop covalent bonds and for which both terms contribute to the embrittling influence on the grain boundary.

| | Free Surface (FS) | | | | Grain Boundary (GB) | | | | GB - FS | | | |
|---|---|---|---|---|---|---|---|---|---|---|---|---|
| | B | C | N | O | B | C | N | O | B | C | N | O |
| $E_B$ | 7.58 | 10.30 | 10.90 | 8.76 | 8.66 | 10.61 | 10.09 | 7.30 | 1.08 | 0.31 | −0. 81 | −1.46 |
| $E_B^m$ | −0.49 | −0.70 | −0.64 | −0.43 | −0.12 | −0.22 | −0.29 | −0.25 | 0.37 | 0.48 | 0.36 | 0.18 |
| $E_B^c$ | 8.07 | 11.00 | 11.54 | 9.19 | 8.78 | 10.83 | 10.38 | 7.55 | 0.71 | −0.17 | −1.16 | − 1.64 |

Table 5.9: Bonding energies $E_B$ in $\left[\frac{J}{m^2}\right]$, split in mechanical contribution $E_B^m$ and chemical contribution $E_B^c$, for different impurities at the $\Sigma 5$ STGB in Mo, at the corresponding free (310) surface, and their differences.

## 5.6 Summary

In this chapter we performed a detailed analysis of the effects of segregated interstitial impurities on the atomic structure and the cohesion of the $\Sigma 5$ STGB in Mo and Nb. Consistent with the interpretation of Cottrell [19] derived from a simple electronic-structure model, the investigation presented here shows that the bonding character of light elements in bcc Mo and Nb depends on the strength of hybridisation due to the relative position of bands and thus on the valence configuration of the elements. Consequently a systematic trend emerges along one row in the periodic table. A simple comparison between the first ionisation energy $I$ of the impurity atom and the work function $\Phi$ of the metal, together with the bandwidth of the metal valence band can already show the direction of this trend. To a certain extent this picture is independent of the grain boundary geometry so that our findings can be cautiously generalised to other grain boundaries as well.

As Geng et al. [40] did for H, B and P in fcc Ni, we found for the two bcc metals Nb and Mo from the difference in binding energies that covalently bonding impurities enhance the cohesion, while polarly bonding impurities reduce it. The underlying mechanism is rather complex. However, by an extensive analysis of the electronic structure at the grain boundary, i.e. by looking at local densities of states, local orbital overlap populations and bonding electron densities it was possible to identify it as the partial replacement of metal-metal bonds across the interface by metal-impurity bonds. In the case of stronger and covalent bonds the reduction of pure metal-metal bonding across the grain boundary is more than compensated and the grain boundary cohesion is increased. In the case of weak and very polar bonds the overall bonding across the interface is weakened and grain boundary embrittlement is promoted.

So far this work supports the validity of Cottrell's "unified theory". It should be noted

however, that for the differences in bonding energies at the grain boundary and at the free surface in the bcc metals the mechanical part of the energy plays a significant role as well, even for these small elements. That means that despite the general ansatz of Cottrell one has to be careful when treating very different environments of the impurity.
Concomitant with the trend in bonding energies one observes a structural one. The bonding character of impurities with the host metal does not depend on the geometry, but it is decisive for the issue of which microscopic translation state of a grain boundary is more favourable. In the bcc transition metals covalently bonding impurities prefer the mirror-symmetric configuration I of the $\Sigma 5$ STGB, where they can find equal bond lengths to an adequate number of first nearest-neighbours. Polarly bonding impurities favour the rather close-packed non-mirror-symmetric configuration II. This is in good agreement with the interpretation of previous results concerning the translation state of the pure grain boundaries [5, 31, 90, 89].

# Chapter 6

# Precipitation of Molybdenum Carbide at the Σ5 Grain Boundary in Mo

To understand the influence of segregated impurities on grain boundary cohesion it is advantageous to investigate grain boundaries in materials containing only one impurity element. In this manner interference of different effects can be avoided (compare chapter 5). Pénisson and co-workers have also taken this point of view and chose the Σ5 (310) [001] STGB in Mo with segregated carbon impurities for a case study [94]. The choice of carbon is standing to reason as its presence in the real material is hardly avoidable. Thus Pénisson et al. performed HRTEM on the Σ5 STGB in a Mo bicrystal before and after carburisation heat treatments. By choosing different carburisation conditions they obtained samples with different C contents. They observed different intra- and intergranular $MoC_x$ phases which will be described below. Of particular interest is a tetragonal substoichiometric phase occurring both as inter- and intragranular precipitate. Inspired by this work in this chapter the microscopic processes leading to $MoC_x$ precipitates at the Σ5 STGB in Mo are investigated. The new Mo-$MoC_x$ interfaces and their effect on the material properties are examined. In general, secondary phase precipitates, such as $MoC_x$ in Mo, are responsible for hardening of the matrix material as they represent obstacles for dislocation movement [49, 62]. How easily the dislocations can overcome these obstacles is determined by composition, crystal structure, shape and size of the particles, as well as by the orientation relationship between matrix and precipitate lattice [49, 62, 43].
In the following the experimental procedure and the results of Pénisson et al. are described

in more detail in section 6.1, then we look at the very beginning of the precipitation, modelled by calculations with two or three C atoms in the supercell, in section 6.2, and finally the atomic structure of a tetragonal MoC film at the $\Sigma 5$ grain boundary is investigated in section 6.3.

## 6.1 Experimental Findings

### 6.1.1 Experimental Procedure

To produce a Mo bicrystal with a $\Sigma 5$ (310)[001] STGB, Pénisson et al. cut and oriented single-crystal rods in the respective orientations and welded them by an electron beam under vacuum conditions [94]. Afterwards the bicrystal was annealed at about 2400 K for 4h in an oxygen atmosphere to eliminate carbon already being present in the bicrystal. Finally the bicrystal was purified by holding it at the same temperature for 14h under high vacuum conditions ($10^{-6}$ Pa) to remove oxygen. To achieve carburisation several purified samples were annealed for 6h at temperatures between 1700 and 2400 K under a $CH_4$ atmosphere ($2{\cdot}10^{-7}$ - $2{\cdot}10^{-6}$ Pa partial pressure). Thus carbon concentrations of 150 - 600 at. ppm in the bulk volume of the bicrystals were obtained. Finally, the samples were quenched at a cooling rate of about 150 $\frac{\mathrm{K}}{\mathrm{s}}$.

### 6.1.2 Results

According to the carburisation conditions, two different carbide morphologies were found at the grain boundary. At very high temperatures and $CH_4$ partial pressures the carbon concentration reached the solubility limit during carburisation. In this case isolated particles of hexagonal $Mo_2C$ occur at the interface. This hexagonal $Mo_2C$ corresponds to the stable carbide phase of bulk molybdenum [119] and has been reported before [70, 71]. It fits well with the surrounding bcc Mo lattice, as the (310) plane in Mo is very similar to the (0001) habit plane of the hexagonal carbide. At lower temperatures, however, the precipitation took place below the temperature of carburisation, during the quenching. In this case Pénisson et al. observed both, a thin and continuous film of tetragonal, non-stoichiometric $MoC_x$ covering the interface and intragranular precipitates of the same structure. In the latter the lattice parameters were measured to be $a = 0.305$ nm (=5.77 Bohr) and $c = 0.406$ nm (=7.67 Bohr). This corresponds to a $c/a = 1.33$. Assuming a linear dependence of the $c/a$ ratio on the carbon content and by taking $c/a = 1$ for bcc Mo ($x = 0$) and

$c/a = \sqrt{2}$ for fcc $Mo_2C$ ($x = 0.5$) as limits, Pénisson et al. derived a C concentration of $x \approx 0.4$.

This kind of precipitate has already been observed by Lepski et al. [73, 74]. After rapid quenching ($2 \cdot 10^4 \frac{K}{s}$) of C doped Mo crystals they received disc shaped particles with a diameter up to 5nm. These turned out to consist of fcc $MoC_x$ with $0.40 \leq x \leq 0.43$. This phase was identified to be a metastable intermediate phase. It originates in a body-centred tetragonal structure from a tetragonal distortion of the bcc Mo lattice, in which C occupies octahedral sites. It can convert by a martensitic transformation[1][43] into a hexagonal close-packed lattice by shearing of the close-packed (111)-planes.

A HRTEM picture of the situation at the grain boundary is shown in figure 6.1. The film has a thickness of about 1 nm. Pénisson et al. note that the interfaces between this second phase and the molybdenum crystals were not well defined. The arrows mark stacking faults which occur in a regular arrangement along the interface, indicating a small lattice misfit between the two phases. The orientation relationship between the tetragonal $MoC_x$ and the bcc Mo is of the kind[2]

$$\left.\begin{array}{rcl} [001]_{Mo} & || & [010]_{MoC_x} \\ (310)_{Mo} & || & (103)_{MoC_x} \end{array}\right\} \tag{6.1}$$

An enlargement of figure 6.1 is shown in figure 6.2 which clearly illustrates this relationship. Here the crystal planes are indicated as white lines and the unit cells of the different phases are also plotted. We can identify the two new interfaces, (6.1) on the left side of the $MoC_x$ film and

$$\left.\begin{array}{rcl} [001]_{Mo} & || & [010]_{MoC_x} \\ (\bar{3}\bar{1}0)_{Mo} & || & (103)_{MoC_x} \end{array}\right\} \tag{6.2}$$

on the right side. At the left interface, in the following called "Interface I", the tilt angle is approximately 40° and thus close to that of the original Σ5 STGB (36.89°). At the right interface, in the following called "Interface II", the crystallographic planes in $MoC_x$ continue under a only very small deviation of approximately 6° into the Mo grain.

After interpretation of their results Pénisson et al. concluded with an imagination of the process of segregation of C and precipitation of $MoC_x$ at the Σ5 STGB in Mo which is

[1] i.e. without change of C concentration

[2] Actually, Pénisson et al. by mistake report the respective crystallographic plane in MoC to be (301) instead of (103). However, relations (6.1) can be justified from figure 6.2, or from the schematic picture of the model structure presented later on in this chapter, figure 6.8.

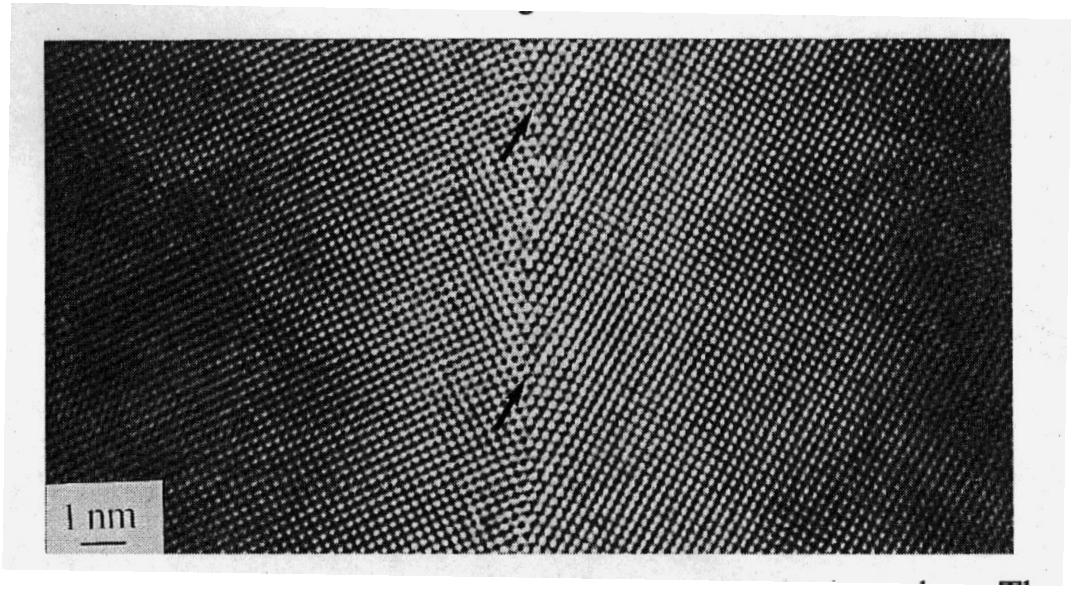


Figure 6.1: High-resolution image of the tetragonal carbide layer covering the Σ5 STGB in Mo [94]. The arrows mark interface dislocations which can be found along the interface in a periodic arrangement.

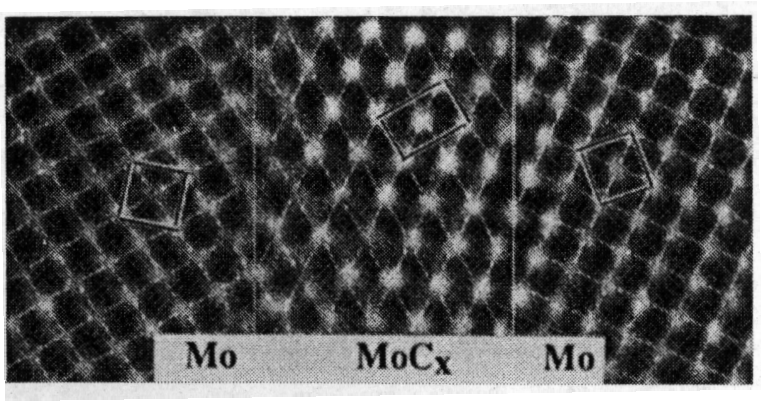


Figure 6.2: Enlargement of figure 6.1 [94]. The white lines mark the crystal planes in both phases. The unit cells of the different structures are also outlined.

consistent with the results of Lepski et al. for the precipitation of $MoC_x$ particles in a Mo matrix. C is segregating via interstitial positions, occupying octahedral sites in the bcc Mo crystal, and causing a tetragonal distortion. The magnitude of the distortion depends on the carbon concentration, the maximum is $c/a = \sqrt{2}$, i.e. a fcc "rocksalt" structure of the carbide. Under the chosen carburisation conditions a C concentration of $x \approx 0.4$ was attained leading to a non-stoichiometric phase with $c/a = 1.33$. The presence of dislocations at the interface indicates that this tetragonal carbide phase is not in equilibrium at the grain boundary but experiences internal incoherency strains due to a small lattice misfit. The stacking faults can be considered as embryos of the hexagonal phase, into which the tetragonal phase is transforming, leading to stable $Mo_2C$ particles at the grain boundary. Modelling such structural phase transformations is out of the scope of the ab-initio study, in the framework of which only static relaxations of atomic positions are performed. However, in the following sections different stages of the process of C segregation and $MoC_x$ precipitation at the $\Sigma 5$ grain boundary are modelled. The initial growth of the precipitate is investigated in the following section, afterwards we turn towards the properties of the two interfaces observed by Pénisson et al. in their HRTEM bicrystal study.

## 6.2 "Nucleation" and "Growth" of the Precipitate

Starting with the mirror-symmetric configuration of the $\Sigma 5$ STGB in Mo with one segregated C atom per interfacial unit cell, the concentration of C at the grain boundary is increased atom by atom. Due to the periodicity of the grain boundary and the size of the supercell the number of interstitial sites to which C can segregate is limited. As discussed in chapter 5 the first C atom at the interface already occupies the only reasonable site directly at the grain boundary. Thus the next C atom inserted at the grain boundary occupies an interstitial site in the Mo layer next to the interface. As we are not going to model the dynamical process of the segregation at this point we will simply probe different sites. Two positions are available for the second atom: in one case C will occupy an octahedral site in the Mo lattice between two Mo atoms in the crystal plane meeting the grain boundary at an angle of 18°, as shown in figure 6.3a). In the other case C is positioned in a corresponding site in the crystal plane meeting the interface at an angle of 108°, cf. 6.4a). By continuing to fill the grain with more C atoms following this scheme both cases lead to a tetragonal distortion of the bcc Mo lattice and finally to a precipitate of tetragonal MoC with c/a > 1. In the first case, 6.3a), the tetragonal c-axis would be oriented such that the

[001] direction of the precipitate meets the grain boundary at an angle of 18°, in the other case, 6.4a) the angle is 108°. The first case leads to an expansion of the structure mainly along the interface, the second mainly perpendicular to it.

As this calculation is meant only to get a rough estimate into which direction the precipitate is growing a complete relaxation of the structures of figures 6.3 and 6.4 was not performed. This would include rigid grain shifts parallel to and volume expansion perpendicular to the interface. We argue that in this first step the C concentration is still low enough to cause only local distortions and no overall changes in the structure. Thus only the atomic positions were relaxed until the forces on the atoms were negligible. Figures 6.3b) and 6.4b) show the relaxed supercells. In both cases the C atom indeed causes rather localised lattice distortions. It pushes apart the two neighbouring Mo atoms along the **c** axis marked in figures 6.3a) and 6.4a). The pure Mo grain on the other side of the interface remains unaffected. The total energies of the supercells are -682.895 Ryd in the first case and -683.126 Ryd in the second. This means the latter configuration is favoured and the precipitate will grow with its c-axis oriented at approximately 108° with respect to the grain boundary. This probably is accompanied by a considerable expansion of the grain perpendicular to the grain boundary. However, obviously a change in the periodicity of the grain boundary, which would come along with the precipitate growing in the other orientation, is more unfavourable than a larger expansion perpendicular to the interface.
Continuing with this configuration the third C atom is put close to the interface. Again there are two possibilities: the third C atom can be positioned opposite to the second, on the other side of the grain boundary as in figure 6.5 or next to it, inside the same grain as in figure 6.6. In both figures the atomic coordinates are already relaxed. In the first case, 6.5, we observe that both grains want to expand along the [310] direction. As this is not possible they get sheared parallel to the interface. In the second case, fig. 6.6, the left grain containing all the carbon atoms is expanding and the right, pure Mo grain is compressed. By this it is also sheared parallel to the interface, as we can see from the deviation of the bond angles from 90°. However, these latter results should not be over-interpreted, as in this case we are running into problems with the supercell size. The third C atom and its periodic image in [310] direction are in the same grain and are getting so close that the centre of the grain can no longer be assumed to be purely Mo bulk-like.

The total energies of the supercells are -705.656 Ryd for the symmetric growth and -705.559 Ryd for the asymmetric one. This means the former configuration (fig. 6.5) is

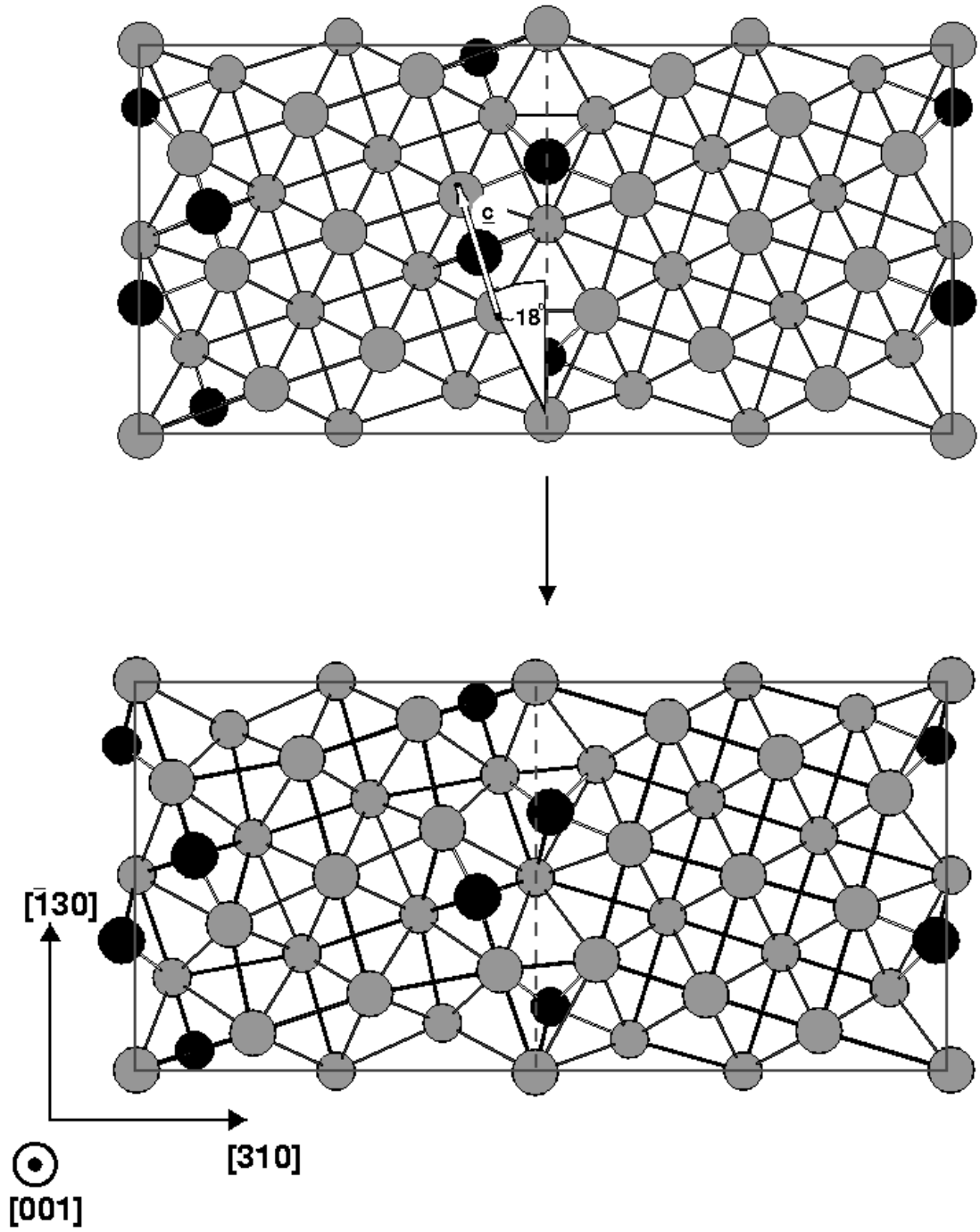


Figure 6.3: Possibility I of putting an additional C atom at the Mo Σ5 STGB with a segregated C impurity. a) unrelaxed supercell b) after relaxation of all atomic positions. The large atoms are positioned in the paper plane, the small atoms are the next layer in [001] direction. Mo atoms are gray, C atoms black.

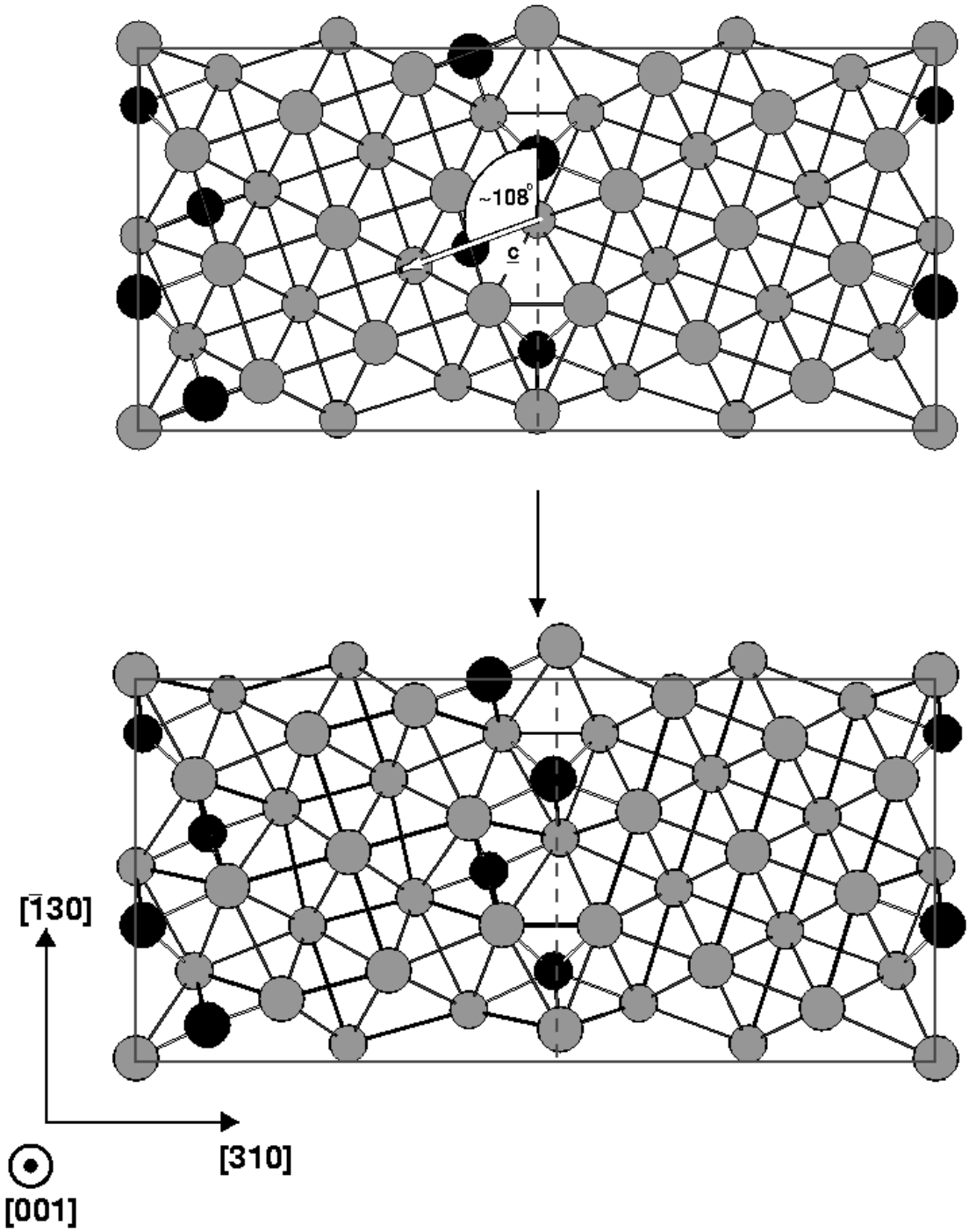


Figure 6.4: Possibility II of putting an additional C atom at the Mo Σ5 STGB with a segregated C impurity. a) unrelaxed supercell b) after relaxation of all atomic positions. The large atoms are positioned in the paper plane, the small atoms are the next layer in [001] direction. Mo atoms are gray, C atoms black.

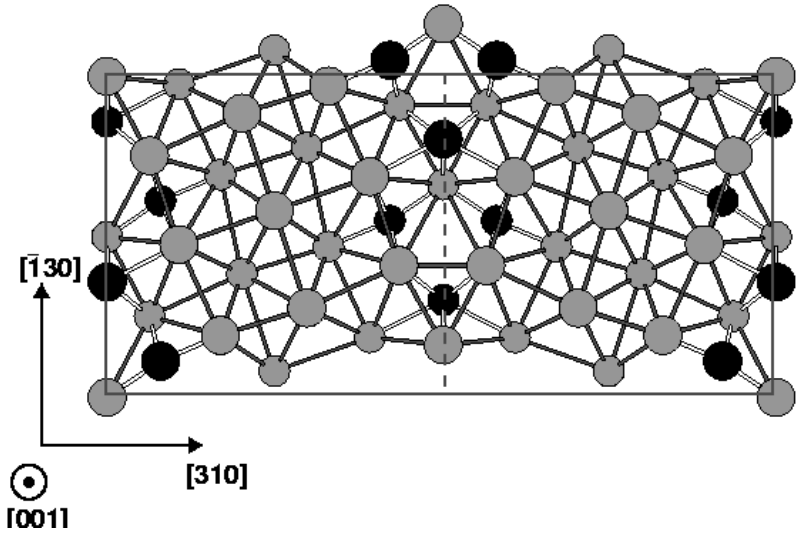


Figure 6.5: Symmetrical growth of the MoC precipitate at the Mo Σ5 STGB, supercell after relaxation of all atomic positions. The large atoms are positioned in the paper plane, the small atoms are the next layer in [001] direction. Mo atoms are gray, C atoms black.

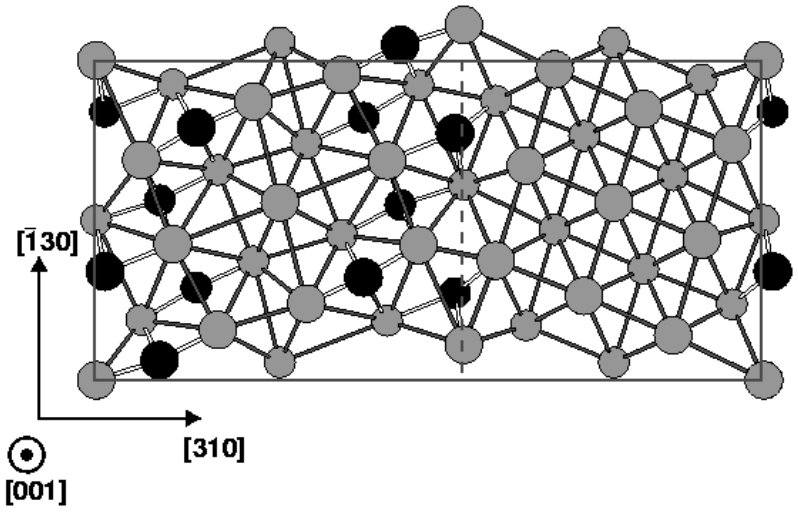


Figure 6.6: Asymmetrical growth of the MoC precipitate at the Mo Σ5 STGB, supercell after relaxation of all atomic positions. The large atoms are positioned in the paper plane, the small atoms are the next layer in [001] direction. Mo atoms are gray, C atoms black.

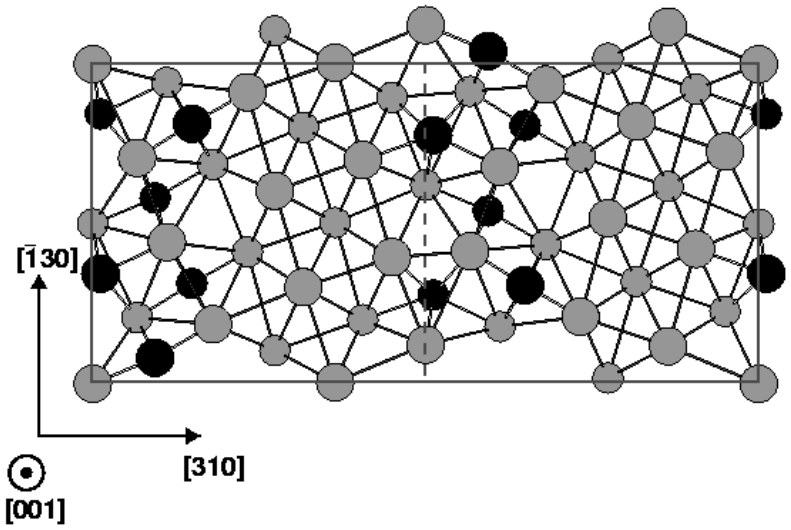


Figure 6.7: Asymmetrical growth of the MoC precipitate at the Mo Σ5 STGB, supercell after relaxation of all atomic positions. The large atoms are positioned in the paper plane, the small atoms are the next layer in [001] direction. Mo atoms are gray, C atoms black.In contrast to the supercell shown in figure 6.6 the inversion symmetry is abandoned, but therefore the precipitates don't grow towards each other.

lower in energy. The reason is the existence of more free space in the first Mo layer next to the grain boundary than further inside the grain. However, from this it is not justified to draw the conclusion that the precipitate would grow in a symmetric fashion, because of the discussed situation of the precipitates getting so close to each other in the asymmetric case. A supercell in which the increasing size of the precipitate is less problematic is shown in figure 6.7. Here the inversion symmetry with respect to the centre of the cell was abandoned (increasing the computational cost) by letting the precipitates grow into different grains. Now there are seven layers of Mo atoms between the carbide precipitates instead of five. Thus the precipitates interact considerably less as in the case of figure 6.5. The change in the total energy of the supercell is dramatic: from -705.559 Ryd for the case shown in 6.5 it is lowered to -705.611 in for the new configuration and thus becomes almost equal to that of the supercell for the symmetrical growth (-705.656 Ryd). This means that at this point we really can not decide whether the precipitate would grow in a symmetrical or asymmetrical fashion. The remaining energy difference is sufficiently small that a complete relaxation of the structures could easily lead to a compensation or even a reversal. The supercell size could be increased to perform further ab-initio calculations and

also allow for volume expansions to clarify this point. However, the additional computational cost would be disproportionate to the amount of further insight into the segregation process that could be gained. It is more meaningful to leave this to a calculation with semi-empirical interatomic potentials. Thus, instead we are going straight away to the end of the process of segregation and precipitation and look at the "finished" precipitate.

## 6.3 The MoC Precipitate: Two New Interfaces

Based on the observations of Pénisson et al. [94] two supercells were constructed to model the two interfaces between the bcc Mo and the body-centred tetragonal (bct) carbide film at the grain boundary. The idea was to take the supercell of the $\Sigma 5$ STGB in Mo (see figure 5.2) and simply replace one grain of Mo by the tetragonal carbide. Two arising problems had to be dealt with, the lattice mismatch between Mo and $MoC_x$ and the non-stoichiometry of the carbide phase. A random occupation of the octahedral sites to achieve a C concentration of $x = 0.4$, as reported by Pénisson et al. [94] would again have required a larger supercell. Starting with the supercell of the $\Sigma 5$ STGB in Mo which contains only one layer of Mo atoms in [001] direction, removing an atom means taking out the whole column of corresponding atoms along [001] in the crystal. Instead of constructing a larger supercell, a stoichiometric tetragonal MoC precipitate was assumed. This choice can be justified not only by practical arguments. Pénisson et al. never determined the C concentration directly (e.g. by spatially resolved energy dispersive X-ray diffraction, or by quantitative electron energy loss spectroscopy [103, 30]). Only the $c/a$ ratio of the precipitate is indicating $x = 0.4$. However, a $c/a$ ratio of $\sqrt{2}$, one of the benchmarks for the derivation of $x$, is also found in stoichiometric fcc MoC [119]. Fcc MoC is a high-temperature carbide phase which has been reported already by Clougherty et al. [18]. It was synthesised by heating up a mixture of $Mo_2C$ and C at a pressure from four to seven GPa and temperatures between 2000 and 2700 K, and could also be retained at atmospheric pressure. Hence, by assuming a stoichiometric tetragonal MoC precipitate an existing structure is modelled and the geometry of the precipitate is unchanged. The influence of the higher C content however will have to be discussed.

Previous ab-initio calculations concerning the properties of molybdenum carbides of different crystal structures and stoichiometries [65, 66] included bct MoC and yielded an equilibrium volume of 282.93 $Bohr^3$, with a $c/a$ ratio of 1.39 ($c = 8.17$ and $a = 5.88$) [65], i.e. a structure very close to fcc MoC. To cope with the lattice mismatch without altering

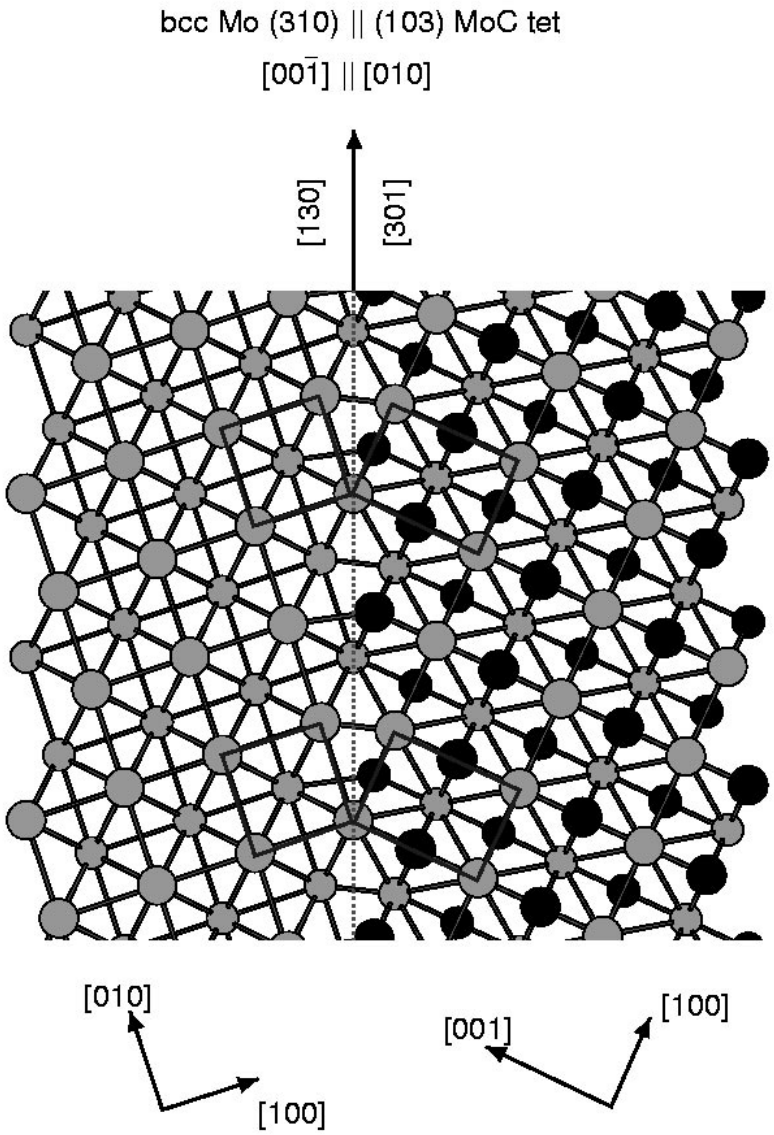


Figure 6.8: Model interface for the precipitation of bct MoC at the $\Sigma 5$ STGB of bcc Mo, "Interface I". The large atoms are positioned in the paper plane, the small atoms are the next layer in [001] direction. Mo atoms are gray, C atoms black.

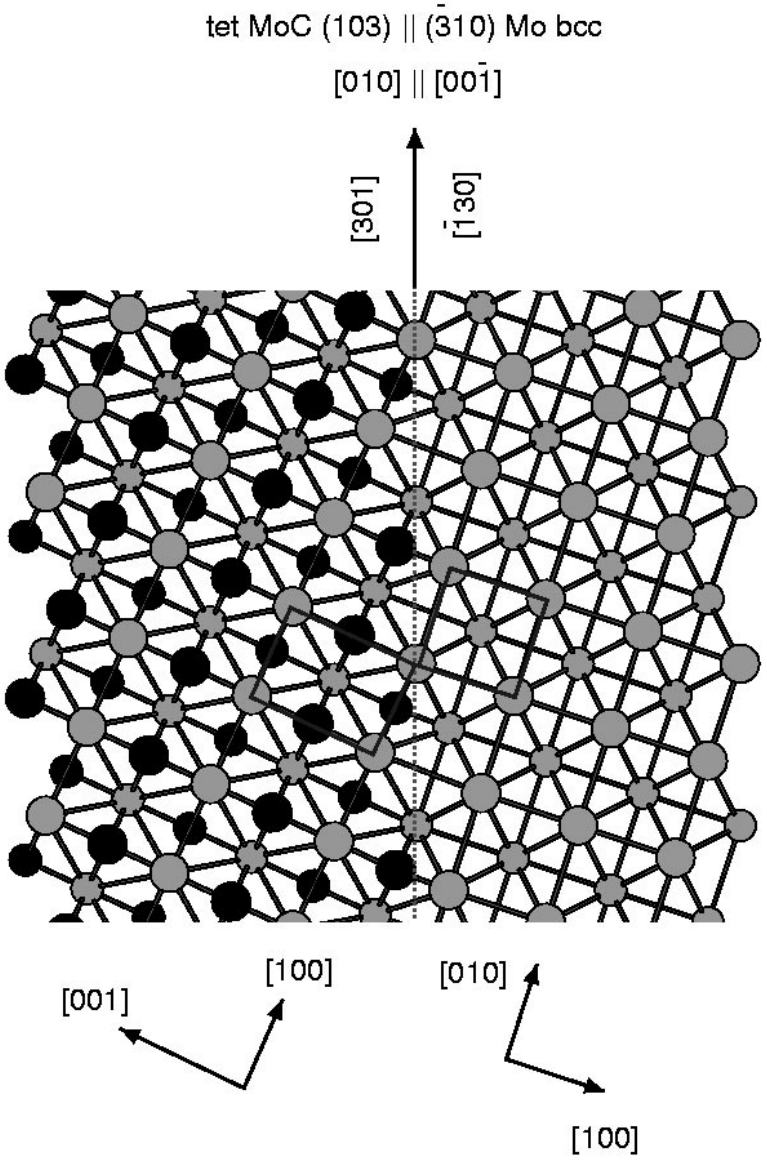


Figure 6.9: Model interface for the precipitation of bct MoC at the Σ5 STGB of bcc Mo, "Interface II". The large atoms are positioned in the paper plane, the small atoms are the next layer in [001] direction. Mo atoms are gray, C atoms black.

the periodicity of the Σ5 STGB the carbide phase was compressed while keeping the $c/a$ ratio fixed. This leads to an $\tilde{a} = 0.956\ a_0$ corresponding to a compression of the tetragonal unit cell by 13% to a volume of 245.95 Bohr$^3$. The effect that this compression has on the interface energy will be discussed later. With this procedure the two model interfaces shown in figures 6.8 and 6.9 were received. So far these are pure geometric constructions, which means the models have atomically abrupt interfaces, despite the report of Pénisson et al. about the interfaces between precipitate and metal lattice being not well defined. Therefore the first step to investigate the properties of a realistic interface model is to probe the microscopic translation state of the phase boundary, including relaxation of all atomic positions. The results of this procedure will be described separately for "Interface I" and "Interface II" in sections 6.3.2 and 6.3.3. As it is reasonable to discuss the energies of possible translation states with respect to the energies of the free surfaces, the possibilities of "cutting" the supercell containing the Mo-MoC-interface into two slabs will be discussed first in the following section.

### 6.3.1 Free Surfaces

The model interfaces I and II of figures 6.8 and 6.9 have a Mo coincidence site belonging to the Mo grain as well as to the MoC precipitate. When breaking the interface apart, however, this Mo atom can only belong to one of the grains. Thus we have either a Mo grain consisting of 9 Mo layers and a MoC grain in which the Mo sublattice has 11 layers or, vice versa a Mo grain containing 11 Mo layers and a MoC grain in which the Mo sublattice has 9 layers. For the precipitate this means that its surface is either Mo terminated (in the first case) or C terminated (in the second case). The total energies of these possible combinations are given in table 6.1. In these calculations all atomic positions have been relaxed. These total energies indicate that the Mo-MoC boundary is more stable against cleavage with a Mo terminated surface of the MoC precipitate than with a C terminated one. Thus the energies of the supercells containing the Mo-MoC-interfaces will be given in the following sections with respect to case A in table 6.1.

### 6.3.2 Interface I: Atomic Structure

To get from the geometric construction to a structurally optimised model of the interface, the microscopic translation state of the grains was probed in all three spatial directions. With respect to the Mo grain these are the [001], [$\bar{1}$30] and [310] directions. While rigid

| | A<br>Mo: 9 layers<br>MoC Mo terminated | B<br>Mo: 11 layers<br>MoC C terminated |
|---|---|---|
| $E^{tot}_{FS,Mo}$ [Ryd] | -285.424 | -348.985 |
| $E^{tot}_{FS,MoC}$ [Ryd] | -461.006 | -397.339 |
| $E^{tot}_{FS,Mo} + E^{tot}_{FS,MoC}$ [Ryd] | -746.430 | -746.324 |

Table 6.1: Total energies of supercells containing Mo and MoC free surfaces. The surface orientations correspond to the phase boundary plane of the interface models, 6.8 and 6.9. There are two possibilities, A and B, of assigning the coincidence-site Mo atom to one of the grains. All atomic positions are relaxed. From the total energies it becomes apparent that the phase boundary is more stable against cleavage with a Mo terminated precipitate is more than with a C terminated one.

grain shifts along [001] and [$\bar{1}$30] change the symmetry of the interface, a shift along [310] results in a volume expansion at the interface. Shifts along this axis have been performed in steps of one or two percent of the Mo bcc lattice parameter $a_0$, always starting from the geometrically constructed supercell. At each step all atomic positions in the supercell were fully relaxed, leading to the energy vs. volume curve shown in figure 6.10a). The total energy of the supercell is given with respect to the energies of the respective free surfaces. The minimum is located approximately at a total volume of 2470 Bohr$^3$, corresponding to an expansion of 17% of $a_0$ perpendicular to the interface. The structure is shown in figure 6.11. Compared to the geometric model, in the optimised model the C atoms of the first layer inside the MoC grain relaxed into the grain boundary layer where they have more space. Here they are sitting again in the centre of the trigonal prism. Starting now from this configuration, rigid grain shifts were performed along [$\bar{1}$30] and [001] to check the structural stability. The respective energies are shown in figure 6.10b). We see a steep energy rise from the minimum configuration. When relaxations of the atomic positions are allowed at the points marking the shift along [$\bar{1}$30], the structure relaxes back to the common minimum of the curves. This means that the Mo-MoC-interface as constructed in figure 6.8 is indeed stable against a relative shift of grains along [$\bar{1}$30].
After shifting the grains along [001] by 10% or 20% of $a_0$ the atoms relax back to the initial configuration as well. However, for very large shifts, in this case 40% of $a_0$, by relaxation of the atomic positions the relative shift of the grains increases even further, up to nearly 50%. To see what has happened the relaxed structure is shown in figure 6.12. Due to the shift of approximately half a lattice constant, atoms that have been marked by big

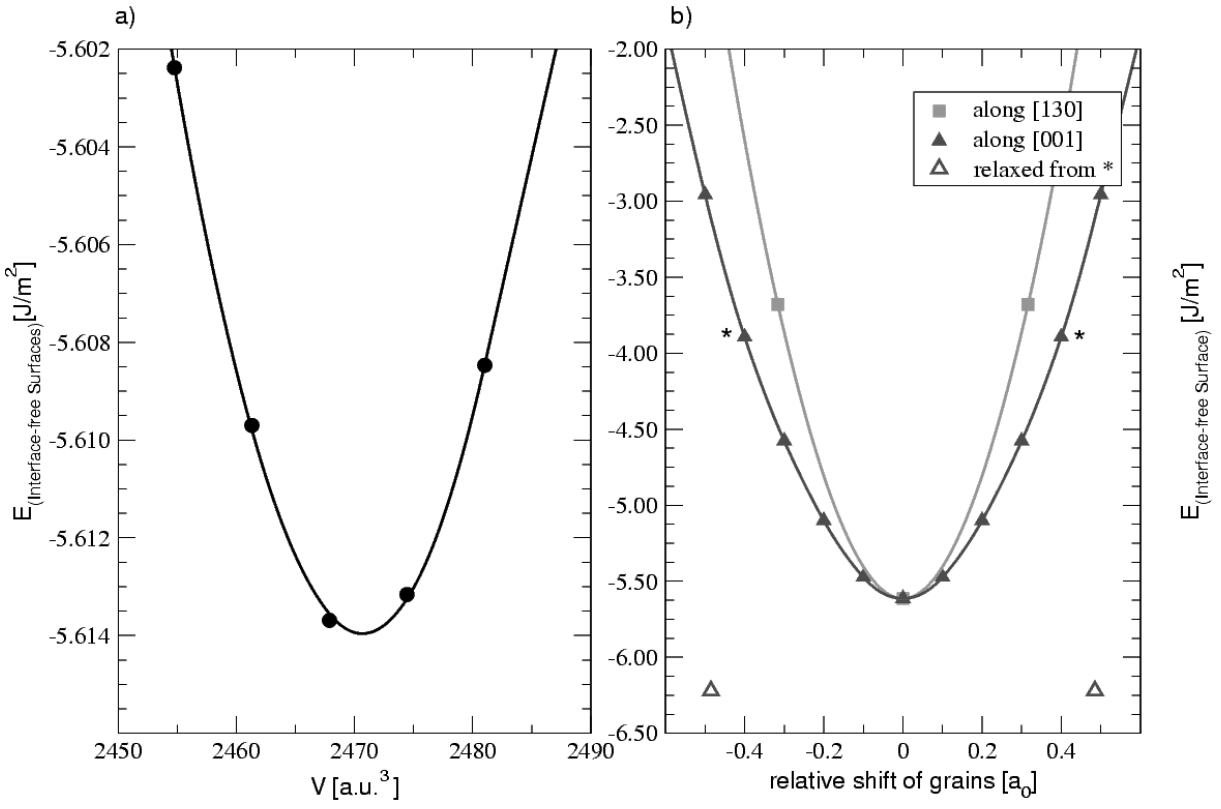


Figure 6.10: Interface I: Optimisation of the structure. Shown is the energy difference between the interface and the corresponding free surfaces a) for volume expansion along [310] with relaxation of the atomic positions, b) for rigid grain shifts along [001] and [-130] (directions refer to the Mo grain).

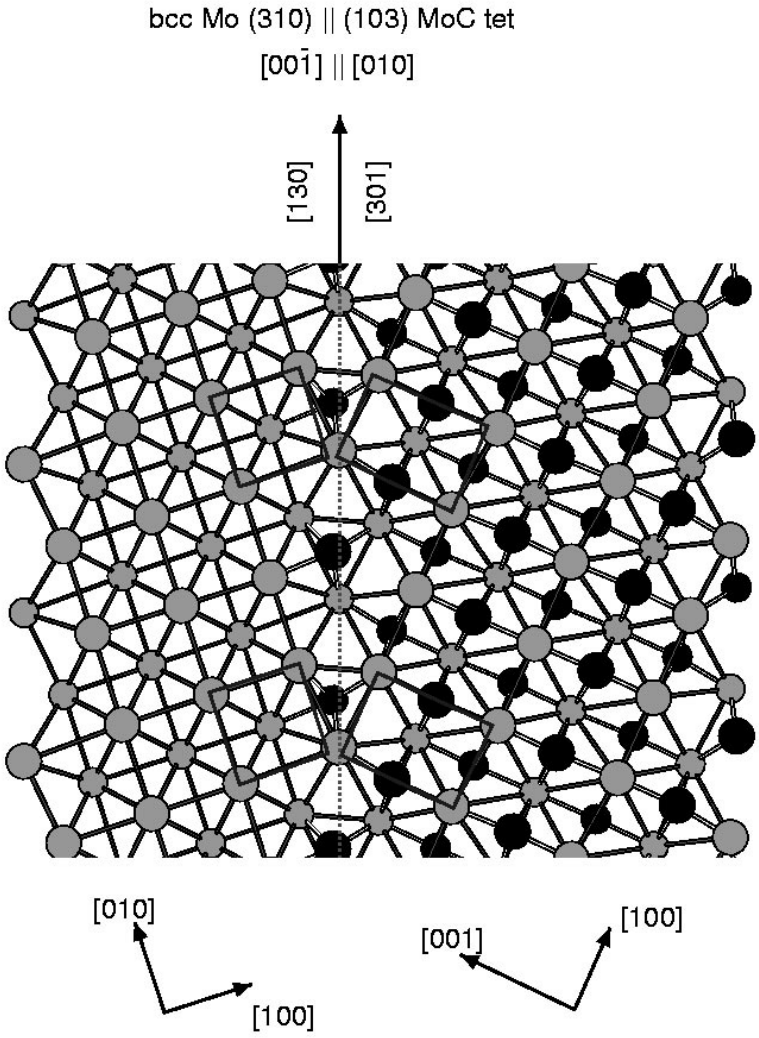


Figure 6.11: Interface I after volume expansion and relaxation of all atomic positions. The large atoms are positioned in the paper plane, the small atoms are the next layer in [001] direction. Mo atoms are gray, C atoms black. Compared to the geometric construction the supercell is expanded by 17% of $a_0$ perpendicular to the interface and the C atoms of the first layer next to the grain boundary relaxed into the interface layer.

circles in the MoC grain are now denoted by small circles and vice versa. The surprising observation is that the Mo-MoC-interface moved by one atomic layer into the Mo grain. At the same time a grain boundary inside MoC evolved. Comparing this situation with the symmetrical variant of the initial growth, figure 6.5, it becomes comprehensive: by displacing the grains C was pushed across the grain boundary into the Mo grain. Thus the phase boundary between the two compositions and the grain boundary between the two crystal orientations are no longer the same. This is favourable because now more C atoms occupy interstitial sites close to the grain boundary, where they have more space. This process is a possible explanation of the experimental finding of a not well defined interface: even if the precipitate grows asymmetrically into one grain and is thus clearly limited by the former $\Sigma 5$ grain boundary, displacements of small amounts of carbon across the interface could soften this sharp boundary.

### 6.3.3 Interface II: Atomic Structure

In the case of Interface II (cf. 6.8) the supercell in the beginning was optimised in the same way as for Interface I. First, rigid grain shifts perpendicular to the interface were performed, always starting from the geometric construction and followed by structural relaxation of all atomic positions at each step. Surprisingly the corresponding energies did not lie on one continuous energy-volume curve, but alternated between an "upper" and "lower" curve shown in figure 6.13a). The curves were completed by taking the atomic positions corresponding to one point in the curve as starting configuration for optimising the coordinates of the neighbouring point[3].

It is possible to proceed continuously from a point in the upper graph to the corresponding point in the lower graph by setting up supercells in which the atomic positions are got by linear combinations of the two cases and by increasing the weight of the coordinates corresponding to the lower curve continuously from zero to one. This is demonstrated in figure 6.13b) for the volume corresponding to the minimum of the upper curve. The flat slope at the start of the "mixing" curve shows that the upper graph is indeed a metastable state in which the structure by chance got trapped.

[3]In detail, the procedure is the following: Usually, always to start with a well-defined structure for each point of curves like those shown in figure 6.13a), the geometrically constructed supercell is cut into two halves at the grain boundary and the two grains are rigidly pulled apart (while the grain boundary stays in place), as indicated in figure 5.7. Then the atomic positions are relaxed. In this special case however, to complete the curves in figure 6.13a) the fully relaxed supercell of a given point was taken, cut into two halves and expanded to the volume of the neighbouring point. Then the atomic positions were relaxed again.

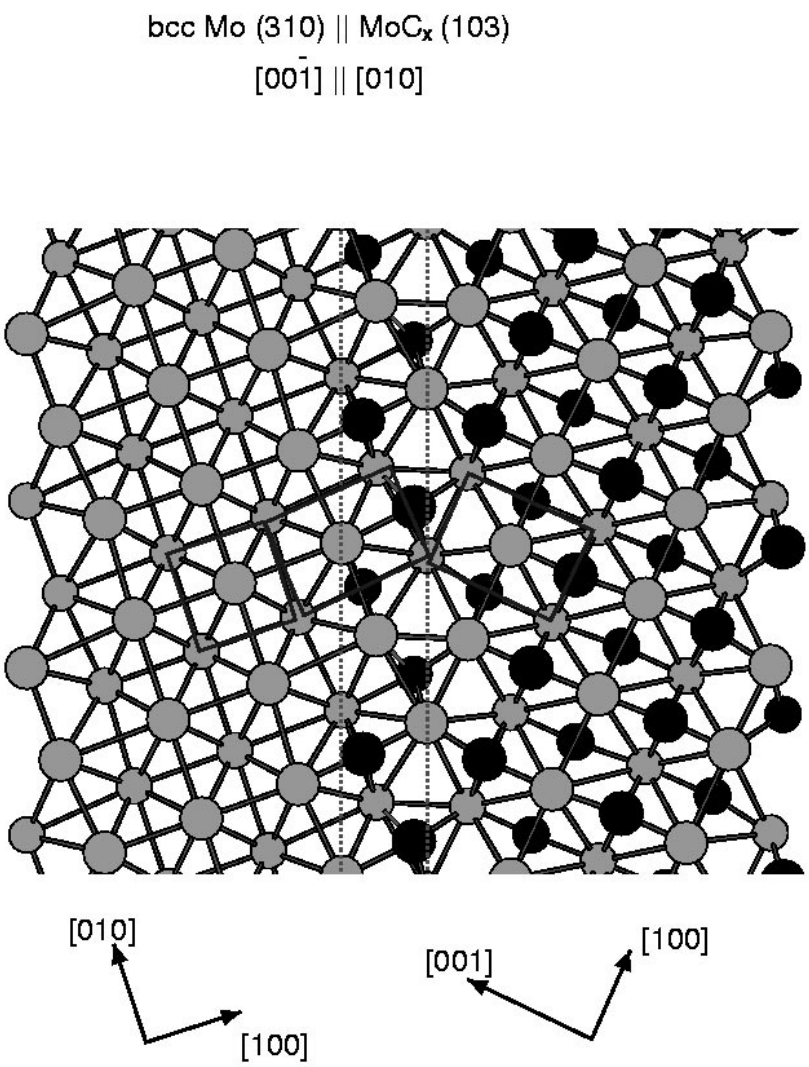


Figure 6.12: Interface I after relaxing the atomic positions at point $*$ in figure 6.10. The large atoms are positioned in the paper plane, the small atoms are the next layer in [001] direction. Mo atoms are gray, C atoms black. The Mo-MoC interface moved into the Mo grain. Therefore a new grain boundary occurs inside the MoC grain.

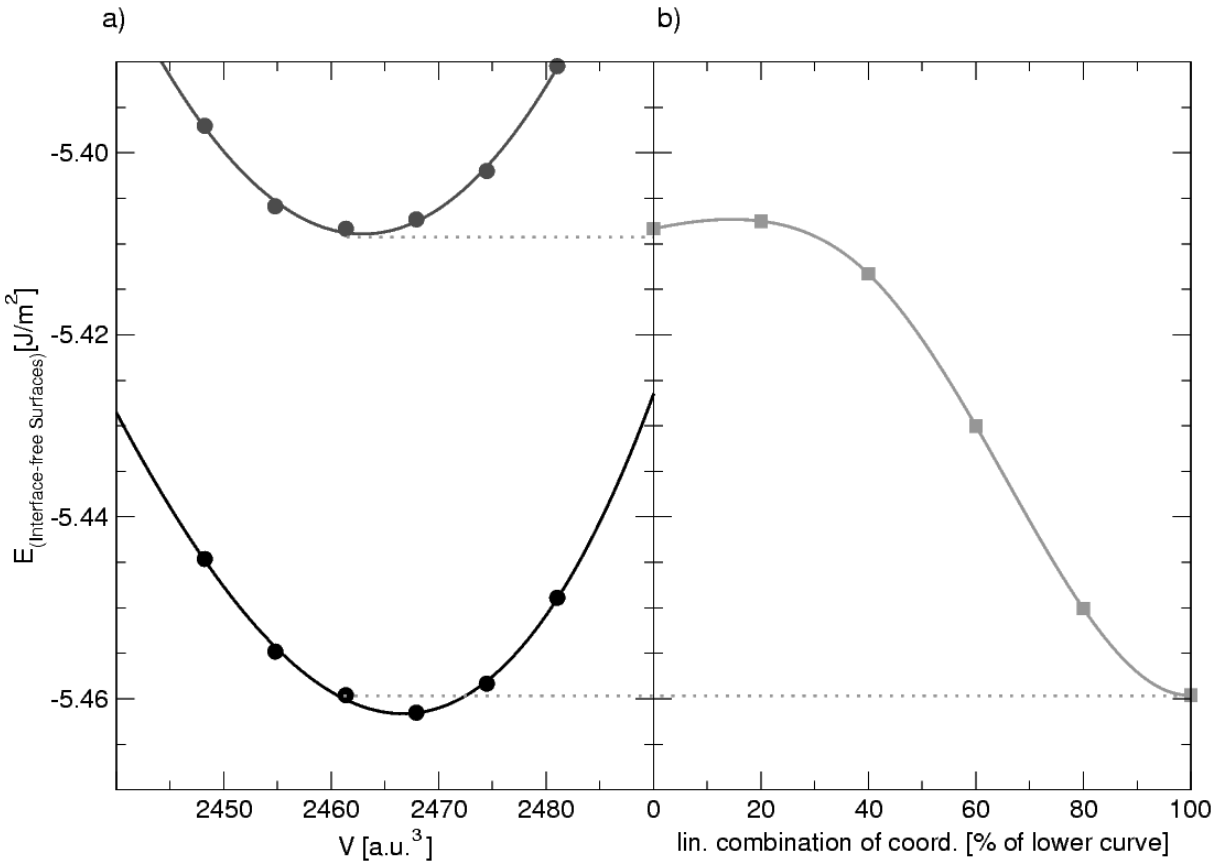


Figure 6.13: Interface II: Optimising the structure. Shown is the energy difference between the interface and the corresponding free surfaces a) for volume expansion along [310] with relaxation of the atomic positions, b) for the transition between the two configurations of a) the grains.

Figure 6.14 shows the relaxed structure at the minimum of the "lower" curve in 6.13a) laid over the atomic positions of the corresponding point of the "upper" curve. The arrows indicate the shifts leading from one configuration to the other. Due to the symmetry imposed by the periodic boundary conditions the atoms marked with "X" are fixed in their positions. It becomes visible that the Mo layer next to the respective interface is shifted towards it, parallel to the MoC c-axis at both sides of the precipitate. By the choice of the precipitate thickness as it was made, these Mo atoms on the left and on the right side of the MoC grain do not belong to the same [001]-column of atoms with respect to the MoC lattice, but to alternating ones. Thus the structure gets sheared in an alternating fashion parallel to the MoC $c$-axis. As the atoms in the central layer of the

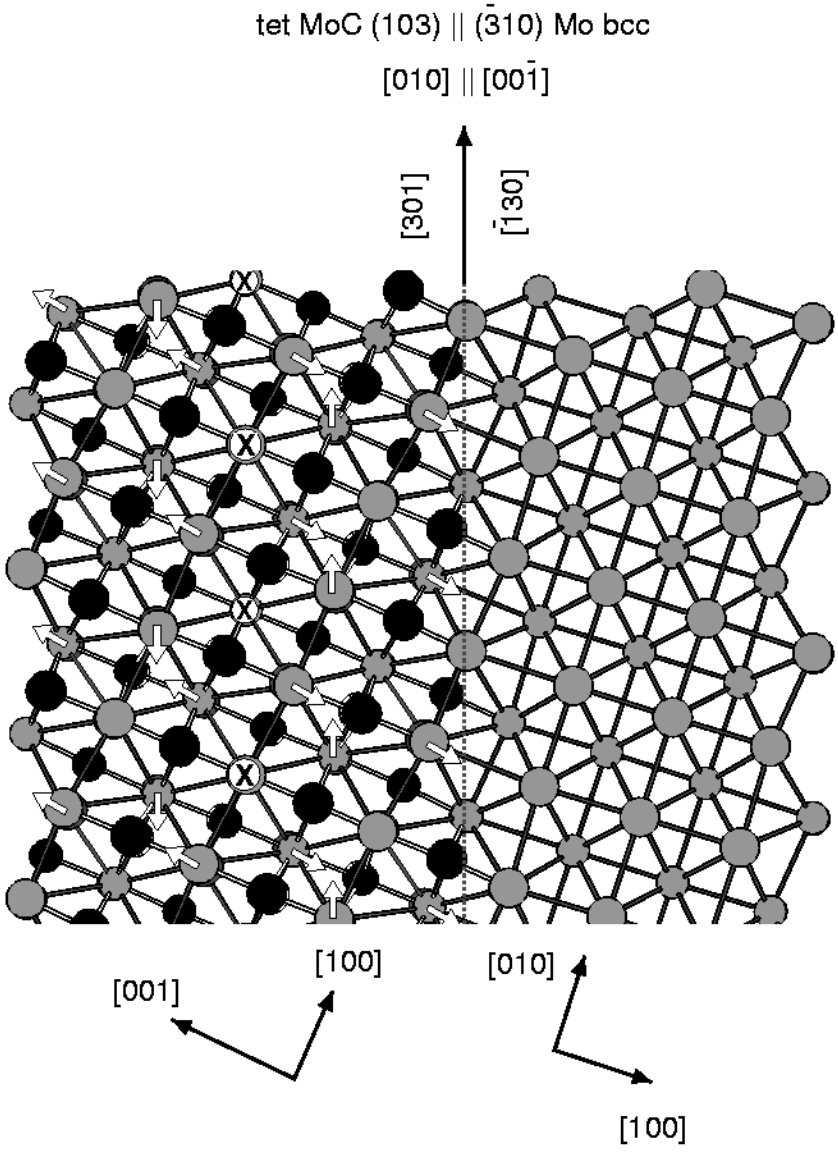


Figure 6.14: Interface II: Overlay of the atomic coordinates of the "upper" and "lower" energy curve in 6.13a) at the volume corresponding to the minimum of the lower curve. The grey and black atoms mark the Mo respective C coordinates in the more favourable configuration. They are laid over those of the less favourable configuration, marked by white and dark grey circles respectively. The large atoms are positioned in the paper plane, the small atoms are the next layer in [001] direction (with respect to the Mo lattice). The arrows indicate the shifts leading from one configuration to the other. Due to the symmetry imposed by the periodic boundary conditions the atoms marked with "X" are fixed in their positions. There is no shift of atoms along the [001]-direction.

precipitate are fixed in their positions, the relative shift of the [001] atomic columns locally is leading to a rotation of the structure around the immobile atoms.
In cases of a precipitate thinner or thicker by two atomic layers these shifts probably had lead to a simple expansion of the MoC grain parallel to [001], as the carbide had been terminated such that the Mo atoms forming the metal layer close to the interface would have been "on top" of each other, i.e. belonging to the same [001]-column of atoms. It is very likely that for such a supercell no comparable metastable configuration exists, as there is no reason why the atoms should not relax homogeneously to their equilibrium distances after pulling the grains apart in a rigid way. This is a point which should be considered in future supercell constructions.
It is interesting to note that the Mo grain remained completely unaffected. As we can see from figure 6.14 the positions corresponding to the upper respective lower curve in figure 6.13a) are exactly the same. This is something we already observed when studying the initial growth of the precipitate: As long as the Mo grain does not contain carbon it behaves extremely stiff.
The procedure of probing the possible translation states of the interface was continued. Rigid grain shifts along the [001] and the $[\bar{1}30]$ directions of the bcc Mo were performed starting from the configuration corresponding to the minimum in the lower curve of figure 6.13a). The resulting energy vs. volume curves are shown in figure 6.15, where again the total energy of the supercell is given with respect to that of the corresponding free surfaces. The atomic positions were relaxed after shifting the grains by 10% respective 40% of $a_0$ along [001] and in both cases the initial structure was obtained again. In contrast to the situation at Interface I, displacements of the grains along [001] do not push C atoms across the grain boundary. This supports our interpretation of what we found at Interface I, because with the relative orientations of Mo and MoC in the configuration of Interface II C atoms wouldn't find more free space in the Mo grain and thus have no motivation to move across the interface.
Relaxation of the atomic positions also has been allowed after shifting the grains by $0.1a_0$ along $[\bar{1}30]$, resulting again in the initial structure. Hence it was confirmed again that the structure is not trapped in any configuration sheared or rotated relatively to the most favourable one. The favoured structure of Interface II therefore is the one shown in figure 6.14 (by the light grey Mo and black C atoms).

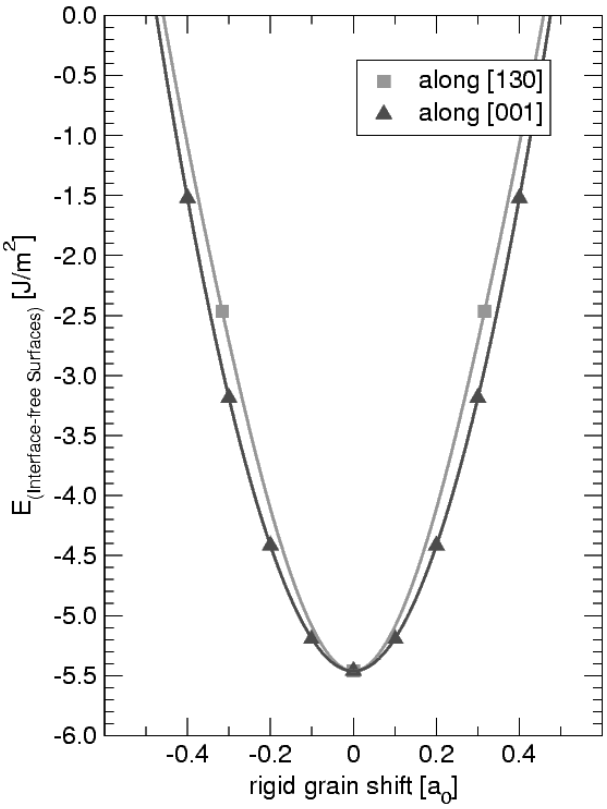


Figure 6.15: Interface II: Optimising the structure. Shown is the energy difference between the interface and the corresponding free surfaces for rigid grain shifts along [001] and [-130] (directions refer to the Mo grain).

### 6.3.4 Work of Separation

To have an estimation of the cohesive properties of the precipitate the work of separation $W_{sep}$ is calculated for the two interfaces. The work of separation is defined as the energy difference per interface area between the supercell of the interface and the two corresponding ones of the free surfaces, with all atomic positions being relaxed, but the cell parameters kept fixed [36]. In case of the MoC surface a full relaxation would include a relaxation of the volume to the equilibrium value of 282.93 Bohr$^3$ per body-centred tetragonal MoC unit cell. This part of the elastic contribution $\Delta E_{el}$ to $W_{sep}$ is estimated by calculating the energy difference between the equilibrium volume and the compressed volume per unit cell and multiplying it with the number of unit cells in the carbide film. The energy vs. volume of tetragonal MoC, as calculated in [65], is shown in figure 6.16. The point corre-

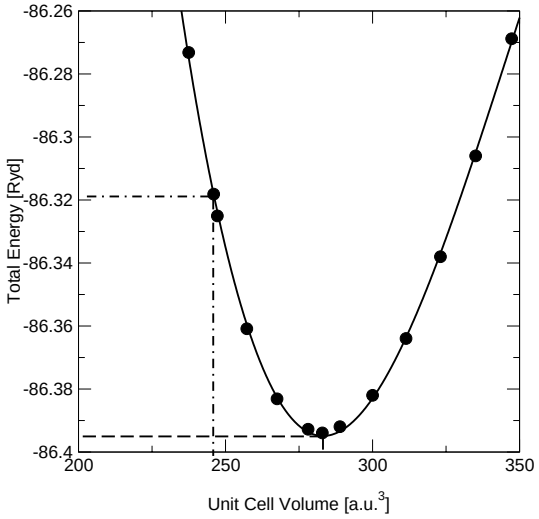


Figure 6.16: Total energy vs. volume of the body centred tetragonal MoC unit cell at a c/a ratio of 1.389. The cell is contains two Mo and C atoms respectively. The dashed lines indicate the energy difference of 0.076 Ryd between the equilibrium volume of 282.93 Bohr$^3$ and the compressed volume of the intergranular precipitate, 245.95 Bohr$^3$.

sponding to the volume of one unit cell in the intergranular film, 245.95 Bohr$^3$ was added supplementary. The energy difference between the two volumina is 0.076 Ryd, this makes $\Delta E_{el,MoC} = 5{\cdot}0.076$ Ryd = 0.380 Ryd for the supercell.
For Interface I the (local) minimum in figure 6.10b) is assumed to represent the equilibrium structure. The energy of the structure after relaxation from point $*$ is of course lower, but in this case the Mo-MoC interface is not well defined and the total energy of the supercell contains contributions from two kinds of interfaces, the Mo-MoC phase boundary and the MoC grain boundary. These contributions cannot be sorted out easily.
For Interface II the minimum of the curves in figure 6.15 represents the equilibrium configuration. The work of separation has been calculated after

$$W_{sep,X} = \frac{E^{tot}_{interfaceX} - \Delta E^{tot}_{el,MoC} - (E^{tot}_{FS,Mo} + E^{tot}_{FS,MoC})}{2A} \tag{6.3}$$

with the energies $E^{tot}_{FS,MoC}$ and $E^{tot}_{FS,Mo}$ given in table 6.1 for case A and the energies of the supercells containing Interface I and II , $E^{tot}_{interfaceI}$ =-751.059 Ryd and $E^{tot}_{interfaceII}$ = -751.037 Ryd, respectively. Using the data calculated for the bonding energy differences in chapter 5.5.4 we can also give the work of separation for the pure $\Sigma 5$ STGB in its two

| | Mo\|Mo I | Mo\|Mo II | Mo\|MoC I | Mo\|MoC II | Mo\|$Mo_xC$ I | Mo\|$Mo_xC$ II |
|---|---|---|---|---|---|---|
| $W_{sep}\left[\frac{J}{m^2}\right]$ | 5.788 | 5.893 | 2.852 | 2.698 | 5.474 | 5.320 |

Table 6.2: Work of separation for the pure Σ5 STGB in Mo in configurations I and II (Mo|Mo I, Mo|Mo II), for the two model Mo-MoC interfaces without taking into account any corrections (Mo|MoC I, Mo|MoC II) and for the two model Mo-MoC interfaces after taking into account corrections due to the compression of the MoC cell as well as the higher C content compared to the experimental observations (Mo|$Mo_xC$ I, Mo|$Mo_xC$)

translation states, configuration I and II. The results are given in table 6.2 According to the work of separation Interface I is more favourable than Interface II. The reason is again the gain in elastic energy for C at the grain boundary. In both cases the work of separation is reduced by approximately a factor of two when comparing it to the work of separation of the pure Mo grain boundary, no matter whether the mirror-symmetric configuration I or the non-mirror-symmetric configuration II is taken as a reference.

Not discussed so far is the influence of the high C content in the model on the interpretation of the results. We do not expect a change in the order of the two interfaces with respect to their energies, as the larger amount of free space at Interface I will remain attractive to C in a $Mo_2C$ phase as well. How the mechanical properties of the precipitate changes however, we do not know so far. In the next chapter, which is dealing with the properties of molybdenum carbides of different symmetry and stoichiometry, we will see that the bulk modulus of molybdenum carbides is *increasing* with increasing carbon content. This means that by choosing MoC instead of $MoC_x$ with $x \approx 0.4$ the elastic contribution in the work of separation was overestimated considerably. This approximation can be refined by calculating the energy difference between the equilibrium volume of fcc $Mo_2C$ and the volume of a unit cell in the carbide grain. This energy difference is smaller not only due to the smaller bulk modulus, but also because the equilibrium volume of fcc $Mo_2C$ is only 255.92 $Bohr^3$ compared to 282.93 $Bohr^3$ of tetragonal (fcc) MoC (see chapter 7), so the compression only amounts to 4%. Thus, with a $Mo_2C$ grain one would get an energy difference for the supercell of about 0.020 Ryd instead of 0.379 Ryd for the MoC grain, i.e. one order of magnitude less. With this new $\Delta E_{el}$ the work of separation for the two interfaces become

$$W_{sep,I} = 5.474 \quad \frac{J}{m^2}$$

and

$$W_{sep,II} = 5.320 \quad \frac{J}{m^2} \qquad .$$

These values are comparable to the work of separation of the pure molybdenum grain boundary given in table 6.2 for configurations I and Ⅱ.

### 6.3.5 Summary

Inspired by the investigations of Pénisson et al. [94] the growth of a $MoC_x$ precipitate at the Σ5 STGB in Mo was modelled by starting with one monolayer of C atoms segregated at the interface and subsequently adding one and two more layers respectively. Relaxing the atomic positions showed that a tetragonal $MoC_x$ precipitate grows with its c-axis meeting the grain boundary at an angle of about 108°. Thus the periodicity of the grain boundary is conserved. One layer of C at each side of the interface turned out to be slightly more favourable than two layers in the same grain, as C finds more free space close to the grain boundary. This doesn't mean however, that the precipitate would grow symmetrically with respect to the grain boundary. With the small model the direction of the growth couldn't be determined, this is a task for future semi-empirical model investigations. However, the HRTEM pictures of Pénisson et al. [94] indicate an asymmetrical growth into one grain. This growth of the precipitate leads to two new Mo-$MoC_x$ interfaces. These were modelled by replacing one of the Mo grains in the supercell by a grain of stoichiometric bct MoC. To cope with the lattice mismatch the MoC was compressed by 13% with respect to its equilibrium volume. This leads to a reduction of the work of separation of the Mo-MoC interfaces. Interface I, the interface where the crystal planes of the Mo sublattice meet at an angle of about 135°, is more favourable by an amount of 154 $\frac{mJ}{m^2}$ than Interface Ⅱ, where the Mo sublattice continues under only a small deviation of 6°. The reason is that at Interface I C atoms have more free space to relax. This is also true for the first layer of MoC next to Interface I, making a displacement of C across the boundary from MoC into Mo favourable. This process is a possible explanation for the apparently not very sharp interfaces Pénisson et al. observed by HRTEM. At Interface Ⅱ a continuous increase of the tetragonal distortion of the bcc Mo lattice was found. Thus, on a HRTEM picture where only Mo but not C is visible this interface is not atomically abrupt as well.
Because of the lattice mismatch, the Mo-MoC interfaces act as traps for misfit-dislocations, as indeed observed by Pénisson et al. . With respect to the macroscopic properties this means that a tetragonal MoC precipitate at the Σ5 STGB in Mo, with the orientation relationships as modelled, will to a certain extend lead to a stiffening of the metal. However, the MoC phase itself can be deformed rather easily, as was seen (accidentally) for the case of Interface Ⅱ. Indeed structural phase transformations from a tetragonal to a hexagonal

Mo sublattice have been reported by Pénisson et al. [94] as well as Lepski et al. [73, 74]. Furthermore, by choosing the stoichiometry MoC instead of $MoC_x$ with $x \approx 0.4$ the bulk modulus of the precipitate was still overestimated, as will be seen in chapter 7. As in all the calculations grains of pure Mo behaved extremely stiff, this leads to the interesting conclusion that small amounts of C lead to $MoC_x$ phases which are more easily deformable than the pure host lattice, but increasing the C content increases again the stiffness of the material.
To complete this study we investigate the unit cells of the corresponding bulk phases, which is done in the next chapter.

# Chapter 7

# Molybdenum Carbides

## 7.1 Introduction

In this chapter the results of ab-initio calculations for molybdenum carbides of different stoichiometry and crystal structures will be presented. Besides the calculation of energies of formations and covalent bond energies, a wide range of electronic structure data such as densities of states, overlap populations and valence electron densities were investigated. The collected data set will serve several purposes: First of all we want to understand the material properties of the molybdenum carbides. This is not only for completeness of our investigations of the precipitation of $MoC_x$ at the $\Sigma 5$ STGB in Mo presented in chapter 6, but also because the bulk phases have many attractive material properties of their own. Among those are high hardness, high melting point and high catalytic activity, combined with comparatively simple crystal structures, making molybdenum carbides an object of strong interest in materials science. From a physicist's point of view it is important to investigate the relationship between electronic structure and crystal symmetry to identify the principles that determine the relative stabilities of the different crystalline phases. Here simple physical models are useful to accomplish our understanding of bonding in crystals. Vice versa, a comparison of our ab-initio data to the results of semi-empirical models serves to evaluate the predictive power of different approaches for this material system. Furthermore the ab-initio data serve as a reference for semi-empirical modelling of interatomic interactions, specifically for tight-binding models of Mo-C interactions. Thus, on the basis of the ab-initio data, the possibilities of fitting the parameters of the environment dependent tight-binding model [116, 48, 47] introduced in chapter 4.2 are going to be discussed, with the aim of using it in the future to simulate a large variety of complex processes like

segregation and precipitation at grain boundaries.

The characteristic features of molybdenum carbides and semi-carbides with simple cubic (sc), body-centred cubic (bcc), face-centred cubic (fcc), hexagonal primitive (hpr) and hexagonal close-packed (hcp) molybdenum sublattices were studied. The different structures are shown in figure 7.1, labelled according to the Mo sublattice. The names in brackets are the conventional names of the structures of MoC. From these we get the $Mo_2C$ structures simply by occupying only half of the C sites such that the symmetry is conserved. Tables 7.1a) and b) list the names and the geometric characteristics of the different structures. The fcc MoC structure with C occupying octahedral sites of the Mo lattice (NaCl) is obtained from the MoC bcc structure by expanding the c/a ratio of the cell from 1 to $\sqrt{2}$. This will play a role later on. The "AsNi" structure corresponds to the "NiAs" structure with the positions of the elements Mo and C interchanged, i.e., C occupying the sites of a hcp sublattice inside hpr Mo.

a)

| MoC structure | Mo sublattice | C sublattice | interstitial site of C in Mo | interstitial site of Mo in C | nn coord. |
|---|---|---|---|---|---|
| bcc | bcc | bcc | octahedral | octahedral | 2+4 |
| CsCl | sc | sc | cubic | cubic | 8 |
| ZnS | fcc | fcc | tetrahedral | tetrahedral | 4 |
| NaCl | fcc | fcc | octahedral | octahedral | 6 |
| AsNi | hpr | hcp | trigonal prismatic | octahedral | 6 |
| NiAs | hcp | hpr | octahedral | trigonal prismatic | 6 |
| WC | hpr | hpr | trigonal prismatic | trigonal prismatic | 6 |

b)

| $Mo_2C$ structure | Mo sublattice | C sublattice | interstitial site of C in Mo | coordination number of C |
|---|---|---|---|---|
| bcc | bcc | sc | octahedral | 2+4 |
| $fcc_t$ | fcc | bcc | tetrahedral | 4 |
| sc | sc | bcc | cubic | 8 |
| hpr | hpr | hpr | trigonal prismatic | 6 |
| $fcc_o$ | fcc | st | octahedral | 6 |
| hcp | hcp | hpr | octahedral | 6 |

Table 7.1: Structure and geometry of the different a) mono-carbides and b) semi-carbides.

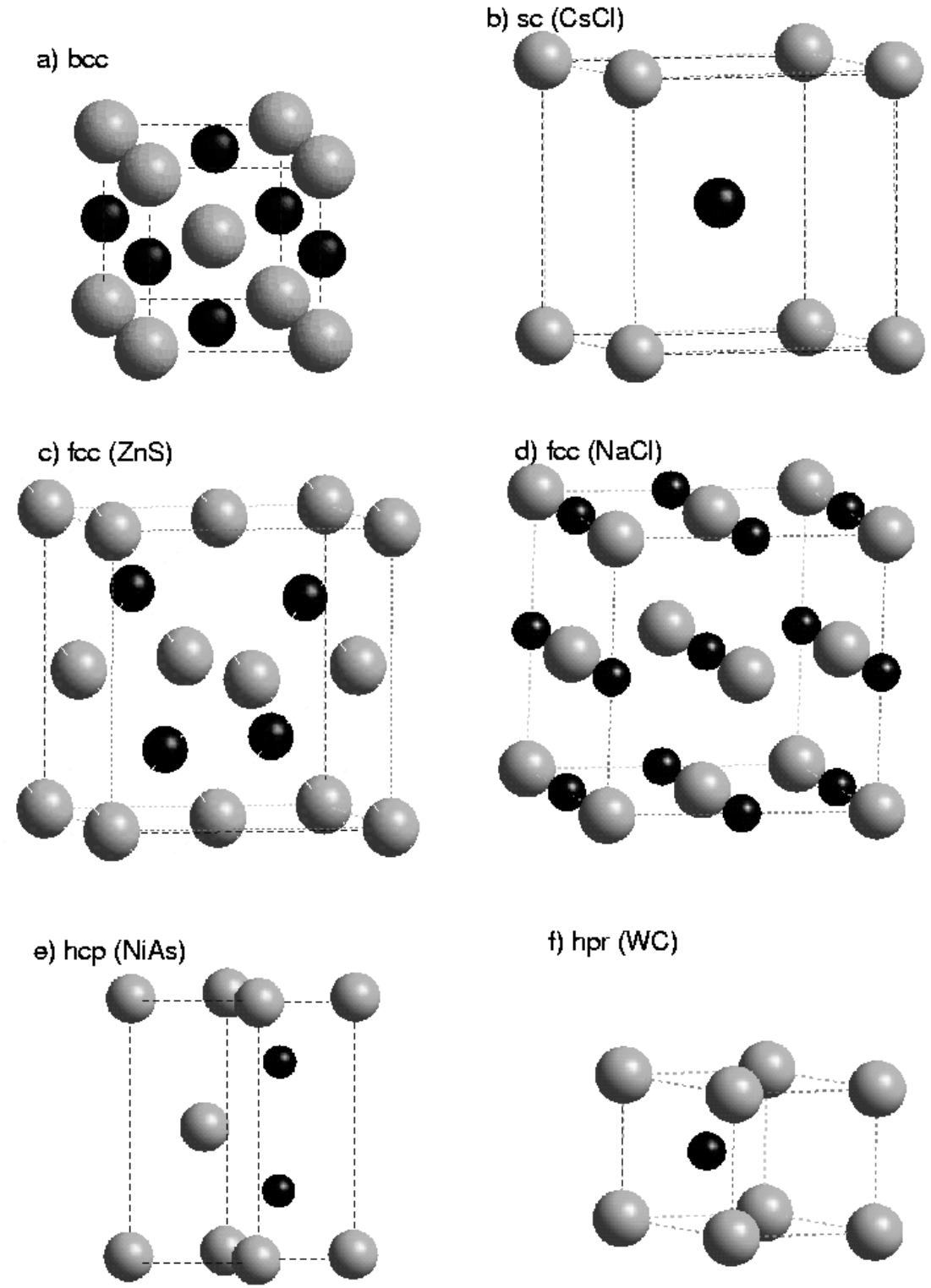


Figure 7.1: Different MoC structures labelled according to the Mo sublattice. The Mo atoms are represented by the big grey balls, the C atoms by the black ones. The names in brackets give the conventional name of the compound. The $Mo_2C$ structures are received by systematically occupying only half of the C sites.

## 7.2 Energies of Formation

As a first step the energies of formation of the structures listed in tables 7.1a) and b) were calculated as a function of the unit cell volumes. For this 8x8x8 Monkhorst-Pack k-point meshes were used for the Brillouin zone integration. As in the grain-boundary calculations, the electron wave functions and the electron density were represented in the mixed basis, consisting of plane waves up to an energy cutoff of 16 Ryd, and local orbitals with $d$ symmetry confined to Mo sites ($R_{loc}^{Mo}$=2.0 Bohr) and with $p$ symmetry for C sites ($r_{loc}^{C}$=1.8 Bohr).

As mentioned above, the NaCl structure can be derived from the bcc structure by varying the $c/a$ ratio. In the calculations the minimum energy occurred at $c/a = 1.39$ [65], which is not equal to $\sqrt{2}$ but close to, so in the following the structure is called "fcc" nevertheless. The energy-volume curves for MoC and $Mo_2C$ are shown in figures 7.2a) and b) respectively. The stable carbide phase is hpr MoC which has the tungsten-carbide structure, a hpr Mo lattice with the C atoms occupying the centre of trigonal Mo prisms and forming a hpr sublattice themselves. The most favourable semi-carbide is hcp $Mo_2C$, where a hpr C lattice is embedded in a hcp Mo lattice, such that C is octahedrally coordinated by Mo. These results are in agreement with experimental observations [77, 119, 112].

## 7.3 Bulk Moduli

From the curvature at the minimum of the energy-volume curves in figures 7.2a) and b) the bulk moduli $B_0$ of the different structures were determined,

$$B_0 = V_0 \left. \frac{\partial^2 E}{\partial V^2} \right|_{V_0} \quad , \tag{7.1}$$

with $V_0$ being the equilibrium volume. This was done by assuming the universal binding curve [111] as an equation of state. Table 7.2 lists the results for the most stable molybdenum carbides and semi-carbides.

The experimental values for hpr molybdenum carbide and tungsten carbide (WC) at room temperature, $B_0^{MoC}$= 385 GPa [82] and $B_0^{WC}$ = 331 GPa [9], show that the calculated values lie in the correct region. Although various measurements of the elastic properties of transition metal carbides have been made during the last decades (for a review see

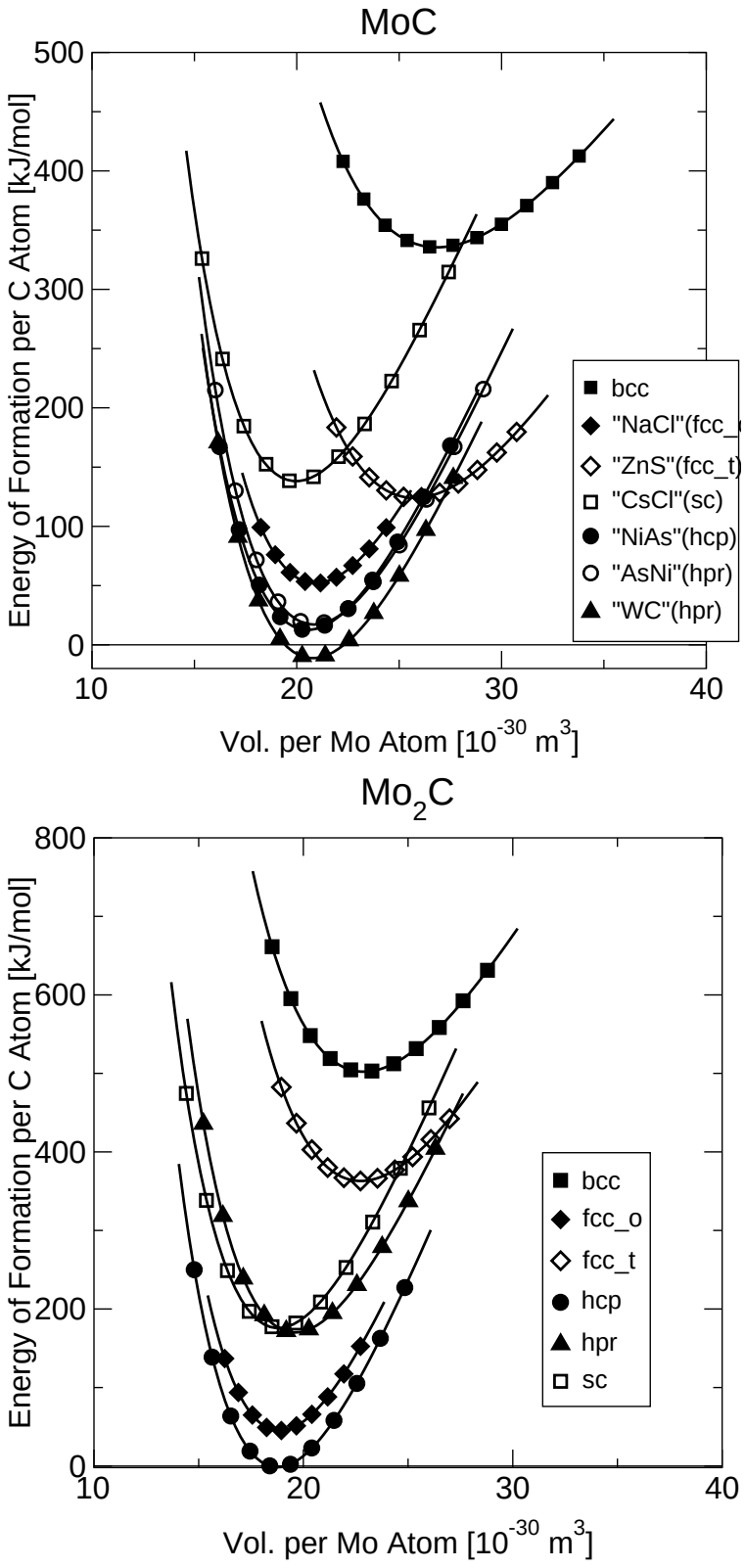


Figure 7.2: Energy of formation vs. volume for different structures of a) MoC b) $Mo_2C$.

| | hpr | hcp | fcc |
|---|---|---|---|
| MoC | **374** | 369 | 359 |
| $Mo_2C$ | 290 | **335** | 310 |

Table 7.2: Bulk moduli in GPa of different molybdenum carbide and semi-carbide phases. The structures are named according to their Mo sublattices. For the carbides as well as the semi-carbides the most favourable structure has the highest bulk modulus (bold).

e.g. ref. [69]), the collected data set is still hardly complete. One reason is the difficulty to prepare single-crystal bulk samples. Therefore, electronic structure calculations are a valuable alternative, even if the calculated values in the strict sense are valid for $T = 0$ K only.

Interestingly the bulk moduli are highest for the respective most favourable structures hpr MoC and hcp $Mo_2C$ and decrease with increasing energy of formation. While in MoC this leads to the order hpr - hcp - fcc of the molybdenum sublattices, in $Mo_2C$ it is hcp - fcc - hpr. In these series the interstitial sites of carbon are trigonal prismatic - octahedral - trigonal prismatic sites in MoC and octahedral - octahedral - trigonal prismatic sites in $Mo_2C$. Obviously there is no direct connection between the geometry of the metal sublattice or the interstitial sites occupied by carbon and the bulk modulus. So for the moment we can only say that the most favourable structures are also the most incompressible ones. Furthermore when comparing equivalent lattices with different carbon contents it also becomes obvious that carbon considerably increases the bulk modulus of the material.

In the following a detailed analysis of the electronic structure of the different carbide phases shall be performed to clarify the relationships between crystal structure and electronic structure.

## 7.4 Densities of States

### 7.4.1 Ab-initio DOS

Figure 7.3 shows the site and angular momentum projected DOS for MoC in the stable WC structure. We can see strong hybridisation between the carbon *s*- and *p*- and the molybdenum *d*-states, which indicates covalent bonds. The overlap between carbon and molybdenum states is so large that only a very small number of states close to the Fermi level (where the site projected DOS for carbon is more or less zero) are left for the pure Mo-Mo interaction. So compared to a pure metal sublattice the presence of C in the Mo

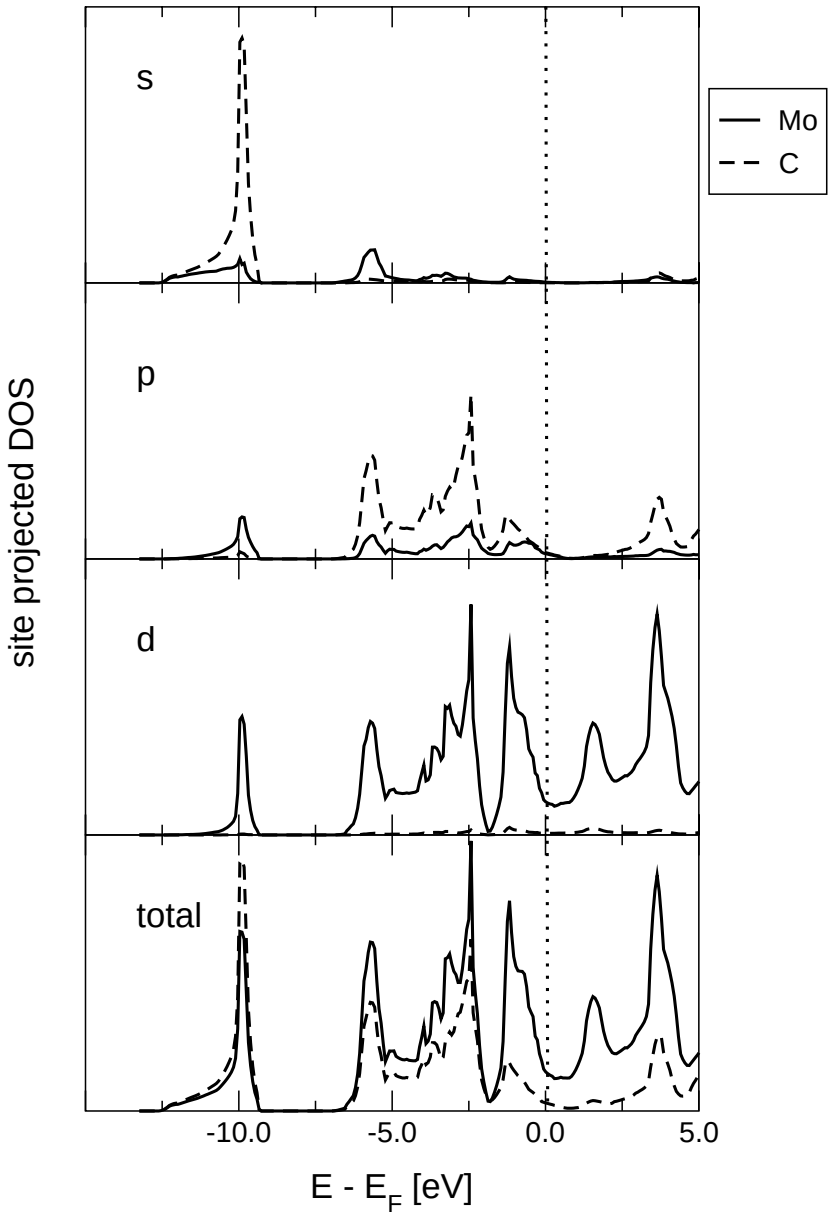


Figure 7.3: Site projected and angular momentum resolved DOS for MoC in the WC structure (hpr).

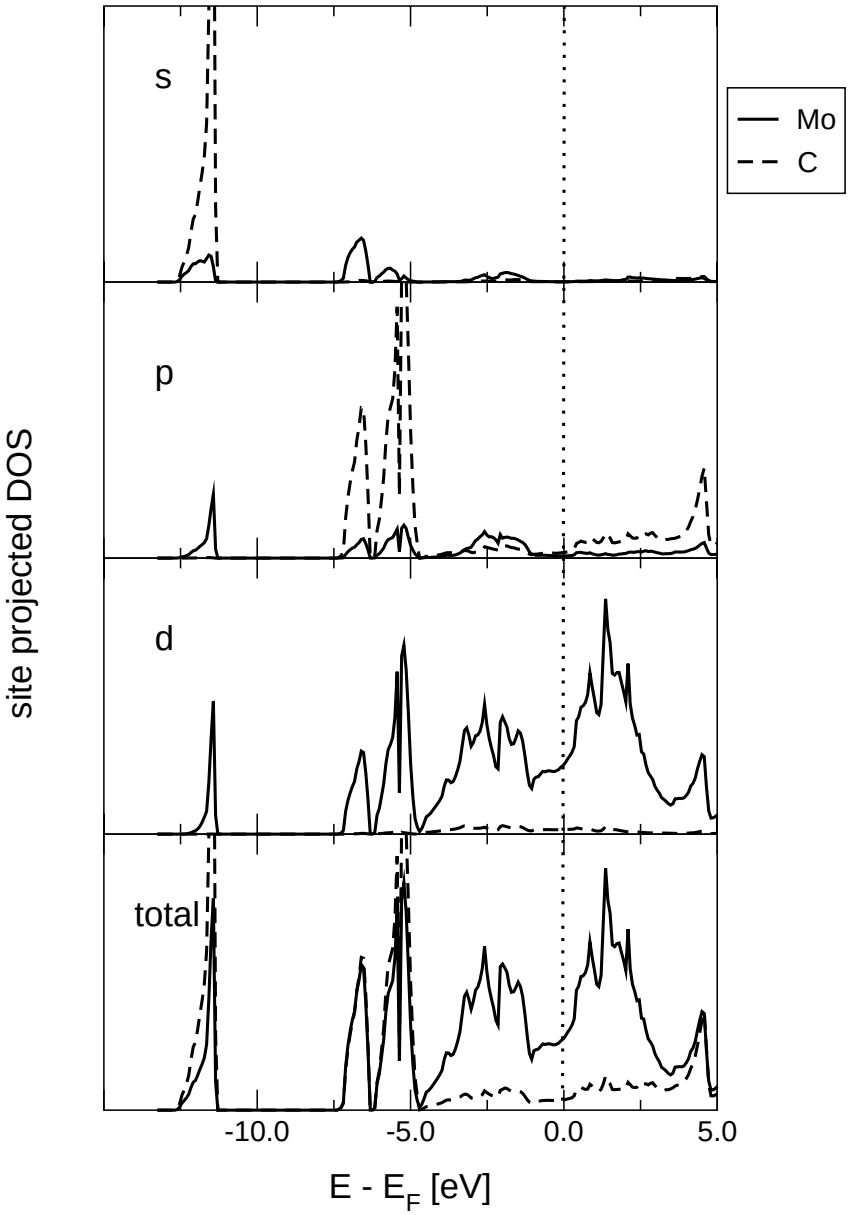


Figure 7.4: Site projected and angular momentum resolved DOS for hcp $Mo_2C$.

lattice weakens the Mo-Mo bonds. They are partly replaced by Mo-C bonds, thus MoC in the WC structure is stable, because the strong covalent-like Mo-C bonds overcompensate the degradation of the metal-metal bonds.
In figure 7.4 we see the site and angular momentum projected DOS for the most favourable semi-carbide, hcp $Mo_2C$. Again we observe hybridisation of C-$s$- and C-$p$- with Mo-$d$-states, but this time the carbon states are lying at the lower edge of the Mo-$d$-band. This situation is comparable to the case of C as an interstitial impurity at the Mo grain boundary, described in chapter 5. So we see how the relative positions of the bands depend on the C concentration: the less C is present the stronger are the Mo-Mo bonds, the hybridisation of states is weaker and the shift of the C states smaller. In $Mo_2C$ the metal-metal bonds are also weakened in comparison to a pure hcp Mo lattice, but they still represent a significant part of the overall bonding in the crystal.
These bonding mechanisms in molybdenum carbides have already been explored in [65]. They also occur in such a manner in the transition metal mono-borides, as shown by Mohn and Pettifor by means of ab-initio calculations [83]. A more quantitative evaluation of Mo-C and Mo-Mo bonds will be given in section 7.6, where the results of calculations of orbital and bond populations are presented.

Figure 7.5 shows the ab-initio calculated DOS for all the different MoC structures we investigated, ordered by their energies of formation, starting on top with the least favourable. We do not expect to see a trend in the total DOS "from bcc to hpr" that follows the one in the energies of formation, as the shape of the DOS will depend on the crystal structure. However, if we focus on the close packed structures NaCl, AsNi, NiAs and WC, where in all cases the nearest-neighbour coordination number is 6, we observe the following: a pseudo-gap in the region of the Mo-$d$ and C-$p$ states which basically marks the upper limit of the occupied C band is present in all structures. From fcc MoC (NaCl) to hpr MoC (WC) it is becoming more narrow and shifting closer to $E_F$. The part of the DOS that can be assigned to Mo-Mo $d$-$d$ interaction only is decreasing towards the Fermi level in the three hexagonal structures, while it is increasing in $fcc_o$ MoC. Thus in the hexagonal structures the metal-metal bonds are slightly lower in energy than in the cubic structure.
It is also interesting to note the similarities between the DOS of the WC and of the CsCl structure. Although the coordination numbers are different combining two rather open primitive lattices together is leading to the same main features in the DOS. Only that in the case of the CsCl structure more Mo-$d$ electrons are needed for Mo-C bonds,

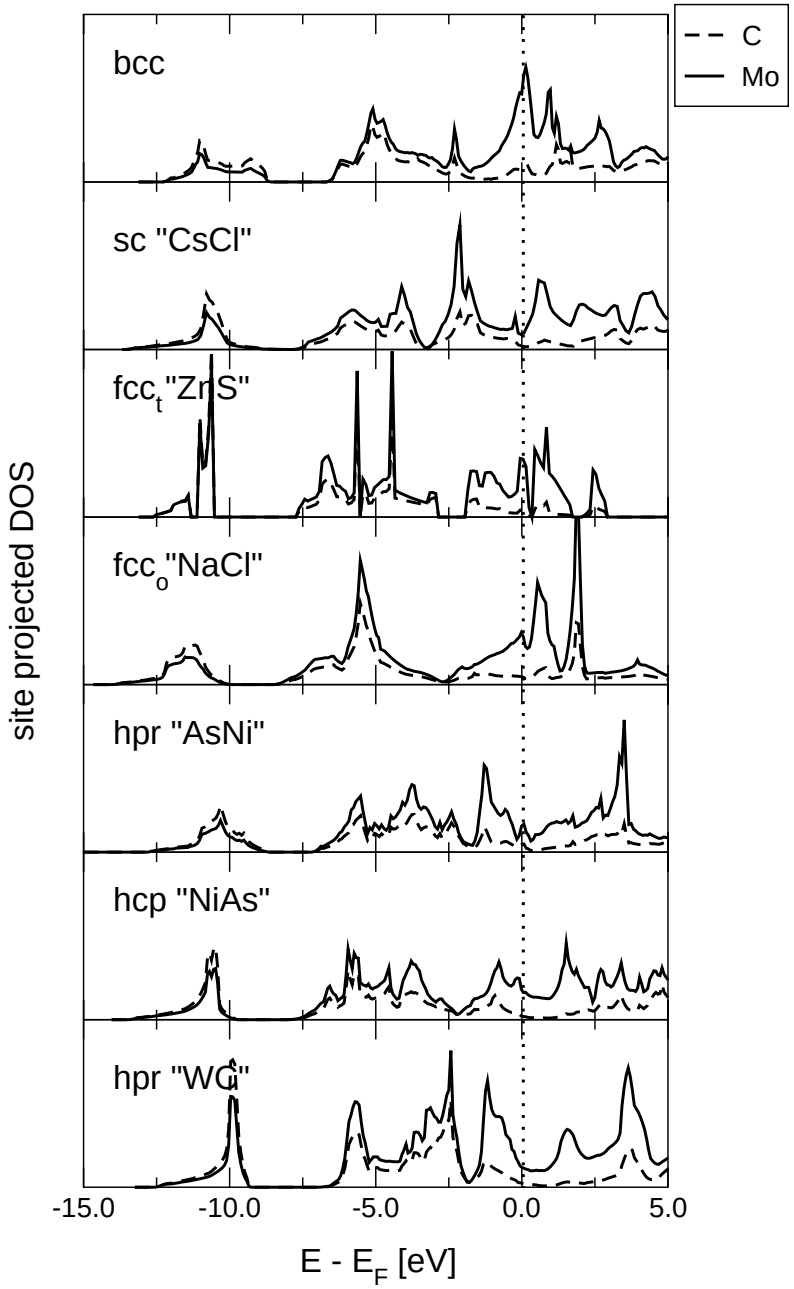


Figure 7.5: Site projected DOS for the different MoC structures.

leaving hardly anything for pure metal-metal bonds. This obviously makes the structure unfavourable.

We can record so far that compared to the pure metal in the molybdenum carbides the Mo-Mo bonds are to a large extend replaced by covalent-like Mo-C bonds. These strong bonds overcompensate the degradation of the metal-metal bonds, however it is favourable with respect to the energy if some states are left for Mo-Mo bonds only. The lower these states are lying in energy and the more clearly they are separated from the hybridised states, the more stable is the compound. The structure that fulfills these criteria best is the tungsten carbide structure, WC-MoC.

Figure 7.6 shows the site projected DOS for the semi-carbides, again ordered according to their energies of formation. As we already observed with hcp $Mo_2C$ in figure 7.4, compared to the mono-carbides more states are left for pure metal-metal bonding. But otherwise the conclusions drawn above also hold for the semi-carbides: the most favoured structure is the one in which the Mo-*d*-states involved in the Mo-Mo-bonding are well separated by the ones strongly hybridised with the C-*p*-states by a pseudo-gap. Furthermore the Mo DOS is decreasing towards a minimum when approaching the Fermi level, thus the Mo-Mo *d*-*d* bonds have a lower energy than in the other structures.

### 7.4.2 Tight-Binding DOS

In terms of a tight binding model the angular momentum projected DOS suggest a splitting of the band energy in C-*s*–Mo-*d*, C-*p*–Mo-*d* and Mo-*d*–Mo-*d* contributions. Pettifor and Podloucky used a *pd*-tight-binding model to predict and explain the structural stabilities of different *pd*-bonded AB compounds [102, 101, 98]. Their canonical TB model consists of *p*-orbitals at the atomic sites A and *d*-orbitals at the sites of species B. The volume of the different compounds is prepared such that the repulsive energy of all tested structures is equal. Then the structural energy difference is given solely by the band energy (*structural energy difference theorem* [98]). These band energies were calculated by Pettifor and Podloucky using the recursion method [55] up to the 20th moment. With this strategy they are able to reproduce structural trends in AB-structure maps [98, 97] and to explain them with arguments of atomic size (range of the *p*- and *d*-orbitals), energy level differences $\epsilon_{pd} = \mathrm{E}_p - \mathrm{E}_d$ and band filling degrees. In our case those arguments are not useful to explain trends in the energies of formation, because the named quantities are constant. Nevertheless we will have a look at the tight-binding DOS that Pettifor and Podloucky calculated for different structures and compare them to our ab-initio DOS of

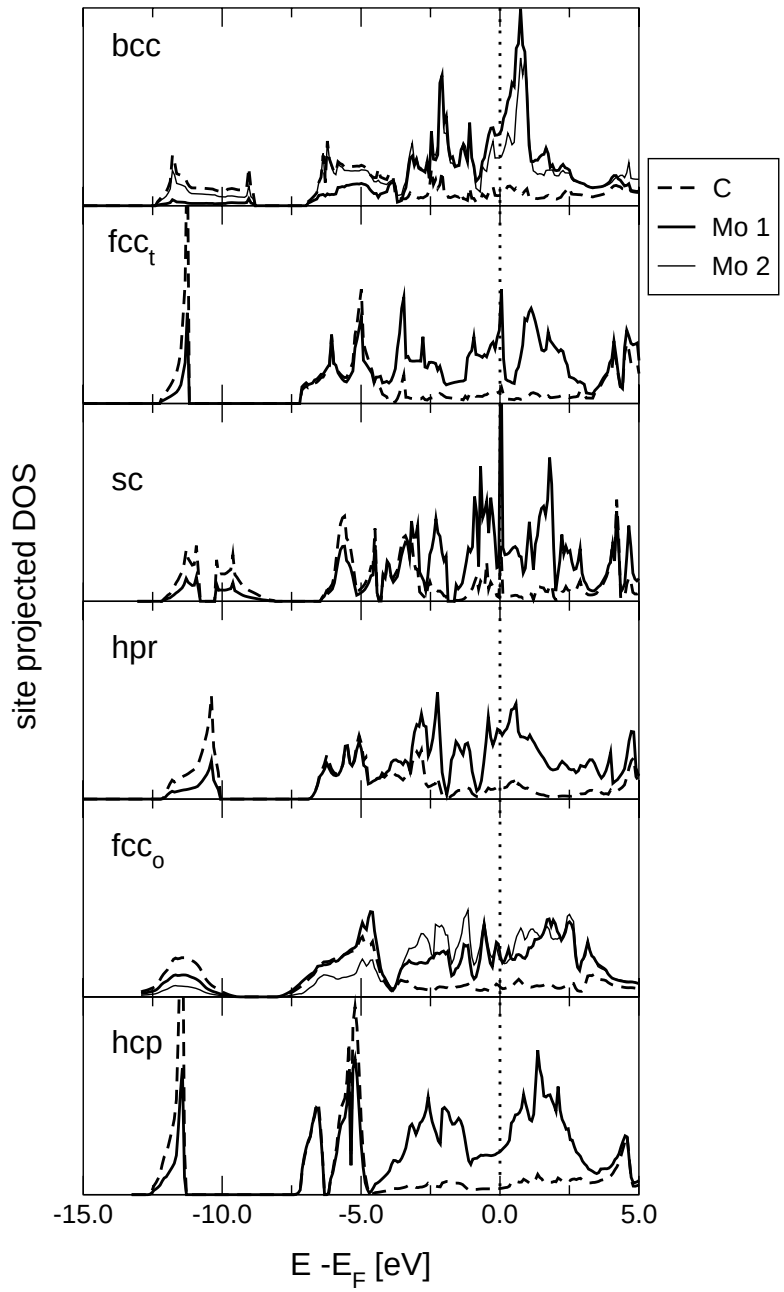


Figure 7.6: Site projected DOS for the different $Mo_2C$ structures.

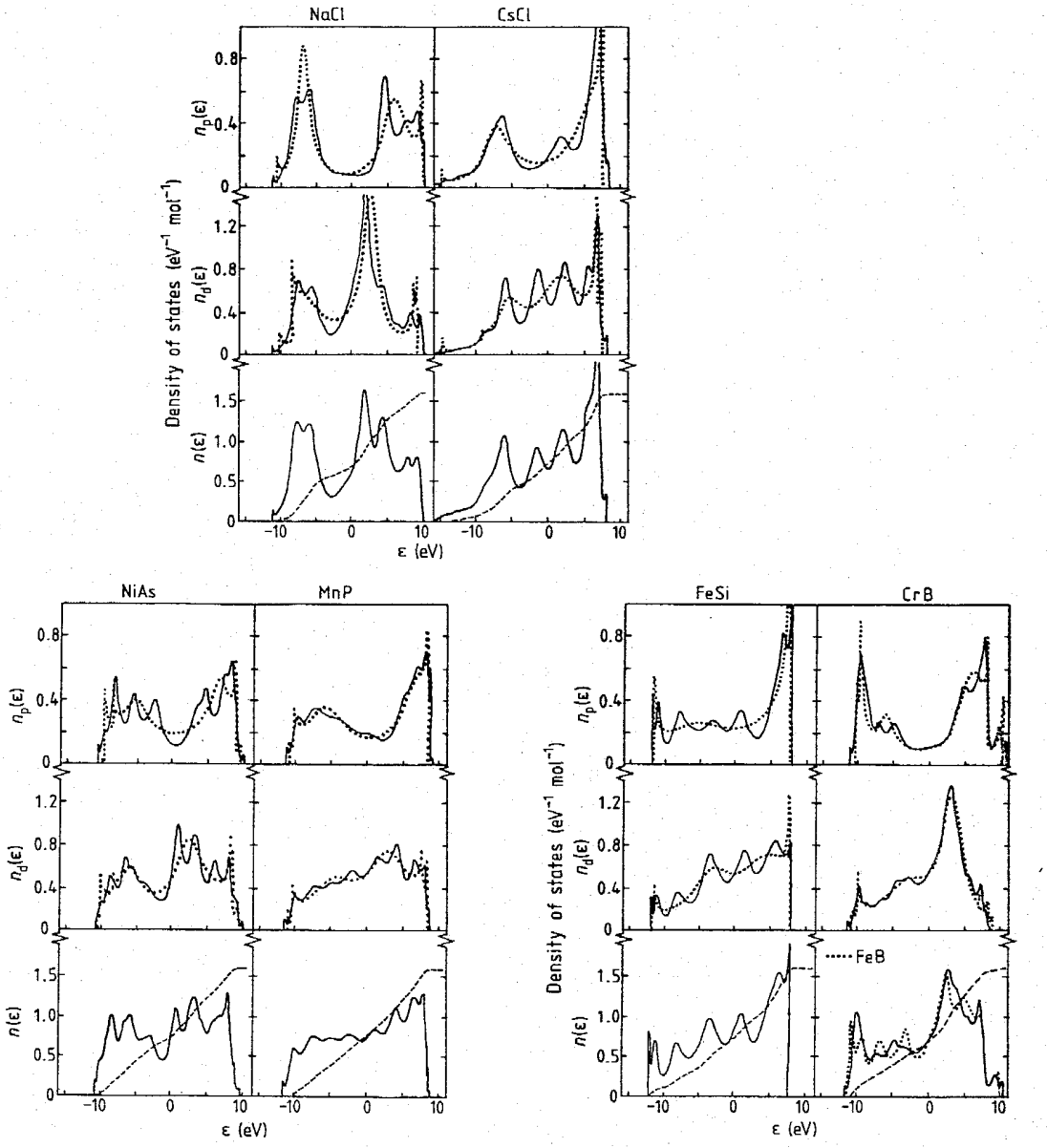


Figure 7.7: Tight-binding $p$, $d$ and total density of states for different crystal structures, for $\epsilon_{pd} = 0$ eV (taken from [102]).

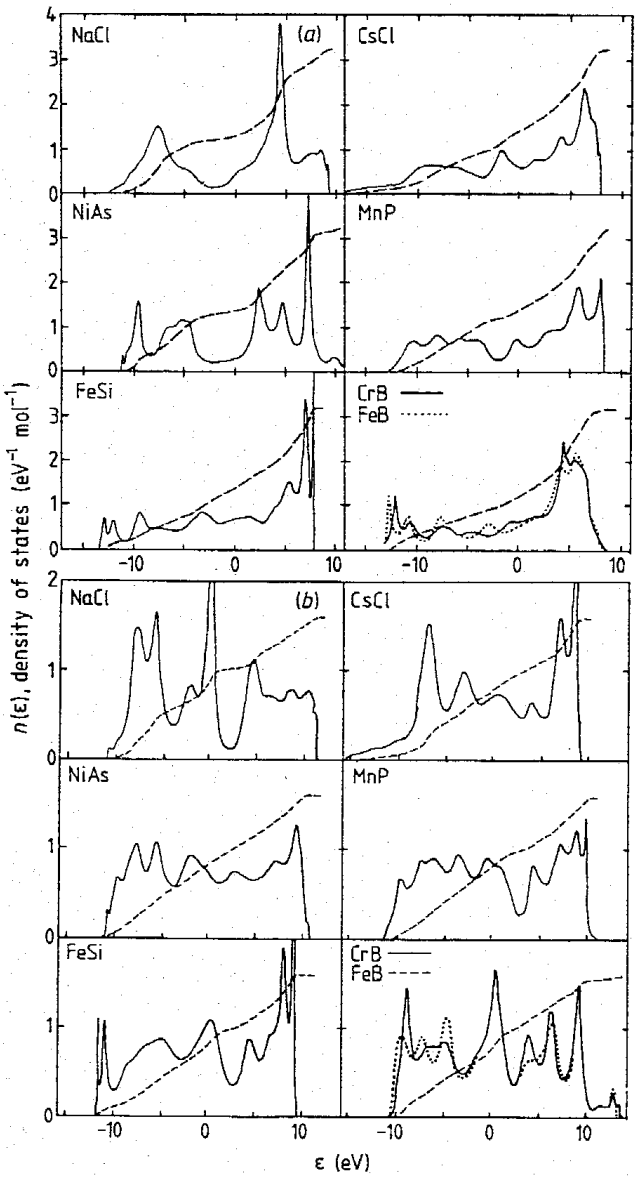


Figure 7.8: Tight-binding total density of states for different crystal structures, for $\epsilon_{pd}$ = -5 and +5 eV (taken from [102]).

the different molybdenum carbides. As such a comparatively simple TB model is able to distinguish between rather similar crystal structures, similarities in the ab-initio and TB-DOS, at least in the significant features, would be rather encouraging for our goal to describe the molybdenum-carbon interaction with a TB model and to get a set of reliable and transferable TB parameters.

Figures 7.7 and 7.8 show the TB-DOS calculated by Pettifor and Podloucky for $\epsilon_{pd} = 0$ and $\epsilon_{pd}$ = -5 and +5 eV respectively. They have chosen the structures NaCl, CsCl, NiAs, MnP, FeSi and CrB.

The atomic energy level separation $\epsilon_{pd}$ for Molybdenum and Carbon can be estimated from their first ionisation energies[1], which are 7.099 eV for Mo and 11.260 eV for C. So $\epsilon_{pd}^{MoC} =$ 4.161 eV and we expect similarities between the upper band (E $\geq$ -7 eV) in the ab-initio DOS of MoC in figure 7.5 and the TB-DOS for $\epsilon_{pd}$ = -5 eV in figure 7.8 in the upper panel. The common structures are the NaCl, CsCl and NiAs structure. The TB *pd*-bands are broader than those calculated ab-initio, because to get the correct cohesive energies they have to cover also those energy regions where also C-*s*– an Mo-*s*– and *p*–states are present in the ab-initio calculation. But apart from that we notice some common features of ab-initio and TB-DOS, if we ignore subtle details in the former. The similarities are most striking for the NaCl structure. Its DOS shows the characteristic broad minimum around -2.5 eV bordered by two large peaks at $\approx$ -5.5 (-7.5) and +4 eV (+4 eV) in the ab-initio (TB) DOS. In the ab-initio DOS the upper peak is splitted into two peaks.

The ab-initio DOS for the NiAs structure displays qualitatively the same shape in the region 0 eV $\geq$ E-$E_F$ $\geq$-7.5 eV as the TB-DOS between +5 $\geq$ E- $E_F$ $\geq$ -11 eV. The same is true for the ab-initio AsNi-DOS. Hence, it doesn't seem to be important which species occupies the hpr and which the hcp lattice. A comparison between the ab-initio DOS of the WC structure and the NiAs- and AsNi-DOS also confirms that the relevant features in the DOS are determined by the crystal symmetry, the former displays the same minima and peaks as the latter ones, only more pronounced.

In the case of CsCl the common features are more difficult to detect. A likely reason is the coordination number of 8 in the cubic lattice, which is rather high for a covalent system. This is difficult to reproduce with only *p* and *d* orbitals [113], therefore in this case the TB-model is less successful in reproducing the ab-initio DOS.

The comparisons undertaken above show that a simple semi-empirical model can reproduce

[1] As we have a relative concentration for Mo:C of 1:1 here it is sensible to use the first ionisation energies of the free atoms for both elements, instead of choosing the work function of Mo as a reference, as in chapter 5

some of the essential features in the electronic structure. One has to cut back with the description of highly-coordinated crystals and the differentiation of very alike structures as e.g. NiAs and AsNi. However, as our TB model is intended to include also C-*s*-, Mo-*s*-, and Mo-*p* orbitals and the parametrisation will be environment-dependent, we are optimistic to overcome most of these deficiencies.

## 7.5 Electron Densities

Figures 7.9 to 7.11 show the valence electron densities in the WC, NiAs and NaCl structures of MoC for different energy ranges between certain features or peaks in the DOS. They give an illustration of the influence of the crystal symmetry on the electron distribution in real space. In the hexagonal carbides (figs. 7.9 and 7.10) the hexagonal c-axis leads to a splitting of the $p$ electron density in one contribution parallel to the basal plane and one perpendicular to it. In contrast to this the electron distribution around the C atom has nearly spherical symmetry throughout all energy ranges in the NaCl structure (fig. 7.11), even in those ranges corresponding to the $p$-states (-8 to -3 and -3 to 0 eV).

Figure 7.12 shows the bonding electron densities for the three most stable mono-carbides. The bonding electron density is the difference between the complete valence electron density in the MoC compound and that of the respective carbon and molybdenum sublattices. In all three cases we see a density distribution that shows the characteristics of a covalent bond between carbon and molybdenum: the electrons are accumulated between two neighbouring atoms. But we also see indications of charge transfer from Mo to C, as the electron density at the Mo site decreased and that at the C site increased. Thus the major part of the bonding electron density is coming from molybdenum. This was already expected after the considerations of section 7.4. There we observed that the valence states of the C atom are lower in energy than the Mo $d$-band. Figure 7.13 shows the bonding electron densities for the three most stable semi-carbides. The bonding characteristics between Mo and C are the same as in MoC. In addition we see a slight increase of the bonding electron density in the vacant interstitial region between the molybdenum atoms. Thus the bonding between these atoms is enhanced. At first glance this seems to be a contradiction to what we found in section 7.4. There we stated that C weakens the metal-metal bonds. After looking at the bonding electron densities we can be more precise: If carbon is put at interstitial sites in a Mo lattice, it weakens the bond between the atoms surrounding this site or even replaces it by Mo-C bonds. However, at the same time bonding charge is transferred to

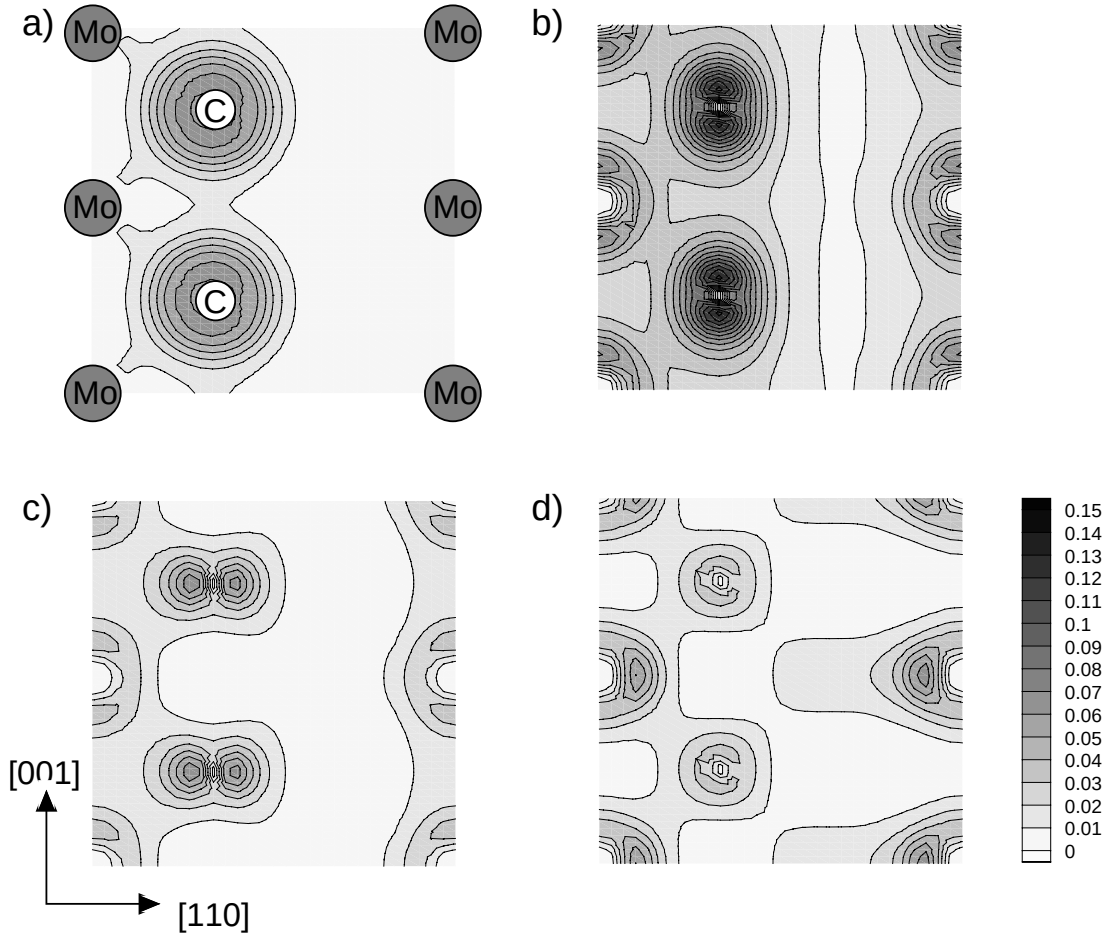


Figure 7.9: *Valence* electron density in [electron/Bohr$^3$] in **MoC hpr** corresponding to different energy levels: a)-12 to -9 eV, b)-6 to -2.8 eV, c)-2.8 to -1.5 eV, and d) -1.5 to 0 eV with respect to $E_F$.

vacant interstitial sites in the Mo lattice, which strengthens the Mo-Mo bonds around or across this site.

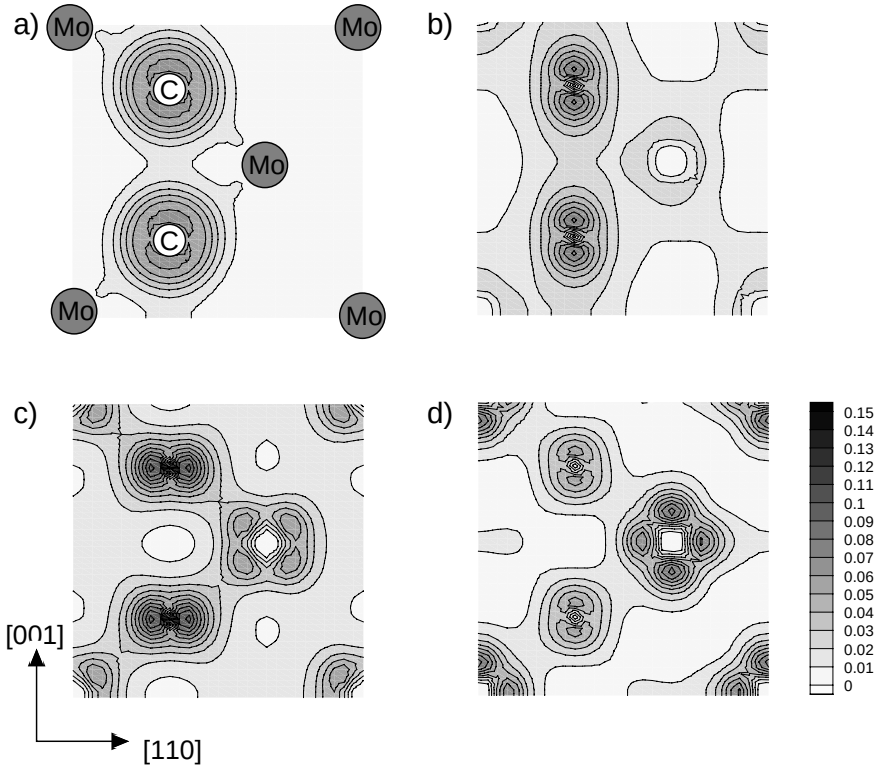


Figure 7.10: *Valence* electron density in [electron/Bohr$^3$] in **MoC hcp** corresponding to different energy levels: a)-13 to -10 eV, b)-7.5 to -5.2 eV, c)-5.2 to -2.2 eV, and d) -2.2 to 0 eV with respect to $E_F$.

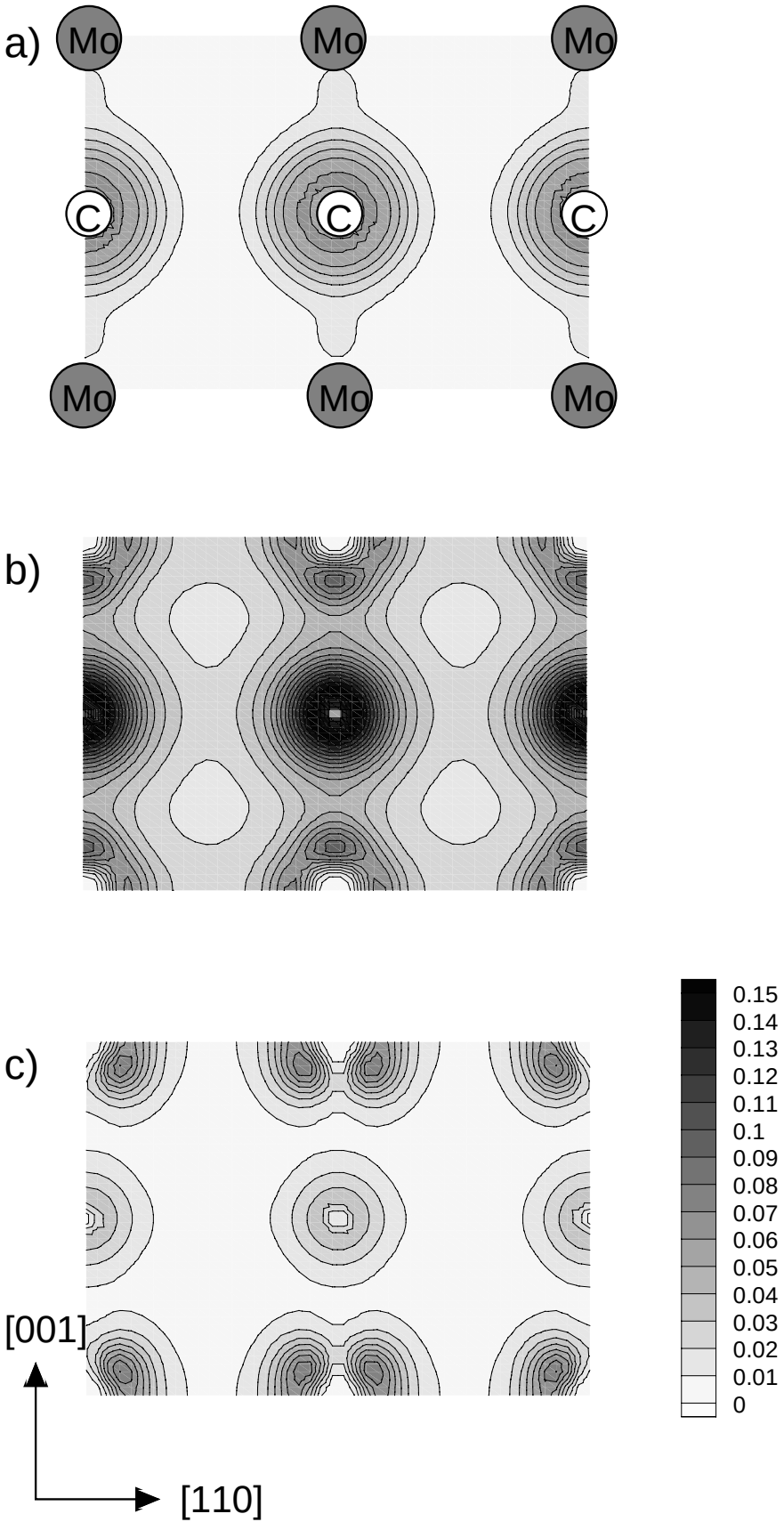


Figure 7.11: *Valence* electron density in [electron/Bohr$^3$] in **MoC fcc** corresponding to different energy levels: a)-14 to -11 eV, b)-8 to -3 eV, and c)-3 to 0 eV with respect to $E_F$.

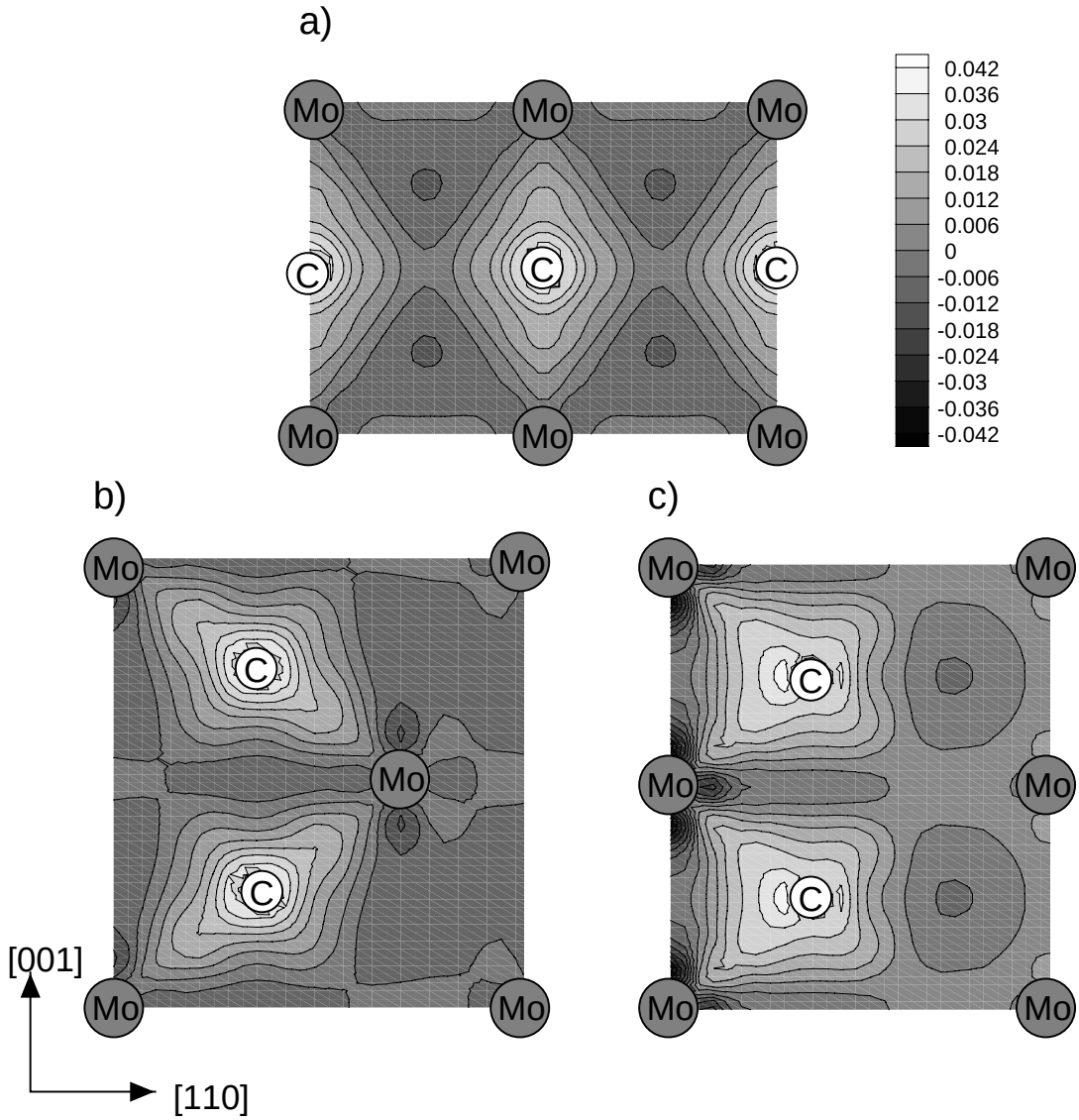


Figure 7.12: *Bonding* electron density in [electron/Bohr$^3$] in **MoC**: a) fcc, b) hcp, and c) hpr.

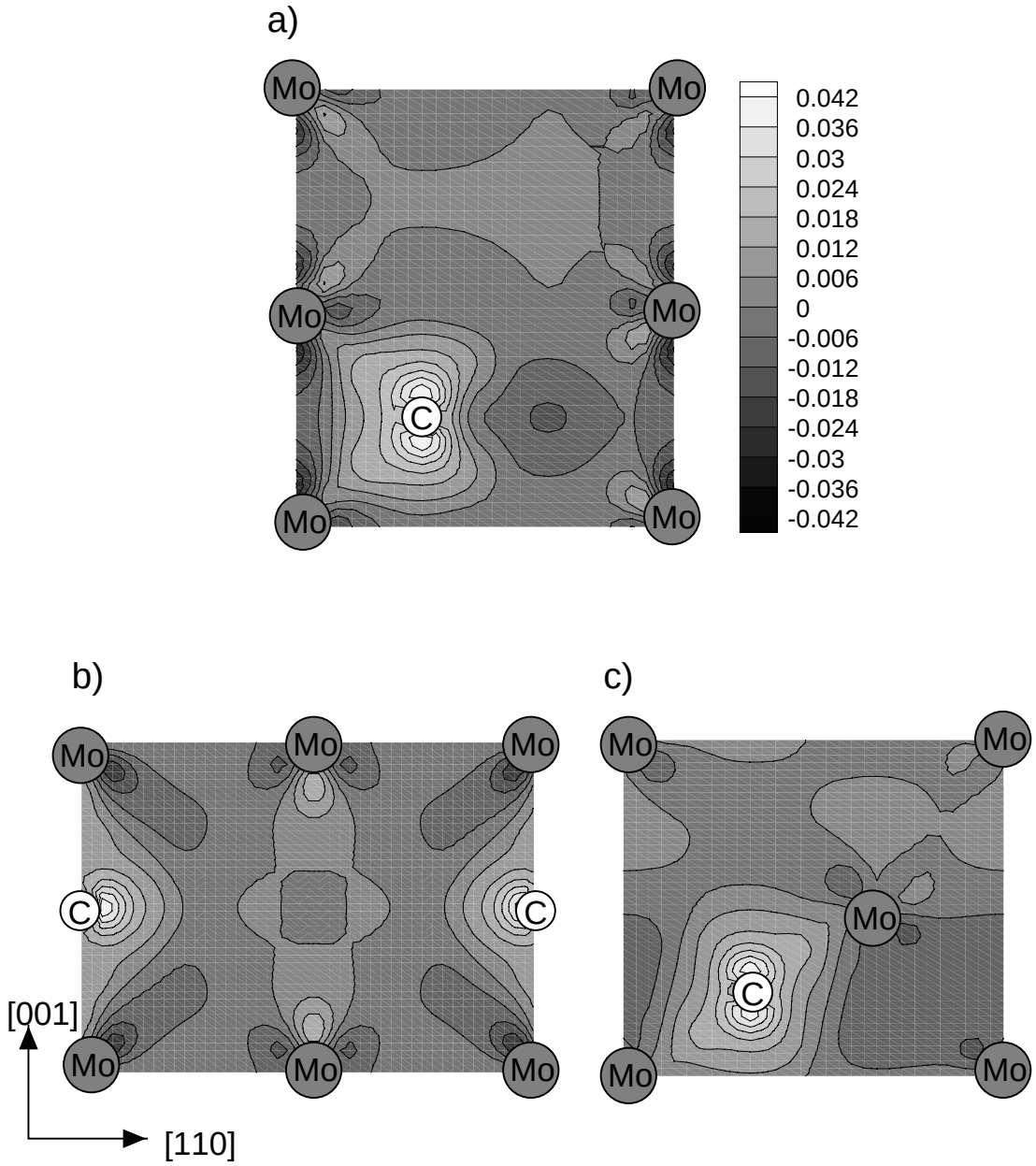


Figure 7.13: *Bonding* electron density in [electron/Bohr$^3$] in $\mathbf{Mo_2C}$: a) hpr, b) fcc, and c) hcp.

## 7.6 Population Analysis

To evaluate quantitatively which orbitals and bonds are playing the most dominant role in the bonding in molybdenum carbides, we Mulliken populations of crystal orbitals (equation 3.54), local orbital-resolved overlap populations (3.60) and covalent bond energies (3.73,3.74) were calculated according to the energy-partitioning scheme of Bester et al. (see section 3.5.4). As for the calculations described in section 5.5.2 atomic pseudo wavefunctions were used for the radial parts of the local atomic-like basis functions (3.40), limited by a cut-off radius of 6.0 Bohr for Mo and 4.0 Bohr for C[2] With the combination of these two basis sets the maximum spillage (3.49) that occurred in the molybdenum-carbide calculations was $1 \cdot 10^{-3}$.

### 7.6.1 On-site Populations

Table 7.3 shows the Mulliken population of the crystal orbitals in MoC, centred at Mo and C respectively. For comparison, the occupation numbers of the atomic orbitals are also given. They are received by simply filling the orbitals of the free atoms according to Hund's rules (cf. e.g. [85]). We see that for all cases the major part of electrons at the Mo atom is located in $d$-orbitals. In contrast to the free atom, also $p$ electrons appear, and the number of $s$ electrons is reduced. In the case of C there is a slight increase in the number of $p$ electrons, while the number of $s$ electrons decreased. Summing up over all crystal orbitals at one site we end up with more than 6 electrons at the Mo atom and less than 4 at the C site, as if a charge transfer from C to Mo had taken place when building a crystal from the free atoms. However, we know from the relative position of bands (cf. 7.5) and from the plots of the bonding electron densities (cf. 7.12) that if a charge transfer took place then only in the other direction, from Mo to C. The results for $q_{tot}$ in table 7.3 therefore are an artefact of the calculations. On the one hand, in the Mulliken partitioning scheme the non-diagonal elements of the overlap matrix S are simply divided by two and the result added to the respective orbital populations. On the other hand some of the local atomic-like basis functions extend further than to the next-nearest-neighbours. Thus e.g. a Mo orbital can represent some of the electrons centred at a C atom. Therefore assigning the orbital populations to specific sites is difficult. Nevertheless, we can see from table 7.3 that the distribution of charge into $s$, $p$, and $d$ states does not depend significantly on the

[2]How this basis set was optimised is described in detail in section 5.5.2

| MoC | $q^s_{Mo}$ | $q^p_{Mo}$ | $q^d_{Mo}$ | $q^{tot}_{Mo}$ | $q^s_C$ | $q^p_C$ | $q^{tot}_C$ |
|---|---|---|---|---|---|---|---|
| bcc | 0.581 | 1.066 | 4.879 | 6.526 | 1.179 | 2.295 | 3.474 |
| CsCl (sc) | 0.513 | 1.089 | 4.863 | 6.465 | 1.216 | 2.319 | 3.535 |
| ZnS ($fcc_t$) | 0.682 | 1.065 | 4.788 | 6.535 | 1.100 | 2.364 | 3.464 |
| NaCl ($fcc_o$) | 0.600 | 1.094 | 4.831 | 6.525 | 1.147 | 2.328 | 3.475 |
| AsNi (hpr) | 0.586 | 1.107 | 4.832 | 6.525 | 1.157 | 2.316 | 3.473 |
| NiAs (hcp) | 0.600 | 1.074 | 4.845 | 6.519 | 1.108 | 2.373 | 3.481 |
| WC (hpr) | 0.583 | 1.109 | 4.825 | 6.517 | 1.125 | 2.357 | 3.482 |
| free atoms | 1.000 | 0.000 | 5.000 | 6.000 | 2.000 | 2.000 | 4.000 |

Table 7.3: Mulliken Population of local orbitals for different MoC compounds and occupation numbers of orbitals of the free atoms. The numbers represent electrons per orbital.

| MoC | $q^s_{Mo} + q^s_C$ | $q^p_{Mo} + q^p_C$ | $q^d_{Mo}$ |
|---|---|---|---|
| bcc | 1.760 | 3.361 | 4.879 |
| CsCl (sc) | 1.729 | 3.408 | 4.863 |
| ZnS ($fcc_t$) | 1.782 | 3.429 | 4.788 |
| NaCl ($fcc_t$) | 1.747 | 3.422 | 4.831 |
| AsNi (hpr) | 1.743 | 3.423 | 4.832 |
| NiAs (hcp) | 1.708 | 3.447 | 4.845 |
| WC (hpr) | 1.708 | 3.466 | 4.825 |

Table 7.4: Mulliken Population of local $s$, $p$ and $d$ orbitals in different MoCs. The numbers represent number of electrons in one angular-momentum type of orbital and are the respective sums of the contributions of orbitals at Mo and C sites given in table 7.3.

crystal symmetry.

In table 7.4 the crystal orbital populations of table 7.3 were summed up for the different angular momenta. In this way one gets the "total" $s$-, $p$- and $d$-populations in the MoC system. Looking at the relative distribution we speculate about which kind of hybrids can result from these orbitals, and thus to which crystal symmetry this would lead. The main types of $s-p-d$ hybridisation, and the coordination numbers and geometries that they lead to, are summarised e.g. in the book of Sutton [113] and repeated in table 7.5. Strictly speaking the predicted geometries only apply to perfectly covalent systems, but since the Mo-C bonds have covalent character, and it was illustrated in the preceeding sections that they play the major role in the bonding, the data of table 7.5 least help for a good guess. Rounding the values in table 7.4 to integer numbers we have two $s$, three $p$ and five $d$ electrons for the hybrids bonding to the nearest-neighbours at the Mo or C site respectively.

We know from section 7.2 that a coordination number of 6 is most favourable. If we assume that all valence electrons are involved in the bonding, then we can easily understand this, as with a lower coordination number more electrons are left over. They could be used of course for next-nearest-neighbour bonding, but from the bonding electron densities we have seen that for this far less electrons are needed. Most electrons are located in the close vicinity of the respective central atom. Thus, assuming a coordination number of six, we have the choice between an octahedral and a trigonal prismatic interstitial site, as can be seen from table 7.5. The latter seems more preferable, as it "consumes" two more of the localised $d$ electrons. In table 7.1a) the interstitial sites for C in Mo, and vice versa are given. All the sixfold coordinated structures are a combination of octahedral and trigonal prismatic interstitial sites. Assuming that the trigonal prismatic one is the most favourable indeed, we understand that "two times trigonal prismatic", which is the WC structure, is the most stable configuration.
Cottrell developed a semi-empirical model which describes rather satisfactorily the relative stabilities of most transition metal carbides [20, 21, 22, 23, 24]. (For some reason he did not include Mo.) He gives a nice descriptive interpretation of the fact that the WC structure is the most favourable for the tungsten carbides, which agrees well with our results for the molybdenum carbides: Assuming that the $d$-$d$ bonds between metal atoms are mainly of $\sigma$ character and thus directed along the lines between Mo-Mo atom pairs around the C atom, the trigonal prismatic cell has the advantage over the octahedral one in enabling the electrons of the $d$-$d$ bonds to avoid better the electronegative regions near the carbon atoms. Thus the WC structure satisfies best the principle that different bonds from an atom - in this case the Mo-C and the Mo-Mo bonds from a given Mo atom - should point in well-separated directions [25].
Table 7.6 shows the Mulliken population of the crystal orbitals in $Mo_2C$. The calculated values do not differ much from those for the corresponding MoC structures, so we can use the same arguments as before. In the semi-carbides we have Mo-C and Mo-Mo nearest-neighbour bonds. Now the octahedral coordination of C with Mo is preferred, because it leaves more $d$ electrons to be used for the Mo-Mo bonds.

### 7.6.2 Orbital Overlap Populations

Figure 7.14 shows the energy resolved local crystal-orbital overlap populations (3.61) for various bonds in the three MoC structures fcc, hcp and hpr. We see that in the $d$-$d$ bonds of Mo a small number of anti-bonding states (negative COOP) becomes occupied, in contrast

| coordination number | atomic orbitals | resulting hybrids |
|---|---|---|
| 2 | sp | linear |
| | dp | linear |
| | sd | bent |
| 3 | $sp^2$ | trigonal plane |
| | $dp^2$ | trigonal plane |
| | $d^2s$ | trigonal plane |
| | $d^2p$ | trigonal pyramid |
| 4 | $sp^3$ | tetrahedral |
| | $d^3s$ | tetrahedral |
| | $dsp^2$ | tetragonal plane |
| 5 | $dsp^3$ | trigonal bipyramid |
| | $d^3sp$ | trigonal bipyramid |
| | $d^4s$ | tetragonal pyramid |
| 6 | $d^2sp^3$ | octahedral |
| | $d^4sp$ | trigonal prism |

Table 7.5: Coordination numbers and bonding geometries for the main types of s-p-d hybridisation [113]

to what is known of bcc Mo, where the Fermi level is exactly at the point at which the change of sign from positive to negative COOP occurs, the maximum number of bonding states being filled. Thus, compared to pure Mo, the Mo-Mo bonds are weakened a bit in MoC. However the maximum filling of bonding states now occurs in the Mo-*d* - C-*p* bonds. The increasing peak size and width in the COOP below the Fermi level indicates that the weight of these bonds relative to the Mo-Mo bonds is increasing when going from fcc to hpr. The overlap of Mo-*d* with C-*s* orbitals leads to bonding states far below the Fermi energy, also stabilising the structure.
For $Mo_2C$ (fig. 7.15) the COOP results are similar, but in the fcc and hcp structures no anti-bonding Mo-*d*-Mo-*d* states are occupied. Furthermore the Mo-Mo and Mo-C bonds are of equal importance.

From the analysis of the crystal orbital populations we derived some qualitative arguments, why MoC tends to crystallise in the hexagonal primitive WC structure, and $Mo_2C$ in the hexagonal close-packed one. However, we still do not have any quantitative values that reproduce the trend given by the energies of compound formation (see e.g. figures 7.2a) and b)). The next feature we therefore examine are the integrated overlap populations of orbitals, i.e. bonding charges. A simple way to calculate the number of electrons that is

| $Mo_2C$ | $q^s_{Mo}$ | $q^p_{Mo}$ | $q^d_{Mo}$ | $q^{tot}_{Mo}$ | $q^s_C$ | $q^p_C$ | $q^{tot}_C$ |
|---|---|---|---|---|---|---|---|
| bcc | 0.609<br>0.627 | 0.961<br>0.849 | 6.242<br>4.809 | 4.672<br>6.258 | 1.129 | 2.344 | 3.473 |
| $fcc_t$ | 0.634<br>0.634 | 0.876<br>0.876 | 6.242<br>4.732 | 4.732<br>6.242 | 1.114 | 2.400 | 3.522 |
| sc | 0.464<br>0.464 | 0.822<br>0.822 | 6.239<br>4.953 | 4.953<br>6.239 | 1.155 | 2.367 | 3.522 |
| hpr | 0.576<br>0.576 | 0.868<br>0.868 | 6.257<br>4.813 | 4.813<br>6.257 | 1.131 | 2.358 | 3.489 |
| $fcc_o$ | 0.597<br>0.590 | 0.975<br>0.784 | 6.368<br>4.726 | 4.796<br>6.100 | 1.133 | 2.400 | 3.533 |
| hcp | 0.604<br>0.604 | 0.875<br>0.875 | 6.247<br>4.768 | 4.768<br>6.247 | 1.139 | 2.366 | 3.505 |

Table 7.6: Mulliken Population of orbitals for different $Mo_2C$s. The values denote electrons per orbital. In the bcc and the $fcc_o$ structure the Mo sites are not equal. In the octahedron surrounding the C site there are two bonds of length $a_0/2$ towards the "first-" nearest-neighbour Mo atom, and four bonds of length $\sqrt{2}a_0/2$ towards the "second-" nearest-neighbours (compare e.g. figure 7.1). The populations given in the respective upper line belong to the first neighbour, the numbers in the respective lower line to the second.

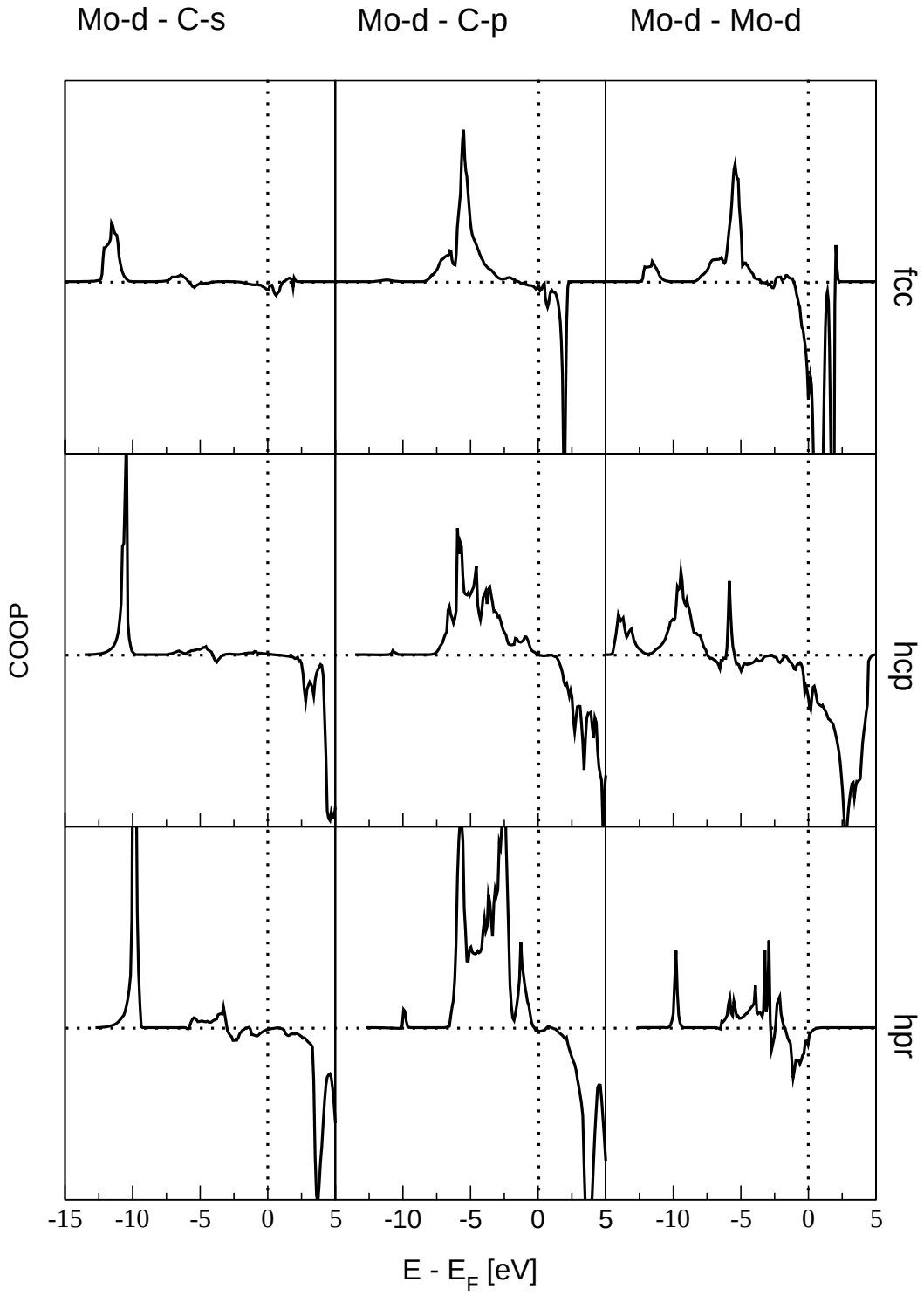


Figure 7.14: Crystal orbital overlap populations (COOP) for fcc (NaCl), hcp (NiAs) and hpr (WC) MoC (from top to bottom).

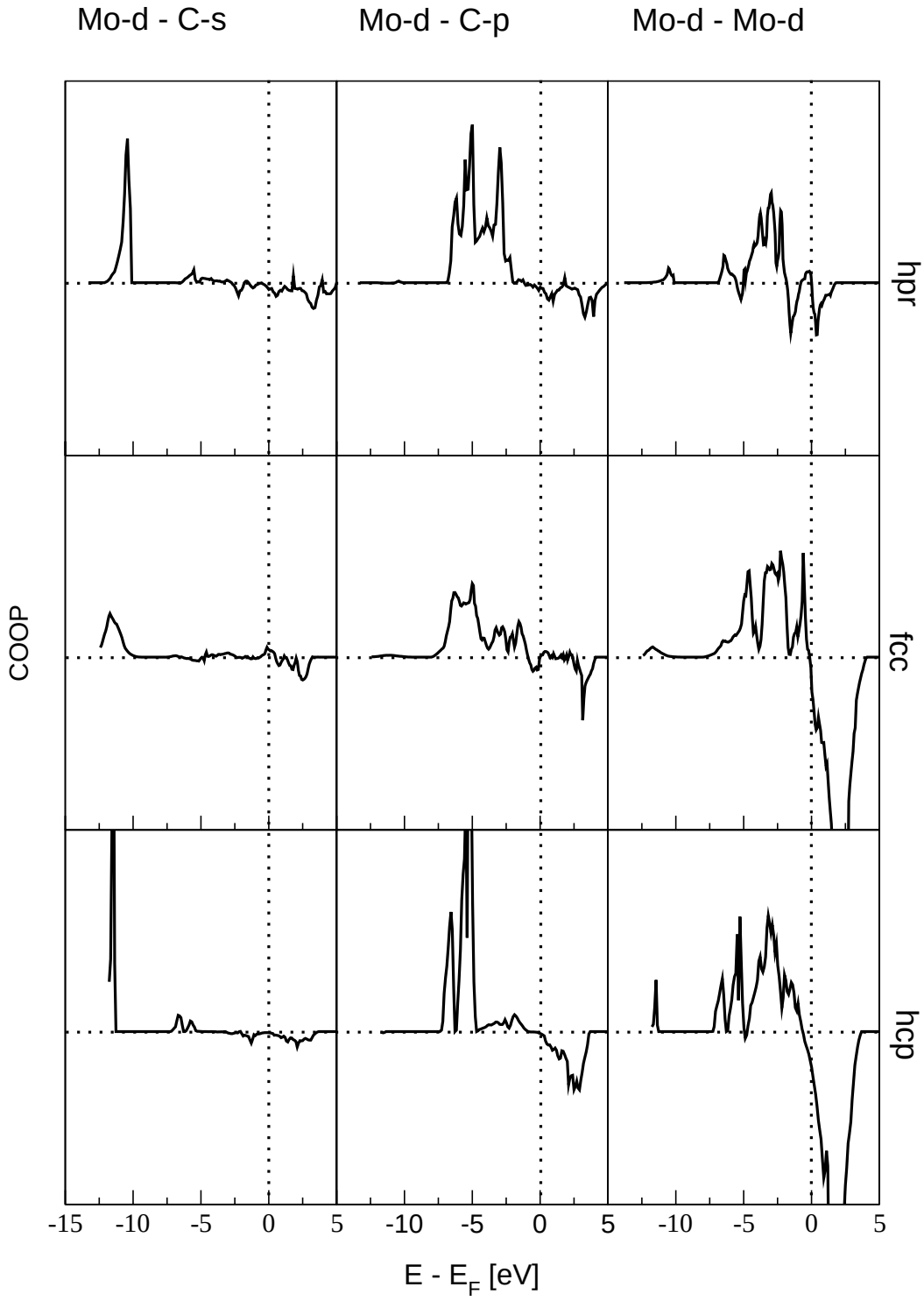


Figure 7.15: Crystal orbital overlap populations (COOP) for hpr, fcc and hcp $Mo_2C$ (from top to bottom).

| MoC | $q_{Mo}$ | $q_C$ | $q_{tot}$ |
|---|---|---|---|
| bcc | 4.705 | 2.358 | 7.063 |
| CsCl (sc) | 4.484 | 2.442 | 6.926 |
| ZnS ($fcc_t$) | 4.562 | 2.214 | 6.776 |
| NaCl ($fcc_o$) | 4.527 | 2.252 | 6.779 |
| AsNi (hpr) | 4.388 | 2.266 | 6.654 |
| NiAs (hcp) | 4.464 | 2.236 | 6.700 |
| WC (hpr) | 4.340 | 2.257 | 6.597 |

Table 7.7: On-site populations [number of electrons] in MoC.

accumulated in *all* bonds in the system is to calculate the on-site populations and subtract them from the total number of electrons. Table 7.7 shows the on-site populations for MoC. On an average the total on-site charge $q_{tot}$ is decreasing when going from the least stable bcc MoC to the most stable WC structure. This means that the total overlap population (per formula unit) is increasing. The same observation holds for the semi-carbides. The on-site populations for the semi-carbides are given in table 7.8. The total sum is decreasing when going from the least stable bcc to the most favourable hcp $Mo_2C$. Obviously maximum stability is coming along with maximum overlap of orbitals.
The covalent bond energy (3.73) connected with the overlap of orbitals is not directly proportional to the total overlap populations discussed here, as bonds coming from different types of orbitals make a different contribution. To analyse these contributions we separate the nearest-neighbour-bonds according to the angular momentum of the overlapping orbitals. This is done in the next section.

## 7.7 Covalent Bond Energies

The covalent bond energy is defined according to the energy partitioning scheme introduced by Bester et al. [6], which was described in chapter 3.5.4. To distinguish it from a metallic bond which could also be described with a (large) set of atomic-like orbitals, a covalent bond is imagined as a bond which is dominated by the hybridisation of those orbitals on the various atoms being already occupied in the respective free atom. So it may also contain "metallic" i.e. spatially homogeneous contributions. To account for those electrons which have been redistributed when building a crystal out of the free atoms the promotion energy (3.70) was calculated as well. It is listed for the different MoC and $Mo_2C$ structures in tables 7.9 and 7.10. The values of each atomic species are very similar for the

| $Mo_2C$ | $q_{Mo}$ | $q_C$ | $q_{tot}$ |
|---|---|---|---|
| bcc | 4.525<br>4.390 | 2.289 | 11.204 |
| $fcc_t$ | 4.385<br>4.385 | 2.256 | 11.026 |
| sc | 4.438<br>4.438 | 2.300 | 11.176 |
| hpr | 4.332<br>4.332 | 2.253 | 10.917 |
| $fcc_o$ | 4.278<br>4.223 | 2.257 | 10.758 |
| hcp | 4.257<br>4.257 | 2.231 | 10.745 |

Table 7.8: On-site populations [number of electrons] in $Mo_2C$.

different geometries. This was expected, as the promotion energy primarily depends on the relative position of the electronic states between which electrons are exchanged, which is not much affected by the crystal structure. The fact that the promotion energy for C is one order of magnitude higher than the one of Mo can be understood with the same argument.

Table 7.11 shows the covalent bond energies for nearest-neighbour Mo-C bonds in the different carbides, split into the contributions of the constituent orbitals. The dominant contribution is the Mo-$d$–C-$p$ bond ($d^{Mo} - p^C$ values in table 7.11). It is very similar for the sixfold coordinated structures NaCl, AsNi, NiAs and WC but it distinguishes between the close-packed (fcc, hcp) and the simple (hpr) Mo sublattice. While the population of orbitals depends on the relative position of bands, their overlap and thus the population and energy of bonds depends on the crystal structure. To compare structures with different coordination numbers, however, does not make sense at this point, because the strength of a single bond depends among other things on the number of nearest-neighbours as can be demonstrated, e.g., by comparing the CsCl and the ZnS structure.

For this reason the different types of bonds have been summed up to the total covalent bond energy per bond and multiplied with the coordination number. The results are given in table 7.12 for the mono-carbides. We see that the nearest-neighbour Mo-C bond is indeed playing the major role. The next-nearest-neighbour bonds are Mo-Mo and C-C bonds

| MoC | $E^{Mo}_{prom}$ | $E^{C}_{prom}$ | $E^{tot}_{prom}$ |
|---|---|---|---|
| bcc | 0.072 | 0.703 | 0.775 |
| CsCl (sc) | 0.099 | 0.653 | 0.752 |
| ZnS ($fcc_t$) | 0.069 | 0.756 | 0.825 |
| NaCl ($fcc_o$) | 0.078 | 0.723 | 0.801 |
| AsNi (hpr) | 0.080 | 0.719 | 0.799 |
| NiAs (hcp) | 0.075 | 0.745 | 0.820 |
| WC (hpr) | 0.084 | 0.734 | 0.818 |

Table 7.9: Promotion energies per atom and per formula unit in different MoC compounds.

respectively. Here the contribution of the C-C bond is anti-bonding, but the absolute value is so small that it is negligible. Summing up nearest- and next-nearest-neighbour contributions gives the "total" covalent bond energy $E^{tot}_{cov}$. No obvious trend emerges for these "total" covalent bond energies which correlates to the one in the energies of formation. However, the most stable WC structure also has the lowest covalent bond energy. Adding the promotion energy doesn't change the situation qualitatively.
In $Mo_2C$ (see table 7.13) the Mo-C bond still represents the major contribution to the bonding energy. But here, due to the stoichiometry the Mo-Mo have similar values as the Mo-C bonds. The C-C bonds, which are next-nearest-neighbour bonds, are again anti-bonding. In some structures their absolute values are considerably higher than in the corresponding mono-carbide. This is most striking for the $fcc_t$ structure, where C is tetrahedrally coordinated with Mo atoms. For the "total" covalent bond energies we see a surprising scheme: the values are higher for the more favourable structures, hcp, $fcc_o$ and hpr, where C is sixfold coordinated with Mo, than for all others. For those structures we obtain a reversed trend: the total covalent bond energy is increasing with decreasing energy of formation.

Finally, starting from a central unit cell and increasing the number of neighbour shells step by step, all contributions to overlap populations and covalent bond energies have been summed up until the further contributions vanished to zero. On average (depending on the individual bond lengths) this was the case after the fifth-nearest-neighbour shell, when we do not distinguish between Mo and C shells. The total overlap populations obtained in this way differ slightly from the difference between total number of valence electrons and the total on-site populations given in tables 7.7 and 7.8, but the trend remains

| $Mo_2C$ | $E^{Mo}_{prom}$ | $E^{C}_{prom}$ | $E^{tot}_{prom}$ |
|---|---|---|---|
| bcc | 0.135<br>0.097 | 0.736 | 1.200 |
| $fcc_t$ | 0.116<br>0.116 | 0.729 | 0.961 |
| sc | 0.104<br>0.104 | 0.700 | 0.908 |
| hpr | 0.110<br>0.110 | 0.728 | 0.948 |
| $fcc_o$ | 0.099<br>0.139 | 0.710 | 0.948 |
| hcp | 0.114<br>0.114 | 0.717 | 0.945 |

Table 7.10: Promotion energies per atom and per formula unit in different $Mo_2C$ compounds.

| MoC | $s^{Mo} - s^{C}$ | $s^{Mo} - p^{C}$ | $p^{Mo} - s^{C}$ | $p^{Mo} - p^{C}$ | $d^{Mo} - s^{C}$ | $d^{Mo} - p^{C}$ |
|---|---|---|---|---|---|---|
| bcc | -0.025<br>-0.011 | -0.024<br>-0.027 | -0.053<br>-0.024 | -0.049<br>-0.049 | -0.067<br>-0.010 | -0.337<br>-0.054 |
| CsCl (sc) | -0.005 | -0.022 | -0.025 | -0.042 | -0.030 | -0.098 |
| ZnS ($fcc_t$) | -0.031 | -0.042 | -0.038 | -0.062 | -0.061 | -0.245 |
| NaCl ($fcc_o$) | -0.015 | -0.029 | -0.033 | -0.048 | -0.036 | -0.142 |
| AsNi (hpr) | -0.014 | -0.029 | -0.033 | -0.047 | -0.046 | -0.151 |
| NiAs (hcp) | -0.015 | -0.030 | -0.028 | -0.044 | -0.038 | -0.146 |
| WC (hpr) | -0.013 | -0.028 | -0.032 | -0.046 | -0.041 | -0.151 |

Table 7.11: Covalent bond energy per bond in different MoC compounds. In bcc MoC not all Mo atoms are equivalent. In the octahedron surrounding the C site there are two bonds of length $a_0/2$ towards the "first" nearest-neighbour Mo atom, and four bonds of length $\sqrt{2}a_0/2$ towards the "second" nearest-neighbours. The energies given in the upper line for the bcc structure belong to the first neighbour, the numbers in the respective lower line to the second.

| MoC | $E^{Mo-Mo}_{cov,NNN}$ | $E^{C-C}_{cov,NNN}$ | $E^{Mo-C}_{cov,NN}$ | $E^{tot}_{cov}$ | $E^{tot}_{cov} + E^{tot}_{prom}$ |
|---|---|---|---|---|---|
| bcc | -0.310 | -0.002 | -1.813 | -2.121 | -1.346 |
| CsCl (sc) | -0.480 | +0.051 | -1.764 | -2.193 | -1.441 |
| ZnS ($fcc_t$) | -0.270 | +0.004 | -1.916 | -2.182 | -1.357 |
| NaCl ($fcc_o$) | -0.312 | +0.006 | -1.826 | -2.132 | -1.331 |
| AsNi (hpr) | -0.427 | +0.008 | -1.845 | -2.280 | -1.481 |
| NiAs (hcp) | -0.313 | +0.008 | -1.880 | -2.185 | -1.365 |
| WC (hpr) | -0.456 | +0.010 | -1.874 | -2.321 | -1.503 |

Table 7.12: Covalent bond energy of nearest-neighbour (NN) and next-nearest-neighbour (NNN) bonds in MoC. The total covalent bond energy per bond (sum over all orbitals in table 7.11) has been multiplied with the respective coordination numbers (table 7.1). The last column presents the sum of covalent bond energy and promotion energy (table 7.9).

| $Mo_2C$ | $E^{Mo-Mo}_{cov,NN}$ | $E^{C-C}_{cov,NNN}$ | $E^{Mo-C}_{cov,NN}$ | $E^{tot}_{cov,NN}$ | $E^{tot}_{cov,NN} + E^{tot}_{prom}$ |
|---|---|---|---|---|---|
| bcc | -2.154 | + 0.000 | -1.947 | -4.001 | -3.033 |
| $fcc_t$ | -1.804 | + 0.109 | -2.314 | -4.009 | -3.048 |
| sc | -1.456 | + 0.001 | -2.538 | -3.993 | -3.085 |
| hpr | -1.728 | + 0.008 | -2.006 | -3.726 | -2.778 |
| $fcc_o$ | -1.124 | + 0.058 | -2.587 | -3.653 | -2.705 |
| hcp | -1.508 | + 0.002 | -2.078 | -3.604 | -2.659 |

Table 7.13: Covalent bond energy of nearest-neighbour (NN) and next-nearest-neighbour (NNN) bonds in $Mo_2C$. The values represent the sum over all orbitals times the respective coordination numbers. The last column shows the sum of NN-covalent bond energy and promotion energy (cf. table 7.10).

unchanged[3]. They are displayed graphically, together with the energies of formation and the total covalent bond energies in figure 7.16. The labels of the upper x-axis refer to the semi-carbides, those of the lower x-axis to the carbides. The left y-axis gives the total overlap population (bonding charge) per unit cell, the right gives energies of formation and covalent bond energies, respectively. The structures are ordered according to their energies of formation, which is decreasing continuously from the left to the right. At the same time the overlap populations increase monotonously. Thus, as concluded already in section 7.6.2, increasing stability of a structure comes along with increasing overlap. For the covalent bond energies we still do not see such a consistent trend, even after summing up all distant contributions.

## 7.8 Distance Dependencies

To go on and discuss the matrix elements occurring in the molybdenum carbide would be the next step. However, for the moment we pass on it as there are still some inconsistencies in the ab-initio data. For example the values calculated for the 3rd nearest neighbour $dd\delta$ hopping terms in figure 7.20 have the wrong sign and the absolute values are far too big. The reason for this has to be clarified first. After analysing the physical relationships between electronic and crystal structures it is discussed now how useful the presented quantities can be for the fitting of the free parameters in a tight-binding model. Therefore we want to investigate the distance dependencies, i.e. the decay behaviour, of overlap populations and covalent bond energies, which are characteristic for the interaction of pairs of atoms. We will especially bear in mind the special features of the environment dependent parametrisation of Tang et al. [116, 48, 47] introduced in chapter 4.2. This section describes ongoing work, thus some of the considerations presented here are still in their initial stage. At some points this causes the presentation to be little appealing, which the reader is kindly asked to excuse.

Even if the covalent bond energies do not reproduce the trend in the energies of formation they can be compared as a first approximation to the band energy part of the total tight-binding energy (4.1). So first of all we look at them to estimate the range of interaction

[3]To put it in other words: if we sum up the on-site populations given in tables 7.7 and 7.8 and the overlap populations displayed in figure 7.16 we obtain a number that slightly differs from the total number of electrons in the unit cell. This difference is of the order of magnitude of "number of electrons times spillage" and illustrates the incompleteness of the local basis set.

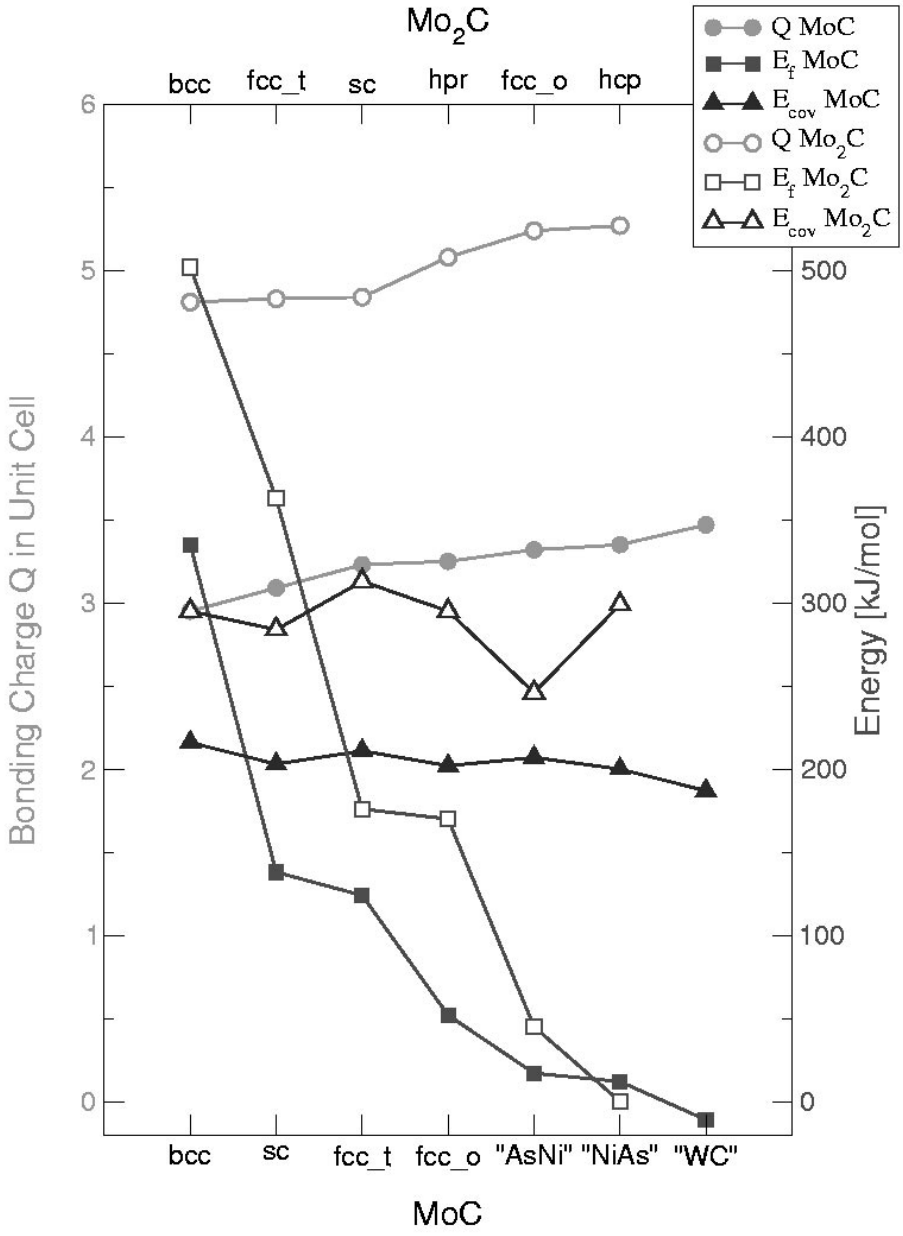


Figure 7.16: Comparison of bond charge Q per unit cell, covalent bond energy $E_{cov}$ and energy of formation $E_f$ for $Mo_2C$ (see upper x-axis) and MoC (see lower x-axis). Structures are ordered corresponding to $E_f$. $E_f$ (right y-axis) goes down with increasing bond charge Q (left y-axis). $E_{cov}$ doesn't show such a systematic behaviour.

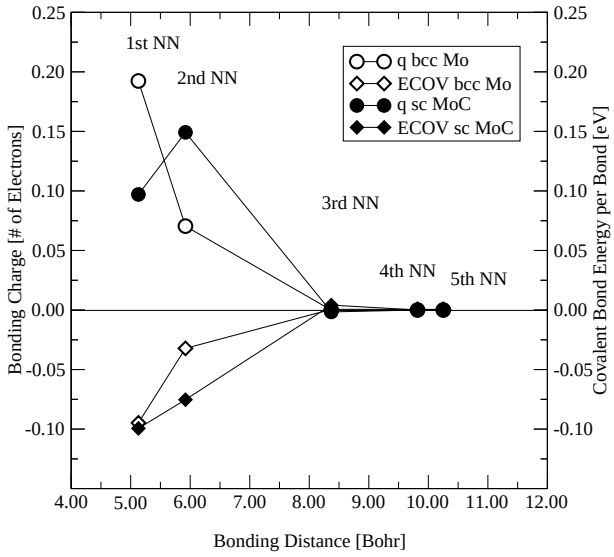


Figure 7.17: Local overlap populations q and covalent bond energies "ECOV", both per bond, in bcc Mo (open symbols) and CsCl (sc) MoC (full symbols). The interatomic distances correspond to the equilibrium volume of bcc Mo. The values for sc MoC were obtained by assuming the same volume and replacing one Mo in the cubic unit cell by a C atom. The central atom is always a Mo atom. In sc MoC the first- and fourth-nearest-neighbours thus are C atoms, the second, third, and fifth neighbours are Mo atoms.

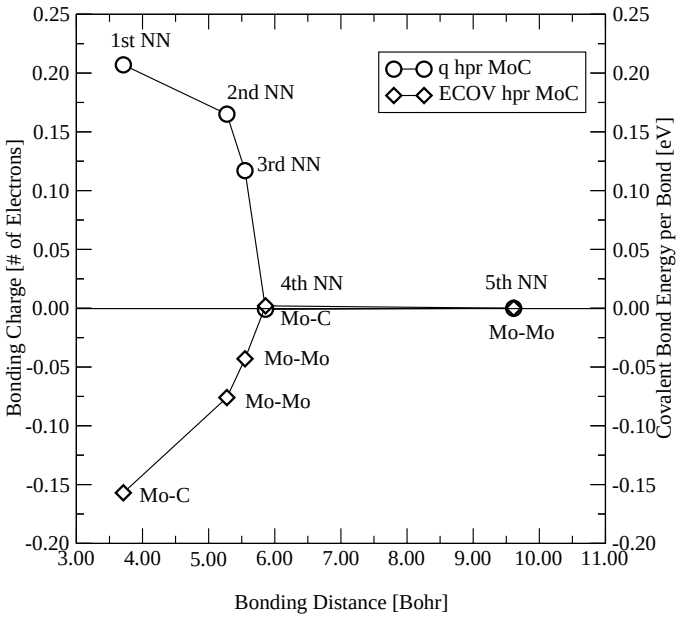


Figure 7.18: Overlap populations q and corresponding covalent bond energies "ECOV" in hpr MoC (WC structure). The interatomic distances correspond to the equilibrium volume of WC MoC. Starting with Mo as a central atom, the first- and fourth-nearest-neighbours are carbon atoms, the second, third and fifth Mo.

between atomic orbitals in molybdenum and the molybdenum carbides. Figure 7.17 shows the total overlap population per bond and the correlated covalent bond energy for the first, second, third, fourth, and fifth-nearest-neighbours in bcc Mo (open symbols) and sc (CsCl) MoC (full symbols). The distances are the interatomic distances in the equilibrium volume of bcc Mo. The open symbols show that in bcc Mo the overlap of neighbouring orbitals and, correspondingly, the covalent bond energy, are close enough to zero to be negligible for and beyond the third-nearest-neighbours. To test the influence of the atomic species, one Mo atom in the cubic unit cell was replaced by carbon, thus getting sc MoC (the CsCl structure) at the equilibrium volume of bcc Mo. The corresponding overlap populations and covalent bond energies are shown in figure 7.17 as full symbols. Starting from a Mo atom as central atom the first-nearest-neighbour atoms are now carbon atoms. We see that the overlap between Mo and C is approximately half the amount of that between Mo and Mo at the same distance. The corresponding covalent bond energy, however, is nearly the same. Thus in MoC a Mo-C bond is considerably stronger than a Mo-Mo bond of the same length.
The overlap population of a Mo-Mo bond in sc MoC in which the Mo atoms are second-nearest-neighbours is approximately twice the amount of the corresponding bond in bcc Mo. Obviously the bonding charge which is not contained in the Mo-C nearest-neighbour bond is shifted to the Mo-Mo second-nearest-neighbour bonds. The overlap with orbitals of the third-nearest-neighbours is again almost zero.

Figure 7.18 shows the overlap populations and covalent bond energies of MoC in the hpr "WC" structure at its equilibrium volume. Here we see that the low absolute value of the Mo-C overlap population in figure 7.17 was an effect of the large volume. For MoC at the equilibrium volume the overlap of first-nearest-neighbour orbitals is the strongest, and it decreases to zero for the fourth-nearest-neighbours. The covalent bond energies show the same trend. The fact that the interaction between two atoms is extended to the third-nearest-neighbours in hpr MoC in contrast to sc MoC has two different origins. Firstly, the bond lengths in hpr MoC are much smaller than in sc MoC, as the latter has been calculated at the equilibrium volume of bcc Mo. Secondly, the environment has changed, leading to a different screening of the interatomic interactions. In the environment-dependent tight-binding model we can describe these two effects separately, by the distance-dependent part of the hopping integrals, equation (4.35), and by the screening function, equation (4.36). The question is whether these two effects can be extracted from the ab-initio data as well.

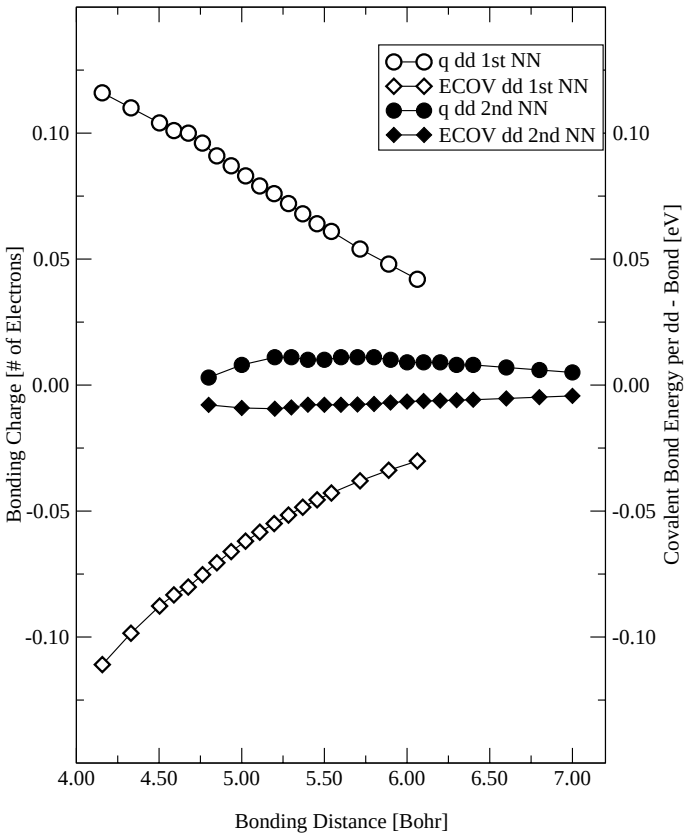


Figure 7.19: Local *dd* overlap populations and corresponding covalent bond energies in bcc Mo for different unit cell volumes. The open symbols show the distance dependency of the first-nearest-neighbour interactions, the full symbols those of the second-nearest-neighbours.

Figure 7.19 shows the *dd*-overlap population and the corresponding covalent bond energy for nearest-neighbour and next-nearest-neighbour bonds in bcc molybdenum for different volumes of the unit cell. This gives an impression of the distance dependence of the *dd*-hopping terms. With the given symmetry of the crystal, the first-nearest-neighbours in bcc Mo are expected 157 to interact rather "unscreened", while the screening for the next-nearest-neighbours is considerable. This can be seen in figure 7.19 by the big reduction

of overlap and covalent bond energies when going from the first to the second-nearest-neighbours at equal distances. Thus, in principle the information about the screening behaviour of the interaction via different orbitals can be gained from the ab-initio data!

When thinking of how to relate the ab-initio data with the quantities in the tight binding model we are facing the problem that the ab-initio data for single bonds between two atoms was received by representing the crystal wavefunction in a *non*-orthogonal LCAO basis. Thus, Hamiltonian as well as non-diagonal overlap matrix elements (3.58, 3.59) occur. The latter do not exist in an orthogonal tight-binding model. Calculating the interaction between two atoms ab-initio we can distinguish between "direct" interaction via overlap of orbitals and the interaction via potentials. In a tight-binding model the overlap is neglected, or, by formally converting the non-orthogonal basis into an orthogonal one by a Löwdin transformation (4.29), the non-orthogonality effects are included in the Hamiltonian matrix elements. As discussed in chapter 4.1.5 this leads to an implicit environment dependency of the Hamiltonian matrix elements.
The covalent bond energies (3.74) include contributions from Hamiltonian as well as overlap matrix elements. Thus, ignoring at first that this implicit environment dependency has a different origin than that of the tight-binding Hamiltonian elements, the free parameters of the hopping terms could be fitted to reproduce the covalent bond energies. However, the transferability of the parameters we expect from this procedure is low, precisely because of the implicit environment dependency. Instead, as suggested above, the explicit environment-dependent contribution shall be extracted from the ab-initio data.
Nguyen Manh et al. derived an analytic expression for environment-dependent tight-binding bond integrals by transforming the non-orthogonal secular equation into an orthogonal one [87]. In this special case surprisingly an expression for the inverse non-orthogonality matrix was obtained which showed striking similarities with the empirically constructed screening function of the environment-dependent tight-binding model of Tang et al. [116], indicating a close relationship between these two quantities. Thus, what will be tried is to relate the screening function (4.36) in the tight-binding hopping terms (4.35) to the ab-initio overlap matrix elements in the local basis (3.58), and the hopping terms themselves to the local Hamiltonian elements (3.59). This procedure has the further advantage of comparing the matrix elements before the Brillouin zone integration is performed. Hence, no phase information of the crystal structure is included in the calculated numbers.
By means of the Slater-Koster rules [109] mentioned in chapter 4.1.6 the Hamiltonian

matrix elements in a two-centre tight-binding model can be expressed in terms of linear combinations of so-called "fundamental hopping terms" (for illustration see figures 4.1 and 4.2):

$$H_{\alpha l x,\alpha' l' x'} = \sum_m c_m V_{ll'm} \quad . \tag{7.2}$$

Here $x$ and $x'$ stand for the x, y, respective z-component in a Cartesian coordinate system. The index m denotes the $\sigma$, $\pi$, or $\delta$ character of the hopping term and the coefficient $c_m$ represents a combination of direction cosines. By inverting the set of linear equations (7.2) we can get the hopping terms expressed in terms of linear combinations of the Hamiltonian matrix elements,

$$V_{ll'm} = \sum_{x,x'} \tilde{c}_{xx'} H_{\alpha l x,\alpha' l' x'} \quad . \tag{7.3}$$

The same procedure applies for the overlap matrix. Figures 7.20 and 7.21 show the hopping and overlap terms of type "$\sigma$", "$\pi$" and "$\delta$", calculated according to equation (7.3), using the ab-initio Hamiltonian and overlap matrix elements represented in a LCAO basis (3.59,3.58). All types of matrix elements in figure 7.20 show discontinuities when going from the first to the second- and third-nearest-neighbours. Even if we focus only on distances close to the respective distances at the equilibrium volume (cf. figure 7.22a)) we can not draw one continuous plot through all points. This illustrates again the environment dependency of the matrix elements. A comparison with the distance dependence of the $dd\sigma$ tight-binding matrix elements for molybdenum in the orthogonal environment dependent parametrisation shows that the values of the ab-initio calculated terms are very close to the tight binding terms for the first and second-nearest-neighbours, but should be almost zero for the third (compare e.g. [46], page 86). Furthermore the comparison shows that the discontinuities between the different nearest-neighbours are by far overestimated. The overlap (cf. figure 7.21), however, smoothly decreases to zero from the first to the third-nearest-neighbours. If we assume as a first approximation that the overlap indeed behaves as the inverse screening, multiplying the hopping terms with the overlap terms could model the product

$$v_{ll'm} = f(r)(1 - S)$$

in the orthogonal tight-binding description of the hopping terms. This has been done in figure 7.22b). It results in a smoothened distance dependency which gets much closer to

the tight-binding description [46], especially the third-nearest-neighbour interactions now decrease in the same way. This is only restricted by the fact that the absolute values are now one order of magnitude too small. Of course the relationship between the overlap in an non-orthogonal basis and the screening in an orthogonal environment-dependent model is not that simple, but the above described tests show that a direct fit of the model's parameters to the ab-initio local matrix elements, even if they are presented in a non-orthogonal basis, is a promising approach.

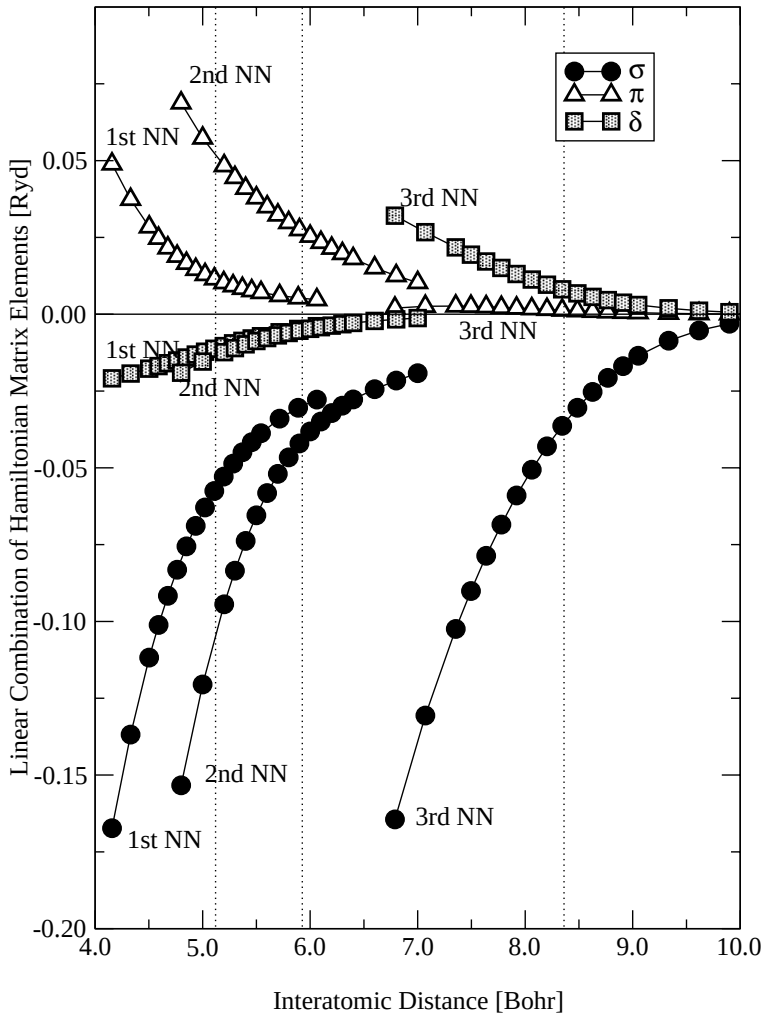


Figure 7.20: Linear combination (7.3) of local ab-initio *dd*-Hamiltonian matrix elements, i.e. hopping terms, of type "$\sigma$", "$\pi$" and "$\delta$", for the first-, second- and third-nearest-neighbours in bcc Mo for different volumina. The dashed lines mark the respective distances in the equilibrium volume.

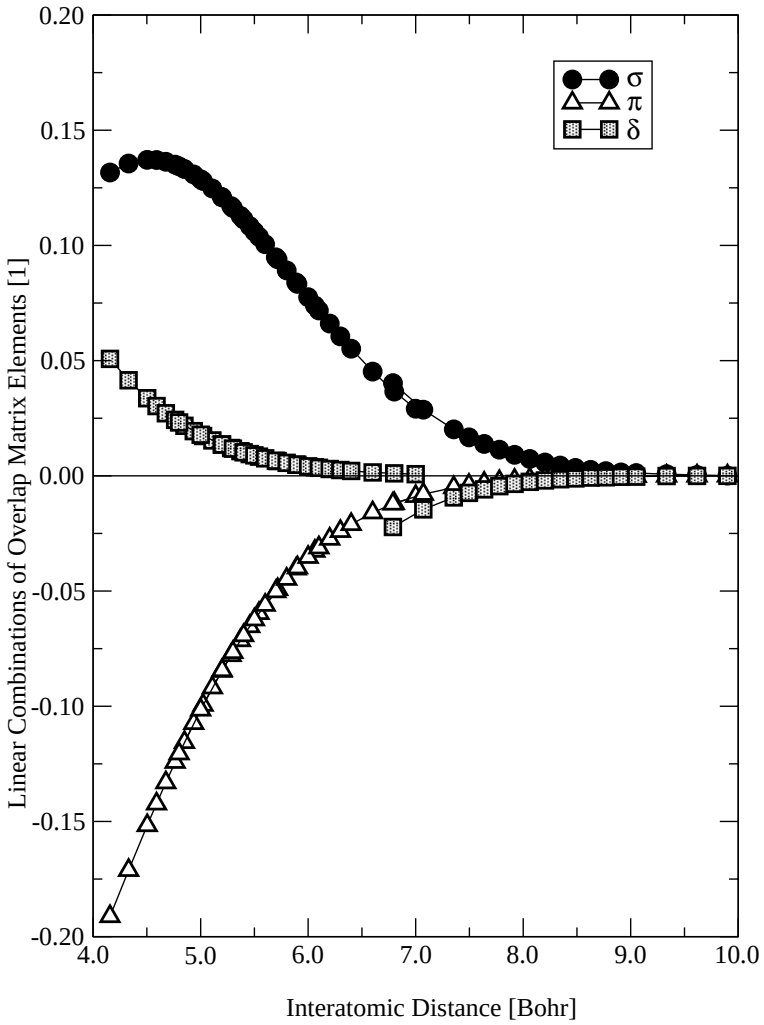


Figure 7.21: Linear combination (7.3) of local ab-initio *dd*-overlap matrix elements, i.e. overlap terms of type "$\sigma$", "$\pi$" and "$\delta$", for the first-, second- and third-nearest-neighbours in bcc Mo for different volumina.

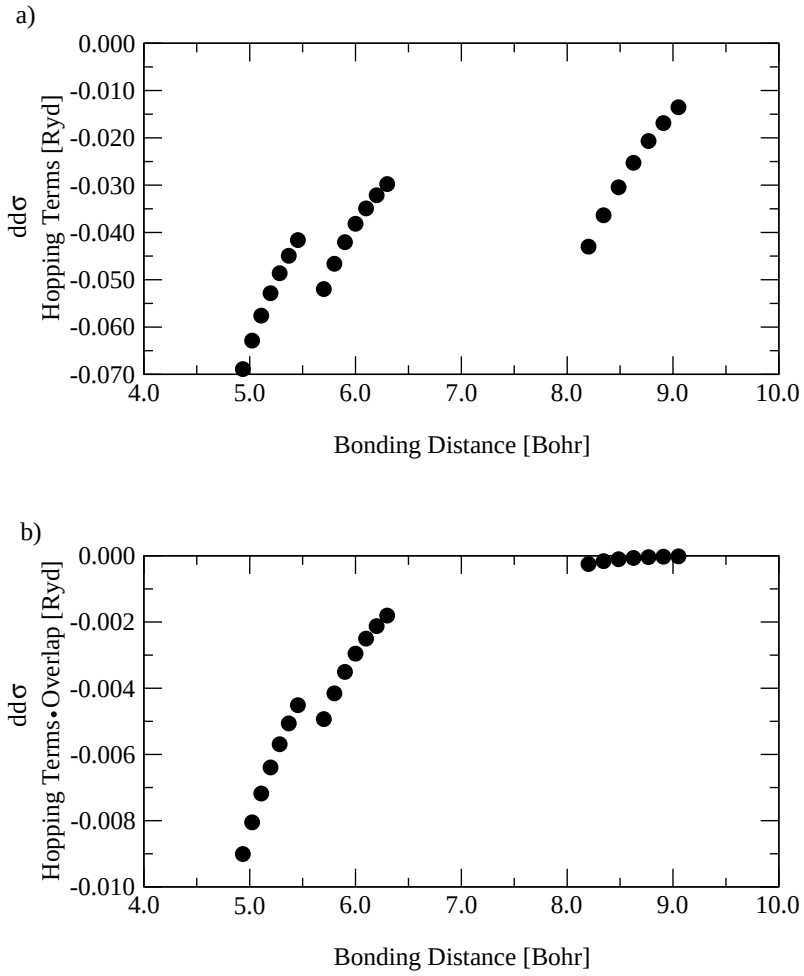


Figure 7.22: Distance dependencies of the $dd\sigma$ terms for distances close to the equilibrium values, calculated as linear combinations of the local ab-initio matrix elements. a) Hopping terms calculated from the Hamiltonian matrix elements b) Product of hopping terms and overlap terms.

## 7.9 Summary

### 7.9.1 Bonding in MoC

The energies of formation of molybdenum mono- and semi-carbides of different crystal structures have been calculated. For the mono-carbides the hexagonal primitive "tungsten-carbide" (WC) structure is most stable and for the semi-carbides the hexagonal close-packed structure is the most favoured one. These results are in agreement with experimental evidence [77, 119, 112].
The bulk moduli of the different structures show that for both, the semi-carbides and the mono-carbides, the most favourable structure is also the most incompressible one.
The bonding mechanism in the molybdenum carbides has already been investigated in chapter 5. The picture gained there could be confirmed and specified:
The site projected densities of states show that the relative positions of the energy levels in molybdenum and carbon are close enough to lead to a strong hybridisation between the molybdenum $s$- and $d$- states and the carbon $s$- and $p$-states. This is independent of the carbon content in the crystal. However, the higher the C concentration is, the more complete is the hybridisation and the less Mo-$d$-states are left for pure metal-metal bonds. Thus, compared to a pure Mo crystal, the metal-metal bonds are partly replaced by Mo-C bonds with strong covalent character. Furthermore, the energy-resolved crystal orbital overlap populations indicate that the remaining Mo-Mo bonds are slightly weakened because in the Mo-C crystal also anti-bonding Mo-Mo states become occupied, which is not the case in the pure metal. Therefore the Mo-C bonds show maximum strength. The comparison of different crystal structures leads to the conclusion that that structure is the most stable in which the most Mo-$d$ states are left for metal-metal bonds and where these bonds are lowest in energy.
The covalent character of the Mo-C bonds was illustrated by plots of the bonding electron density. These plots also indicate charge transfer from the metal to carbon, which can be expected from the relative positions of the bands. For $Mo_2C$ these plots show an additional effect of C occupying some of the interstitial sites in Mo. Bonding charge is transferred to vacant interstitial sites in the Mo lattice, strengthening the metal-metal bonds around these sites.
The question, what makes a specific crystal structure favourable with respect to another can be answered by means of rather simple physical pictures. The types of orbitals present in the MoC crystal in principle allow for $d^2sp^3$ or $d^4sp$ hybridisation at a central atom.

These lead either to octahedral or trigonal prismatic coordination, if we assume purely covalent bonds. The analysis of orbital populations showed that in MoC the trigonal prism is favoured, thus explaining the stability of the WC structure. This is also in agreement with the imagination that in a compound different bonds originating at the same atom should avoid each other as much as possible [25]. In $Mo_2C$, where the metal-metal bonds play a major role, we derived that the $d^2sp^3$ hybridisation leaves more $d$-electrons for Mo-Mo bonds.
The population of the orbitals does not depend significantly on the crystal structure, neither does the promotion energy. These two quantities are determined by the relative positions of the electron states. However, the extent of overlap of orbitals at neighbouring atoms does depend on the crystal structure. The analysis of local orbital overlap population shows indeed, that the trend in the energies of formation is reproduced by the total overlap population per formula unit. Thus, maximum stability comes along with maximum overlap. The extension to the corresponding energy contribution to the bonding energy, the covalent bond energy, is not straightforward however. The analysis of the covalent bond energy for nearest-neighbour bonds shows that this quantity indeed distinguishes between the different types of coordination. However, the trend in the energies of formation is again not reproduced, even if all contributions are summed up to a total covalent bond energy.

### 7.9.2 Semi-Empirical Modelling

A comparison of ab-initio calculated DOS and the DOS derived from a simple $pd$-tight binding model showed, that such a simplified model can indeed reproduce most significant features in the electronic structure. This is encouraging for our intention to describe the Mo-C interaction by an environment-dependent tight-binding model, for which the previously determined and validated parameters describing the Mo-Mo [48, 47] and C-C [116] interactions, respectively, shall be kept fixed. The deficiencies of the $pd$-model should be overcome by a more complex parametrisation.
From the extensive set of ab-initio data it was tried to extract valuable information for fitting the free parameters of the environment-dependent tight-binding model introduced in chapter 4.2. From overlap populations and covalent bond energies of the different contributions to a Mo-C bond, as given in table 7.11, the relative amplitudes of the hopping terms arising from orbitals with different angular momenta were estimated. Distance dependencies of the same quantities allow for a prediction of the cut-off radii and show the

influence of the environment when comparing first and second-nearest-neighbour interactions.

Instead of varying somehow arbitrarily the free parameters of the model until the important features of the molybdenum carbides, e.g. the band structures and the total-energy-volume relations, are reproduced correctly, an alternative approach is suggested. Although the local matrix elements calculated in the ab-initio program are represented in a non-orthogonal basis - in contrast to the orthogonal basis which is assumed in the tight-binding model - it seems a promising approach to fit the parameters of the tight-binding hopping terms directly to the corresponding ab-initio data. The hopping and overlap terms can be calculated by inverting the Slater-Koster rules as linear combination of the ab-initio matrix elements, cf. equation (7.3). Furthermore the investigation of the relationship between non-orthogonality and environment-dependency, although being rather preliminary, indicates the possibility to derive separately the distance-dependent part and the screening in the environment-dependent parametrisation from the ab-initio data. This approach promises a high transferability of the fitted parameters.

# Chapter 8

# Summary and Conclusions

In the work in hand the results of ab-initio investigations for grain and phase boundaries were presented. The calculations were based on the local density functional theory and were carried out using the mixed-basis pseudopotential method [81]. The three central topics of the study were

- the segregation of interstitial impurities at the $\Sigma 5$ STGB in the transition metals Nb and Mo,
- the precipitation of molybdenum carbide at the $\Sigma 5$ STGB in Mo, and
- the properties of different $MoC_x$ bulk phases.

The results of this research shall be summarised by considering, where applicable, these different aspects of the investigation:

- Microscopic insights into the material properties,
- comparison to simple physical, or chemical models, respectively,
- methodological insights from ab-initio analysis, and
- semi-empirical modelling of interatomic molybdenum-carbon interactions.

## 8.1 Light Elements at the Σ5 STGB in Nb and Mo

### 8.1.1 Influence on the Material Properties

The influence of the light interstitial impurity elements B, C, N, and O on the atomic and electronic structures of the Σ5 STGB in Nb and Mo was investigated. Bonding energy differences were calculated to deduce the cohesion-enhancing respective interface-embrittling influences of the impurities.
The results are summarised in the following table:

| | B | C | N | O |
|---|---|---|---|---|
| interatomic bonding character | covalent | covalent | polar | polar |
| grain boundary translation state | I | I | II | II |
| influence of impurity | cohesion enhancing | cohesion enhancing | interface embrittling | interface embrittling |

The following trend emerged: when going from B via C and N to O, the bonding character between the impurity and the host metal changes from dominantly covalent to dominantly polar. Through the different bonding character the impurities have different influences on the microscopic translation state of the grain boundaries. With B at the interface the mirror-symmetric configuration I of the Σ5 STGB in Nb and Mo is favoured. The energy difference between this configuration and the non-mirror-symmetric one, Ⅱ, becomes smaller, changes sign and increases in the other direction when going via C and N to O (cf. figure 5.9). With O at the grain boundary the non-mirror-symmetric configuration Ⅱ of the grain boundary is favoured. At the same time the effect that the impurity has on the cohesive properties changes from cohesion-enhancing to interface-embrittling (cf. table 5.9). The underlying mechanism was identified to be the partial replacement of metal-metal bonds across the interface by metal-impurity bonds. In the case of stronger and covalent bonds, the reduction of the pure metal-metal bonding across the grain boundary is more than compensated and the grain boundary cohesion is increased. In the case of weak and very polar bonds the overall bonding across the interface is weakened and grain boundary embrittlement is promoted.

The observations that the presence of light impurities can alter the translation state of a grain boundary, and that different elements have opposite effects, are of considerable impact for experimental studies of grain boundary structures. As described in the introduction and in chapter 5, numerous efforts have been taken on to determine the microscopic translation state of symmetrical tilt grain boundaries by means of high resolution transmission electron microscopy (HRTEM). Except for the case of Nb [15], the bicrystal specimen of the different transition metals were anticipated to be absolutely pure or the influence of impurities was not discussed at all. However, it has to be faced that even very low impurity contents can alter the translation state of a grain boundary, at least locally. Together with the fact that different impurities can have opposite effects which may compensate each other, this makes the determination of the intrinsic translation state of a pure grain boundary an extremely difficult task. Thus, this work hopefully inspires further experimental investigations of grain boundaries explicitely doped with different impurity elements, to isolate and evaluate the respective effects on the microscopic translation state.

### 8.1.2 Interpretation by Simple Models

By means of Cottrell's unified theory [19] we are able to explain the findings on the basis of comparatively simple physical and chemical models.
One statement of Cottrell's model is that the bonding character between an impurity and the host metal depends on the relative positions of the electronic states. An ample overlap of states leads to a strong hybridisation and to a sharing of the electrons populating these states, and thus to covalent bonds. In case that the valence state of the impurity is lying far below the metal valence band, however, charge is transferred from the metal to the impurity, leading to a further increase of the gap and to ionic (better: polar) bonding behaviour. This explains the change from dominantly covalent to dominantly polar metal-impurity bonds when going from B via C and N to O at the grain boundaries in Nb or Mo, because in this series the first ionisation energies increase on the average with increasing atomic number (see table 5.2). This indicates an increasing gap between the valence states of the metal and the impurity.
According to Cottrell, covalently bonding impurities generally strengthen the interfacial cohesion, whereas polarly bonding impurities decrease it. This is in agreement with the presented results. Cottrell argues that the covalently bonding impurities prefer the environment of the grain boundary over that of the free surface, since for them the bonding energy dominated by the hybridisation energy, which is proportional to $\sqrt{z}$, with $z$ being

the coordination number. As the grain boundary is providing the higher coordination number, the bonding energy is also higher in this environment. For polarly bonding impurities homogeneous contributions (derived e.g. from the effective-medium theory) to the bonding energy are dominating. For them the hybridisation energy is a negative contribution to the bonding energy, what makes the grain boundary less favourable than the free surface. This is in agreement with the calculated bonding energy differences and also partly explains the structural trend we observed: Covalently bonding impurities prefer the more open structure of the mirror-symmetric grain boundary, as it provides the maximum number of bonding partners at more or less equal distances, whereas polarly bonding impurities prefer the more close-packed structure of the non-mirror-symmetric grain boundary, which provides a more spatially homogeneous environment.

### 8.1.3 Insights from Ab-initio Analysis

Cottrell's unified theory gives a descriptive explanation of the ab-initio results presented in this work. It is helpful for interpreting the ab-initio electronic structure data, which is available in large amounts. For instance we have seen that the ab-initio calculated densities of states indicate the relative positions of the electronic states and thus are valuable to estimate the strength of hybridisation and the bonding character (figures 5.10 to 5.13). The strength of the bonds can be evaluated by calculating orbital overlap populations (cf. table 5.7), and their spatial distribution can be visualised e.g. by two dimensional plots of the bonding electron density (see figures 5.14 to 5.17). The discussion of these different quantities in chapter 5 has shown that it is essential to combine several of the named tools, as e.g. the interpretation of the integrated DOS or the bonding electron density alone would have been misleading. At this point it is important to have simple, descriptive models to develop an imagination of the physical process behind the data. A disagreement between the ab-initio results and the model then either tells us to take into account further data - or to check the assumptions of the model.

Indeed Cottrell's model is based on many, partly radical assumptions, thus its legitimation has been questionable. However, with the ab-initio calculations of electronic structures and bonding energy differences we were able to justify the basis of Cottrell's model to a large extent. Still, one has to be careful when transferring it to other systems. For instance the model is completely independent of the grain boundary geometry. To some extent this could be confirmed, as e.g. the type of bonds between impurity and host metal atom does not depend on the translation state of the grain boundary. However, as became

visible with the analysis of the bonding energy differences in terms of chemical and elastic contributions, the elastic part of the bonding energy, due to relaxations of the atomic positions in different environments, does play a role even for small interstitial elements.

## 8.2 Precipitation of Molybdenum Carbide

### 8.2.1 Influence on the Material Properties

Inspired by the investigations of Pénisson et al. [94] the growth of a $MoC_x$ precipitate at the $\Sigma 5$ STGB in Mo was modelled. It was found that a tetragonal precipitate grows with its c-axis meeting the grain boundary at an angle of about 108°. Although this leads to a larger expansion of the Mo lattice perpendicular to the interface than with other geometrically possible orientations, it is more favourable, because in this way the periodicity of the grain boundary is conserved.
This growth of the precipitate leads to two new Mo-$MoC_x$ interfaces, with $x \approx 0.4$, also observed by Pénisson et al. [94]. To model these with a small supercell one of the two bcc Mo grains in the supercell was replaced by a grain of stoichiometric bct MoC. To cope with the lattice misfit between the bcc Mo and the bct MoC bulk phases the MoC lattice was compressed by 13%. To take into account the elastic effects due to this compression, as well as the influence of the higher C concentration with respect to the experimental observation [94], we the compressibility of the precipitate was compared to that of a tetragonal $Mo_2C$ bulk phase. Thus the following values for the work of separation, $W_{sep}$, were received:

| | Mo\|Mo I | Mo\|Mo II | Mo\|$MoC_x$ I | Mo\|$MoC_x$ II |
|---|---|---|---|---|
| $W_{sep}\left[\frac{J}{m^2}\right]$ | 5.788 | 5.893 | 5.474 | 5.320 |

The comparison with the values for the pure $\Sigma 5$ STGB in Mo in the mirror-symmetric configuration I, as well as the non-mirror-symmetric configuration II (Mo|Mo I, respective Mo|Mo II) shows that the adhesive properties of the Mo-Mo interfaces and the Mo-$MoC_x$ are similar. Thus, the precipitate does not promote interfacial embrittlement in the material.

Interface I (cf. fig. 6.8), where the crystal planes of the Mo sublattice meet at an angle of about 135°, is more favourable by an amount of 154 $\frac{mJ}{m^2}$ than interface II (cf. fig. 6.9),

where the Mo sublattice continues under only a small deviation of 6°. The reason is that at interface I the C atoms have more free space to relax. This is also true for the first layer of MoC next to interface I, making a displacement of C across the boundary from MoC into Mo favourable. This process is a possible explanation for the apparently not very sharp interfaces Pénisson et al. [94] observed by HRTEM. At interface II a continuous increase of the tetragonal distortion of the bcc Mo lattice was found. Thus, on a HRTEM picture, where only Mo but not C is visible, this interface is not atomically abrupt as well.

Because of the lattice mismatch, the Mo-MoC interfaces act as traps for misfit-dislocations, as indeed observed by Pénisson et al. [94]. With respect to the macroscopic properties this means that such a tetragonal MoC precipitate at the $\Sigma 5$ STGB in Mo will lead to a stiffening of the metalto a certain extent. However, we know from experiment that the tetragonal $MoC_x$ phase is not stable. Structural phase transformations from a tetragonal to a hexagonal Mo sublattice have been reported by Pénisson et al. [94] as well as earlier by Lepski et al. [73, 74].

### 8.2.2 Insights from Ab-initio Analysis

During the investigation of the precipitation process a lot of experience was gained concerning the choice of the supercell used for the calculations. To investigate the nucleation and growth of the precipitate it was started with the supercell of the pure $\Sigma 5$ STGB (cf. figure 5.2) with one monolayer of C atoms segregated at the interface and subsequently one and two more layers were added, respectively. As mentioned above, by this procedure we the probable crystal structure as well as the orientation relationship of the growing precipitate were determined, but not the direction of the growth. For this the supercell was already too small.
Another problem arose when investigating the two new Mo-MoC interfaces which emerge due to the precipitate. The special choice of the precipitates' thickness lead to an atomic structure, which, after expanding the cell and relaxing the atomic positions, got trapped in a metastable configuration. This configuration was slightly rotated with respect to the stable one (cf. figure 6.14). This curio could have been avoided with two layers of MoC more or less in the supercell. This is an aspect of the supercell construction which one should be aware of in future investigations.

More than any other part of this work, the investigation of the precipitation of $MoC_x$ at the $\Sigma 5$ STGB in Mo demonstrated the need of a good semi-empirical Mo-C model for calculations with larger supercells as well as for dynamical simulations.

## 8.3 Molybdenum Carbide Bulk Phases

### 8.3.1 Material Properties

The energies of formation of molybdenum mono- and semi-carbides of different crystal structures were calculated and the electronic structures investigated. The bonding between molybdenum and carbon turned out to be dominantly covalent, independent of the carbon content in the crystal. For the mono-carbides the hexagonal primitive "tungsten-carbide" (WC) structure is most stable, and for the semi-carbides the hexagonal close-packed structure is the most favoured one. These results are in agreement with experimental observations [77, 112, 119].
The bulk moduli of the different structures (table 7.2) show that for both, the semi-carbides and the mono-carbides, the most favourable structure is also the most incompressible one.

### 8.3.2 Insights from Ab-initio Analysis

In the course of chapter 7 it again became apparent that it is essential to analyse several representations of the electronic structures in the crystal, in order to arrive at a consistent interpretation of the data.
The bonding mechanism in the molybdenum carbides was already investigated in chapter 5, and was identified there as the partial replacement of pure metal-metal bonds by covalent-like metal-carbon bonds. This picture could be further specified:
The site-projected densities of states of the stable carbide (cf. figure 7.3) and semi-carbide (cf. figure 7.4) show that with higher C concentration the hybridisation between the molybdenum *s*- and *d*- states and the carbon *s*- and *p*-states is more complete, and fewer Mo-*d*-states are left for pure metal-metal bonds. The energy-resolved crystal-orbital overlap populations (figures 7.14 and 7.15) indicate that the remaining Mo-Mo bonds are slightly weakened because in the Mo-C crystal also anti-bonding Mo-Mo states become occupied, which is not the case in the pure metal. Therefore the Mo-C bonds show maximum strength. The comparison of different crystal structures leads to the conclusion of that

structure being the most stable in which the most Mo-$d$ states are left for metal-metal bonds and where these bonds are lowest in energy.
The covalent character of the Mo-C bonds was illustrated by plots of the bonding electron density (figures 7.12 and 7.13). These plots also indicate charge transfer from the metal to carbon, which can be expected from the relative positions of the bands. For $Mo_2C$ these plots show an additional effect of C occupying only parts of the interstitial sites in Mo. Bonding charge is transferred to vacant interstitial sites in the Mo lattice and strengthens the metal-metal bonds around these sites.

### 8.3.3 Comparison to Simple Models

One aim of chapter 7 was to find out what makes a specific crystal structure favourable with respect to another. As it turned out, this question can be answered best by means of rather simple physical pictures. The types of orbitals present in the MoC crystal in principle allow for $d^2sp^3$ or $d^4sp$ hybridisation between the orbitals of neighbouring Mo-C atom pairs. These lead either to octahedral or trigonal prismatic coordination, if we assume purely covalent bonds. The analysis of orbital populations showed that in MoC the trigonal prism is favoured, thus explaining the stability of the WC structure. This is also in agreement with the imagination that in a compound different bonds originating at the same atom should avoid each other as much as possible [25]. In $Mo_2C$, where the metal-metal bonds play a major role, we derived that the $d^2sp^3$ hybridisation leaves more $d$-electrons for Mo-Mo bonds.

### 8.3.4 Semi-Empirical Modelling - The Future

In many parts of this work the need for a semi-empirical model became apparent, e.g. to test easily the relationship between the interface geometry of grain boundaries in Mo and the influence of C on the grain boundary cohesion, to be able to vary generously the C concentration at justifiable computational cost, and to treat complex dynamical or kinetical problems as segregation and precipitation.
The thorough investigation of the electronic structures of the different molybdenum carbides and semi-carbides generated a broad ab-initio data set which can be used now to fit the parameters of a suitable semi-empirical tight-binding model.

The first question is, how complex does the model have to be, to provide high transferability of the parameters and thus high reliability, i.e. the power to predict the properties of molybdenum carbides with a wide range of crystal structures and carbon concentrations. At the same time the effort of fitting the parameters shall be kept as small as possible.
A comparison of ab-initio calculated DOS and the DOS derived from a simple *pd*-tight binding model showed, that such a simplified model can indeed reproduce most significant features in the electronic structure, but has some deficiencies. The presented study gives confidence that one should be able to overcome these deficiencies by the more complex parametrisation of the environment-dependent tight-binding model introduced in chapter 4.2. It is intended to use the previously determined and validated parameters describing the Mo-Mo [47, 48] and C-C [116] interactions. One can be optimistic that these previously determined parameters can be kept fixed, and fit only the Mo-C interactions. Thus it shall be achieved that the model will be applicable to a wide range of concentrations and at the same time the complexity of the fit shall be kept as low as possible.

The next task is to choose a fit strategy. First general information is extracted from the ab-initio data for fitting the free parameters of the environment-dependent tight-binding model: From overlap populations and covalent bond energies of the different contributions to a Mo-C bond (cf. table 7.11) the relative amplitudes of the hopping terms arising from orbitals with different angular momenta are estimated. Distance dependencies of the same quantities allow for a prediction of the cut-off radii and show the influence of the environment when comparing first- and second-nearest-neighbour interactions.
Next, instead of varying somehow arbitrarily the free parameters of the model until the important features of the molybdenum carbides, e.g. the band structures and the total-energy-volume relations, are reproduced with sufficient accuracy, an alternative approach is suggested. It seems promising to fit the parameters of the tight-binding hopping terms directly to the corresponding local matrix elements calculated in the ab-initio program. The hopping and overlap terms can be calculated by inverting the Slater-Koster rules as linear combinations of the local matrix elements (cf. equation (7.3)). Furthermore the investigation of the relationship between non-orthogonality and environment-dependency, although being rather preliminary, indicates the possibility to derive separately the distance-dependent part and the screening in our parametrisation from the ab-initio data. This new approach promises a high transferability of the fitted parameters to many crystal structures and compositions.

# Appendix A

# Geometry and Nomenclature of Grain Boundaries

## A.1 Macroscopic and Microscopic Degrees of Freedom

The minimum number of geometric variables required to characterise an interface completely is called the number of geometrical degrees of freedom (DOF) [114]. We distinguish between the macroscopic and microscopic degrees of freedom. The macroscopic DOF are the misorientation relation between the crystals and the inclination of the interface normal. If we imagine the creation of an interface as geometrical construction we can describe it as two crystal surfaces with normal vectors $\mathbf{n_1}$ and $\mathbf{n_2}$ being brought together and afterwards being rotated relatively to each other. The orientation relationship between the two normals can be characterised by the tilt axis $\mathbf{n} = \mathbf{n_1} \times \mathbf{n_2}$ and the tilt angle $\theta_{tilt}$ by which we have to rotate e.g. $\mathbf{n_1}$ around $\mathbf{n}$ to orient it parallel to $\mathbf{n_2}$. This consumes four degrees of freedom. The fifth is the twist angle $\theta_{twist}$ by which one crystal is rotated with respect to the other around the interface normal ($\mathbf{n_1}||\mathbf{n_2}$). In a non-centrosymmetric crystal the chirality is the sixth degree of freedom.
The microscopic degrees of freedom are determined by atomic relaxation at the interface, i.e. they adjust themselves to the macroscopic degrees of freedom such that the energy of the system is minimised. They are the translation vector $\mathbf{t}$ describing the relative shift of grains and, in a crystal with an atomic basis containing more than one atom, the termination of the interface.

Thus, in the most general case there are four microscopic and six macroscopic, i.e. ten, degrees of freedom. In the following we will restrict ourselves to the discussion of centrosymmetric crystals, limiting the number of macroscopic DOF to five.

## A.2 Tilt and Twist Components

As described above, we can construct the rotation relating the two crystals forming a grain boundary by a rotation around an axis in the interface plane (*tilt*) and a rotation around the interface normal (*twist*). If one of the two rotation angles $\theta_{tilt}$ or $\theta_{twist}$ is zero we speak of a pure twist or pure tilt grain boundary, respectively. In the case of a pure tilt grain boundary it is further distinguished between *symmetric* and *asymmetric* tilt boundaries. In the case of a symmetric tilt grain boundary (STGB), the bisecting line of the tilt angle is contained in the interface plane. For special microscopic translations $\mathbf{t}$, the relationship between the crystals in a symmetric tilt grain boundary can be described as a mirror reflection in the boundary plane. STGBs have the same Miller index form in either crystal and only two macroscopic degrees of freedom. At an asymmetric tilt grain boundary two crystals meet with different Miller index forms. They have four macroscopic DOF.

## A.3 Coincidence Site Lattices

In case of a homophase interface, i.e. when the two crystals share the same structure, a superlattice may arise relating the two component crystals. Such a *coincidence site lattice* (CSL) is often used to characterise the geometry of a grain boundary. The density of the CSL points is given by

$$\Sigma = \frac{\Omega_{CSL}}{\Omega_0} \tag{A.1}$$

where $\Omega_{CSL}$ and $\Omega_0$ are the volume of the CSL and the crystal unit cell respectively.

## A.4 Nomenclature of Grain Boundaries

With the definitions introduced in the last sections we can understand the nomenclature of grain boundaries as it is used in this work: the $\Sigma 5$ (310) [001] 36.87° STGB is a *symmetric tilt grain boundary* with the (310) plane being the grain boundary plane and the [001]

direction being the tilt axis. The latter is lying in the interface plane. The tilt angle is 36.87°. The volume of the CSL unit cell is five times that of the original bcc unit cell.

# Appendix B

# Conversion of Units

In this work different units of energy and length have been used. They shall be briefly summarised.
In electron theory it is common to use "atomic units" to reduce the number of constants in the physical formulae. The unit of length is the first Bohr radius in the hydrogen atom, also called "atomic unit" (a.u.):

$$1 \text{ Bohr} = 1 \text{ a.u.} = 0.529 \text{ Å}.$$

The unit of energy is the first ionisation energy of hydrogen, one Rydberg.

$$1 \text{ Rydberg} = 13.606 \text{ eV}.$$

The relations to SI units are

$$1 \text{ Bohr} = 0.0529 \text{ nm}$$
$$1 \text{ Rydberg} = 2.179 \cdot 10^{-18} \text{ J}$$

# Appendix C

# Comments About the Tight Binding Implementation

In this section the main aspects of the implementation of the environment dependent tight binding model into the code of Schilfgaarde et al. is outlined. The implementation was performed under the demand of touching the existing routines as little as possible and of adjusting the new implementation to the given structure. At some points this leads to a reduction of the performance which shall be discussed.

Table C.1 gives a schematic outline of the structure of the tight binding code of Schilfgaarde et al. for ordinary two-centre tight- binding models, as implemented by Paxton. The bold letters mark the different routines. After reading in the crystal structure, atomic coordinates and the TB model parameters (A) the nearest-neighbour list for all atoms is created in the next routine, resulting in a list of n pairs[1] (B). Then the Hamiltonian matrix elements are set up for all the n pairs and saved in n $n_l \times n_l$ submatrices, where $n_l$ is the number of orbitals at the respective atoms of pair n (C). The matrix elements are constructed out of Slater-Koster hopping integrals which are parametrised according to the chosen model. If not only the energy but also the atomic forces shall be calculated, the derivatives of all matrix elements are calculated too, and saved in separate matrices. The matrices are passed over to the next routine (D), where a loop runs over all k-points to calculate the eigenvalues and to accumulate them to the band energy $E_{band}$. If the forces are required the band structure contribution is calculated in parallel. An additional option is to calculate the density of states, which is done separately after the k-point loop.

The next step (E) is to set up the repulsive interaction for all n pairs (and its derivatives

[1] where $(\alpha_1, \alpha_2)$ and the inverse $(\alpha_2, \alpha_1)$ count as two pairs

with respect to the atomic positions) and to sum up the contributions to the repulsive energy $E_{rep}$ (ant the repulsive part of the forces, $F^{rep}$). At the same time the total energy $E_{tot} = E_{band} + E_{rep}$ is calculated (as well as the total forces, $F = F^{band} + F^{rep}$). In a last step (F) the atoms can be displaced and the new atomic coordinates are determined according to the acting forces (relaxation) or to Newton's equations (molecular dynamics)..

| | sequence of subroutines | options |
|---|---|---|
| **A** | read crystal structure,<br>type of tb model<br>and parameters | |
| **B** | make neighbour list | |
| **C** | set up Hamiltonian<br>matrix elements<br>for all n pairs | calculate derivatives<br>of all matrix elements |
| **D** | k-point loop:<br>calculate eigenvalues,<br>$E_{band}$ | calculate $F^{band}$<br>calculate DOS |
| **E** | set up repulsive inter-<br>action for all n pairs<br>calculate $E_{rep}$ and<br>$E_{tot} = E_{band} + E_{rep}$ | calculate derivatives<br>calculate $F^{rep}$ and<br>$F = F^{band} + F^{rep}$ |
| **F** | | relax forces<br>(static or MD) |

Table C.1: Schematic outline of the sequence of tight-binding subroutines in the code of Schilfgaarde et al.

In the following the additions that were implemented will be introduced, first for the band structure energy (parts C,D) and then for the part in which repulsive and total energy are calculated (E).

# C.1 The Band Structure Part

Figure C.1 shows a schematic diagram of the implementation in the band structure part. The boxes drawn by solid lines with the respective loops around them mark the parts of Paxton's original program. The dashed boxes together with the respective loops mark the subroutines which were newly implemented, as was as well the additional loop "over m" plotted as a thin solid line in routine **D**. The loop variables are the pairs of atoms n, the k-points k, and the "type" of atom m ($\alpha$, $\alpha'$, $\alpha''$ or $\alpha'''$).
Let us discuss the calculation of the energy first. After the nearest neighbour list is created in part **B**, in case of the environment-dependent parametrisation a part $\mathbf{B}_2$ is inserted in which extra loops are run over all pairs n to calculate the screening functions and the effective coordination numbers. For each pair n $(\alpha, \alpha')$ a second loop over the nearest-neigbours n' of the respective central atom $\alpha$ is run, to identify the common nearest-neighbours $\alpha''$ of $\alpha$ and $\alpha'$ and to calculate the screening functions (4.36) of hopping and on-site matrix elements (4.35) and of the effective coordination numbers (4.39), as well as the coordination numbers themselves. Then these quantities are passed over to the next subroutine, in which the Hamiltonian matrix elements for all n pairs are set up according to (4.35) as a new option. The matrix is diagonalised for each k-point in the next routine, **C**, where also the band energy is calculated.
If the forces are also required the derivatives of the screening functions and the effective coordination numbers are calculated in routine $\mathbf{B}_2$ in parallel to the integrated values. Here the derivatives with respect to the coordinates of basis atom $\beta$ are of three different kinds,

- $\alpha$: $\beta$ is equal to the central atom,
- $\alpha'$: $\beta$ is equal to the second atom of the pair,
- $\{\alpha''\}$: $\beta$ is a common neighbour of both, $\alpha$ and $\alpha'$.

Due to the periodic boundary conditions $\alpha'$ and $\alpha''$ can be the periodic images of $\beta$, so all three cases can be true at the same time. Thereby the number of elements passed on to the next routine is rather large. In the next step, when the derivatives of the Hamiltonian matrix elements are calculated, the number of derivatives increases once more, as in this case there is the fourth possibility, $\alpha'''$, i.e., that $\beta$ is a nearest neighbour of $\alpha'$, but not of $\alpha$. This case plays a role in the derivatives of the scaled bond lengths (4.38) via the derivative of the effective coordination number of $\alpha'$, $g_{\alpha'}$. To get the contributions from atoms of type $\alpha''$ and $\alpha'''$ two additional loops are passed over all n' neighbours of $\alpha$ and all

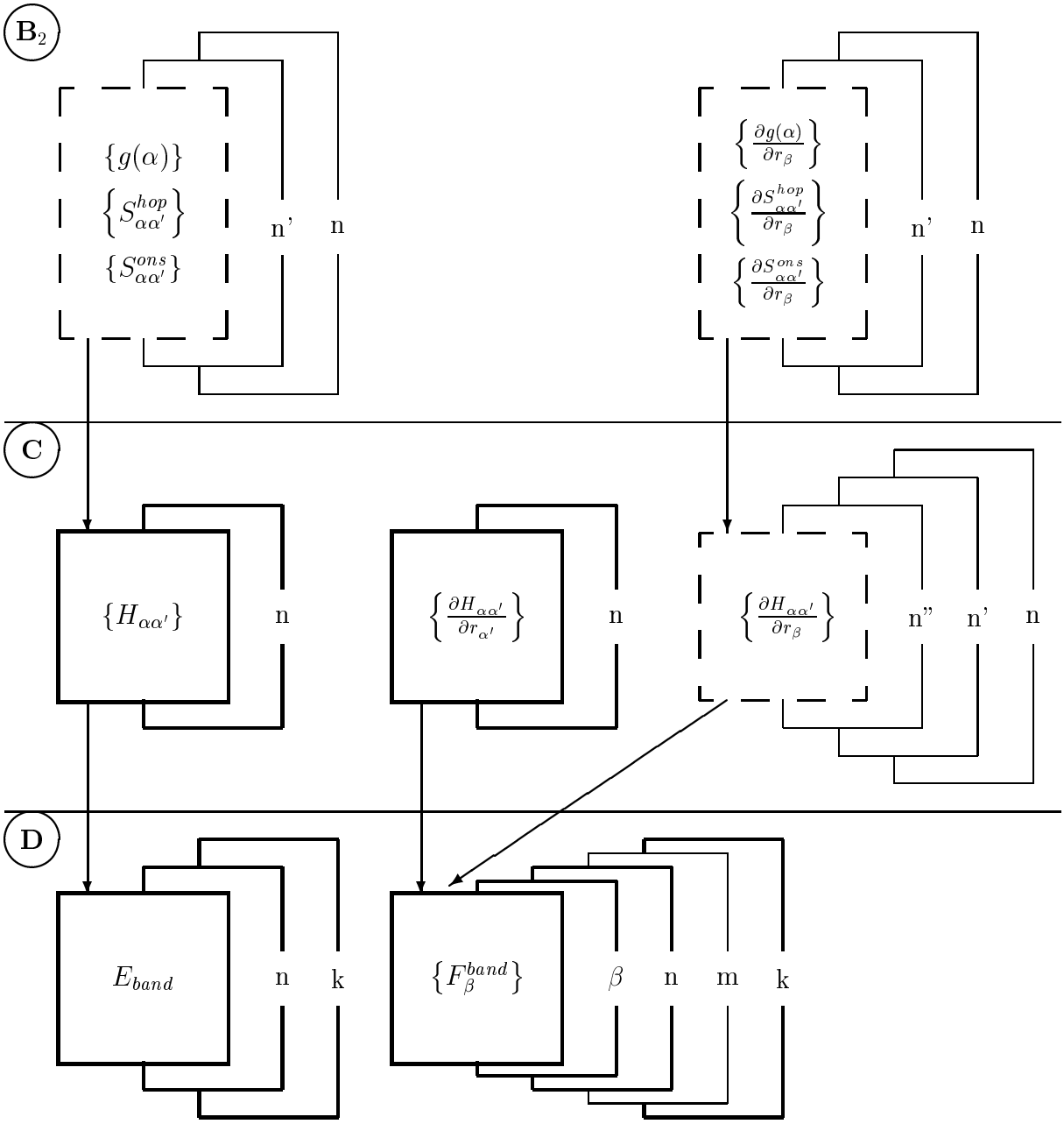


Figure C.1: Schematic diagram of the implementation of the environment dependent tight-bindin model into the band structure part of the code of Schilfgaarde et al. . The boxes drawn by solid lines with the respective loops around them mark the tight-binding parts of Paxton's original program. The dashed boxes together with the respective loops are subroutines which were newly implemented, as was as well the additional loop "over m" plotted as a thin solid line in routine **D**. The loop variables are the pairs of atoms n, the k-points k, and the "type" of atom m ($\alpha$, $\alpha'$, $\alpha''$ or $\alpha'''$).

n" neighbours of $\alpha'$. All these derivatives are passed on to routine **D** where the integration over the first Brillouin zone takes place. In practice this requires a very large work space, which drastically limits the possible number of atoms in the basis at the time being. A way to avoid this, which has already been tested, is not to keep the Hamiltonian matrix in the workspace but to write the data on the hard disk. However, the time which is needed for that almost compensates the gain in computational speed by using a semi-empirical method. A second alternative which has not been considered in the current first version but is planned for a revised and optimised version of the code, is to calculate the derivatives of the screening function and the matrix elements one by one just at the point where they are needed inside the k-point loop in routine **D**, without saving the whole matrix. This procedure, which indeed was already employed by Haas, is similar to the way in which the derivatives of the repulsive contributions are calculated, as will be described in the following section. The additional loops over all pairs needed in this case are minor disadvantages. However, for practical reasons of the implementation that shall not be given here it will no longer be possible to keep to the given structure of Paxton's original code. Instead, the subroutine of **D** calculating the forces $\{F^{band}\}$ will have to be replaced completely. In the current version, the only addition in routine **D** is an additional loop over the type of atom, m, to collect the different contributions for each basis atom.
Nevertheless, at least for the extension of the environment-dependent tight-binding model to systems with more than one elemental component, the current code is applicable and sufficient, since only small unit cells are needed for the fitting of the additional tight-binding parameters for the Mo-C interaction.

## C.2 The Repulsive Part

Diagram C.2 schematically shows how the repulsive energy and the corresponding forces are calculated, in general or when using the environment dependent model. Again, boxes drawn by thick solid lines as well as the corresponding loop mark the original parts of the routine while the dashed box has been added. In Paxton's original version a loop is passed over all n pairs, the repulsive interaction $\phi_{\alpha\alpha'}$ is calculated for this pair and added to the total repulsive energy $E_{rep}$. If the forces are required, the derivative of the pairwise function is calculated in the same step as the function itself. It is added to the forces acting on basis atom $\alpha$.
If the environment dependent parametrisation is used, an additional loop over the n' neigh-

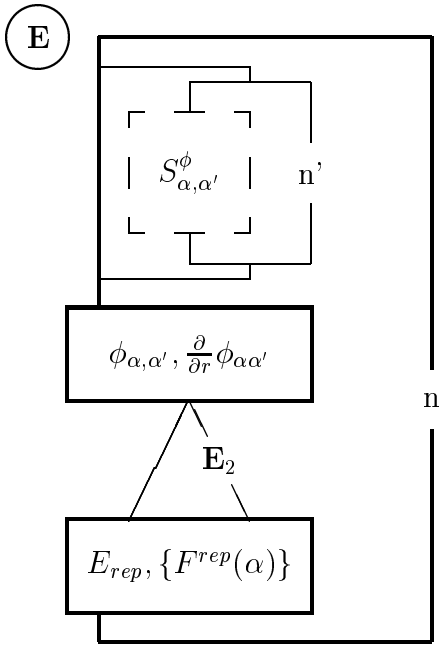


Figure C.2: Schematic diagram of the implementation of the environment dependent parametrisation for the repulsive energy $E_{rep}$ into Paxton's tight binding part of the code of Schilfgaarde et al. . The boxes drawn by thick solid lines, as well as the corresponding loop over all pairs n mark the original part of the program. The dashed box with its loop over n' represents the subroutine which has been added to calculate the repulsive energy within the environment dependent model. $S^{\phi}_{\alpha\alpha'}$ is the screening function for the pairwise repulsive interaction $\phi_{\alpha\alpha'}$. To calculate it an additional loop over the n' neighbours of the central atom $\alpha$ is run. If the forces are required, in case of the environment dependent model the original parts calculating the derivatives and the forces are ignored. Instead a routine $\mathbf{E}_2$ is used, which is described schematically in figure C.3.

bours of $\alpha$ is passed to calculate the screening function $\mathrm{S}^{\phi}_{\alpha\alpha'}$ of the pairwise repulsive interaction before $\phi_{\alpha\alpha'}$ for the respective pair of atoms is set up. If the forces are required, the original parts calculating thederivatives $\frac{\partial}{\partial r}\phi_{\alpha\alpha'}$ and the forces $\{F^{rep}(\alpha)\}$ are ignored. Instead, after the pairwise term $\phi_{\alpha\alpha'}$ was calculated, a subroutine $\mathbf{E}_2$ is passed, which is shown schematically in figure C.3. Then the scheme of the original program is followed again and the contribution of the respective pair of atoms is added to the repulsive energy. In $\mathbf{E}_2$, which is run for each pair $(\alpha, \alpha')$, within an additional loop over all n' neighbours of $\alpha$ the derivatives $\frac{\partial}{\partial r_\beta}$ of the screening function for pairwise repulsive interactions, $S^{\phi}_{\alpha\alpha'}$, are calculated. Here $\beta$ equals succesively $\alpha$, $\alpha'$, and the $\{\alpha''\}$. Subsequently the derivatives of the repulsive interactions are calculated. As in the case of the Hamiltonian matrix elements, there are four types of derivatives. Besides the cases named above, $\beta$ can be $\alpha'''$, a neighbour of $\alpha'$, but not of $\alpha$, which enters via the derivatives of the scaled bond length (the derivatives of the screening function are zero for this case). To get all contributions of type $\alpha''$ and $\alpha'''$ loops over all n' neighbours of $\alpha$ and all n" neighbours of $\alpha'$ are run. In contrast to the way the forces are calculated in the original code, the different derivatives do not only contribute to the force acting on the central atom $\alpha$, but also to the forces acting on the basis atoms of which $\alpha'$, the $\{\alpha''\}$ and the $\{\alpha'''\}$ are periodic images.

For the repulsive interactions it was rather simple to replace the original routine calculating the forces by a separate one for the environment-dependent model. The described scheme saves a loop over all atoms and many lines of code in contrast to what would have been necessary to stick to the given structure. In the case of the band structure part it is the opposite, as using the given structure enables us to use all the subroutines needed for the Brillouin zone integration without any alterations. However, as explained above this leads to a rather bad performance, making the effort attractive to write an independent routine following the scheme used for the repulsive interactions.

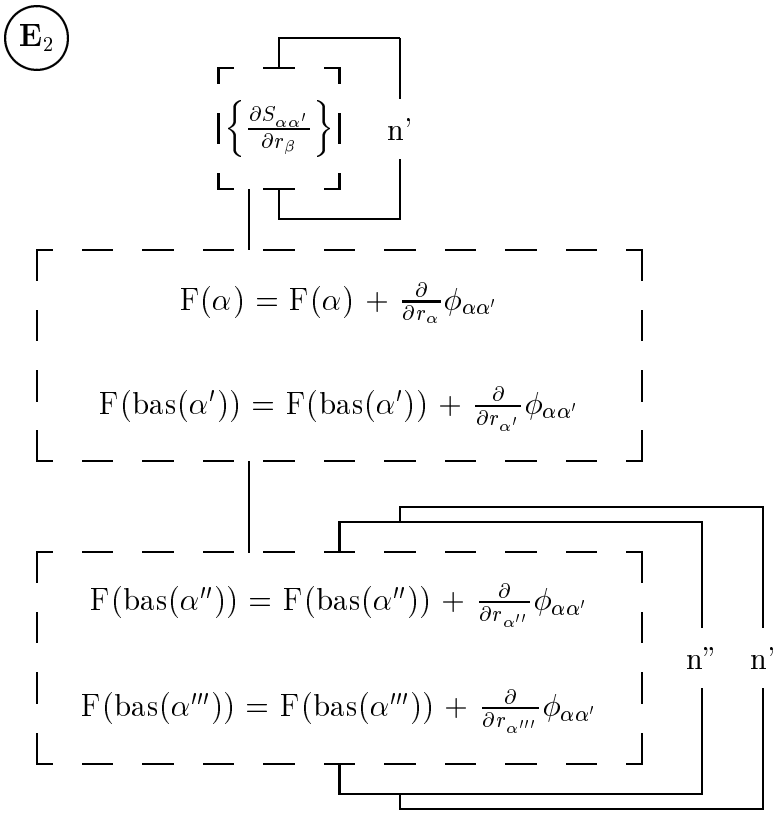


Figure C.3: Schematic diagram of routine $\mathbf{E}_2$ which is part of the environment-dependent parametrisation of the repulsive energy and forces (c.f. C.2). For each pair $(\alpha, \alpha')$ the derivatives of the screening function $S^{\phi}_{\alpha\alpha'}$ with respect to the coordinates of $\beta$ are calculated, where $\beta$ is the central atom $\alpha$, the neighbour $\alpha'$ and the common neigbours $\alpha''$ in succession. Then the contributions of the derivatives of the pairwise repulsive interactions $\phi_{\alpha\alpha'}$ to the forces acting on the corresponding basis atoms are calculated. To get the contributions of type $\alpha''$ and $\alpha'''$ (a neighbour of $\alpha'$ but not of $\alpha$) loops over the neighbours n' of $\alpha$ and n" of $\alpha'$ are run.

# Bibliography


[1] *Gmelin Handbuch der inorganischen Chemie*, vol. Nb: Vol. A. Verlag Chemie, Weinheim/Bergstr., 1969.

[2] *Gmelin Handbook of Inorganic Chemistry*, vol. Mo: Vol. A1. Springer Verlag, Berlin, Heidelberg, New York, Tokyo, 1985.

[3] *Gmelin Handbook of Inorganic Chemistry*, vol. Mo: Suppl. Vol. A2a. Springer Verlag, Berlin, Heidelberg, New York, Tokyo, 1985.

[4] Periodic table of the elements. Wiley-VCH, 1999.

[5] Beck, O. Elektronentheoretische Untersuchung von inneren Grenzflächen in Übergangsmetallen. Diplomarbeit, Institut für Theoretische und Angewandte Physik, Universität Stuttgart und Max-Planck-Institut für Metallforschung, Stuttgart, 1997.

[6] Bester, G., and Fähnle, M. *J. Phys. Cond. Mat.* **13** (2001), 11541.

[7] Born, M., and R., O. J. *Ann. Physik* **84** (1927), 457.

[8] Briant, C. L., and Messmer, R. P. *Acta Metall.* **32**, 11 (1984), 2043.

[9] Brown, H. L., Armstrong, P. E., and P., K. C. *J. Chem. Phys.* **45** (1966), 547.

[10] Buckley, D. H., Ferrante, J., Pashley, M. D., and Smith, J. R. *Mat. Sci. Eng.* **83** (1986), 177.

[11] Buseck, P., Cowley, J., and L., E. *High-Resolution Transmission Electron Microscopy*. Oxford University Press, New York, 1988.

[12] Campbell, G. H., Belak, J., and Moriarty, J. A. *Acta. mater.* **47** (1999), 3977.

[13] Campbell, G. H., Belak, J., and Moriarty, J. A. *Scripta Mat.* **43** (2000), 659.

[14] Campbell, G. H., Foiles, S. M., Gumbsch, P., Rühle, M., and King, W. E. *Phys. Rev. Lett.* **70** (1993), 449.

[15] Campbell, G. H., King, W. E., Foiles, S. M., Gumbsch, P., and Rühle, M. *Mat. Res. Soc. Symp. Proc.* **238** (1992), 163.

[16] Ceperley, D. M., and Alder, B. J. *Phys. Rev. Lett.* **45** (1980), 566.

[17] Clarke, W. A. T., McMahon Jr., C. J., Wagoner, R. H., and Wei, R. P. *Mat. Sci. Eng.* **83** (1986), 205.

[18] Clougherty, E. V., Lothrop, K. H., and Kafalas, J. A. *Nature* **191** (1961), 1194.

[19] Cottrell, A. H. *Mater. Sc. Techn.* **6** (1990), 807.

[20] Cottrell, A. H. *Mater. Sc. Techn.* **10** (1994), 22.

[21] Cottrell, A. H. *Mater. Sc. Techn.* **10** (1994), 788.

[22] Cottrell, A. H. *Mater. Sc. Techn.* **11** (1995), 97.

[23] Cottrell, A. H. *Mater. Sc. Techn.* **11** (1995), 209.

[24] Cottrell, A. H. *Mater. Sc. Techn.* **11** (1995), 329.

[25] Cottrell, A. H. *Chemical Bonding in Transition Metal Carbides.* University Press Cambridge, The Institute of Materials, London, 1995.

[26] Cyrot-Lackmann, F. *J. Phys. Chem. Sol.* **29** (1968), 1235.

[27] Daw, M. S., and Baskes, M. I. *Phys. Rev.* **B 29** (1984), 6443.

[28] Dirac, P. A. M. *Proc. Cambridge Phil. Soc.* **B 26** (1930), 376.

[29] Dronskowski, R., and Blöchl, P. E. *J.Phys.Chem.* **97** (1993), 8617.

[30] Egerton. *Electron Energy-Loss Spectroscopy in the Electron Microscope.* Plenum Press, New York, 1996.

[31] Elsässer, C., Beck, O., Ochs, T., and Meyer, B. *Mat. Res. Soc. Symp. Proc.* **492** (1998), 121.

[32] Elsässer, C., Takeuchi, N., Ho, K.-M., Chan, C. . T., Braun, P., and Fähnle, M. *J. Phys.: Condens. Matter* **2** (1990), 4371.

[33] Fermi, E. *Z. Physik* **48** (1928), 73.

[34] Ferrante, J., and Smith, J. R. *Phys. Rev. B 31*, 6 (1985), 3427.

[35] Feynman, R. P. *Phys. Rev.* **56** (1939), 340.

[36] Finnis, M. W. *J. Phys.: Condens. Matter* **8** (1996), 5811.

[37] Foulkes, W. M. C. PhD thesis, 1987.

[38] Fu, C.-L., and Ho, K.-M. *Phys. Rev. B* **28** (1983), 5480.

[39] Geng, W. T., Freeman, A. J., and Olson, G. B. *Phys. Rev. B* **63** (2001), 165415.

[40] Geng, W. T., Freeman, A. J., Wu, R., Geller, C. B., and Raynolds, J. *Phys. Rev. B* **60**, 10 (1999), 7149.

[41] Geng, W. T., Freeman, A. J., Wu, R., and Olson, G. B. *Phys. Rev. B* **62** (2000), 6208.

[42] Goringe, C. M., Bowler, D. R., and Hernández, E. *Rep. Prog. Phys.* **60** (1997), 1447.

[43] Gottstein, G. *Physikalische Grundlagen der Metallkunde.* Springer Verlag, Berlin Heidelberg New York, 1998.

[44] Guillermet, A. F., Häglund, J., and Grimvall, G. *Phys. Rev. B* **45** (1992), 11557.

[45] Guillermet, A. F., Häglund, J., and Grimvall, G. *Phys. Rev. B* **48** (1993), 11673.

[46] Haas, H. Doctoral thesis, Universität Stuttgart, 1997.

[47] Haas, H., Wang, C. Z., Fähnle, M., Elsässer, C., and Ho, K. *Symposium Mater. Res. Soc.* (1998), 327.

[48] Haas, H., Wang, C. Z., Fähnle, M., Elsässer, C., and Ho, K. M. *Phys. Rev. B* **57**, 3 (1998), 1461.

[49] Haasen, P. *Physikalische Metallkunde.* Springer Verlag, Berlin Heidelberg New York, 1974.

[50] Häglund, J., Grimvall, G., Jarlborg, T., and Guillermet, A. *Phys. Rev. B* **43** (1991), 14400.

[51] Harris, J. *Phys. Rev. B* **39** (1985), 1770.

[52] Harrison, W. A. *Electronic structure and the properties of solids.* Dover Publications Inc., New York, 1989.

[53] Hartweck, W., and Grabke, H. J. *Acta Metall.* **29** (1981), 1237.

[54] Hashimoto, M., Ishida, Y., Wakayama, S., Yamamoto, R., Doyama, M., and Fujiwara, T. *Acta Metall.* **32**, 1 (1983), 13.

[55] Haydock, R., Heine, V., and Kelly, M. J. *J.Phys. C* **8** (1975), 2591.

[56] Hiratsuka, K., Watanabe, K., Hashimoto, I., and Yamaguchi, H. *Phil. Mag. A* **74** (1996), 465.

[57] Ho, K. M., Elsässer, C., Chan, C. T., and Fähnle, M. *J. Phys.: Condens. Matter* **4** (1992), 5207.

[58] Hoffmann, R. *J.Phys.: Condens. Matter* **5**, A1 (1993).

[59] Hohenberg, P., and Kohn, W. *Phys. Rev. B* **136** (1964), 864.

[60] Hong, T., Smith, J. R., and Srolovitz, D. J. *Phys. Rev. B* **47**, 20 (1993), 13 615.

[61] Hong, T., Smith, J. R., and Srolovitz, D. J. *Acta metall. mater.* **43**, 7 (1995), 2721.

[62] Hornbogen, E., and Warlimont, H. *Metallkunde.* Springer Verlag, Berlin Heidelberg New York, 2001.

[63] Itsumi, Y., and Ellis, D. E. *J. Mater. Res.* **11** (1996), 2206.

[64] Itsumi, Y., and Ellis, D. E. *J. Mater. Res.* **11** (1996), 2214.

[65] Janisch, R. Diploma thesis, Universität Stuttgart, 1999.

[66] Janisch, R., Ochs, T., Merkle, A., and Elsässer, C. *Mat. Res. Soc. Symp. Proc. S* **578** (2000), 405.

[67] Keys, L. *Metals Forum* **2** (1979), 164.

[68] Kohn, W., and Sham, L. J. *Phys. Rev. A* **140** (1965), 1133.

[69] Kral, C., Lengauer, W., Rafaja, D., and Ettmayer, P. *Journal of Alloys and Compounds* (1998), 215.

[70] Kumar, A., and Eyre, B. L. *Acta Metall.* **26** (1978), 569.

[71] Lang, J. M., Dahmen, U., and Westmacott, K. H. *phys. stat. sol. a* **75** (1983), 409.

[72] Lennard-Jones, J. E. *Proc. R. Soc. London A* **106** (1924), 463.

[73] Lepski, D., and Burck, P. *phys. stat. sol. a* **64** (1981), 625.

[74] Lepski, D., and Burck, P. *phys. stat. sol. a* **70** (1982), 571.

[75] Louie, S. G., Froyen, S., and Cohen, M. L. *Phys. Rev. B* **26** (1982), 1738.

[76] Louie, S. G., Ho, K.-M., and Cohen, M. L. *Phys. Rev. B* **19** (1979), 1774.

[77] Lu, J., Hugosson, H., Eriksson, O., Nordström, L., and Jansson, U. *Thin Solid Films* **370** (2000), 203.

[78] Marinopoulos, A. G., Vitek, V., and Carlsson, A. E. *Phil. Mag. A* **72** (1995), 1311.

[79] Messmer, R. P., and Briant, C. L. *Acta Metall.* **30** (1981), 457.

[80] Meyer, B. Doctoral thesis, Universität Stuttgart, 1998.

[81] Meyer, B., Elsässer, C., and Fähnle, M. Fortran90 program for mixed-basis pseudopotential calculations for crystals. Max-Planck-Institut für Metallforschung Stuttgart, 1998.

[82] Miodownik, A. P. *Mater. Sci. Technol.* **10** (1994), 190.

[83] Mohn, P., and Pettifor, D. G. *J.Phys.C: Solid State Phys.* **21** (1988), 2829.

[84] Moreno, J., and Soler, J. M. *Phys. Rev. B* **45** (1992), 13891.

[85] Mortimer, C. E. *Chemie.* Georg Thieme Verlag, Stuttgart, 1976.

[86] Mulliken, R. S. *J. Chem. Phys.* **23** (1955), 1833.

[87] Nguyen-Manh, D., Pettifor, D. G., and Vitek, V. *Phys. Rev. Lett.* **85**, 19 (2000), 4136.

[88] Nørskov, J. K., and Lang, N. D. *Phys. Rev. B* **21** (1980), 2131.

[89] Ochs, T. Doctoral thesis, Universität Stuttgart, 2001.

[90] Ochs, T., Beck, O., Elsässer, C., and Meyer, B. *Phil. Mag. A* **80** (2000), 351.

[91] Pashley, M. D., and Pethica, J. B. *J. Vac. Sci. Technol. A* **3** (1985), 757.

[92] Pauling, L. *The Nature of the Chemical Bond and the Structure of Molecules and Crystals.* Cornell University Press, Ithaca NY, 1960.

[93] Paxton, A. T. *J. Phys. D: Appl. Phys* **29** (1996), 1689.

[94] Pénisson, J. M., Bacia, M., and Biscondi, M. *Phil. Mag. A* **73** (1996), 859.

[95] Pepper, S. V. *J. Appl. Phys.* **50** (1979), 8062.

[96] Perdew, J. P., and Zunger, A. *Phys. Rev. B* **23** (1981), 5048.

[97] Pettifor, D. G. *Solid State Communications* **51** (1984), 31.

[98] Pettifor, D. G. *J.Phys:C:Solid State Phys.* **19** (1986), 285.

[99] Pettifor, D. G. *Solid State Physics* **40** (1987), 43.

[100] Pettifor, D. G., and Cottrell, A. H. *Electron Theory in Alloy Design.* The Institute Of Materials, Oxford, 1992.

[101] Pettifor, D. G., and Podloucky, R. *Phys. Rev. Lett.* **53** (1984), 1080.

[102] Pettifor, D. G., and Podloucky, R. *J.Phys:C:Solid State Phys.* **19** (1986), 315.

[103] Reimer, L. *Energy-Filtering Transmission Electron Microscopy.* Springer Verlag, Berlin, 1995.

[104] Rice, R. J., and Wang, J.-S. *Mat. Sci. Eng. A* **107** (1989), 23.

[105] Sanchez-Portal, D., Artacho, E., and Soler, J. M. *Solid State Comm.* **95**, 10 (1995), 685.

[106] Sanchez-Portal, D., Artacho, E., and Soler, J. M. *J.Phys.: Condens. Matter* **8** (1996), 3859.

[107] Sharma, R. R. *Phys. Rev. B* **19** (1979), 2813.

[108] Sigle, W. unpublished results. Max-Planck-Institut für Metallforschung, Stuttgart, 2002.

[109] Slater, J. C., and Koster, G. F. *Phys. Rev.* **94**, 6 (1954), 1498.

[110] Smith, J. R., and Cianciolo, T. V. *Surf. Sci. L* **210** (1988), 299.

[111] Smith, J. R., Ferrante, J., and Rose, J. H. *Phys. Rev. B* **25**, 2 (1981), 1419.

[112] Storms, E. K. *The Refractory Carbides.* Academic Press, New York and London, 1967.

[113] Sutton, A. P. *Electronic Structure of Materials.* Oxford University Press, Oxford, 1993.

[114] Sutton, A. P., and Balluffi, R. W. *Interfaces in Crystalline Materials.* Clarendon Press, Oxford, 1995.

[115] Taheri, M. *Mat. Sci. Eng.* **32** (1978), 221.

[116] Tang, M. S., Wang, C. Z., Chan, C. T., and Ho, K. M. *Phys. Rev. B* **53**, 3 (1996), 979.

[117] Tersoff, J. *Phys. Rev. Lett.* **56** (1986), 632.

[118] Thomas, L. H. *Proc. Cambridge Phil. Soc.* **23** (1927), 542.

[119] Toth, L. E. *The Transition Metal Carbides.* Academic Press, New York and London, 1971.

[120] Wu, R., Freeman, A. J., and Olson, G. B. *Phys.Rev.B* **50** (1994), 75.

[121] Wu, R., Freeman, A. J., and Olson, G. B. *Phys.Rev.B* **53** (1996), 7504.

[122] Wu, X., Hu, B., and Zheng, Q. *Chinese Phys. Lett.* **5**, 4 (1987), 157.

[123] Xu, C. H., Wang, C. Z., Chan, C. T., and Ho, K. M. *J.Phys.: Condens. Matter* **4** (1992), 6047.

[124] Zhong, L., Wu, R., Freeman, A. J., and Olson, G. B. *Phys. Rev. B* **55** (1997), 11133.

# Acknowledgements

I wish to thank

Prof. Manfred Rühle for the kind reception in his department and for providing the departmental facilities.

exceptionally Prof. Christian Elsässer for his steady guidance and support.

Prof. Ulrich Weiss for taking on the "*Mitbericht*".

my past and present colleagues of "the theory group" for the great working environment and many fruitful discussions.

my colleagues of the Rühle department for their comradeship and many insights into the "experimental reality".

Stefano Fabris for helping me along with the tight-binding implementation.

everyone who proofread my thesis.

my friends who accompanied my way by some means or other, especially Elmar, Erik, Felix and Franziska.

my family; in particular my mother for her continuous encouragement and support.